Universidad Autónoma de Madrid
Facultad de Ciencias
Departamento de Física de la Materia Condensada

Optical and Magnetic Tweezers for Applications in Single-Molecule Biophysics and Nanotechnology

Tesis elaborada por

Benjamin Gollnick

para optar al grado de

Doctor en Biofísica

Diciembre de 2014

Director de tesis: Dr. Fernando Moreno Herrero, científico titular del Consejo Superior de Investigaciones Científicas (Centro Nacional de Biotecnología (CNB–CSIC), Departamento de Estructura de Macromoléculas)

Tutor: Prof. Dr. Julio Gómez Herrero, catedrático de la Universidad Autónoma de Madrid (UAM, Facultad de Ciencias, Departamento de Física de la Materia Condensada)

Día de la entrega: 2 de diciembre de 2014

Día de la defensa: 22 de enero de 2015

Miembros del tribunal de tesis:

- Prof. Dr. Juan José Sáenz Gutiérrez, catedrático de la Universidad Autónoma de Madrid (UAM) — *presidente*
- Dr. José Ricardo Arias González de la Aleja, investigador del Instituto Madrileño de Estudios Avanzados en Nanociencia (IMDEA Nanociencia) — *secretario*
- Prof. Dr. Felix Ritort Farrán, catedrático de la Universidad de Barcelona (UB) — *vocal 1*
- Dr. Carlo Manzo, investigador (research fellow) del Instituto de Ciencias Fotónicas (ICFO), Catelldefels (Barcelona) — *vocal 2*
- Dr. Jorge Alegre Cebollada, investigador (jefe de grupo) del Centro Nacional de Investigaciones Cardiovasculares (CNIC), Madrid — *vocal 3*
- Prof. Dr. Francisco Monroy Muñoz, profesor titular de la Universidad Complutense de Madrid (UCM) — *suplente 1*
- Dra. Montserrat Calleja Gómez, investigadora científica del Instituto de Microelectrónica de Madrid (IMM–CNM–CSIC) — *suplente 2*

Dedicated to my family and friends

Preface

"Was lange währt, wird endlich gut." According to this popular German saying, some things may take a bit more time to get finished properly. In that sense, giving birth to this thesis truly needed some effort but has been worth the wait. It is the product of work carried out during the last six years in the field of biological physics and could not have been accomplished without the help and support from a lot of people. Some of them I would like to mention here in particular.

First and foremost, I want to express my gratitude to my supervisor, Dr. Fernando Moreno, for giving me the chance to participate in the exciting process of establishing a new research laboratory. Fernando was brave enough to lend me a lot of responsibility and freedom from the very beginning, which has enabled me to gain valuable experiences I would probably not have made during a "conventional" PhD project. Although things have not always been easy, the outcome now feels even more rewarding, especially the one of Chap. 3. Thanks to Fernando, I have also been able to get to know the magnetic tweezers technique and learn some of the basics of molecular biology, which for sure will be useful for my future career.

Secondly, I thank the seven members of the examination committee for assuming the duty of reviewing the manuscript and (if applicable) posing their questions on the day of defence. I should also mention Prof. Julio Gómez, who has served as my tutor at the university throughout these years.

Some parts of this thesis would never have seen the light without external collaborations. I want to acknowledge Prof. Mark Dillingham and his (former) group members at the University of Bristol, in particular Neville Gilhooly, for providing us with DNA and protein samples and performing the bulk measurements shown in Chap. 5; but more importantly, for our fantastically organised mutual visits and all the fruitful discussions.

I was also very lucky to spend two months in the group of Dr. Ulrich Keyser at the Cavendish Laboratory of the University of Cambridge. Since the good old times in Leipzig, Ulrich has always been a great mentor willing to share his knowledge about optical traps (and all sorts of other things). I thank him and all members of his lab for making my research stay such a pleasant one. I am especially grateful to Nadanai Laohakunakorn for letting me contribute to what turned out to be a very productive short-term project (see Chap. 4). Prof. Sandip Ghosal from Northwestern University needs to be acknowledged for figuring out the theory behind the microsphere rotations, and Prof. Dirk Aarts and Dr. Roel Dullens from the University of Oxford for preparing the dimpled colloids.

At this point, I would also like to mention Hergen Brutzer, Lorenz Steinbock and Oliver Otto, all former co-workers and now friends from Germany, who have helped me through their dissertations to bring this thesis come to life.

As far as internal collaborations are concerned, I am indebted to various (former) members of the groups led by Dr. Borja Ibarra and Dr. Ricardo Arias for a lot of help with all kinds of technical issues, mainly during the initial and final stages of my principal PhD project. In particular, I would like to thank Borja for both sharing his stocks of microspheres and teaching me how to functionalise them by myself. Many thanks also to Dr. Elías Herrero and José Morín for providing me with DNA samples and buffers (and for advising me how

to use them properly), apart from their data shown as reference curves in Chap. 3. Ricardo, together with Silvia Hormeño, needs to be mentioned as an expert in optical equipment and in setting up microscopes, which proved beneficial in the early days of construction of our optical tweezers instrument. Moreover, all of them introduced me to the challenging but yet so important task of pulling pipettes and fabricating flow cells.

It has been a privilege to share the office with great colleagues, some of whom I can now consider as true friends. I would like to thank Dr. Carolina Carrasco, not only for carrying out the magnetic tweezers experiments shown in Chap. 5 and helping me translate parts of this document into Spanish, but also for being such an enjoyable person to work with. The same holds for Maru Fuentes, who has been much more than just a constant backup facilitating me the paperwork necessary to hand in this thesis, apart from proofreading parts of it and correcting my translations. Francesca Zuttion deserves a special mention, not only since she contributed some of the data described in Chap. 5, but also because she once took on with remarkable persistence a set of rather tedious measurements while I was in England. I also remember Maite Arranz as a very sympathetic computer scientist and valuable source of programming knowledge, even though we never developed the same kind of love for LabVIEW. Finally, I should acknowledge César L. Pastrana for performing essential magnetic tweezers force calibrations and always being disposed to help out. To all of you and everyone else in room number B.18: I wish you the very best for your future!

I also need to recognise the work done by various services and administrative departments at the CNB (*almacén*, *compras*, *mantenimiento*, *personal*, *viajes* etc.) that make the life of a researcher a lot easier. In particular, I am grateful to Nicasio and (his successor) Daniel from the mechanical workshop (*taller*) for fabricating increasingly accurate components for our experimental setups. The technical drawings I have handed in during the last six years could make up an entire thesis chapter by themselves!

I would also like to say thanks to all the (former) people from labs S.0/S.5 who I have had the pleasure to get to know, especially to Adriana, Ana, Elías, María, Rebeca and Silvia for our nice conversations during and after lunch.

Last but not least, I want to thank my entire family in Germany, especially my parents, for consistently supporting me from the distance, and for always showing great interest in the things I have been doing.

Here in Spain, Virtudes deserves the highest gratitude of all because without her patience and steady encouragement, especially during the most difficult times, this thesis would never have been written.

I end my acknowledgements by thanking the Spanish Ministry of Education for granting me with an FPU PhD scholarship during four years of my postgraduate studies, including the costs for my two-month stay in Cambridge, and the European Research Council and the Spanish Ministry of Science and Innovation for providing my supervisor with the complementary funding I needed to initiate and terminate my research projects.

Benjamin Gollnick
Madrid, December 2014

Abstract

Over the last few decades, continuous improvements of microscopy techniques have constituted one of the driving forces for the interdisciplinary field of single-molecule biophysics – a scientific environment that bridges areas of physics, biology, chemistry and micro-/nanotechnology, amongst others. This dissertation deals with the design, construction and use of two types of instruments based upon optical microscopes: optical and magnetic tweezers to manipulate individual biomolecules such as DNA or proteins in solution.

First of all, the assembly of a tailor-made optical tweezers setup in an inverted microscope configuration with a single objective is discussed. Such a design provides free access to the top side of the sample stage, facilitating for instance the implementation of different flow cell types. Thanks to the development of an application-specific software, the system can exploit both video- and laser-based position detection methods – the latter via back-reflections of an additional low-power laser. We have calibrated the trap stiffness for polystyrene microspheres by spectral analysis of thermal fluctuations and viscous drag measurements. Using a micropipette as a mechanical anchor point for pulling experiments, trapping-laser-induced thermal drift effects can be minimised by active control of the objective temperature and sample stage position corrections. In its current state, the entire assembly is able to carry out and measure force–extension curves of various DNA substrates, with a precision that resembles the one of other optical trapping instruments.

In a second project, an optical tweezers device equivalent to the aforementioned is employed in combination with an ionic current sensing platform to probe electrically induced fluid flows through glass nanopipettes. Rotation rates and frictional forces, exhibited by optically trapped microspheres with a small cavity, relate directly to the local flow field outside the pore and comply with the Landau–Squire solution of the Navier–Stokes equations. Raster-scanning the area in front of the pipette tip with this micrometric anemometer, the volume flow rate at the pore exit turns out to be on the order of tens of picolitres per second – below the majority of velocities assessable with other flow-measuring techniques.

Finally, the implementation of a customised temperature control system in a magnetic tweezers instrument is presented. Simplicity and flexibility of the thermostat make it attractive for other techniques based on inverted microscopes. Between ambient and physiological conditions, thermal settings inside the buffer volume are adjustable with a precision of 0.1 °C. We have tested the complete setup with the molecular motor AddAB, a helicase–nuclease protein complex that moves along double-stranded DNA. In comparison with results from bulk assays, the thermally stabilised magnetic tweezers yield the same relative exponential increase of AddAB velocity with temperature. Absolute translocation rate values from single-molecule and ensemble measurements can be matched by saturating the effective ATP concentration near the protein in the magnetic tweezers flow cell.

Resumen

Durante las últimas décadas, el continuo perfeccionamiento de las técnicas de microscopía ha sido una de las fuerzas motrices para el campo interdisciplinar de la biofísica a nivel de molécula individual – un entorno científico que abarca áreas de física, biología, química y micro-/nanotecnología, entre otras. Esta tesis trata sobre el diseño, la construcción y el uso de dos tipos de instrumentos basados en microscopios ópticos: pinzas ópticas y magnéticas para manipular biomoléculas individuales como el ADN o proteínas en solución.

En primer lugar, se describe el montaje de unas pinzas ópticas confeccionadas a medida en una configuración de microscopio invertido de un solo objetivo. Este diseño proporciona libre acceso a la parte superior de la mesa de muestras, lo que facilita por ejemplo la implementación de diferentes tipos de celda líquida. Gracias al desarrollo de un software específico, el sistema puede aprovechar métodos de detección de la posición tanto por vídeo como por luz láser – en el segundo caso a través de las reflexiones de un láser adicional de baja potencia. Hemos calibrado la rigidez de la trampa para microesferas de poliestireno mediante el análisis espectral de las fluctuaciones térmicas y medidas de fricción de fluido. Usando una micropipeta como punto de anclaje mecánico durante ensayos con moléculas estiradas, los efectos de la deriva térmica inducida por el láser de atrapamiento se pueden minimizar mediante un control activo de la temperatura del objetivo y correcciones de la posición de la mesa de muestras. En su estado actual, el aparato íntegro es capaz de realizar y medir curvas fuerza–extensión de diversos sustratos de ADN, con una precisión similar a la de otros instrumentos de atrapamiento óptico.

En un segundo proyecto, un dispositivo de pinzas ópticas equivalente al ya mencionado se emplea junto con un sistema de detección de corrientes iónicas para sondear flujos inducidos eléctricamente en nanopipetas de vidrio. Las velocidades de rotación y fuerzas de arrastre, exhibidas por microesferas atrapadas que presentan una pequeña concavidad, están en relación directa con el campo de flujo local y cumplen con la solución de Landau–Squire de las ecuaciones de Navier–Stokes. Escaneando el área delante del poro de la pipeta con este anemómetro micrométrico, el flujo de volumen en la salida resulta ser del orden de decenas de picolitros por segundo – por debajo de la mayoría de las velocidades que se pueden evaluar con otras técnicas de medición de flujo.

Por último, se presenta la implementación de un sistema personalizado de control de temperatura en unas pinzas magnéticas. La sencillez y flexibilidad del termostato lo hacen atractivo para otras técnicas basadas en microscopios invertidos. En el rango definido entre las temperaturas ambientales y fisiológicas, las condiciones térmicas dentro de la celda líquida se pueden ajustar con una precisión de 0.1 °C. Hemos aplicado el instrumento al estudio del motor molecular AddAB, un complejo proteico helicasa–nucleasa que camina a lo largo del ADN de cadena doble. En comparación con resultados de ensayos en volumen, las pinzas magnéticas térmicamente estabilizadas miden el mismo aumento exponencial relativo de la velocidad de AddAB con la temperatura. Los valores absolutos de velocidad detectados a nivel de molécula individual y en volumen se pueden asimilar saturando la concentración eficaz de ATP cerca de la proteína en la celda líquida de las pinzas magnéticas.

Contents

1. Introduction

1.1. The relevance of single-molecule approaches

Most analytical methods in biochemistry and molecular biology make use of sample volumes that contain huge numbers (on the order of millions) of the biological object under study – usually a certain molecule or molecular assembly. Well-established routines of this kind may give precise numerical values reflecting the *average* performance of large populations during a single experiment and are consequently referred to as ensemble or bulk techniques. One of their major shortcomings is that, by accentuating prominent signal contributors they miss out on minor contributions and can hardly infer any information about fluctuations in the molecular behaviour with time or among different sample subsets. Such heterogeneities are important however in several ways: from a physical viewpoint, as they can reveal valuable details not detectable at the ensemble level, e.g. intermediate states or rare events during protein folding; and from a physiological perspective, as in many cases only a low copy number of a certain species is present in each cell of a living organism, making it susceptible to the inherent stochastic nature of biomolecular function.

Although the history of experiments with individual biological molecules in solution can be traced back to a study from 1961 [Greulich, 2004] in which microdroplets were used to monitor the reaction catalysed by single β-galactosidase enzymes [Rotman, 1961], it has been primarily during the last thirty years that extensive technological effort has established a second kind of methods, sensitive enough to directly explore the dynamics and – in some cases – mechanics of *individual* proteins or nucleic acids at biologically relevant length, force and time scales. In doing so, these so-called single-molecule techniques are capable of providing, with ever-increasing resolution, complementary information that is inaccessible to their bulk counterparts. Figure 1.1 shows a diagram that reflects the interdisciplinarity of science based on experiments probing only one molecule at a time.

1.2. Scope of the dissertation

This thesis describes the development and application of two different optical microscopy techniques for biophysical experiments at the single-molecule level: optical and magnetic tweezers. Right from the start, the constraints of planning and construction were simplicity and flexibility, considering that the customised setups might have to adapt to different types of (single-molecule) assays.

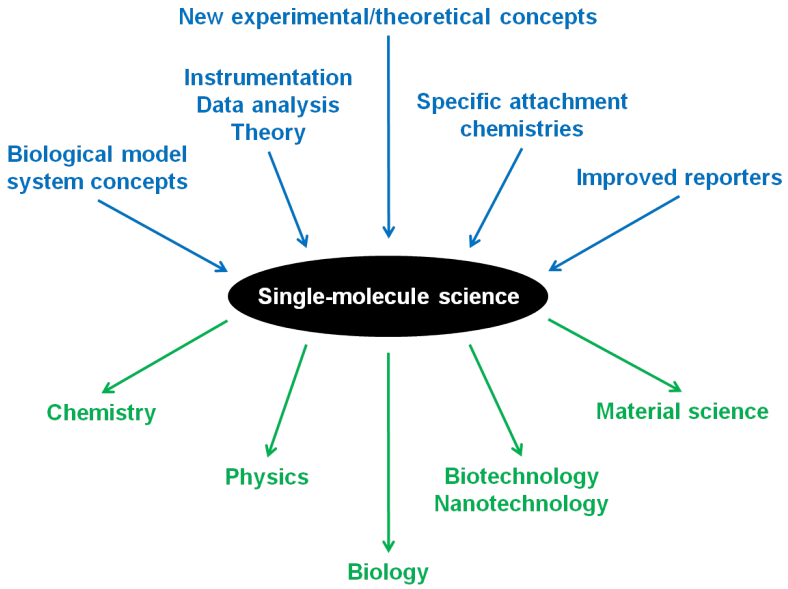

Figure 1.1. The interdisciplinary nature of single-molecule science. Studies with individual biomolecules rely on progress in different research areas (blue) and have an impact on a variety of disciplines (green). This PhD thesis focuses on developments in instrumentation and data analysis, as well as on novel experimental approaches, leading to new contributions in biological physics and nanotechnology. [Figure modified from [Deniz et al., 2008].]

1.2.1. Objectives

One can formulate three principal goals concerning the work carried out – primarily during the last five years – in the context of the herein documented PhD projects. The first one was defined at the beginning, while the other two originated in the course of time:

- Design, assembly and characterisation of an optical tweezers (OT) instrument in an inverted microscope configuration, with free access to the space on top of the sample cell; first experiments with DNA molecules and, potentially, protein–DNA constructs.
- Utilisation of the acquired technical knowledge about OT to investigate the properties of a well-controlled experimental method such as glass nanopipettes; measurements of the typical, electrically induced flows at the pore exit via the behaviour of optically trapped, slightly asymmetric microspheres.
- Development and start-up of a temperature control system for upright, permanent-magnet-based magnetic tweezers (MT); application of the thermally controlled microscope to the study of DNA translocation kinetics using a protein model system.

1.2.2. Outline

Given the aforementioned objectives, I have structured the content of this dissertation as follows:

- **Chapter 2** presents some general information about the force-measuring single-molecule techniques we have developed and employed.
- **Chapter 3** provides a detailed description of a single-beam OT apparatus built from scratch, corresponding calibration procedures and proof-of-principle force–extension measurements with DNA substrates.
- **Chapter 4** shows how such a setup can be applied to determine the volume flow rate through glass nanopores – which represent another powerful approach for the detection of individual molecules.
- **Chapter 5** explains the implementation of a modular thermostat unit in tailor-made MT. This device was used to study the temperature dependence of translocation along double-stranded (ds)DNA by the bacterial helicase–nuclease AddAB, a protein involved in the initial steps of dsDNA break repair by homologous recombination.
- **Chapter 6** completes the manuscript with the main conclusions.

2. Force spectroscopy techniques based on optical microscopes

The ability to directly measure forces and displacements at piconewton ($1\,\mathrm{pN} = 10^{-12}\,\mathrm{N}$) and nanometre ($1\,\mathrm{nm} = 10^{-9}\,\mathrm{m}$) resolution was a breakthrough for basic research at the interface of biology, chemistry and physics. Considering that the thermal energy at room temperature ($T = 25\,^{\circ}\mathrm{C} = 298\,\mathrm{K}$) is just $k_\mathrm{B}T = 4.11 \cdot 10^{-21}\,\mathrm{N{\cdot}m} = 4.11\,\mathrm{pN{\cdot}nm}$ (with k_B being the Boltzmann constant) for an individual biomolecule in its natural environment, it becomes clear that these are the orders of magnitude that govern the function of practically all known living systems. To date, a growing number of laboratories around the world applies single-molecule approaches to study the fundamental processes of life [Ritort, 2006]. In this context, it is safe to say that the most widespread force-measuring techniques are optical tweezers (OT), magnetic tweezers (MT) and atomic force microscopy (AFM) [Neuman and Nagy, 2008]. This chapter focuses on the description of the first two methods, which constitute the main subject of this thesis. As an extensive amount of literature exists, only aspects that are crucial for the understanding of the remaining manuscript will be discussed. In both cases, these comprise a short introduction, the underlying physics of force/position determination and some general design considerations.

2.1. Optical tweezers

2.1.1. Introduction from a historical perspective

Although optical micromanipulation became available only in recent decades, the basic principle of light interacting with matter dates back to the early 17$^{\mathrm{th}}$ century, when Johannes Kepler pointed out that the tail of a comet always faces away from the sun [Heidarzadeh, 2008] – an effect due to solar wind as we know today. After the formulation of electromagnetism by James Clerk Maxwell in the 19$^{\mathrm{th}}$ [Maxwell, 1861] and seminal work on radiation pressure by Peter Debye at the start of the 20$^{\mathrm{th}}$ century [Debye, 1909], the first successful application of a laser in 1960 [Maiman, 1960] paved the way to the utilisation of the cumulative momentum from an intense source of photons as a scientific tool. In fact, only nine years later, Arthur Ashkin pioneered the field of optical trapping by confining single microparticles between two counterpropagating laser beams [Ashkin, 1970]. However, it took him and his team until 1986 to establish what he then called "single-beam gradient force radiation-pressure particle trap", today commonly known as "optical tweezers" [Ashkin et al.,

1986]. After discovering – rather by coincidence – that it was also possible to trap *living* matter with laser light [Ashkin and Dziedzic, 1987], Ashkin's exceptional invention lead to unprecedented experiments in biological physics and boosted the evolution of the newly created field of single-molecule science.

Already in 1990, Block and colleagues published a study in which they used OT to directly monitor the motion of single copies of the motor protein kinesin along microtubules [Block et al., 1990]. Three years later, their instrument provided enough control and precision for them to resolve the 8 nm steps by which kinesin advances [Svoboda et al., 1993]. In 1996, Bustamante and co-workers were the first to apply OT technology for measuring the mechanical response of individually stretched DNA molecules up to forces of 80 pN [Smith et al., 1996]. In all three studies, a paradigm of force-measuring single-molecule techniques based on optical microscopes becomes apparent: as the biological object is too small to be observed directly, it has to be manipulated by – and its behaviour inferred from – the movement of much larger handles or probes. In the case of optical traps, these are usually micrometre-sized spheres made of polystyrene or silica [Bustamante et al., 2000]. For about 25 years now, OT have contributed substantially to the broadening of our knowledge about key biological phenomena: from motion cycles of molecular motors to the elastic properties of nucleic acids to fundamental cellular processes such as transcription or translation [Fazal and Block, 2011; Hormeño and Arias-Gonzalez, 2006]. At the same time, instruments have undergone a continuous evolution in terms of increased resolution and combination with other techniques such as fluorescence microscopy, enabling the performance of ever more complex experiments at sub-nanometre and sub-piconewton precision [Moffitt et al., 2008].

At present, there exist principally two different approaches to confine micrometric particles with laser light: (i) optical traps relying on the balancing effects of two counterpropagating beams [Smith et al., 1996] and (ii) single-beam traps according to Ashkin's nomenclature, allowing micromanipulation through tight focusing of a single laser only [Ashkin et al., 1986]. Although the former have advantages such as the possibility to directly measure the applied force without prior calibration of the trapping potential [Grange et al., 2002; Smith et al., 2003], in the following only the latter and more flexible type of OT is introduced as it corresponds to the experimental setup relevant for this thesis. After the basic theoretical issues, I will introduce the most important components of such an instrument and explain the principles of force calibration and position detection.

2.1.2. Essential theory of optical trapping

An optical trap is created by coupling a collimated laser beam in a microscope objective with high numerical aperture (NA). In the vicinity of the focal spot, dielectric particles with a refractive index n_p larger than the one of the surrounding medium n_m can be immobilised [Ashkin et al., 1986]. For arbitrary particle shapes and wavelengths of

light, a complete theoretical framework of the involved light–matter interactions is difficult to construct. Even in the most common case, in which the laser wavelength in solution λ is similar to the radius r_p of a trapped microsphere, an adequate description of the observed phenomena requires elaborate formalisms such as generalised Lorenz–Mie theory [Nieminen et al., 2007], whose predictions were verified experimentally only ten years ago [Rohrbach, 2005]. Luckily, the limiting cases of $r_\mathrm{p} \gg \lambda$ (ray optics or Mie scattering regime) and $r_\mathrm{p} \ll \lambda$ (wave optics or Rayleigh scattering regime) provide intuitive descriptions of the fundamentals of optical trapping.

Mie scattering regime

For $r_\mathrm{p} \gg \lambda$, a spherical particle can be considered as a lens that refracts the incoming light rays [Ashkin et al., 1986]. Figure 2.1 depicts two situations explaining the origins of lateral and axial trapping. Essentially, as light regarded as a continuous flux of photons carries momentum, refraction at the particle surface corresponds to a certain momentum change per time interval, i.e. a force, which due to Newton's third law has to be compensated by the particle in the opposite direction. In this way, a lateral intensity slope leads to a net force driving the particle to higher intensities, whereas strong focusing of a laser induces an axial gradient force that is always directed towards the point of convergence [Ashkin, 1992].

Note that in this picture the scattering force, which originates from a certain portion of the refracted/reflected light and points in the propagation direction of the beam, is not shown. In reality, stable trapping in three dimensions is only achieved when the overall axial gradient force exceeds the scattering force, with the trap centre being located slightly above the focal region in Fig. 2.1 – at a distance Δz that can be approximated as $\pi w_0^2/\sqrt{3}\lambda$, where w_0 denotes the focal spot size (radius) of a Gaussian beam (see Subsect. 3.3.1) [Ashkin et al., 1986]. In the best case, if we assume a diffraction-limited spot of diameter $2w_0 \approx \lambda$, for a laser with $\lambda = 800\,\mathrm{nm}$ in water (corresponding to $\lambda_0 = 1064\,\mathrm{nm}$ in air) we obtain $\Delta z \approx 360\,\mathrm{nm}$.

Rayleigh scattering regime

For $r_\mathrm{p} \ll \lambda$, the above description no longer holds and the wave properties of light have to be considered. In this case, the trapped particle can be regarded as a Hertzian dipole in an inhomogeneous electromagnetic field. Up to a sign, the gradient force F_grad is then given by [Ashkin et al., 1986]

$$\begin{aligned} \vec{F}_\mathrm{grad} &= -\vec{\nabla} U_\mathrm{OT} = \frac{1}{2}\vec{\nabla}(\vec{\mu}_\mathrm{e} \cdot \vec{E}) \\ &= \frac{1}{2}\alpha_\mathrm{p}^* \vec{\nabla}|\vec{E}|^2 \propto r_\mathrm{p}^3 \vec{\nabla}\mathcal{I}_0\,, \end{aligned} \tag{2.1}$$

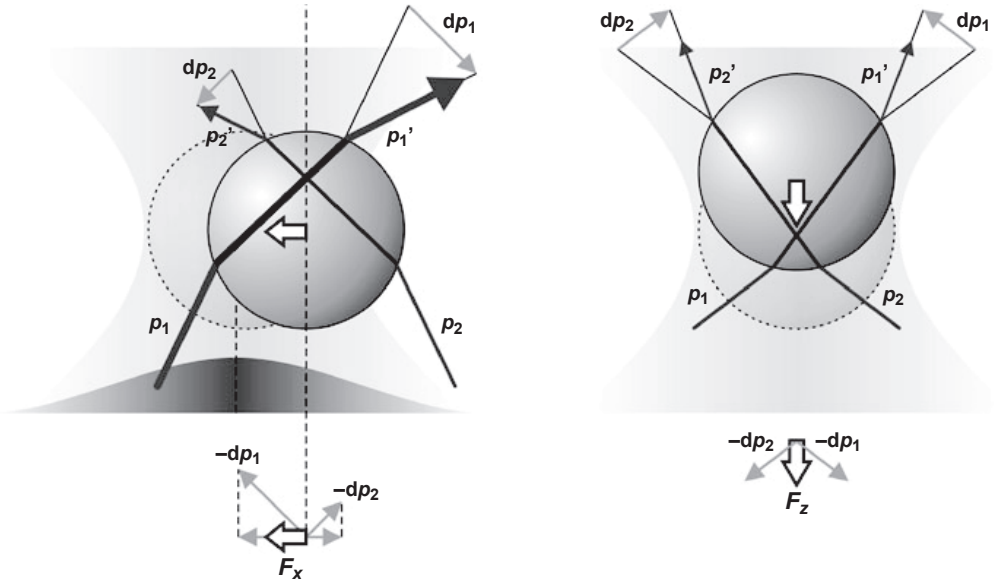

Figure 2.1. The ray optics picture of optical trapping (*side view*). A microsphere acts as a lens refracting light rays of different intensities (arrow thicknesses) from a convergent laser beam (with Gaussian intensity profile) propagating upwards (in the $+Z$-direction). Due to momentum conservation, the transfer of momenta p (black/grey arrows) results in net restoring forces F (white arrows). **(Left)** A lateral intensity gradient pulls the particle in the direction of the optical axis. **(Right)** A tightly focused beam gives rise to an axial force pointing to the focal region. [Figure modified from [van Mameren et al., 2011].]

where $\vec{E}$ is the electric field, U_{OT} the potential energy of the interaction, $\vec{\mu}_{\mathrm{e}} = \alpha^*_{\mathrm{p}}\vec{E}$ the induced electric dipole moment of a particle with polarisability $\alpha^*_{\mathrm{p}} \propto r^3_{\mathrm{p}}$, and $\mathcal{I}_0$ the intensity of the incident laser beam. The factor of one half arises from the fact that the dipole is induced, not permanent [Grimm et al., 2000]. Note that $\vec{F}_{\mathrm{grad}}$ is always aligned with the direction of the intensity gradient (towards the focus) and proportional to the particle volume within the Rayleigh limit.

The absolute value of the scattering force F_{scat} reads [Ashkin et al., 1986]

$$\begin{aligned} F_{\mathrm{scat}} &= \frac{\Delta p}{\Delta t} = \frac{n_{\mathrm{m}}\Delta E}{c_0^*\Delta t} \\ &= \frac{n_{\mathrm{m}}P_{\mathrm{scat}}}{c_0^*} \propto \frac{r_{\mathrm{p}}^6}{\lambda^4}\mathcal{I}_0\,, \end{aligned} \tag{2.2}$$

where $\Delta p = n_{\mathrm{m}}\Delta E/c_0^*$ describes the photonic momentum/energy transfer in a medium (c_0^* denotes the speed of light in vacuum) and $P_{\mathrm{scat}} := Q_{\mathrm{scat}}P_0 \propto \mathcal{I}_0 r_{\mathrm{p}}^6/\lambda^4$ is the scattered part of the total incident laser power P_0 [Ashkin et al., 1986]. Typical values of $n_{\mathrm{m}} = 1.33$, $P_0 = 100\,\mathrm{mW}$ and $Q_{\mathrm{scat}} = 0.01$ lead to an approximate scattering force of 5 pN, proving that OT operate in a biologically relevant force range. Note that F_{scat} is proportional to the *squared* particle volume within the Rayleigh limit.

Intuitive derivation of trap stiffness

From the above equation for the gradient force in the wave optics regime (Eq. 2.1), it follows that the potential energy U_{OT} of an optical trap is proportional to the intensity distribution $\mathcal{I}(\vec{r})$ of the laser,

$$\begin{aligned} U_{\mathrm{OT}}(\vec{r}) &= -\frac{1}{2}\vec{\mu}_{\mathrm{e}}(\vec{r}) \cdot \vec{E}(\vec{r}) \\ &= -\frac{1}{2}\alpha_{\mathrm{p}}^{*}|\vec{E}(\vec{r})|^2 \propto \mathcal{I}(\vec{r})\,, \end{aligned} \tag{2.3}$$

where $\vec{r} = (x, y, z)$ is the radial distance vector starting at the centre of the trap. For a Gaussian beam profile it holds that

$$\mathcal{I}(\vec{r}) \propto \mathrm{e}^{-|\vec{r}|^2} \approx 1 - |\vec{r}|^2\,, \tag{2.4}$$

making use of the first two terms of the Taylor expansion valid for small values of $|\vec{r}|$ [Otto, 2011]. Consequently, it follows that the force exerted on a particle confined near the trap centre satisfies

$$\begin{aligned} \vec{F}_{\mathrm{OT}}(\vec{r}) &= -\vec{\nabla} U_{\mathrm{OT}}(\vec{r}) \propto -\vec{\nabla}\mathcal{I}(\vec{r}) \\ &= k_{\mathrm{trap}}^{\mathrm{OT}}\vec{r}\,, \end{aligned} \tag{2.5}$$

with a proportionality factor $k_{\mathrm{trap}}^{\mathrm{OT}}$ called optical trap stiffness in analogy to the force constant of a linear spring fulfilling Hooke's law [Neuman and Block, 2004]. This proves the harmonic character of the laser trapping potential for small displacements. In the following, for the sake of simplicity, Eq. 2.5 will be used in one dimension only, taking the following form:

$$F_{\mathrm{OT}} = -k_{\mathrm{trap}}^{\mathrm{OT}} x\,. \tag{2.6}$$

Here, x denotes the lateral deviation from the trap centre located at the origin and the minus sign accounts for the restoring character of the force. Note that, since overall gradient and scattering force show different dependences on particle size (see Eqs. 2.1 and 2.2), there exists a bead diameter $d_{\mathrm{p}} = 2r_{\mathrm{p}}$ at which the optical confinement is most efficient, i.e. with a maximum $k_{\mathrm{trap}}^{\mathrm{OT}}$ for a certain laser power [Simmons et al., 1996]. According to electromagnetic theory and as proven experimentally, this case corresponds to $d_{\mathrm{p}} \approx \lambda$ [Rohrbach, 2005].

2.1.3. Simple optical tweezers layout

A basic OT setup requires only few components: a trapping laser, a couple of lenses/mirrors for beam expansion/steering, a high-NA objective, a light source and

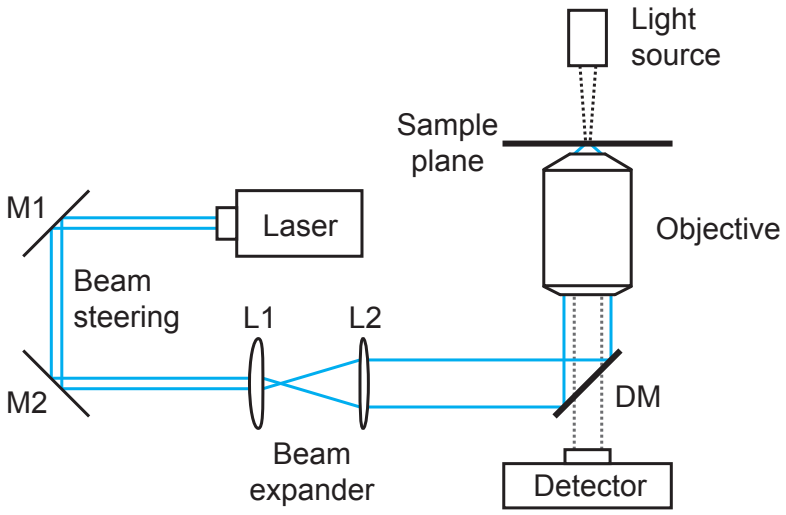

Figure 2.2. Essential components of a single-beam optical tweezers (OT) instrument in an inverted microscope configuration (*not to scale*). A collimated laser beam (*top view*) is aligned by two mirrors (M), expanded by a pair of lenses (L) and coupled into the back aperture of an infinity-corrected microscope objective (*side view*) via a dichroic mirror (DM). With standard brightfield illumination from above, the optical trap is created in the sample plane and monitored by video tracking (or laser-based detection in reflection). Note that this particular scheme lacks information about micro-/nanometric positioning systems for sample cell and objective, as well as additional optics necessary to create an image in the detector plane. [Figure adapted from [Otto, 2011].]

a detector to monitor particle position. The latter can either be a camera for video microscopy or a sensor for laser-based detection (see Sect. 2.3). Figure 2.2 depicts a typical configuration based on the design of an inverted microscope, which – depending on the particular requirements – can either be commercial or custom-built [Neuman and Block, 2004].

The trapping laser should be a continuous-wave, single-mode model delivering a stable Gaussian intensity profile with high spatial coherence [Dholakia et al., 2008]. Although other transverse electromagnetic (TEM) modes such as those of Laguerre–Gaussian beams may be beneficial for certain experiments [Simpson et al., 1998], the fundamental (Gaussian) TEM_{00} mode remains most common. The choice of the wavelength depends on the application: for biophysical studies, the window between 750 and 1100 nm in the near infrared (IR) mostly shows low absorption of water and biological material, therefore reducing radiation damage [Svoboda and Block, 1994]. The commonly used wavelengths are 830 and 1064 nm: the former corresponds to diode lasers and leads to minimum sample heating, but has traditionally been limited to output powers P_{out} smaller than 250 mW [Neuman and Block, 2004; Neuman et al., 1999]; the latter refers to the more widespread neodymium-doped yttrium–aluminium garnet (Nd:YAG) laser, which can offer output powers of up to 100 W as well as superb beam stability, while still being relatively harmless to biological material [Ashkin et al., 1987; Neuman

and Block, 2004; Neuman et al., 1999]. For $\lambda_0 = 1064\,\mathrm{nm}$, sample heating in aqueous environment has been quantified as $\sim 1\,^\circ\mathrm{C}$ per 100 mW of power at the focus [Peterman et al., 2003].

Apart from the laser, the objective lens is the other crucial part for creating a stable optical trap in three dimensions. The laser beam is typically expanded by a pair of (plano-)convex lenses with a certain focal length ratio to slightly overfill the back aperture of the objective (see Fig. 2.2). This way, the lateral light rays – which contribute most to the gradient force according to the right part of Fig. 2.1 – correspond to higher intensities and the trapping efficiency is increased [Ashkin, 1992]. For the same reason, to achieve a diffraction-limited spot, the objective needs to have a high numerical aperture given by $\mathrm{NA} = n_\mathrm{m} \sin\alpha$, where α is the half-angle of the converging light cone. Modern objectives used for optical trapping microscopes consist of various lenses providing high levels of image correction and are designed for the use with an immersion liquid with $n_\mathrm{m} > 1$. With α coming close to $90\,^\circ$, the main drawback is a short working distance of 300 µm or less [Neuman and Block, 2004]. The highest gradients can be obtained with oil-immersion objectives, however, the refractive index mismatch between the immersion liquid and the aqueous sample solution leads to spherical aberrations limiting the effective working distance to typically less than 20 µm in this case [Vermeulen et al., 2006]. As a consequence, for most experiments deeper in solution, water-immersion objectives are the proper choice.

Trapping laser and microscope objective are the essential components of an optical trap, but in order to be able to efficiently carry out biophysical measurements at the single-molecule level, the choice of the other parts of the assembly is equally important: sample stage positioning system, position/force detection devices, microfluidics control unit and hardware–software interfaces are all to be carefully selected and will be discussed in detail in Chap. 3 of this thesis.

2.1.4. Force calibration in the frequency domain

Although direct force measurement schemes have been successfully applied in dual-beam OT setups for decades [Smith et al., 2003], they are hard to put into practice in single-beam gradient force traps that rely on tightly focused laser beams because all the forward-scattered light has to be collected by a condenser lens [Grange et al., 2002]. So far, to the best of my knowledge, direct force detection has only been implemented in one single-beam setup [Farré et al., 2012]. In the remaining cases – as in the instrument described in Chap. 3 –, force monitoring is achieved by determining the relation between force and position and subsequent position detection [Neuman and Block, 2004]. The following paragraphs elucidate the theoretical concepts relevant for such a calibration procedure and deduce the main formula for trap stiffness evaluation in Fourier space.

Equation of motion for a confined Brownian particle

Having established a relation between force and displacement in an optical trap, we can now describe the position fluctuations of a trapped object with time. As without any outer influence the behaviour would be governed by free diffusion through the surrounding medium, the following Langevin equation can be used to describe its movements (in one dimension for simplicity) [Berg-Sørensen and Flyvbjerg, 2004]:

$$\underbrace{m\frac{\mathrm{d}^2x(t)}{\mathrm{d}t^2}}_{\text{Inertial force}} + \underbrace{\beta\frac{\mathrm{d}x(t)}{\mathrm{d}t}}_{\text{Drag force}} + \underbrace{k_{\mathrm{trap}}x(t)}_{\text{Spring force}} \quad = \quad \underbrace{F_{\mathrm{B}}(t)}_{\text{Random force}} \quad . \tag{2.7}$$

This formula corresponds to an oscillating particle of mass m confined by a harmonic (not necessarily optical) potential well exhibiting a linear trap stiffness k_{trap} in a medium with hydrodynamic drag coefficient β. Due to continuous, random collisions with surrounding solvent molecules, the oscillator is driven by a Brownian force $F_{\mathrm{B}}(t) = \sqrt{2\beta k_{\mathrm{B}}T}\varphi(t)$ that corresponds to a stochastic Gaussian process $\varphi(t)$ with time average $\langle\varphi(t)\rangle = 0$, auto-correlation function $\langle\varphi(t)\varphi(t-t')\rangle = \delta(t')$, and power spectrum or power spectral density (PSD) $S_\varphi(f) := |\mathcal{F}\{\varphi(t)\}|^2 = \text{const.}$ [Berg-Sørensen and Flyvbjerg, 2004]. Note that $\delta(t)$ stands for the Dirac delta function and $\mathcal{F}\{...\}$ for the Fourier transform operator. Consequently, $F_{\mathrm{B}}(t)$ describes a white noise with PSD [Gittes and Schmidt, 1998b]

$$\begin{aligned} S_{F_{\mathrm{B}}}(f) := |\mathcal{F}\{F_{\mathrm{B}}(t)\}|^2 \quad &\underset{(\mathrm{WK})}{=} \quad \int_{-\infty}^{\infty} \langle F_{\mathrm{B}}(t)F_{\mathrm{B}}(t-t')\rangle\, \mathrm{e}^{-2\pi \mathrm{i} f t'}\, \mathrm{d}t' \\ &\underset{(f\geq 0)}{=} \quad 2\int_{-\infty}^{\infty} 2\beta k_{\mathrm{B}}T\, \underbrace{\langle\varphi(t)\varphi(t-t')\rangle}_{\delta(t')}\, \mathrm{e}^{-2\pi \mathrm{i} f t'}\, \mathrm{d}t' \\ &= \quad 4\beta k_{\mathrm{B}}T \underbrace{\int_{-\infty}^{\infty} \delta(t')\, \mathrm{e}^{-2\pi \mathrm{i} f t'}\, \mathrm{d}t'}_{\mathcal{F}\{\delta(t')\}\,\equiv\, S_\varphi(f)\,=\,1} = 4\beta k_{\mathrm{B}}T\,. \end{aligned} \tag{2.8}$$

Here, "WK" denotes the use of the Wiener–Knichin theorem, which relates the auto-correlation function of a stationary random process to its power spectrum [Chatfield, 2013], and $f \geq 0$ indicates that we only consider positive frequencies, i.e. the one-sided PSD, which introduces the additional factor of two.

As our situation corresponds to low Reynolds numbers $Re \mathrel{\widehat{=}} \frac{\text{Inertial forces}}{\text{Drag forces}} \ll 1$ [Purcell, 1977], the first term of Eq. 2.7 can be dropped and we end up with

$$\beta\frac{\mathrm{d}x(t)}{\mathrm{d}t} + k_{\mathrm{trap}}x(t) = F_{\mathrm{B}}(t)\,. \tag{2.9}$$

Indeed, if we consider the drag constant of a small sphere far away from any surface, according to Stokes' law [Gittes and Schmidt, 1998b]

$$\beta = 6\pi\eta r_\mathrm{p}\,, \tag{2.10}$$

where η is the dynamic viscosity of the medium. As a consequence, for a time constant of inertial effects $\tau_\mathrm{inert} := m/\beta$ and typical experimental parameters ($m = 10^{-12}\,\mathrm{g}$, $\eta = 1\,\mathrm{g/(m{\cdot}s)}$, $r_\mathrm{p} = 10^{-6}\,\mathrm{m}$) it holds: $\tau_\mathrm{inert} \approx 10^{-7}\,\mathrm{s} = 0.1\,\mu\mathrm{s}$, which is much too fast for commonly used maximum sampling frequencies of tens of kilohertz. This proves that the type of oscillator considered in this subsection is highly overdamped, so that inertial contributions can be neglected.

Spectral analysis of particle fluctuations

Although the dynamics of individual molecular events require data to be analysed in the time domain, an accurate calibration of the stiffness near the optical trap centre benefits from observations in the frequency domain, as they allow to pinpoint noise sources other than the unavoidable wiggling of the trapped particle due to Brownian motion, e.g. electronic noise and thermal drift. Not taking into account these additional contributions might bias the results derived from particle fluctuations [Gittes and Schmidt, 1998b]. Switching to the frequency domain by taking the Fourier transform on both sides of Eq. 2.9 (with $\mathcal{F}\{\mathrm{d}x(t)/\mathrm{d}t\} = -2\pi\mathrm{i}f\mathcal{F}\{x(t)\}$ and $\mathrm{i}^2 := -1$) yields the complex expression

$$\begin{aligned} -2\pi\mathrm{i}f\beta\mathcal{F}\{x(t)\} + k_\mathrm{trap}\,\mathcal{F}\{x(t)\} &= \mathcal{F}\{F_\mathrm{B}(t)\}\,, \\ \Leftrightarrow\ \mathcal{F}\{x(t)\} &= \frac{\mathcal{F}\{F_\mathrm{B}(t)\}}{2\pi\beta(f_\mathrm{c} - \mathrm{i}f)}\,, \end{aligned} \tag{2.11}$$

where f_c denotes the characteristic corner or cut-off frequency defined by

$$f_\mathrm{c} = \frac{1}{\tau_\mathrm{c}} := \frac{k_\mathrm{trap}}{2\pi\beta}\,. \tag{2.12}$$

Here, τ_c is the relaxation time constant of a particle moving in the potential well. With typical optical trap stiffness values $k_\mathrm{trap}^\mathrm{OT} \equiv k_\mathrm{trap} = 10^{-3}$–$10^{-4}\,\mathrm{N/m} = 0.01$–$0.1\,\mathrm{g/s^2}$ and the above used orders of magnitude for β, we obtain $f_\mathrm{c} \approx 0.1$–$1\,\mathrm{kHz}$ equivalent to $\tau_\mathrm{c} \approx 1$–$10\,\mathrm{ms}$. Taking the squared modulus on both sides of Eq. 2.11 and utilising the result for $S_{F_\mathrm{B}}(f)$ in Eq. 2.8, we can obtain an expression for the PSD of the time-dependent position signal $x(t)$ [Gittes and Schmidt, 1998b]:

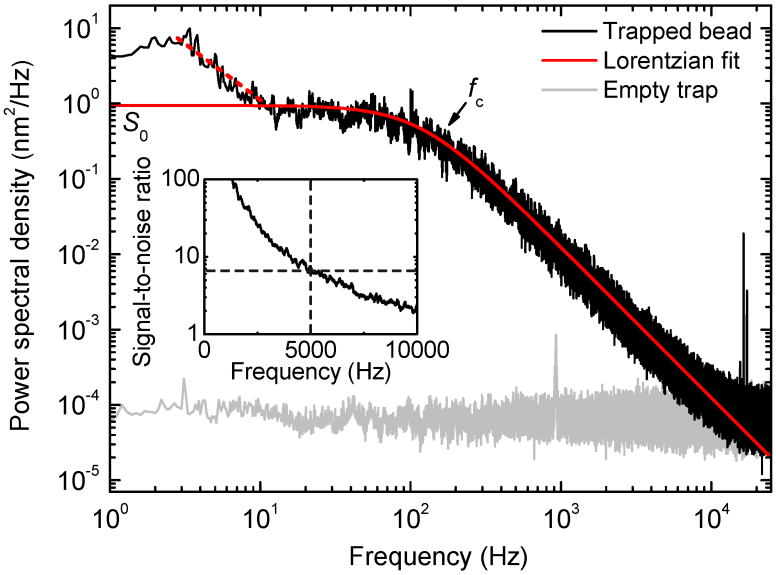

Figure 2.3. Power spectral density (PSD) of an optically trapped microsphere. Black data correspond to a time series acquired during 10 s at 50 kHz for a particle of 3.18 µm in diameter confined at 150 mW of pre-objective laser power. We observe a corner frequency $f_c \approx 150$ Hz. Note that low-frequency noise (dashed red line) makes a direct readout of the intercept S_0 (given by Eq. 2.14) impossible. The red curve shows a fit of Lorentzian shape as defined by Eq. 2.13. At frequencies ≥ 10 kHz, the curve starts to deviate considerably from the experimental data, which can be attributed to background noise from the detector electronics (grey data). The signal-to-noise ratio (inset) stays above 6 up to ~ 5 kHz – an upper frequency limit for our curve fitting routines.

$$\begin{aligned} S_x(f) &= \frac{S_{F_B}(f)}{4\pi^2\beta^2|f_c - \mathrm{i}f|^2}\,, \\ &\underset{(2.8)}{=} \frac{k_B T}{\pi^2\beta(f_c^2 + f^2)}\,, \end{aligned} \tag{2.13}$$

where $|f_c - \mathrm{i}f| := \sqrt{(f_c - \mathrm{i}f)(f_c + \mathrm{i}f)}$. This equation describes a Lorentzian function with units $[x]^2$/Hz as represented in Fig. 2.3. We can see that the corner frequency according to Eq. 2.12 divides the spectrum into two regimes:

$$\text{for } f \ll f_c\,, \quad S_x(f) \approx S_x(0) := S_0 = \frac{k_B T}{\pi^2\beta f_c^2} \underset{(2.12)}{=} \frac{4\beta k_B T}{k_{\mathrm{trap}}^2}\,; \tag{2.14}$$

$$\text{for } f \gg f_c\,, \quad S_x(f) \approx \lim_{f_c \to 0}\{S_x(f)\} = \frac{k_B T}{\pi^2\beta f^2} \propto \frac{1}{f^2}\,. \tag{2.15}$$

This means that on long time scales, the trapped particle is thoroughly confined in the optical potential well at a constant PSD, whereas on short time scales it does not "feel"

the restoring forces from the trap and performs free diffusion with a characteristic $(1/f^2)$-dependence [Gittes and Schmidt, 1998b]. Note that in reality, $S_0 = 2S_x(f_c)$ is often difficult to determine due to the presence of low-frequency noise, making a direct calculation of k_{trap} infeasible. Instead, a Lorentzian fit of the PSD according to Eq. 2.13 gives more reliable results. In Fig. 2.3, due to additional noise sources, data fitting is restricted to an effective interval between 20 and 5000 Hz.

2.2. Magnetic tweezers

2.2.1. Introduction from a historical perspective

With (electro)magnetism already being a well established field of study at the beginning of the last century, the origin of the application of magnetic forces to actively manipulate biological tissue at microscopic scales can be set to the year 1949 [de Vlaminck and Dekker, 2012], in which Francis Crick – before turning to the task of unravelling the structure of DNA – together with Arthur Hughes was the first to drag and twist small magnetic particles through the cytoplasm of cells by means of either permanent or electrically induced magnets [Crick and Hughes, 1950]. Those experiments accomplished the groundwork for magnetic microrheometry techniques capable of exerting tiny pulling forces, which were refined in the mid/late 1990s by Erich Sackmann and his team to study the viscoelastic behaviour of polymer networks [Ziemann et al., 1994] and living cells [Bausch et al., 1998].

At the molecular level and a couple of years earlier, Smith and colleagues had been the first to apply magnetic microspheres as handles for pulling on individual DNA molecules used as tethers between the beads and the surface of a coverslip in an inverted microscope [Smith et al., 1992]. They used permanent magnets aligned in the XY-plane and buffer flow to stretch the filaments practically parallel to the glass surface, which had the inconvenience of increased viscous drag exerted on the spheres. In 1996, Strick and co-workers published a study that relied on a different experimental configuration: with similar DNA attachment chemistries, they placed the magnets above the fluid chamber, leaving only a small gap for the illumination, thus creating a magnetic field gradient that resulted in an upwards-directed force (perpendicular to the coverslip surface) [Strick et al., 1996]. Their design (equivalent to the one shown in Fig. 2.4) represented the prototype of MT built for single-molecule studies involving nucleic acids, as it permitted to easily provoke changes not only in the extension, but also in the twist of a tethered molecule by rotating the magnets around the Z-axis, e.g. to study DNA supercoiling [Strick et al., 1998].

In analogy to the OT technique invented one decade earlier, both the (electro)magnetic instrument type mostly used for cellular studies, and the configuration with permanent magnets developed for probing individual DNA molecules were given the name "magnetic tweezers". Strictly speaking, designs belonging to the second category con-

stitute "pullers" rather than tweezers because their working principle differs from the one of an optical trap: the magnetic force points in the same direction always and increases non-linearly with decreasing distance from the beads [Carrasco Pulido and Moreno-Herrero, 2011]. Some realisations of the electromagnetic MT version were originally meant to be used with single molecules as well (for an early contribution, see e.g. Ref. [Haber and Wirtz, 2000]). However, the complexity of creating a stable force feedback, apart from hysteresis and sample heating effects already present at moderate forces, has not yet made them competitive in comparison with the rather simple design that involves a permanent magnetic field [Neuman and Nagy, 2008]. Still, they have proven useful for applications requiring fast switching of the field, e.g. for monitoring torque release by rotary molecular motors [Rondelez et al., 2005].

From here on, with magnetic tweezers (MT) I will only refer to the type of apparatus that employs permanent magnets – which is the relevant one for the experiments shown in this thesis and most single-molecule studies in general. For now more or less 15 years, this kind of instrument has contributed greatly to new discoveries in biophysics related to the force/torque response of individual molecules [Vilfan et al., 2009]. In particular, it has enabled real-time studies of fundamental cellular processes driven by proteins associated with twisted DNA, such as supercoil removal triggered by topoisomerases [Strick et al., 2000]. Just as in the case of OT, the increased use of MT has been accompanied by continuous improvements of the technique [de Vlaminck and Dekker, 2012], not only in terms of resolution [Kim and Saleh, 2009] and combination with other microscopic methods such as total internal reflection fluorescence (TIRF) detection [Brutzer et al., 2012], but also with respect to alternative magnet configurations enabling new kinds of experiments – e.g. torque measurements [Lipfert et al., 2010] – and multiplexed assays capable of following hundreds of single-molecule activities at the same time [de Vlaminck et al., 2011].

2.2.2. Basic concepts of magnetic micromanipulation

Standard MT are created by bringing a pair of strong rare-earth magnets close to a flow cell (see Fig. 2.4) containing (super)paramagnetic microspheres tethered to the bottom surface by a linker molecule, typically dsDNA (see Fig. 2.5) [Neuman and Nagy, 2008]. The external $\vec{B}$-field created by the magnets induces a magnetic dipole moment $\vec{\mu}_\mathrm{m}$ in every bead, giving rise to a potential energy

$$U_\mathrm{MT} = -\frac{1}{2}\vec{\mu}_\mathrm{m}(\vec{B}) \cdot \vec{B}\,, \tag{2.16}$$

where the magnetic moment itself depends on the field, and the factor of one half is – just as in Eq. 2.3 – due to the fact that we consider an induced effect, i.e. any residual magnetisation is close to zero, corresponding to a time average $\langle|\vec{\mu}_\mathrm{m}(0)|\rangle \approx 0$ [Jackson, 1975]. For large enough field strengths (larger than 0.1 T for commonly used beads of

1 µm in diameter [Neuman et al., 2007]), the moment reaches a saturation value $\mu_{\mathrm{m}}^{\mathrm{sat}}$ and eventually aligns with $\vec{B}$, such that the force experienced by each particle is

$$\vec{F}_{\mathrm{MT}} = -\vec{\nabla}U_{\mathrm{MT}} = \frac{1}{2}\vec{\nabla}(\vec{\mu}_{\mathrm{m}}^{\mathrm{sat}} \cdot \vec{B}) \underset{(\vec{\mu}\,\|\,\vec{B})}{=} \frac{1}{2}\mu_{\mathrm{m}}^{\mathrm{sat}}\vec{\nabla}|\vec{B}|\,, \tag{2.17}$$

depending on the gradient of the magnetic field only [Lipfert et al., 2009]. In Fig. 2.5, a magnetic microsphere tethered to the sample cell surface will therefore feel a pulling force pointing upwards, in the direction of higher field strengths, i.e. more closely spaced magnetic field lines, whereas a (non-magnetic) reference bead will stay on the surface.

Keeping the magnet position fixed, MT – in contrast to OT – provide a constant force field for single-molecule experiments, with an effective force variation of around $10^{-6}\,\mathrm{pN/nm} = 10^{-9}\,\mathrm{N/m}$ only [Neuman et al., 2007]. This is because the typical distance ($\sim 1\,\mathrm{mm}$) of the magnets to the microspheres bound to the glass surface is enormous in comparison with the characteristic axial position changes ($\sim 1\,\mu\mathrm{m}$) of the spheres, the latter of which can thus be considered to reside within a region of stable magnetic field gradient in Z. In addition, the lines of the $\vec{B}$-field are more or less homogeneously distributed in the XY-plane, so that a single bead feels practically no lateral forces [Carrasco Pulido and Moreno-Herrero, 2011].

2.2.3. Simple magnetic tweezers layout

In comparison with any OT instrument, an elementary MT setup is rather straightforward to assemble because no laser is required. Essential components include: a pair of strong permanent magnets, a high-NA (oil-immersion) objective, a (nearly) monochromatic light source and a video camera to monitor particle positions, where the latter can either rely on a charge-coupled device (CCD) or a complementary metal-oxide-semiconductor (CMOS) sensor (see Subsect. 2.3.1) [de Vlaminck and Dekker, 2012]. Figure 2.4 depicts a standard configuration based on a customised inverted microscope.

The magnets are usually machined from alloys of rare-earth elements into small cubes of an edge length on the order of 5 mm. The most widespread compound is neodymium–iron–boron (NdFeB) [Lionnet et al., 2012], which carries very high magnetisations giving rise to magnetic field strengths of up to 1.4 T close to the magnet surface [Lipfert et al., 2009], saturating the magnetisation of typical superparamagnetic beads located at a few millimetres distance (see previous subsection). A pair of such cubic magnets – special coatings prevent the material from oxidising – is commonly introduced in a holder made of either paramagnetic aluminium or magnetically soft iron (which does not retain its magnetisation once the external field is removed). The latter effectively acts as an iron yoke that reduces stray fields [Neuman and Nagy, 2008] and may increase the resulting pulling forces slightly – or at least suppress the influence of

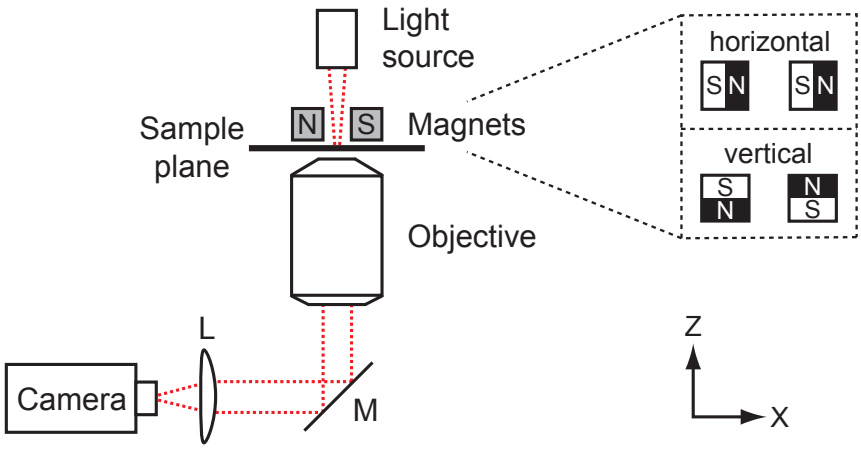

Figure 2.4. Essential components of a magnetic tweezers (MT) instrument in an inverted microscope configuration (*side view, not to scale*). **(Left)** The sample is illuminated by a (nearly) monochromatic light source, creating a diffraction signal that is analysed through an infinity-corrected objective, reflected by a mirror (M) and imaged via a tube lens (L) onto a video camera chip. Leaving a small gap for the illumination, a pair of cubic permanent magnets is placed in close proximity above the sample cell and aligned with respect to the optical axis such as to create a magnetic field (with field lines going north (N) to south (S)) that exerts tiny pulling forces on microspheres tethered to the bottom of the fluid chamber (see Fig. 2.5). Note that an obligatory nanometric positioning stage for objective or sample cell is not indicated. **(Right)** The two magnets shown on the left can be fixed in their holder with the poles aligned either horizontally or vertically. The latter configuration yields higher forces at the same distance from the upper cover glass.

negative ("pushing") forces [Lipfert et al., 2009]. The permanent magnets can be mounted either in horizontal alignment with opposing poles facing each other, or such that the poles are aligned vertically in anti-parallel orientation (see Fig. 2.4). While the first configuration is mechanically more easy to establish and provides better force resolution for experiments below $\sim 4\,\mathrm{pN}$, the second one is highly sensitive to the size of the gap between the cubes and can give rise to forces up to 100 pN, depending on the diameter of the magnetic microspheres and the minimum magnet–sample distance [Lipfert et al., 2009].

Apart from the magnet assembly, the bead-imaging components comprise the other essential parts of a typical MT setup. First of all, in order to be able to distinguish particle heights (Z-positions) by their corresponding diffraction patterns (see Subsect. 2.3.1), the instrument requires practically parallel illumination with a sufficiently long coherence length $l_{\mathrm{coh}} \approx \lambda_0^2/\Delta\lambda \sim 10\,\mu\mathrm{m}$. For CCD cameras with limited frame rate, a strong light-emitting diode (LED) in the visible wavelength range with a typical spectral width $\Delta\lambda \approx 20\,\mathrm{nm}$ in combination with appropriate lenses fulfils this requirement [Lionnet et al., 2012]. However, if a faster CMOS sensor is to be employed at acquisition frequencies above 500 Hz, a brighter light source, e.g. a mercury arc lamp [Brutzer, 2012] must be implemented. Superluminescent diodes (SLDs) and diode

lasers offer alternatives, although current modulations at frequencies in the MHz-range are necessary to reduce speckle noise from too large laser coherence lengths [Dulin et al., 2014]. Concerning the microscope objective, the arguments stated before in the context of OT (see Subsect. 2.1.3) still apply. Since MT experiments take place within a few micrometres from the coverslip surface inside the fluid chamber (see Fig. 2.5), the highest NAs from oil-immersion objectives can be exploited. Those have the advantage that their immersion liquid does not evaporate with time and provides an efficient means to transmit heat to the sample (see Chap. 5). Finally, the camera model has to be chosen according to the specific requirements, but should provide a compromise between a large sensor area (for multiplexed experiments) and short exposure times (for increased temporal resolution).

In addition, other components such as translational/rotational motors for the magnets, microfluidics control parts and software routines that coordinate the main pieces of hardware need to functionally fit into the whole assembly, too. Importantly, to obtain accurate calibration patterns (so-called look-up tables) of the diffraction-induced intensity distributions at different heights above the cover glass – as represented in Fig. 2.7 for magnetic microspheres of 1 µm in diameter –, either the objective or the sample cell need to be mounted on a piezoelectric Z-translation stage. Such a device should allow for adjustments of the relative position between focal plane and glass surface with nanometric accuracy [Carrasco Pulido and Moreno-Herrero, 2011] within a range of at least 10 µm [Lionnet et al., 2012].

2.2.4. Force calibration according to the equipartition method

At a certain magnet height above the sample cell, a magnetic microsphere connected to the surface by a partially stretched DNA linker (with extension L) is constantly fluctuating around its equilibirum position due to the thermally induced bombardment by solvent molecules – just like a particle confined in an optical trap. For small lateral deviations $\Delta x = x - x_0$ from equilibrium, represented by angles θ with respect to the Z-axis, the system can be modelled as an inverted pendulum with length L, governed by a linear response relation that takes the following form (in one dimension) [Strick et al., 1996]:

$$F_{\mathrm{R}} \;=\; k_{\mathrm{trap}}^{\mathrm{MT}} \Delta x \underset{(x_0 = 0)}{=} k_{\mathrm{trap}}^{\mathrm{MT}} x \,. \tag{2.18}$$

Here, F_{R} denotes the restoring force caused by the applied magnetic field gradient, $k_{\mathrm{trap}}^{\mathrm{MT}}$ the magnetic "trap stiffness" (in analogy to $k_{\mathrm{trap}}^{\mathrm{OT}}$) and x the position of the bead with respect to $x_0 \equiv 0$ for simplicity. Up to a sign, this equation is identical to Eq. 2.6 describing the behaviour near the centre of an optical trap. Consequently, the bead–DNA configuration considered here can also be treated as a harmonic oscillator. As given by the equipartition theorem, the time-averaged kinetic energy of such a

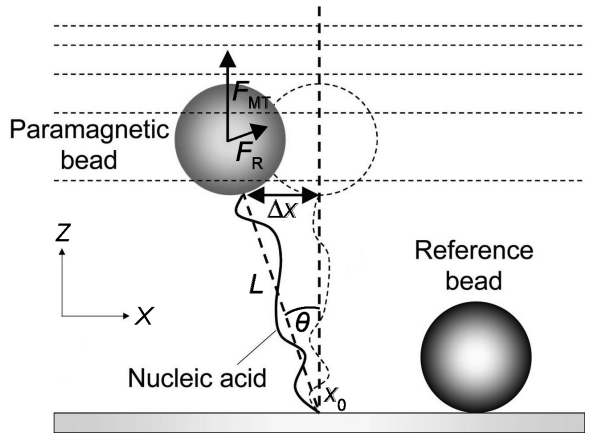

Figure 2.5. Force calibration in magnetic tweezers (MT). A (super)paramagnetic microsphere tethered to the sample chamber surface via a nucleic acid linker with extension L feels a restoring force F_{R} due to the action of the magnetic field (horizontal lines) for small deviations Δx from its equilibrium position x_0. The magnetic pulling force F_{MT} can be assessed through the variance of the lateral position fluctuations according to Eq. 2.23. A (non-magnetic) bead directly bound to the surface serves as a reference to optically determine Z-extensions (see Fig. 2.7) and correct for low-frequency drift. [Figure modified from [Vilfan et al., 2009].]

system is in general just half its thermal energy for each degree of freedom [Carrasco Pulido and Moreno-Herrero, 2011]:

$$\frac{1}{2}k_{\mathrm{trap}}\langle x^2\rangle = \frac{1}{2}k_{\mathrm{B}}T\,, \tag{2.19}$$

where $\langle x^2\rangle$ is the mean squared displacement (MSD), which relates to the variance (Var) by

$$\mathrm{Var}(x) \;=\; \langle x^2\rangle - \langle x\rangle^2 \underset{(x_0\,\equiv\,\langle x\rangle\,=\,0)}{=} \langle x^2\rangle\,. \tag{2.20}$$

According to Fig. 2.5, for small lateral deviations fulfilling $\Delta x \ll L$, the corresponding axial position change Δz is negligible ($\sqrt{(\Delta x)^2+(\Delta z)^2} \approx \Delta x$), such that $\Delta x/L = \sin\theta \approx \tan\theta \approx \theta$ and therefore

$$F_{\mathrm{R}} \approx F_{\mathrm{MT}}\cdot\sin\theta \underset{(x_0\,=\,0)}{=} F_{\mathrm{MT}}\cdot\frac{x}{L} \tag{2.21}$$

$$\underset{(2.18)}{\Rightarrow} \quad k_{\mathrm{trap}}^{\mathrm{MT}} \;=\; \frac{F_{\mathrm{MT}}}{L}\,. \tag{2.22}$$

Inserting this last result in Eq. 2.19, we end up with a relation that allows to determine the force F_{MT} exerted by the magnets on a microsphere, only by measuring the lateral MSD [Strick et al., 1996]:

$$F_{\mathrm{MT}} = \frac{k_{\mathrm{B}}TL}{\langle x^2 \rangle} \,. \tag{2.23}$$

2.2.5. Gauging of magnet distance and DNA extension

Moving the magnets upwards (away from the sample cell), within a wide force range the value of F_{MT} decays more or less exponentially with increasing magnet height [Neuman et al., 2007]. To be able to apply accurate pulling forces to dsDNA, this dependence needs to be quantified for every new magnet configuration before any single-molecule experiment can be carried out. DNA molecules with a well-defined crystallographic contour length L_0 – measured in base pairs (bp) that constitute the building blocks of the heteropolymer and are stacked at a mean distance of 0.34 nm (see Fig. 3.2) – are tethered to magnetic beads whose position fluctuations are monitored and analysed according to the formalism described in the previous subsection. The left panel of Fig. 2.6 depicts a typical calibration curve for 1 µm superparamagnetic beads at several Z-distances D of the magnet pair from the sample cell.

Once the force has been calibrated, the behaviour of a (different) DNA molecule can be checked by measuring the end-to-end distance (i.e. the extension) as the height difference between the magnetic bead in solution and a reference bead directly stuck to the surface (see Fig. 2.5). The right panel of Fig. 2.6 shows a representative force–extension (F–z) relationship for applied loads of up to 5 pN that can be explained by considering dsDNA as an isotropic, semi-flexible polymer whose continuous bending is determined by Brownian motion. For this so-called worm-like-chain (WLC) model, the following interpolation formula exists [Bustamante et al., 1994]:

$$F(z) = \frac{k_{\mathrm{B}}T}{L_{\mathrm{p}}} \left[\frac{1}{4(1 - z/L_0)^2} - \frac{1}{4} + \frac{z}{L_0} \right] . \tag{2.24}$$

Here, $F \equiv F_{\mathrm{MT}}$ and $z \equiv L$; L_{p} denotes the persistence length of DNA, which is on the order of 50 nm and defines a characteristic length scale below which the molecule behaves more like a rigid rod and above which it can be considered rather flexible [Doi, 1988]. Conversion factors $\mathcal{K}$ to associate end-to-end distance changes with positions along the DNA double strand can thus be defined by

$$\mathcal{K}(F) := \frac{z(F)}{L_0} \cdot 0.34 \, \frac{\mathrm{nm}}{\mathrm{bp}} \,. \tag{2.25}$$

From the results in Fig. 2.6 we obtain e.g. $\mathcal{K}(1\,\mathrm{pN}) \approx (1.6/1.8) \cdot 0.34\,\mathrm{nm/bp} \approx 0.30\,\mathrm{nm/bp}$.

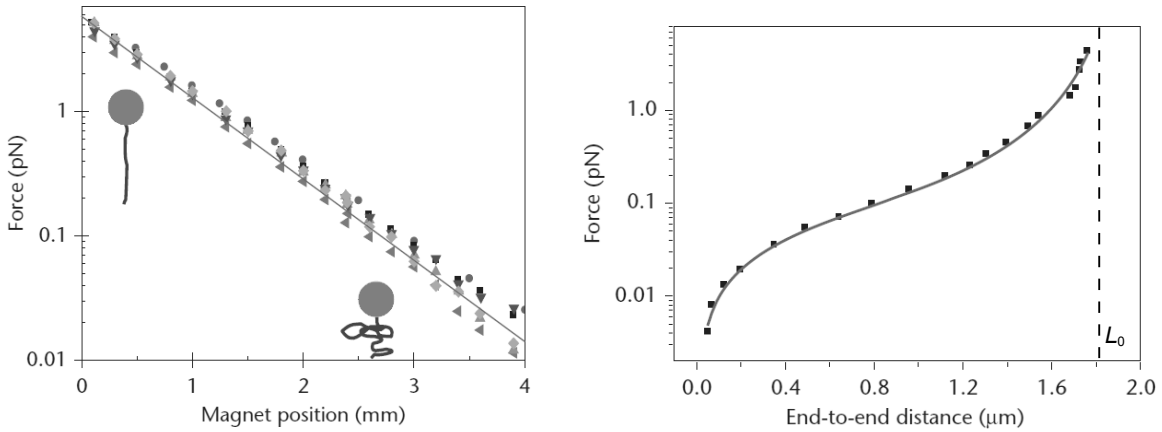

Figure 2.6. Essential reference measurements in magnetic tweezers (MT). **(Left)** Calibrating pulling force (F_{MT}) against magnet position (D) using dsDNA. Each kind of symbol indicates a different magnetic microsphere of 1 μm in diameter, tethered to a DNA molecule with contour length $L_0 = 7.6\,\mathrm{kbp}$. The dependence adjusts to an equation of type $F_{\mathrm{MT}} = F_{\mathrm{MT}}^{\mathrm{max}} \exp(-D/D_0)$, where $D = 0$ ($F_{\mathrm{MT}} = F_{\mathrm{MT}}^{\mathrm{max}}$) corresponds to the magnets touching the cover glass. The increased dispersion at low forces is due to bead–surface interactions. **(Right)** Monitoring DNA extension (end-to-end distance) versus (previously calibrated) force. The response of a 5.3 kbp (1.8 μm) DNA sample at typical salt conditions is fitted by a curve describing a worm-like chain according to Eq. 2.24. Comparing the observed extensions to L_0 obtained from the fit, conversion factors (in nm/bp) can be defined for forces up to $\sim 10\,\mathrm{pN}$. [Figures modified from [Carrasco Pulido and Moreno-Herrero, 2011].]

2.2.6. Magnetic force assessment in the frequency domain

Following the argumentation delivered in Subsect. 2.1.4 on page 13, calculating the variance from time series in real space is possible but prone to errors due to thermal drift and other external noise sources, which might lead to an underestimation of the magnetic pulling force. A more accurate calibration of MT systems relies on the formalism in Fourier space derived earlier for OT and revisited in the following paragraphs.

Comparison with optical trap stiffness

Also in MT, bead fluctuations are governed by the Langevin equation introduced in Eq. 2.7 – with $k_{\mathrm{trap}} \equiv k_{\mathrm{trap}}^{\mathrm{MT}}$. Again, inertial effects can be neglected, and the result for the PSD of $x(t)$ is equivalent to the one shown in Eq. 2.13, where the corner frequency now reads:

$$f_{\mathrm{c}} = \frac{1}{\tau_{\mathrm{c}}} \equiv \frac{k_{\mathrm{trap}}^{\mathrm{MT}}}{2\pi\beta} \underset{(2.22)}{=} \frac{F_{\mathrm{MT}}}{2\pi\beta L}\,. \tag{2.26}$$

Typical orders of magnitude ($F_{\mathrm{MT}} = 1\,\mathrm{pN}$, $L = 1\,\mu\mathrm{m}$) imply $k_{\mathrm{trap}}^{\mathrm{MT}} = 10^{-6}\,\mathrm{N/m} \ll k_{\mathrm{trap}}^{\mathrm{OT}}$

(check the text right after Eq. 2.12), so that $f_c \approx 10\,\mathrm{Hz}$ and $\tau_c \approx 100\,\mathrm{ms}$ when considering the drag constant β defined in Eq. 2.10 to be the same as before. Such long time constants are necessary for the use of CCD cameras with shutter times around 10 ms as position detectors in MT (see Subsect. 2.3.1). For nucleic acid tethers in the micrometre range, this regime of low frequencies corresponds to applied forces that are 10–100 times smaller than those typically probed with OT, making MT a more suitable instrument at loads below 1 pN [Neuman and Nagy, 2008]. Equation 2.26 also implies that – for the same magnet configuration –, higher forces can be more easily calibrated with longer DNA tethers (or larger beads), at the cost of extended data acquisition intervals [Lionnet et al., 2012].

Calculating the variance from the power spectrum

According to Parseval's theorem, which basically states that the sum/integral of a squared function is equal to the sum/integral of the squared Fourier transform of that function [Chatfield, 2013], we have

$$\mathrm{Var}(x(t)) := \int_{-\infty}^{\infty} |x(t)|^2 \,\mathrm{d}t = \int_{0}^{\infty} |\mathcal{F}\{x(t)\}|^2 \,\mathrm{d}f = \int_{0}^{\infty} S_x(f) \,\mathrm{d}f\,, \tag{2.27}$$

where in the last step we have simply made use of the definition of the PSD of position fluctuations: $S_x(f) := |\mathcal{F}\{x(t)\}|^2$. The variance that corresponds to a certain trap stiffness can thus be recovered from data analysis in Fourier space alone. Note that we only have to integrate over positive frequencies to account for the one-sided power spectrum as derived in Subsect. 2.1.4. If $\mathrm{Var}(x) \equiv \langle x^2 \rangle$ (see Eq. 2.20), inserting Eq. 2.13 in the above equation yields

$$\langle x^2 \rangle = \int_{0}^{\infty} \frac{k_\mathrm{B}T}{\pi^2\beta(f_c^2 + f^2)} \,\mathrm{d}f \underset{(2.14)}{=} \int_{0}^{\infty} \frac{S_0 f_c^2}{f_c^2 + f^2} \,\mathrm{d}f = S_0 \int_{0}^{\infty} \frac{1}{1 + \left(\frac{f}{f_c}\right)^2} \,\mathrm{d}f\,, \tag{2.28}$$

with $S_0 \equiv S_x(0)$ as before. This integral can be solved analytically giving

$$\langle x^2 \rangle = S_0 f_c \left[\arctan\left(\frac{f}{f_c}\right)\right]_0^{\infty} = \frac{\pi}{2} S_0 f_c \underset{(2.14)}{=} \frac{k_\mathrm{B}T}{2\pi\beta f_c} \underset{(2.12)}{=} \frac{k_\mathrm{B}T}{k_\mathrm{trap}}\,, \tag{2.29}$$

which is just the expression in Eq. 2.19 derived from the equipartition theorem for the energy of a one-dimensional harmonic oscillator. This implies that the variance can be obtained as the area under the Lorentzian curve that best fits the power spectral density, such as the one depicted in Fig. 2.3. Using Eq. 2.23, the magnetic pulling force can be evaluated thereafter.

Note that in practice, to minimise the influence of additional noise sources in the spectrum when calibrating the trap stiffness (of OT) or pulling force (of MT), the

arctangent function in Eq. 2.29 has to be evaluated between two finite limits (as conveyed by Eq. 3.17), e.g. between 20 and 2000 Hz in case of the data shown in Fig. 2.3. The uppermost limit is set by the so-called Nyquist frequency, which determines the detection bandwidth of the system and is just half the sampling frequency [Chatfield, 2013], i.e. 25 kHz in Fig. 2.3. Since bead fluctuations occur at unlimited bandwidth, aliasing effects – which artificially inflate the signal amplitudes at high frequencies – may have to be considered by incorporating a correction in the fitting curve that depends on the data acquisition rate [Berg-Sørensen and Flyvbjerg, 2004].

In addition, for systems that rely on video detection (see next section) like MT, the signal captured for each camera frame corresponds to an average obtained over the finite exposure time. This effect is called windowing and leads to a reduction of the amplitudes, which – depending on the length of the exposure – might have to be accounted for by a second correction to the Lorentzian function defined in Eq. 2.13 [Vilfan et al., 2009].

2.3. Position detection schemes

Studying biophysical phenomena at the single-molecule level via micrometer-sized handles requires position determination with high accuracy. For example, the currently most advanced optical trapping microscopes can achieve ångström resolution and thus resolve individual steps of e.g. RNA polymerases [Abbondanzieri et al., 2005]. There exist essentially two ways of monitoring the particle position in optical and magnetic tweezers: video- and laser-based detection [Neuman and Block, 2004; Neuman and Nagy, 2008], both of which have been exploited in the setups described in Chaps. 3–5. The following paragraphs shortly describe the main advantages and shortcomings of either method, leaving further details to the cited references.

2.3.1. Video-based detection

This approach is in general easier to implement because apart from the simple assemblies depicted in Figs. 2.2 and 2.4, no further hardware is required. It relies on image acquisition by a camera – based on either CCD or CMOS technology – and subsequent processing and analysis of each frame by a particle tracking computer algorithm [Neuman and Block, 2004]. Spatial precision and accuracy depend on the resolution of the camera and the goodness of the algorithm [Cheezum et al., 2001], temporal performance on camera speed, data streaming rate and computational capabilities.

In the case of CCDs, the fact that each pixel produces a signal proportional to the incoming light intensity that has to be read out and processed separately, typically limits the maximum frame rate to less than 120 Hz at full sensor readout for devices with around one million pixels [Neuman and Block, 2004]. CMOS sensors on the other hand have the readout electronics directly built into each pixel, thus offering

bandwidths of several kilohertz at almost comparable sensitivities [Gibson et al., 2008; Otto et al., 2008]. However, shorter shutter times require the light source to provide sufficient brightness for efficient discrimination of particles from background noise [Otto et al., 2010].

Video-based $XY(Z)$-tracking has the advantage of being able to follow various particles at the same time, providing information about their absolute positions, which makes it the method of choice in multiplexed MT [de Vlaminck and Dekker, 2012]. It has been proven to work reliably in real time, yielding nanometric accuracies at high bandwidths in combination with modern CMOS cameras and optimised software routines [Otto et al., 2011a]. Its temporal resolution is limited though when used with CCD devices (see above and Chaps. 3/5).

Lateral position determination

To be able to measure real distances in the horizontal plane, the effective pixel size on the camera image has to be calibrated, e.g. using a micrometre grid. Nanometre accuracy in XY-tracking is commonly achieved by determination of the maximum of the intensity distribution representing a trapped particle (see Fig. 3.10a), for which several types of algorithms can be applied [Cheezum et al., 2001]. A method that is often used in OT and MT as it offers a compromise between good precision and fast execution times, apart from being applicable to particles within a wide size range, is cross-correlation transformation [Gosse and Croquette, 2002]. Our implementation of this strategy is shortly discussed in Chap. 3.

Axial position determination

In standard (OT) microscopes under white light illumination, defining real distances in Z from video camera images over several micrometres can be difficult (see Fig. 3.10b). In contrast, for (MT) systems that are illuminated by nearly monochromatic light – from an LED source for instance –, Gosse and Croquette introduced an efficient way of tracking axial positions of particles tethered close to the surface by correlating the appearance of their diffraction patterns with previously obtained calibration profiles [Gosse and Croquette, 2002]. This approach set a standard for many video-based Z-position detection methods used today, including the one implemented in our MT setup (see Chap. 5). Figure 2.7 shows an example of optical images of a 1 µm bead at different positions from the focal plane of the objective, together with the reference profile from a particle stuck to the glass surface. The DNA extension z (or L in Fig. 2.5) can be monitored in real time by tracking the heights of tethered bead and reference bead at the same time, where the latter additionally allows for correcting low-frequency noise due to e.g. thermal drift.

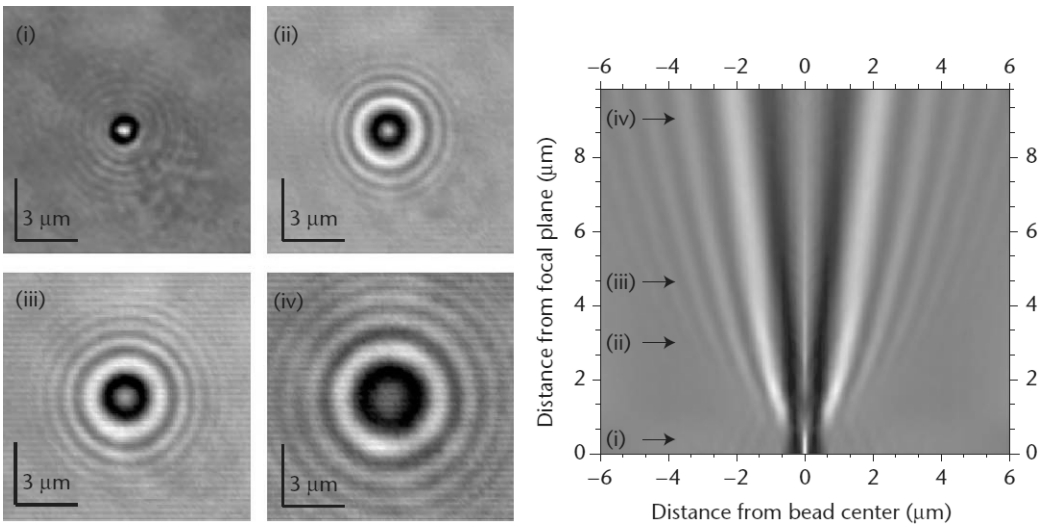

Figure 2.7. The principle of axial displacement detection in magnetic tweezers (MT). **(Left)** Four optical images of a 1 µm sphere as seen by a CCD camera from below, depicting characteristic diffraction rings at various distances (between (i) 0 and (iv) 9 µm) above the focal plane. **(Right)** The corresponding calibration profile (*side view*) of a similar microsphere glued to the flow cell surface. Arrows indicate height values corresponding to the bottom views on the left. For each camera frame, accurate Z-positions can be obtained by comparing radial intensity profiles of bead images with the look-up table. [Figure modified from [Carrasco Pulido and Moreno-Herrero, 2011].]

2.3.2. Laser-based detection

Position determination via laser scattering offers an alternative to the previous method. It is based on analysing the signal from laser light altered by a trapped particle on an electronic sensor providing around 0.1 nm of resolution at bandwidths of 100 kHz and beyond – either a position-sensitive detector (PsD) or a quadrant photodiode (QPD) [Neuman and Block, 2004]. While position-sensitive (also called lateral effect) devices consist of a single sensing area and usually offer larger detection ranges, QPDs are made up of four separate areas with individual voltage outputs and can determine position fluctuations around a central zero value with higher sensitivities [Huisstede et al., 2005].

(Quadrant) photo detector response

XY-displacements with respect to zero are deduced from differential signals of the pairwise summed voltages V as depicted in Fig. 2.8:

$$x^{\mathrm{QPD}} = (V_{\mathrm{C}} + V_{\mathrm{D}}) - (V_{\mathrm{A}} + V_{\mathrm{B}})\,, \quad y^{\mathrm{QPD}} = (V_{\mathrm{A}} + V_{\mathrm{C}}) - (V_{\mathrm{B}} + V_{\mathrm{D}})\,; \tag{2.30}$$

while axial positions z^{QPD} can be associated with the total intensity Σ^{QPD} [Neuman and Block, 2004]:

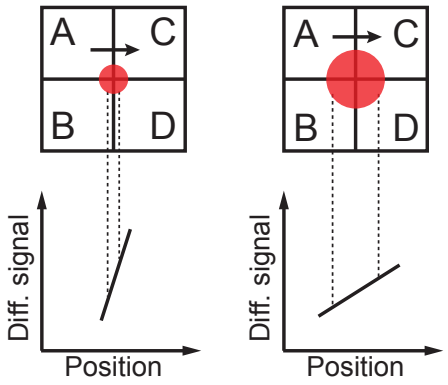

Figure 2.8. Dependence of quadrant photodiode (QPD) detection sensitivity and range on the size of the laser spot. If a small/large spot is scanned across the central area of the detector, the differential signals (voltages) according to Eqs. 2.30 change fast/slowly; the slopes of the straight lines represent the sensitivity. The interval over which the signal change is more or less constant and all four quadrants receive sufficient laser power defines a (linear) detection range (marked by dotted lines).

$$z^{\mathrm{QPD}} \sim \Sigma^{\mathrm{QPD}} := V_{\mathrm{A}} + V_{\mathrm{B}} + V_{\mathrm{C}} + V_{\mathrm{D}}\,. \tag{2.31}$$

To convert PsD or QPD signals into real distances, a detector sensitivity $\mathcal{S}$ in V/m has to be calibrated first. For small bead deviations, this can be done via comparison of the low-frequency limits of the corresponding power spectra:

$$\mathcal{S} = \sqrt{S_0^{\mathrm{u}}/S_0}\,, \tag{2.32}$$

where S_0^{u} denotes the intersect at $f = 0$ of the *uncalibrated* PSD given in V^2/Hz and S_0 can be determined via the corner frequency according to Eq. 2.14 from a Lorentzian fit of the *uncalibrated* PSD as well, provided the drag coefficient β is known. Figure 2.3 contains QPD data corresponding to the Y-direction, with the sensitivity calibrated as stated here. However, to minimise any dependency of $\mathcal{S}$ on the total beam intensity, unless otherwise stated we always use the normalised differential signals defined by

$$x_{\mathrm{norm}}^{\mathrm{QPD}} := \frac{x^{\mathrm{QPD}}}{\Sigma^{\mathrm{QPD}}}\,, \quad y_{\mathrm{norm}}^{\mathrm{QPD}} := \frac{y^{\mathrm{QPD}}}{\Sigma^{\mathrm{QPD}}}\,. \tag{2.33}$$

Note that in the case of QPDs, the sensitivity along with the detection range are functions of the laser spot size on the sensor (Fig. 2.8) [Huisstede et al., 2005]. Further details on QPD calibration can be found in Chap. 3.

Implementation strategies

Laser-based position detection can be implemented either in transmission or reflection; in the first case, the forward-scattered intensity is usually detected in the back focal plane of a condenser [Gittes and Schmidt, 1998a] – although other configurations have been used over the last decades [Neuman and Block, 2004; Verdeny et al., 2011]; in the second case, the objective itself collects the backward-scattered fraction of the laser light, which can be analysed by a detector in the image plane [Shivashankar et al., 1998]. Our implementation of direct imaging detection in reflection using a QPD is discussed in more detail in Chap. 3. Since backscattered intensities may be very small, the captured amount of reflected light can come close to the background noise levels of the electronics (see Fig. 2.3), and increased detector shot noise is observed for an empty trap [Huisstede et al., 2005]. In certain configurations, using a second (low-power) detection laser instead of the trapping laser itself can increase the signal-to-noise ratio (inset of Fig. 2.3) and furthermore ensures a constant detector signal under varying trap stiffness conditions [Keyser et al., 2006; Neuman and Block, 2004; Shivashankar et al., 1998]. One drawback is that a single device can normally monitor the position fluctuations of one particle only. In imaging detection, any laser drift may imply periodic realignment of the detection laser with respect to the trapping laser path [Keyser et al., 2006]. On the other hand, detection at high bandwidths and – especially when employed in transmission – in three dimensions is often easier to implement than in video-based detection schemes [Neuman and Block, 2004].

3. Optical tweezers with backscattering detection and active drift control

In this chapter, the development, start-up and characterisation of a customised single-beam optical tweezers (OT) instrument is discussed. The setup, adapted from a design originally proposed for the use with solid-state nanopores [Keyser et al., 2006], relies on an inverted microscope without space restrictions above the sample cell. In order to minimise trapping-laser-induced thermal drift effects in a surface-coupled configuration involving a micropipette, we artificially raise the objective temperature beforehand. Moreover, we exploit video detection in three dimensions to establish continuous position feedbacks capable of counteracting artefacts during single-molecule measurements. To monitor the position variations of a trapped microsphere with high bandwidth, the back-reflected intensities from an independent low-power laser are read out on a quadrant photodiode (QPD). A comprehensive, custom-written software interface coordinates the numerous functions of the entire hardware assembly. To test the performance of the optical trapping system, we investigate the force–extension behaviour while stretching a well-characterised dsDNA molecule and unzipping a known DNA hairpin. Introducing corrections that respond to anharmonicities of the trapping potential for certain microspheres enables us to match our results with reference curves from a separate OT microscope.

3.1. Introduction

3.1.1. Reflection-based position monitoring in optical trapping systems

As mentioned in the previous chapter, the most established laser-based position detection technique in force-measuring, single-beam OT is back-focal-plane interferometry in transmission [Neuman and Nagy, 2008]. One of its advantages is that it provides three-dimensional readout capabilities without being affected by pointing fluctuations of the laser, i.e. by absolute position variations of the optical trap [Neuman and Block, 2004]. Instead, it exclusively probes the relative displacements of microspheres from the trap centre, and interpretation of the corresponding signals on conveniently placed photo detectors is well understood [Gittes and Schmidt, 1998b]. In fact, one of the few commercial OT systems able to acquire reliable data in single-molecule experiments has the very same detection principle implemented [JPK Instruments, 2014].

Still, there are situations in which it is simply not possible to employ the aforementioned detection method. These correspond to experimental layouts that require open

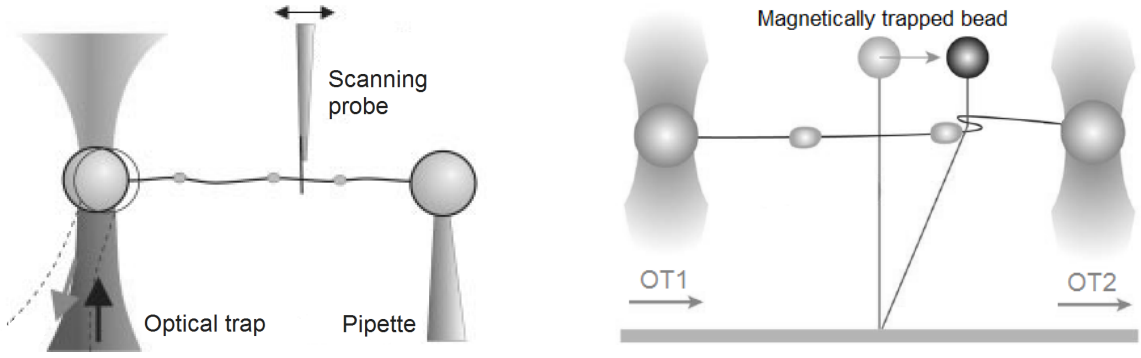

Figure 3.1. Two hybrid optical tweezers (OT) techniques that do *not* support position detection in transmission (*side views*, *not to scale*). Both methods need free access to the sample cell from the top. **(Left)** Scanning probe OT. A sharp tip comparable to the ones used in AFM probes the structure of a protein-covered DNA substrate. Associated frictional forces can be measured via a single optical trap. Position detection is possible via back-reflections of the trapping laser beam. [Figure modified from [Huisstede et al., 2007].] **(Right)** Combined OT and magnetic tweezers (MT). Two optical traps are moved synchronously in the horizontal plane to scan a DNA loop through a vertically aligned DNA molecule that tethers a magnetic bead to the cover glass and is partially stretched due to the force from a magnetic field. The presence of protein roadblock structures ("knots") is sensed via deflections of the bead. Position detection is provided via a combination of laser reflection analysis and video microscopy. [Figure modified from [van Loenhout et al., 2013].]

space above the (inverted) microscope, making the use of a condenser objective for transmission-based position monitoring infeasible. This may apply to OT setups used in conjunction with other techniques, such as ionic current sensing [Keyser et al., 2006] or scanning probe microscopy [Huisstede et al., 2007]. Equivalently, a combination of OT with permanent-magnet-based magnetic tweezers (MT) in axial configuration [van Loenhout et al., 2013] also impedes the incorporation of high-numerical-aperture (high-NA) optics above the fluid chamber. In all these cases, the bespoke instrumentation needs to offer a possibility for position detection somewhere below the sample stage, i.e. via the objective used for optical trapping and camera imaging at the same time (see Fig. 2.2). Figure 3.1 shows two examples of hybrid OT instruments taking advantage of position readout in an inverted microscope configuration with a single objective only.

In our case, the principal motivation to build an optical trapping system with free access to the sample cell from the top was to maintain the assembly as simple and flexible as possible – while keeping performance trade-offs at a minimum. Future extensions of the OT apparatus, concerning for instance a potential incorporation of a permanent magnet head providing force-clamp capabilities with high resolution at low forces would not be supported otherwise. To monitor particle positions in the absence of a condenser, we employ both camera detection under standard illumination and QPD analysis of backscattered light from a detection laser.

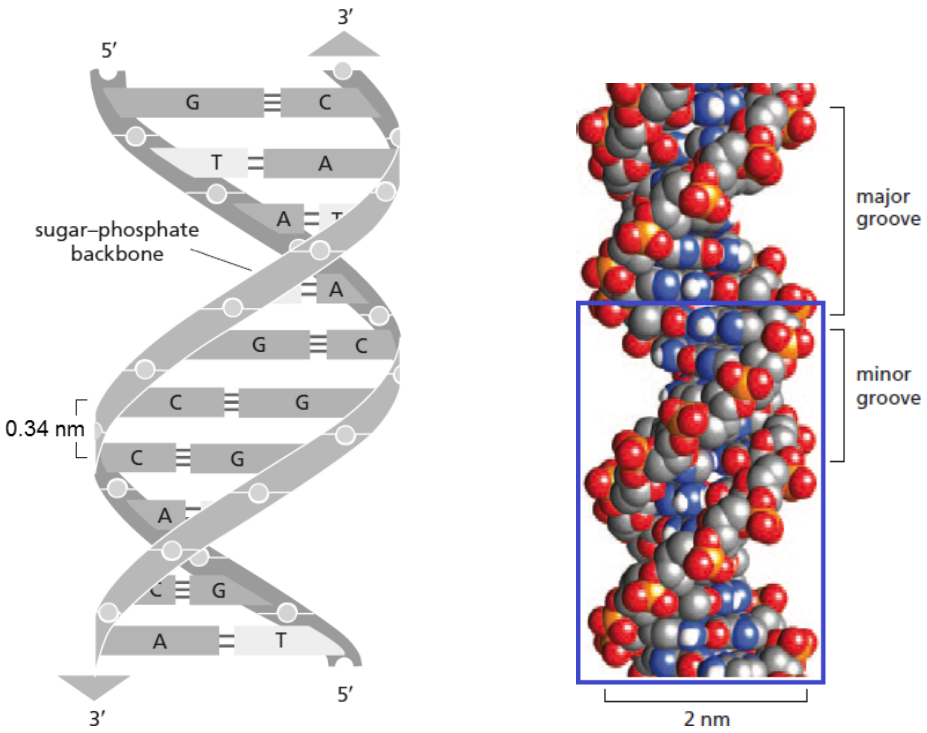

Figure 3.2. The structure of double-stranded (ds)DNA. **(Left)** Schematic double helix consisting of two antiparallel polynucleotide chains ("ribbons") coiled around each other. Covalently linked sugar–phosphate residues (circles) build the negatively charged outward backbone and define the polarity (3' or 5') of each strand, whereas bases adenine (A), guanine (G), thymine (T) and cytosine (C) form AT- and GC-pairs on the inside via two and three hydrogen bonds, respectively. Base-pair separation is 0.34 nm on average for the (physiological) B-form of DNA. **(Right)** Space-filling model of the atomic composition of the macromolecule. The blue rectangle corresponds to one helical repeat of 10 bp as shown on the left. The right-handed double helix is 2 nm in diameter and presents two grooves of different width (major/minor). Atoms are coloured as follows: nitrogen (N) ↔ blue; oxygen (O) ↔ red; phosphor (P) ↔ orange; carbon (C) ↔ grey; and hydrogen (H) ↔ white. [Figures modified from [Alberts et al., 2013].]

3.1.2. Basic structural and mechanical features of double-stranded DNA

In 1953, relying on experimental work by Rosalind Franklin and Maurice Wilkins, James D. Watson and Francis Crick presented a model for the structure of DNA (short for "deoxyribose nucleic acid"). They revealed that the macromolecule exhibits the shape of a double helix as illustrated in Fig. 3.2, made up of two single DNA strands running in opposite directions, with a strongly charged sugar-phosphate backbone on the outside and pairs of vertically stacked bases, holding the strands together on the inside [Watson and Crick, 1953]. Base pairing through relatively weak hydrogen bonds is reversible and complementary, i.e. each kind of base (A, T, G or C) on one strand only binds to a unique sort of base on the other strand, exclusively forming pairs of type AT (or TA) and GC (or CG). The two qualities of reversibility and specificity

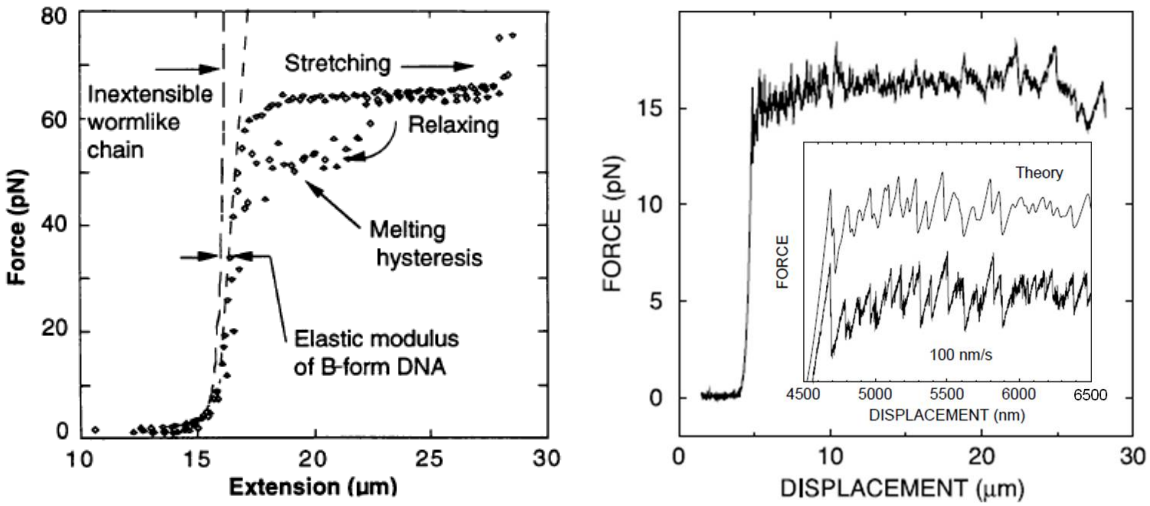

Figure 3.3. Typical force–extension relationships when stretching and unzipping dsDNA. **(Left)** Stretching a single 48 kbp λ-phage DNA molecule up to 80 pN of force with OT. Below 1 pN (entropic regime), the molecule is randomly coiled, complying with the model of an inextensible worm-like chain (WLC) up to ∼10 pN. Between 10 and ∼40–60 pN (enthalpic regime), a steep linear increase in force is observed and the DNA extended to its crystallographic contour length L_0 (16.3 µm in this case), with an elastic modulus that accounts for its resistance to stretching. Around 65 pN, dsDNA undergoes a cooperative (overstretching) transition that leads to a physical alteration of the duplex and an increase in extension up to $\sim 1.7 L_0$. Hysteresis during relaxation indicates dissipated energy while reforming the duplex. [Figure taken from [Smith et al., 1996].] **(Right)** Mechanical unzipping of a λ-phage DNA construct by OT. After an initial force increase as shown on the left, opening of the double helix starts at ∼15 pN. Pulling both DNA strands apart at a velocity of 100 nm/s, a characteristic saw-tooth pattern (inset) is observed. Peaks/valleys in force correspond to GC-/AT-rich regions of the substrate (see Fig. 3.2) and correlate with a theoretical description (curve intentionally offset) that takes into account the base-pair binding energies. [Figure modified from [Bockelmann et al., 2002].]

are critical for practically all functions of DNA in living beings [Alberts et al., 1989], in particular for the mechanisms by which the genetic information – stored in the one-dimensional DNA sequence – is efficiently copied (during replication) and transformed into proteins (during transcription and subsequent translation). Figure 3.2 depicts some more details of the most common structure of double-stranded (ds)DNA.

From a mechanical viewpoint, dsDNA in solution represents an extraordinary polymer because of its increased stiffness: due to base-pair stacking and intertwined helices, bending of the molecule is a lot more difficult in comparison with other polymers, in particular with single-stranded (ss)DNA: the persistence length introduced in Eq. 2.24 is ∼50 nm for dsDNA and only ∼2 nm for ssDNA at physiological buffer conditions [Bustamante et al., 2003; Murphy et al., 2004]. When applying a tension between the two extremes of a dsDNA molecules with a technique like OT, the resulting behaviour of the molecular extension for a changing force is very well documented for a variety

of experimental conditions. For example, it has been studied in detail as a function of ionic strength [Baumann et al., 1997; Wenner et al., 2002], pH [Williams et al., 2001a] and temperature [Mao et al., 2005; Williams et al., 2001b]. In fact, the characteristic force–extension relation of a worm-like chain (WLC), illustrated in the left panel of Fig. 3.3, can serve as a standard to determine all important calibration parameters merely by comparing the behaviour of two different but known DNA substrates with the same OT instrument [Rickgauer et al., 2006]. We have performed dsDNA force–extension measurements as the one represented in Fig. 3.16 foremost to check the linear ranges of trap stiffness and detector sensitivity, and to compare our results with reference data from an OT instrument working with two counterpropagating beams (equivalent to the one described in Ref. [Smith et al., 2003]).

The force at which the DNA double helix can be separated into two single DNA strands when "unzipping" it from one of the duplex ends oscillates around a constant mean value in direct dependence on the base pair sequence, as shown in the right panel of Fig. 3.3. The resulting pattern provides another way to evaluate the performance of force spectroscopy equipment, as the number of observed peaks/valleys directly correlates with the spatial resolution of the instrument [Bockelmann et al., 2002]. Again, we have carried out such measurements (see Fig. 3.17) in order to compare the signal obtained in our trapping microscope with the one from a dual-beam setup (see above), and to check the validity of calibration parameters for optically trapped microspheres of a different size.

3.2. Experimental materials and methods

3.2.1. Software design platform

The entire control software of the OT instrument (and of the setups used in Chaps. 4 and 5), as well as many of the routines for data analysis were developed in LabVIEW (short for "laboratory virtual instrument engineering workbench") 2009 SP1 (National Instruments, TX, USA). LabVIEW is a graphical programming environment that offers a rather intuitive access to the code and does not require knowledge in text-based programming languages, which facilitates the exchange and reuse of (certain parts of) LabVIEW-based software programs. We specifically chose version 2009 SP1 (build number 9.0.1) because it provides a good balance between performance and compatibility with hardware controllers available for a 32-bit computer running Microsoft Windows XP SP3. In particular, it offers multi-threading, i.e. the possibility to execute certain processes in parallel within the same or among different program instances, as well as virtual real-time control through so-called "timed structures". These structures are able to circumvent the operating system, allowing us to directly assign a specific process with defined priority to a single core of the central processing unit (CPU). We made use of the mentioned features to design our software interface as a group of several LabVIEW programs, with the main one additionally containing

various while loops running in parallel (see Fig. 3.7). Two of these loops (the time-critical ones in charge of image acquisition and processing) are *timed* structures, in equivalence to the approach first described by Otto and colleagues [Otto et al., 2010].

3.2.2. Flow cell fabrication

Similar to the making of chambers used for the MT described in Chap. 5, fluid chambers as the one depicted in Fig. 3.6a were assembled as sandwiches of two #1 coverslips (24×60 mm, thickness 0.13–0.16 mm; BB024060A1, Menzel-Gläser, Germany) with two layers of plastic paraffin film (Parafilm M, Bemis, WI, USA) in between. To establish connections between the lateral channels (1 and 3) with the central one (2), thin capillary tubing (inner/outer diameter 25/100 µm; King Precision Glass, CA, USA) was introduced between the two Parafilm layers. Likewise, slightly thinner tubing (inner/outer diameter 40/80 µm) from the same provider – previously pulled to a micropipette with tip diameter around 0.5 µm (using a tailor-made vertical pipette puller built around a heated platinum filament, based on a design by Steven B. Smith [Smith, 2008]) – was placed between the layers such that the tip reached the central region of the reaction channel (see Fig. 3.6b). The sample cell assembly was thermally sealed on a heating plate at 150 °C during 1–2 min. Both the in-/outlet holes in one of the cover glasses and the channel pattern in the Parafilm gaskets were obtained by means of a laser engraver (VLS2.30, Universal Laser Systems, AZ, USA).

3.2.3. Microspheres used in trapping assays

Functionalised spherical microparticles made of polystyrene with a mass density of 1.05 g/mL were purchased from Spherotech (Lake Forest, IL, USA) and showed a typical dispersion in diameter of 3–5 %, given by the standard deviation of the size distribution from Coulter counter measurements provided by the manufacturer. In practice, as the diameter is needed to determine the drag coefficient according to Eq. 2.10, the error due to particle size variations is one of the most prominent ones in trap stiffness calibrations [Neuman and Block, 2004].

Polystyrene microspheres (ref. SVP-20-5) coated with streptavidin (SA) had a nominal diameter of 2.10 µm. Anti-digoxigenin (Anti-Dig) particles were fabricated from protein-G-coated spheres with mean diameters of 2.16 or 3.18 µm (refs. PGP-20-5/PGP-30-5). From here on, for the sake of simplicity, the particles referred to in this chapter will be denoted and distinguished as 2 and 3 µm beads, with the precise values as stated in this paragraph. The antibody coating was established by means of the cross-linking agent dimethyl pimelimidate (DMP; Thermo Fisher Scientific, IL, USA), according to a protocol provided by Dr. Borja Ibarra (IMDEA Nanoscience, Madrid). In brief, the reaction was initiated by incubating protein-G-covered microspheres with solutions containing DMP and Anti-Dig (Roche, Switzerland) simultaneously during ~ 1 h. Subsequent quenching was achieved by buffer exchange and incubation with a

solution containing Tris (1 M), during ~ 2 h. The final product was washed at least twice and stored in phosphate buffered saline (PBS) solution (pH 7.0) at 4 °C.

3.2.4. DNA substrates for pulling experiments

The 4 kbp substrate used for the DNA stretching experiment shown in Fig. 3.16 was constructed by Elías Herrero according to the protocol described in Ref. [Herrero-Galán et al., 2012]. Essentially, the molecule corresponds to a central fragment of λ-DNA (located between base pairs 30286 and 34286) with ~ 50 % GC-content, which was synthesised by polymerase chain reaction (PCR) and subsequently ligated to ~ 500-bp-long handles containing multiple labels of biotin (Bio) and digoxigenin (Dig), respectively.

The construct used for the hairpin unzipping measurement illustrated in Fig. 3.17 was fabricated by Borja Ibarra according to a modified version of the procedure corresponding to the substrates used in Ref. [Morin et al., 2012] and contains a single Bio and multiple Dig labels. The 2.5 kbp region that is actually opened when pulling with the micropipette corresponds to a fragment of dsDNA from bacteriophage Φ29.

3.3. Theoretical concepts

3.3.1. Focal spot size and depth for a Gaussian beam

The lasers described in this chapter all operate in TEM_{00}-mode and therefore show an exponentially decaying intensity profile at radial deviations from the optical axis (see Eq. 2.4). A common definition of the beam half-width (or more simply, the beam radius) is the distance w at which the intensity has dropped to a fraction $1/\mathrm{e}^2$, such that

$$\mathcal{I}(w) = \mathcal{I}_0 \mathrm{e}^{-2} \,. \tag{3.1}$$

If such a Gaussian beam is focused by a lens, the half-width in the vicinity of the focal region along the optical axis (Z) can be described by the following hyperbolic equation [Hecht, 2002]:

$$w(z) = w_0 \left[1 + \left(\frac{\lambda_0 z}{\pi n_\mathrm{m} w_0^2} \right)^2 \right]^{1/2} \tag{3.2}$$

where w_0 denotes the radius at the beam waist (at $z = 0$), and n_m is the refractive index of the medium. Far from the focal region, i.e. for $z \gg w_0$ ($z \geq 0$ for simplicity), it follows that

$$w(z) \approx \frac{\lambda_0 z}{\pi n_\mathrm{m} w_0} \tag{3.3}$$

and, equivalently,

$$\frac{\Theta}{2} \approx \frac{\lambda_0}{\pi n_\mathrm{m} w_0}\,, \tag{3.4}$$

where we have introduced the beam divergence angle Θ in the far field that fulfils $\sin\Theta \approx \Theta \approx 2w(z)/z$. If we now consider a collimated beam of diameter D_beam entering a convex lens of focal length f_L at a half-width $w \equiv D_\mathrm{beam}/2 \ll f_\mathrm{L}$, so that $\Theta \approx D_\mathrm{beam}/f_\mathrm{L}$ as well, from Eq. 3.4 we obtain the following estimate for the focal spot diameter of a focused Gaussian laser beam:

$$2w_0 \approx \frac{4\lambda_0 f_\mathrm{L}}{\pi n_\mathrm{m} D_\mathrm{beam}} = \frac{2\lambda_0}{\pi n_\mathrm{m} \mathrm{NA}_\mathrm{beam}}\,, \tag{3.5}$$

with

$$\mathrm{NA}_\mathrm{beam} := \frac{D_\mathrm{beam}}{2f_\mathrm{L}} \tag{3.6}$$

being the effective numerical aperture of the beam. Going back to Eq. 3.2, a beam radius $w(z = z_\mathrm{R}) \equiv \sqrt{2}w_0$ implies

$$z_\mathrm{R} := \frac{\pi n_\mathrm{m} w_0^2}{\lambda_0}\,, \tag{3.7}$$

which is known as the Rayleigh range [Hecht, 2002]. This quantity can be used to approximate a focal depth $2z_\mathrm{R}$ by plugging in the expression for w_0 from Eq. 3.5, so that we end with

$$2z_\mathrm{R} \approx \frac{8\lambda_0 f_\mathrm{L}^2}{\pi n_\mathrm{m} D_\mathrm{beam}^2} \underset{(3.6)}{=} \frac{2\lambda_0}{\pi n_\mathrm{m} \mathrm{NA}_\mathrm{beam}^2}\,. \tag{3.8}$$

3.3.2. Proportional–integral–derivative (PID) feedback

A control loop is a feedback mechanism that tries to correct differences between a measured process variable X_meas and the desired setpoint X_set [Åström and Hägglund, 1995]. A linear feedback mechanism that is widely used in all types of control systems is the PID controller, which according to Fig. 3.4 attempts to minimise the error $e := X_\mathrm{set} - X_\mathrm{corr}$ (where X_corr is the processed/corrected value of X_meas) by calculating a corrective action that is applied to the manipulated variable Y_out. The change in Y_out for consecutive controller iterations is based on three separate contributions: a proportional term $\mathcal{X}_\mathrm{P}$ that corresponds to the response to the current error, an integral term $\mathcal{X}_\mathrm{I}$ that accounts for the response to the sum of recent errors, and a derivative term $\mathcal{X}_\mathrm{D}$ that determines the response to the rate at which the error has

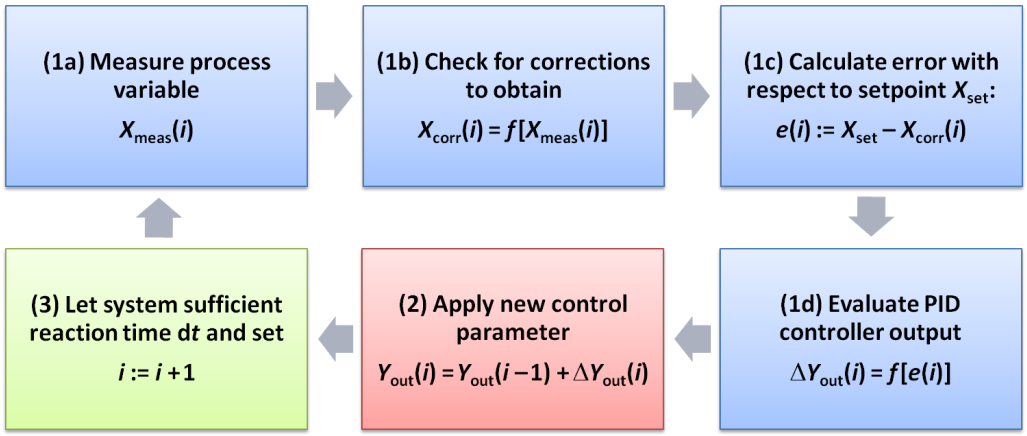

Figure 3.4. Flow chart of the procedure for software-based proportional–integral–derivative (PID) feedbacks. The algorithm is composed of three sequential frames (blue, red and green) inside a continuous loop structure. The essential steps in the first frame are (1a) the measurement of the process variable X_{meas} (e.g. laser power or objective temperature) and (1d) the calculation of the PID controller output, which corresponds to a change of the manipulated variable Y_{out} (i.e. laser current or heating foil voltage). Step 1b only applies if it proves necessary/possible to determine a corrected value X_{corr} as a function of X_{meas}. The second frame serves for executing the evaluated control parameter variation ΔY_{out}, while the last one ensures a constant response time before the next loop iteration i starts.

been changing [Åström and Hägglund, 1995]. This behaviour can be expressed by the following equation:

$$\Delta Y_{\mathrm{out}}(t) = s' \left[\mathcal{X}_{\mathrm{P}}(t) + \mathcal{X}_{\mathrm{I}}(t) + \mathcal{X}_{\mathrm{D}}(t)\right] , \tag{3.9}$$

where s' denotes a linear conversion factor with units $[s'] = [Y_{\mathrm{out}}]/[X_{\mathrm{meas}}]$. For the case of iterative loop updates at frequencies on the order of 1–20 Hz, which correspond to the software-based feedbacks described in this thesis – used for laser power stabilisation, temperature control and active piezo stage position corrections –, the individual contributions can be expressed in discrete form as follows [Åström and Hägglund, 1995]:

$$\mathcal{X}_{\mathrm{P}}(t_i) = K_{\mathrm{P}} \cdot e(t_i) , \tag{3.10}$$

$$\mathcal{X}_{\mathrm{I}}(t_i) = K_{\mathrm{I}} \cdot \sum_{j=1}^{i} e(t_j)(t_i - t_{i-1}) , \tag{3.11}$$

$$\mathcal{X}_{\mathrm{D}}(t_i) = K_{\mathrm{D}} \cdot \frac{e(t_i) - e(t_{i-1})}{t_i - t_{i-1}} . \tag{3.12}$$

Note that the time increment $\mathrm{d}t_i =: t_i - t_{i-1}$ might fluctuate slightly between consecutive iterations of our LabVIEW software and is therefore not assumed to be constant.

K_P, K_I and K_D are the proportional, integral and derivative gain corresponding to the simplest (non-interacting) form of the PID controller, which is implemented as such in the software. The latter two contributions can be represented in terms of K_P to obtain an overall expression with a physical meaning (and explicitly correct parameter units):

$$K_\mathrm{I} := \frac{K_\mathrm{P}}{\mathcal{T}_\mathrm{I}}\,, \quad K_\mathrm{D} := K_\mathrm{P} \cdot \mathcal{T}_\mathrm{D}\,. \tag{3.13}$$

Here, $\mathcal{T}_\mathrm{I}$ and $\mathcal{T}_\mathrm{D}$ are the so-called integral and derivative time, whose values can be assessed with the commonly used calibration methods introduced by Ziegler and Nichols [Åström and Hägglund, 1995; Zuttion, 2013], which were applied for tuning most of the feedbacks in this thesis. Setting $\mathrm{d}e(t_i) =: e(t_i) - e(t_{i-1})$, we thus obtain two equivalent formulas for the controller output:

$$\Delta Y_\mathrm{out}(t_i) \;=\; s' \left[K_\mathrm{P} \cdot e(t_i) + K_\mathrm{I} \cdot \sum_{j=1}^{i} e(t_j)\mathrm{d}t_i + K_\mathrm{D} \cdot \frac{\mathrm{d}e(t_i)}{\mathrm{d}t_i} \right] \tag{3.14}$$

$$\underset{(3.13)}{=} s' \cdot K_\mathrm{P} \left[e(t_i) + \frac{1}{\mathcal{T}_\mathrm{I}} \cdot \sum_{j=1}^{i} e(t_j)\mathrm{d}t_i + \mathcal{T}_\mathrm{D} \cdot \frac{\mathrm{d}e(t_i)}{\mathrm{d}t_i} \right]. \tag{3.15}$$

3.4. Results and discussion

In the following – in addition to calibration and force–extension measurements – the main components that constitute the OT instrument are presented in detail. Even though – in a more application-focused context – the corresponding paragraphs would rather belong to the *materials and methods* section, they represent the major part of my work as a PhD student and therefore deserve a more accurate description here.

3.4.1. The optical trapping system as a whole

Figure 3.5 gives a schematic impression of the entire OT setup. Small differences with respect to the real arrangement in our laboratory are explained in the caption. The apparatus is mounted as a customised inverted microscope on an optical breadboard ($120 \times 90\,\mathrm{cm}$; Thorlabs, NJ, USA), incorporated in a rigid framework (Newport, CA, USA) with a shelf that provides space for all hardware controllers, and a vibration isolation circuit through passive damping by means of compressed air at a pressure of $\sim 3.5\,\mathrm{bar}$. The whole rack is covered by a layer of laser safety curtain (Doppelstoff, Rudolf Breuer, Germany), with practically all controllers and power supplies kept outside to reduce electrical and thermal noise.

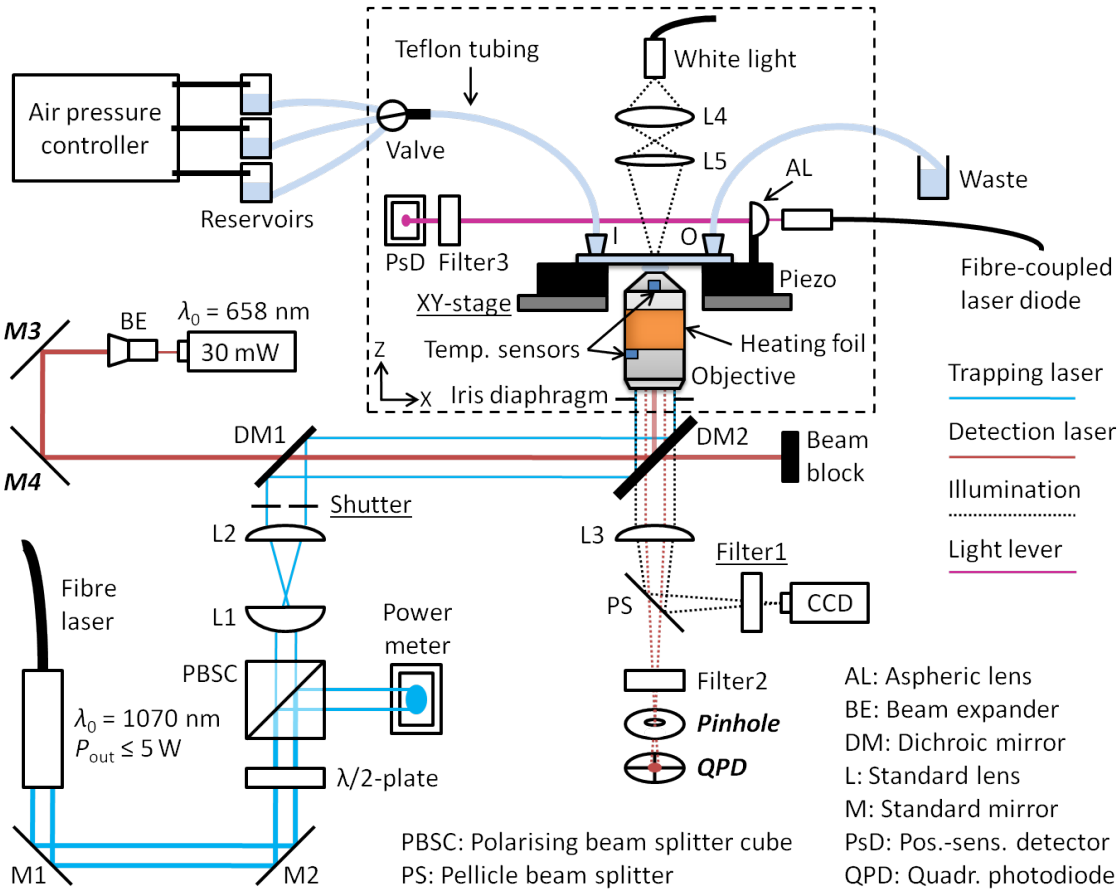

Figure 3.5. Schematic overview of the optical tweezers (OT) setup as described in the text (*not to scale*). The dashed rectangle encloses sample stage parts illustrated from the side (PsD in perspective); all other optical components are represented in top view (Power meter, Pinhole and QPD in perspective). The distance between the blue lines indicates the diameter of the trapping laser beam (line thickness accounts for beam power in this case). Please note that in reality, the objective is fixed in XY but attached to a linear micrometre stage for coarse positioning in Z (not shown). Note also that, for the sake of clarity, one 45 ° standard mirror between DM2 and Iris diaphragm is not represented here either. Labels in bold italics indicate parts (M3, M4, Pinhole and QPD) that require periodic realignment during trapping experiments to ensure accurate laser-based imaging detection. Underlined labels refer to components (Filter1, Shutter and XY-stage) that were specifically automated to facilitate the use of the microscope, which – for safety reasons and to minimise noise due to air currents and ambient light – is completely enclosed by laser-proof fabric (not shown).

The following paragraphs describe the principal elements of the OT system – most of them shown in Fig. 3.5 – one by one. A list summarising the important references can be found in Table A.1 in the appendix. Unless otherwise noted, lenses and mirrors are standard (laser-quality) versions with a diameter of 1 inch $\widehat{=}$ 25.4 mm and broadband surface coating for the specific wavelength range. Although most components are commercially available, various mechanical parts had to be adapted

to our particular layout and were developed by means of computer-aided design (CAD) software SolidWorks (Dassault Systèmes, France). In comparison with turnkey optical microscopes, a setup assembled from scratch gives us higher flexibility for beam path alignment and integration of different position detection systems, and – above all – the possibility to leave the space on top of the sample cell open.

3.4.2. Implementation of the trapping laser

To form a single, static optical trap inside the fluid chamber, we employ a continuous-wave, single-mode ytterbium fibre laser (YLM-5-LP-SC, IPG Photonics, MA, USA) with a maximum output power of 5 W. In such a device, the optical fibre itself is doped with the rare-earth element and serves as the active amplification medium, offering superior beam quality at a compact size, high powers and moderate costs [Lee et al., 2007]. In our case, a collimator coupled to the fibre end yields a TEM_{00}-beam with quality factor $M^2 < 1.05$ (specifying the relative deviation from the ideal, diffraction-limited Gaussian beam considered in Subsect. 3.3.1) at a diameter of 5 mm (corresponding to the $1/\mathrm{e}^2$-level, see Eq. 3.1) and a nominal infrared (IR) wavelength $\lambda_0 = 1070\,\mathrm{nm}$. This last value differs by only 0.5 % from the more commonly used 1064 nm (see Subsect. 2.1.3), and we can take for granted that all components designed for the latter wavelength serve equally well in our system. To avoid confusions, we treat the herein used trapping laser as if it delivered a 1064-nm-wave from now on.

The polarisation state of the laser light was checked experimentally to be linear in a plane perpendicular to the optical table, at an extinction ratio of around 20 dB, i.e. the fraction of the respective power values is $P_\perp/P_\parallel \approx 100$. After reflection at two standard mirrors (M1/2; Thorlabs) for alignment, we let the beam pass through a $\lambda/2$-plate (Thorlabs), which rotates the polarisation direction by an adjustable angle, and a polarising beam splitter cube (PBSC; Newport), which divides the intensity into two orthogonally polarised components.

Since the laser works best at a total output power P_{out} close to its nominal maximum value [Neuman and Block, 2004] and we do not need more than 900 mW entering the back aperture of the objective, we adjust the waveplate such as to couple out a large portion of $\sim 80\,\%$ from the beam path, which reaches a high-threshold thermal power meter (UP19K-15S-H5, Gentec-EO, QC, Canada) that measures on-the-fly and is connected to the computer via USB. From Subsect. 2.1.2 we know that $k_{\mathrm{trap}} \propto P_0$, which implies $k_{\mathrm{trap}} \propto P_{\mathrm{OT}}$, where P_{OT} ($> P_0$) denotes the pre-objective laser power used for optical trapping and thus represents the $\sim 20\,\%$ transmitted through the PBSC towards the sample stage. As a consequence, by using the power meter readings and simultaneous software access to the laser controller via standard serial communication, we are able to establish an active feedback that minimises power-related instabilities of the optical trap stiffness (see Subsect. 3.4.9).

We also quantified pointing fluctuations of the expanded laser beam – which may

lead to position variations of the trap centre – at a distance $\sim 1\,\mathrm{m}$ from the fibre collimator output by monitoring the location of the peak intensity on a beam profiling camera (Beamage Focus II, Gentec-EO) with time. During a period of $\sim 1\,\mathrm{h}$, we found a maximum value $\leq 20\,\mu\mathrm{rad}$, which is better than the typically encountered values for the common solid-state lasers used for OT in the far field [Neuman and Block, 2004].

Beyond the PBSC, the transmitted power passes through a telescope composed of two plano-convex lenses (L1/2; Linos, Germany) with focal lengths $f_{\mathrm{L1}} = 50\,\mathrm{mm}$ and $f_{\mathrm{L2}} = 100\,\mathrm{mm}$, which expand the laser beam twofold to a final diameter of $\sim 10\,\mathrm{mm}$. From fibre output to L2, the trapping laser path is completely covered by an additional black box to further minimise disturbances due to air currents and dust particles. Right after the exit aperture of the box, a computer-controlled electronic shutter (04ESC121, CVI Melles Griot, NY, USA) provides a safe way of instantly switching the trapping potential on/off without altering the laser output power. The beam is then reflected at two dichroic mirrors (DM1: 25 mm, G340763000; and DM2: 50 mm, G340765000; Linos) with dielectric coating "DLHS IR 1064 nm" – which reflects more than 99.8 % in the near IR –, so that practically all the expanded beam (linearly polarised in the horizontal plane) reaches the objective.

3.4.3. Implementation of the detection laser

To efficiently exploit the reflected light from an optically trapped particle and probe its position at high bandwidths, we incorporated an additional diode laser (51nanoFCM, Schäfter+Kirchhoff, Germany) with $\lambda_0 = 658\,\mathrm{nm}$ and $P_{\mathrm{out}} \leq 30\,\mathrm{mW}$ into the system. Note that, with the optical components mounted as shown in Fig. 3.5, it would not be feasible to use the trapping laser itself for this purpose because DM2 reflects practically all IR light back towards DM1. An efficient readout of backscattered trapping laser intensities would therefore require a different type of beam splitting device (such as a PBSC). In any case, as already mentioned at the end of Subsect. 2.3.2, using an additional laser for position detection in reflection has the advantage of a typically increased signal-to-noise ratio [Keyser et al., 2006], apart from the better responsivity of most photo detectors in the visible range [Huisstede et al., 2005].

The red laser exits a polarisation-maintaining, single-mode fibre cable with integrated collimator, yielding a horizontally linearly polarised, Gaussian intensity distribution with a diameter of $\sim 1\,\mathrm{mm}$. The output power can be adjusted by software, although we always run it at its maximum value, which – after a warm-up time of at least 30 min – gives rise to a highly stable signal with a measured root-mean-square (RMS)/peak-to-peak (PTP) noise $\leq 0.01/0.10\,\%$. This superior performance is possible because of intrinsic frequency modulations (above 300 MHz) – much faster than any detectable frequency during trapping experiments – of the laser signal, which suppress potential mode hopping and lead to a slightly increased line width $\Delta\lambda \approx 1.5\,\mathrm{nm}$, corresponding to a reduced coherence length $l_{\mathrm{coh}} \approx \lambda_0^2/\Delta\lambda \approx 300\,\mu\mathrm{m}$ that has the benefit of greatly eliminating laser speckle noise (observe the camera snapshots in Fig. 3.11a).

Twofold expansion of the detection laser is achieved by a commercial beam expander (BE; Thorlabs) with a collimation adjuster, which serves for tuning the divergence angle of the outgoing light cone and hence the Z-position of the red laser focus relative to the optical trap centre for different microsphere sizes. Expanding the additional laser by a factor of two, a slightly smaller focal spot and correspondingly higher reflections from the surface of the confined bead are obtained without creating a too large intensity gradient that might interfere with the optical trap. Using the same procedure as for the IR laser, the maximum pointing fluctuations of the expanded 2 mm beam at ~ 0.5 m from the fibre collimator output were determined as ≤ 4 µrad in this case, which is smaller than the value stated by the manufacturer.

Two standard mirrors (M3/4; Thorlabs) are used to align the visible beam relative to the infrared one and need to be readjusted from time to time to ensure accurate outcomes of particle positions from imaging detection. Note that dichroic mirrors DM1/2 (see previous subsection) are both transparent for $\geq 95\,\%$ of the radiation at 658 nm, so that only a small (but sufficiently large) portion of the initial diode laser power enters the objective, and a beam block behind DM2 becomes necessary.

3.4.4. Microscope objective features

We use a water-immersion objective (UPLSAPO 60XW, Olympus, Japan) with 60-fold magnification and NA = 1.2, providing the highest levels of flat-field and aberration corrections [Davidson and Abramowitz, 2002]. It has a conveniently high working distance of 130 µm, enabling trapping experiments at a distance of ~ 100 µm above the fluid chamber surface without detrimental effects on trap stiffness [Vermeulen et al., 2006], and transmits $\sim 87\,\%$ at 658 nm and $\sim 50\,\%$ at 1064 nm.

Its physical back aperture is 8 mm in diameter, although the effective back aperture according to Eq. 3.6 (corresponding to NA = 1.2) is given by $2\,\mathrm{NA} f_{\mathrm{MO}} = 7.2$ mm, with $f_{\mathrm{MO}} = 3$ mm being the objective front focal length [Mahamdeh et al., 2011]. In order to reduce heating of the objective barrel by the expanded IR laser overfilling the back aperture, we place an iris diaphragm with a diameter of 8 mm underneath at a distance of ~ 10 mm (fixed to the opposite side of the objective holder). The insets of Fig. 3.8b show the IR laser beam profile before and after passing through the diaphragm. The ratio of expanded beam diameter and effective back aperture defines an overfilling ratio, which in our case is $\sim 10/7.2 \approx 1.4$. Considering the power losses at DM1/2, iris diaphragm and inside the objective, we can say that only $\sim 30\,\%$ of the pre-objective trapping power (measured after L2) enter the fluid chamber, whereas in the case of the detection laser the number reduces to $\leq 5\,\%$ because of the low reflection at DM2 (see above).

As visible in Fig. 3.9a, the objective has a correction collar to compensate for cover glass thickness, which should always be set to the correct value to minimise optical aberrations. We found that a value of 0.13 mm corresponds to the best compromise

between good image quality and maximum trap stiffness when using coverslips with a thickness of 0.13–0.16 mm (see Subsect. 3.2.2), in accordance with the results presented in Ref. [Reihani et al., 2011]. Note that the correction collar itself restricts in part the access to the objective barrel, limiting for instance the space for attachment of resistive foil heaters used to artificially raise the temperature (see Subsect. 3.4.9).

The objective is installed on top of a stable, custom-made support that is screwed to a linear Z-translation stage (Newport) for coarse adjustments of axial positions. Recall that in our setup the optical trap is static in XY: as depicted in Fig. 3.5, lateral positions are varied only via an XY-translation stage and a piezoelectric stage holding the fluid chamber, both of which are addressed in the following subsection.

3.4.5. Sample stage assembly

Piezoelectric three-dimensional nanopositioner

All experiments described in this chapter were performed in fluid chambers that correspond to the design introduced in Subsect. 3.2.2, with an internal thickness of $\sim 200\,\mu$m corresponding to two Parafilm layers as spacers. For precise control over the optical trap via movements of the sample stage, one such chamber is mounted onto a piezo(electric) XYZ-positioning system (P-517.3CD, Physik Instrumente, Germany) as shown in Fig. 3.6a and controlled by a digital high-voltage controller (E-710.3CD, Physik Instrumente), connected to the computer via a GPIB interface. It allows for multi-axis motion with a resolution of 1 nm and has a range of 100 (20) µm in XY (Z). Due to the lack of independent outputs of our controller model, position readout is only possible via GPIB at a reduced frequency of 55 Hz when all three axes are monitored.

We have used the stage for measurements requiring both slow (e.g. DNA force–extension curves at down to 100 nm/s) and fast (e.g. Stokes drag calibrations at up to 2 mm/s) piezo velocities. In order to improve the linearity of the nanopositioner, especially at the slowest velocities – and due to the fact that, during the use of movement cycles defined via standard command sequences sent to the controller, the communication with the piezo via GPIB is blocked and no positions can be read out –, we employ an alternative way of predefining motion parameters via wave functions associated to a generator that is stored in the EEPROM (short for "electrically erasable programmable read-only memory") of the controller. That way, upon activation of such a wave generator, communication via GPIB remains possible at all times, and we are still able to directly read out positions and – more importantly – switch on active position feedbacks based on additional piezo steps along the axes not accessed by the generator. To be able to use all these different features at the same time, we had to implement them in the main software interface in a parallel way and avoid mutual interferences by making use of certain structural elements provided with LabVIEW (see Fig. 3.7).

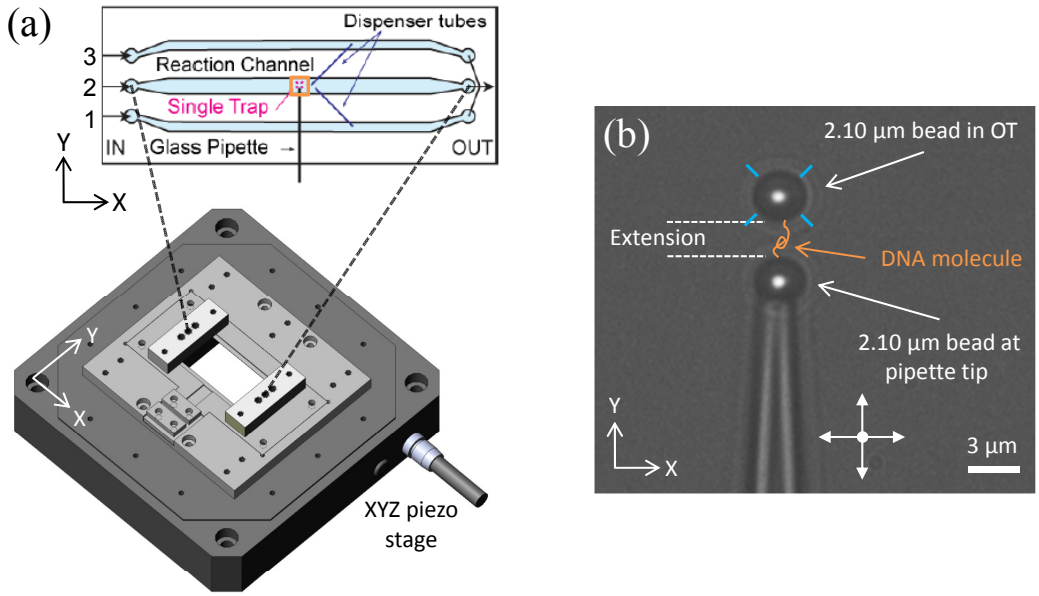

Figure 3.6. Sample cell configuration for single-molecule experiments. **(a)** Fluid chambers (*top*) contain three channels: 1 and 3 are filled by hand with microspheres of different types, some of which can enter the central reaction channel (2) via thin dispenser tubes. The flow velocity through this slightly wider channel is modulated by a pressure controller as shown in Fig. 3.5. A glass micropipette is introduced with its tip close to the channel centre (indicated by the orange rectangle) – where OT measurements are performed. The entire fluid chamber is mounted on top of a piezoelectric positioning stage (dark grey, *bottom*), and in between custom-made holder parts (light grey) that provide sufficiently tight fixing, leak-less fluid manipulation and good access for the microscope objective from below. **(b)** Pipette tip and optical trap constitute two anchor points for bead handles flushed through channels 1 and 3, respectively. The behaviour of (invisible) biomolecules such as DNA is inferred from the movement of both microspheres, where the position of the trap centre is kept constant and the pipette moved in XYZ together with the piezo stage to exert forces and/or correct for thermal drift.

Light-lever system

To provide a way of quantifying the Y-position of the piezo stage independently at high bandwidths, we installed a so-called light-lever (LL) assembly along the X-axis (as illustrated in Fig. 3.5, adapted from a design initially proposed by Bustamante and co-workers [Smith et al., 2003]). Such an arrangement consists of a beam from a fibre-coupled laser diode (LPS-635-FC, Thorlabs) that is collimated by an aspheric lens (AL; C140TME-B, Thorlabs) in close proximity (< 1 mm) to the fibre output and projected onto a position-sensitive detector (PsD; PDP90A, Thorlabs) at a large distance (~ 600 mm in our case). A neutral density filter (Filter3; Thorlabs) ensures that the maximum voltage level of the PsD is not exceeded. In this manner, a small transverse displacement of the lens (mounted on the piezo) with respect to the fibre output (fixed to the micrometer stage but *not* to the piezo) translates into a large

signal on the PsD, resulting in our case in a sensitivity of $\sim 0.4\,\mathrm{V/\mu m} \approx 0.4\,\mathrm{mm/\mu m}$. This means that a piezo move of e.g. 10 nm is magnified ~ 400 times to a displacement of $\sim 4\,\mu\mathrm{m}$ on the PsD (which is still perfectly detectable).

This light-based detection method offers a signal that is stable within the finite time of a (DNA) pulling experiment and can offer increased positional resolution due to its high bandwidth of up to 15 kHz. Indeed, we observe a voltage readout noise of $< 0.5\,\mathrm{mV}$ on the detector at 10 kHz, corresponding to a resolution in micropipette position of $\sim 1\,\mathrm{nm}$. PsD signals are monitored via a sensor controller (TPA101, Thorlabs) connected by BNC cables to an external connector block (NI BNC-2120, National Instruments), which in turn communicates with an internal, high-performance data acquisition (DAQ) card (NI PCIe-6351, National Instruments) offering multi-channel sample rates of up to 1 MHz.

Automated micrometer stage

For coarse control in XY, the nanopositioning system itself is mounted onto a custom-made micrometer stage that is driven by motorised actuators (TRA25CC, Newport) interfaced to the computer in series and controlled by an external joystick via LabVIEW. By this means, it is possible to "move" the optical trap through the fluid chamber (in reality, the chamber is moved and trap kept fixed) with an accuracy of $\sim 1\,\mu\mathrm{m}$ in a semi-automatic manner. In particular, remote control of the micrometer stage with a joystick greatly facilitates the movements between strategic positions such as the pipette tip and the dispenser exits inside the central channel (channel 2 in Fig. 3.6a), therefore enhancing the throughput of single-molecule experiments with the OT instrument.

3.4.6. Pressure controller for accurate fluid flow adjustments

To be able to adjust the volume flow rate through the central reaction channel with the necessary precision, we integrated a high-resolution air pressure controller (MFCS, Fluigent, France) with an adjustable pressure range of 0–25 mbar in the experimental setup. This device is controlled by LabVIEW-software via USB and proves particularly important for our sample cell configuration involving a micropipette at half-height ($\sim 100\,\mu\mathrm{m}$) of the microfluidic chamber – where the linear flow velocity is strongest (see Fig. 5.11b) and may disturb the optically trapped particle if not modulated smoothly enough. This situation is totally different from the one encountered during MT experiments (see e.g. Subsect. 5.4.4), where a less delicate flow control with standard syringe pumps poses no problem.

As illustrated in Fig. 3.5, three pressure outlets connected to fluid reservoirs with different types of solutions can be controlled independently and are connected to the reaction volume of the fluid chamber via a manual valve. A waste bottle collects the buffer leaving the chamber at the other end. Note that excess solution from channels

1 and 3 is collected in separate small Eppendorf tubes to avoid contaminations. All three waste recipients need to be placed with their water levels at a slightly higher altitude than the one of the fluid chamber (in the case of channels 1 and 3) and the one of the inlet buffer bottles (in the case of channel 2). Since the controller is unable to apply negative pressures, only in such a configuration – due to the counteracting effects of hydrostatic pressure – the flow can be efficiently stopped in the reaction channel.

3.4.7. Implementation of camera imaging and laser-based detection

White-light imaging beam path

The reaction volume is illuminated from the top by means of an optical arrangement complying with the principal requirement of Köhler illumination [Davidson and Abramowitz, 2002]: an evenly distributed light intensity in the sample plane. We use a standard halogen light source (150 W; Schott, Germany) coupled into a fibre light guide with an effective output aperture of 8 mm (Navitar, NY, USA). Using two biconvex lenses (L4/5; Newport) with focal lengths $f_{\mathrm{L4}} = 25\,\mathrm{mm}$ (collector lens) and $f_{\mathrm{L5}} = 75\,\mathrm{mm}$ (condenser lens) in combination with an iris diaphragm (aperture diaphragm; Thorlabs) conveniently placed between them (not shown in Fig. 3.5) – to eliminate unnecessary background illumination –, we are able to create a slightly converging light cone (NA ≈ 0.1) with a minimum diameter of $\sim 1\,\mathrm{mm}$ centred on the objective front lens.

From the objective back aperture, the white light emerges being slightly divergent, passes DM2 with more than 95 % of its intensity and is focused on the chip of a CCD camera (TM-6740CL, JAI Pulnix, CA, USA) by a tube lens (L3: precision achromatic doublet lens; PAC064AR.14, Newport) of focal length $f_{\mathrm{L3}} = 200\,\mathrm{mm}$. Since our objective is infinity-corrected for a tube length of 180 mm, we effectively increase its magnification by a factor of $200/180 \approx 1.11$. Indeed, calibrating the pixel (px) conversion factor of our camera with a standard micrometer grid, we obtain a value of $\sim 110\,\mathrm{nm/px}$, which – at a physical pixel size of $7.4 \times 7.4\,\mu\mathrm{m}$ – corresponds to a magnification of $\sim 67 \approx 1.11 \cdot 60$.

The camera is connected to a frame grabber card (NI PCI-1428, National Instruments) via a medium-configuration Camera Link connection and offers a repetition rate of 200 Hz at full readout of the sensor ($640 \times 480\,\mathrm{px}$). The frame rate can be augmented up to 1.25 kHz without binning if the region of interest (ROI) is reduced to a central area of $224 \times 160\,\mathrm{px}$. However, due to data transfer and computational limitations during online video tracking, and for best image contrast with our standard illumination, we are restricted to a maximum frame rate of 500–600 Hz. In practice, almost all measurements shown in this chapter were performed at 200 Hz.

Note that, in order to separate the white light from the backscattered detection laser signal, we employ a pellicle beam splitter (PS; Thorlabs) at 45 ° after L3 that only

reflects 8 % of the total intensity. Using such a very thin optical element has the advantage that no ghost images due to reflections at multiple surfaces become visible. An automated low-pass filter (Filter1; Newport) right in front of the CCD ensures that no light from detection or trapping laser reaches the chip during normal operation. Removal of the filter becomes necessary for instance during alignment of the detection laser spot with respect to the glass surface (see the snapshots in Fig. 3.11a).

Laser detection beam path

The intensities of the red low-power laser due to reflections at coverslips and particles in the optical trap are captured by the objective together with the white light and pass through DM2 practically unaltered. Assuming that $\sim 10\,\%$ of the laser radiation entering the fluid chamber are scattered back, we can estimate that far less than 1 % of the nominal detection laser output power P_{out} eventually reaches the photo detector. Note also that, since DM2 has a thickness of 10 mm, lateral displacements of beams transmitted through the mirror at an angle of 45 ° have to be taken into account. In reality, the light rays "below" DM2 in Fig. 3.5 are slightly shifted to the right, by a total amount of ~ 3 mm according to the laws of refraction. This is why practically all optical components upstream DM2 could be mounted on rails along the borehole lines of the breadboard, while the components downstream DM2 had to be fixed in a way that permitted lateral position adjustments to correct for the beam offset.

The reflected laser signal is also focused by tube lens L3 (see above), $\sim 92\,\%$ of its intensity pass through the PS (see above) and subsequently through a laser line filter (Filter2, Newport) that blocks light not corresponding to the red spectrum. According to Eqs. 3.5 and 3.8, the weakly focused Gaussian beam with $D_{\mathrm{beam}} \approx 2$ mm has an approximate focal spot diameter $2w_0 \approx 85\,\mu$m and a focal depth $2z_{\mathrm{R}} \approx 17$ mm. In order to filter out signal contributions due to background reflections, we place a pinhole (Thorlabs) of 150 µm in diameter within the focal region, increasing in this way the signal-to-noise ratio of the image projected onto the photodiode [Keyser et al., 2006]. We operate the QPD (2901-M, New Focus, CA, USA) – itself mounted on a three-way micrometer stage (Thorlabs) – in its highest amplification mode corresponding to a maximum power level of only 30 µW at the sensor. This proves that less than 0.1 % of the maximum laser output power (30 mW) are sufficient for our reflection-based position detection scheme.

Our turnkey QPD device has all signal processing electronics implemented inside its compact housing, so that voltages can be monitored directly via BNC connections to the external connector block controlled by the DAQ card (see Subsect. 3.4.5). Signal normalisation according to Eq. 2.33 can be done afterwards by software. Although the photo detector offers a maximum bandwidth of 100 kHz, for calibration measurements we never surpass an acquisition rate of 50 kHz – which still corresponds to oversampling (see Fig. 2.3). During force–extension measurements, we normally choose a rate of 10 kHz for all channels (including QPD/PsD data), which proves more than sufficient.

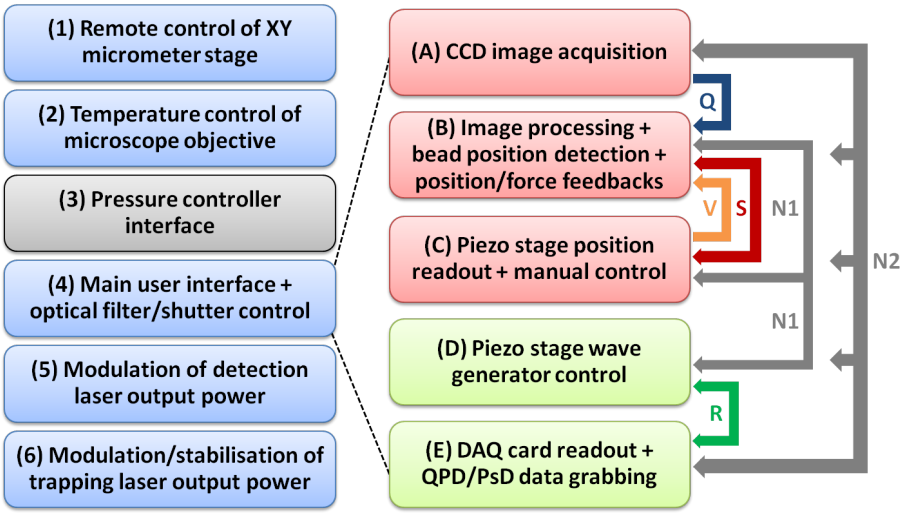

Figure 3.7. Principal structure of the optical tweezers (OT) software environment. The main application consists of six separate LabVIEW programs running continuously in parallel (*left*). The main user interface itself contains five while-loop structures that execute in parallel at various iteration rates (*right*). Camera images are passed from the acquisition (A) to the processing loop (B) via a queue structure (Q) that minimises the number of lost frames. Piezo positions are delivered from the slower readout loop (C) via local variables (V). Semaphores (S) are used to coordinate piezo readout and piezo-based position/force feedbacks, avoiding concurrent access to the hardware controller. Along the same lines, notifier N1 is in charge of defining which piezo-related functions are allowed to execute in loops B, C and D at the same time. The loops dedicated to piezo wave generator movements (D) and DAQ card functions (E) deserve a special mention because they become hardware-controlled when wave functions are run and photo detector data acquired at high bandwidth, respectively. A rendezvous structure (R) guarantees a synchronised start of the two tasks if required. All five loops communicate via notifier N2 to ensure correct process termination and storage of all data when the main program is stopped.

3.4.8. Development of the optical tweezers software

As already motivated in Subsect. 3.2.1, we created a graphical user interface in LabVIEW for controlling all of our optical trapping equipment. Figure 3.7 shows that the software is organised in a highly parallel manner, which has the additional advantage that changes in the graphical code can be made more easily. Among the principal programs (1, 2, 4–6) depicted in blue (only the application responsible for the pressure controller – shown in grey – is *not* custom-made), the main interface (4) is by far the one that requires most resources as it contains time-critical processes usually running at $\sim 200\,\mathrm{Hz}$. Note that the numbering refers to the order in which the software pieces should be started while preparing the OT for operation. The loop structures of programs 1, 2, 5 and 6 are all set to repetition rates of $\leq 10\,\mathrm{Hz}$.

Within the main interface, loops shown in red contain functions that remain always linked to the software, while green ones can get controlled externally by their corre-

sponding hardware and are thus able to work at much higher sample rates. Loop B can be considered as the program core as it comprises all procedures related to image processing, position calculations, active feedbacks and data storage. As a timed loop set to execute as fast as possible (i.e. with $\mathrm{d}t_i := 0$), it directly depends on the delivery of images from the CCD data acquisition loop A and can compensate sporadic accumulations of camera frames in the queue by automatically incrementing its speed if necessary. Having two independent loops A and B therefore ensures *image acquisition* at a constant frame rate (normally 200 Hz), even though image display and *position detection* may be slightly "out of phase" [Otto et al., 2010]. The repetition rates of the remaining loops are: C $\leftrightarrow$ 55 Hz, D $\leftrightarrow$ 10 Hz, E $\leftrightarrow$ 100 Hz. Please note that these values correspond to loops D and E in idle and simple readout/monitoring mode, respectively. As soon as a wave generator is started and/or photo detector data streamed to the hard disk, D and E can partially uncouple from the software and the operating system, thus enabling their tasks to be carried out at several kilohertz – and without losing the option of intervention by the experimenter.

3.4.9. PID control of trapping laser and objective temperature

Stabilisation of the laser output power

As already mentioned in Subsect. 3.4.2, our IR fibre laser used for trapping provides a high-quality beam at considerable output powers. However, due to the length of the gain medium (i.e. the fibre), it is also somewhat susceptible to power fluctuations. To avoid uncertainties in trap stiffness due to low-frequency noise, we established a software-based control loop feedback according to the scheme shown in Fig. 3.4, with laser power and laser controller current being measured and manipulated variable, respectively. From Eq. 3.14 it becomes clear that one of the necessary parameters of a PID controller is the sensitivity s' that provides a linear conversion between both variables. This quantity was determined beforehand by annotating the output powers for well-defined current values – in-/decreased in small steps.

Since the laser controller is connected to the computer via standard serial bus, the update rate of the feedback is limited to 5 Hz. In any case, we would not want to try to correct for faster fluctuations in order not to introduce artificial noise at relevant frequencies in the power spectrum of a trapped microsphere. Note also that it is good practice to use a running average of the measured variable as the corrected value X_{corr} in order to filter out high-frequency variations and correspondingly reduce the fluctuations in the PID controller output. Figure 3.8 shows the typical short-term power fluctuations with and without active feedback at a moderate P_{OT}-value of 400 mW. Obviously, the feedback improves the power stability by approximately one order of magnitude, so that we do not have to worry about the corresponding uncertainties any longer.

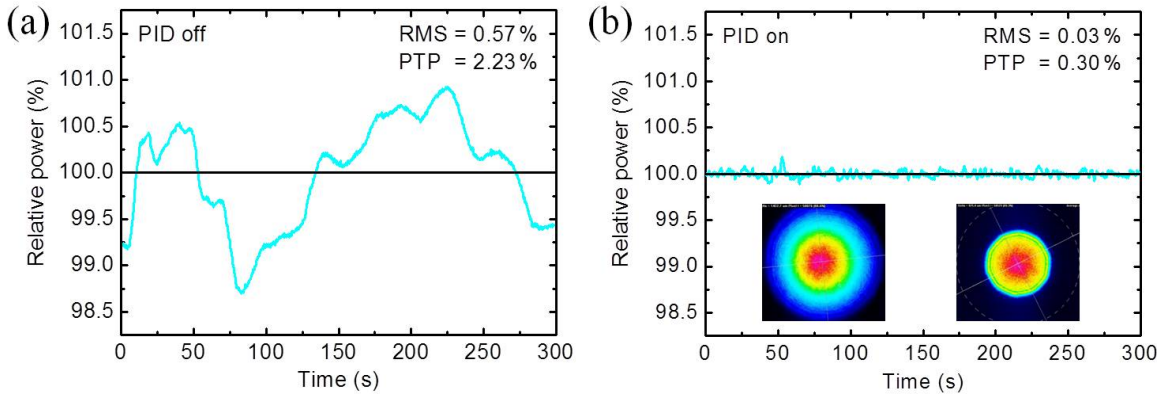

Figure 3.8. Power stability of the infrared (IR) trapping laser. **(a)** Without active feedback, the fibre laser shows root-mean-square (RMS) and peak-to-peak (PTP) fluctuations around the power setpoint that are significant in comparison with other noise sources in OT measurements. **(b)** By means of a PID controller based on the scheme presented in Fig. 3.4, power instabilities are reduced by at least 75 % and thus made negligible. Two images taken by a beam profiler camera show the Gaussian intensity distribution of the laser when expanded to $\sim 10\,\mathrm{mm}$ in diameter (*left*), and after passing through the iris diaphragm set to 8 mm (*right*) that is located right below the microscope objective (see Fig. 3.5).

External heating of the microscope objective

In order to minimise unspecific warming of the microscope objective lens due to partial absorption of trapping laser intensities, giving rise to an axial drift of $\sim 1\,\mu\mathrm{m}/^{\circ}\mathrm{C}$, we follow the strategy proposed by Mahamdeh and Schäffer and artificially raise the temperature of the objective barrel prior to activation of the trap, therefore reducing the impact of laser-related effects [Mahamdeh and Schäffer, 2009]. To this end, we combined a single resistive foil heater ($R = 13.6\,\Omega$; HK5237R13.6L12A, Minco, France) with two high-precision platinum resistance (Pt100) temperature sensors (PTFC101T, Correge, France), attached to the objective barrel as indicated in Fig. 3.9a. To maintain the temperature stable within 0.1°C, we implemented a PID feedback based on the software used for trapping laser stabilisation (see previous paragraphs), with measured and manipulated variable now being the temperature from sensor $\mathrm{T_b}$ and the voltage applied to the heating foil, respectively.

This approach is totally equivalent to the one used for controlling the objective temperature in our thermally stabilised MT apparatus (see Chap. 5). For details about heater/sensor attachment and calibration, temperature data acquisition and processing, PID feedback tuning, and computer control of the heater voltage via a programmable power supply unit, the reader is kindly referred to Subsects. 5.4.1 et seqq. The sensitivity of the OT heating circuit was found to be $s_{\mathrm{OT}} = 3.0\,\mathrm{V}^2/^{\circ}\mathrm{C}$, which is smaller than the one of our MT assembly (see Fig. 5.6a) because of different heating foil models, and due to the fact that in the case of the MT circuit, the sensor used for the feedback is located farer away (at a position similar to the one of $\mathrm{T_t}$).

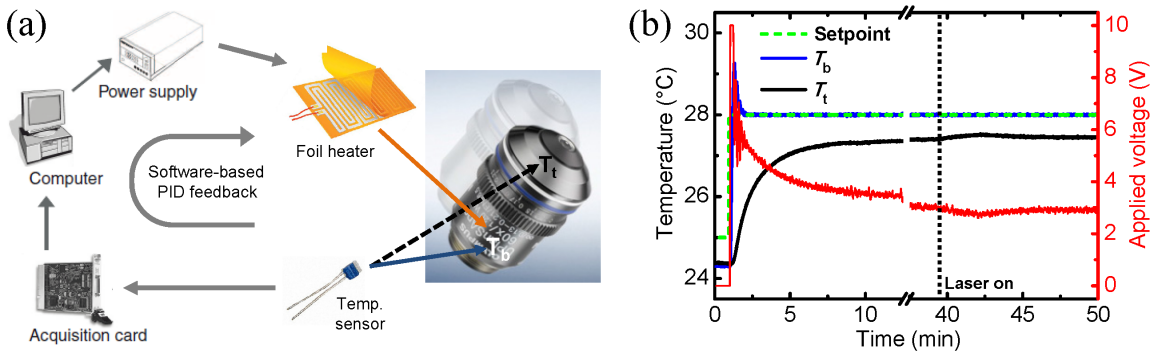

Figure 3.9. Temperature control of the microscope objective. **(a)** Heating circuit to reduce laser-induced effects. Stable objective temperatures above ambient conditions are achieved by means of one flexible foil heater and two high-precision temperature sensors (*bottom*: T_b; *top*: T_t). Heater and T_b are attached close to each other – right below the coverslip correction collar – and coordinated by a PID feedback according to Fig. 3.4 (see Chap. 5 for more details). [Figure adapted from [Mahamdeh and Schäffer, 2009].] **(b)** Typical temperature response during OT experiments. Starting at $\sim 24\,°C$, activation of the thermostat after 1 min leads to a steep increase of temperature T_b, which stabilises within 1–3 min at the setpoint (28 °C in this case). Equilibration of T_t takes ~ 10 min and is accompanied by a steady decrease of the voltage applied to the resistive heating foil. Apart from temperature variations right after switching the trapping laser on/off (after 39 min in this case), stabilities of $\leq 0.1\,°C$ can be maintained for both T_b and T_t during intervals of tens of minutes, whose exact length depends on the amount of applied laser power and ambient temperature changes.

The typical time response when setting the objective to a certain temperature before starting an experiment is shown in Fig. 3.9b. Temperatures stabilise to values that limit thermally induced axial drift to less than 100 nm over several minutes, even with the trapping laser switched on, giving rise to a small and stable thermal gradient across the objective barrel. It is worth noting that for all measurements shown in this chapter, we did never permanently heat the objective to more than 5 °C above room temperature, with T_b not exceeding 30 °C in most cases, which corresponds to a slightly lower T_t-value near the front aperture.

Apart from providing information about gradients across the barrel, the use of two sensors enabled us to establish a more direct feedback when compared with the one of the MT setup (see Chap. 5), with T_b being attached right below the heating element. It should be pointed out that – since OT experiments are performed at 100 µm above the lower cover slip –, in comparison with the situation in the MT-based arrangement, heating the OT water-immersion objective to moderate temperatures has only a small effect on the thermal conditions *inside* the fluid chamber. In fact, it is safe to assume that the major contribution of heat near the sample comes from the laser focus itself, which – at a maximum power of ~ 300 mW in the chamber – induces a temperature increase of $\sim 3\,°C$ for $\lambda_0 = 1064$ nm [Peterman et al., 2003]. Please note that such heating effects decrease with increasing size of the trapped microsphere.

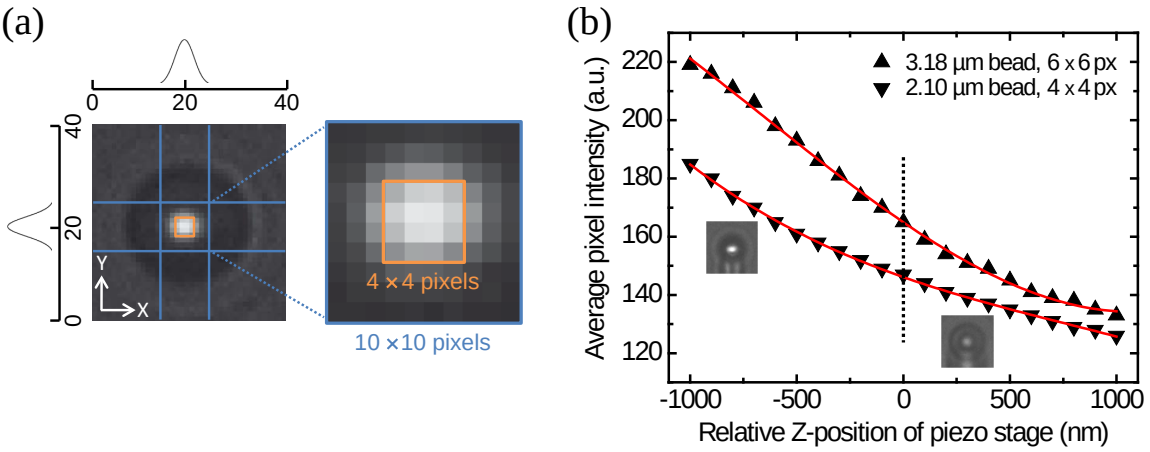

Figure 3.10. Video-based position determination in the optical tweezers (OT) instrument. **(a)** For accurate tracking of the XY-centre of a trapped microsphere, from a region of interest of $\sim 40 \times 40$ px (*left*) only a central square of 10 px edge length (*right*) is chosen in the case of 2 µm beads. To obtain information about position variations in Z, we choose an even smaller quadratic region of 4 px edge length and calculate its average pixel intensity under fixed illumination conditions. **(b)** With a bead attached to the pipette, initially at the height of an identical, optically trapped bead (see Fig. 3.6b), the change in mean intensity of the central pixels is monitored as the piezoelectric stage is moved up and down with respect to the zero (reference) position (dashed vertical line) in well-defined steps. Within an interval of ±1 µm, the resulting dependences are monotonically decreasing for the studied microsphere sizes and can be fitted by polynomial calibration curves (red lines) to extract relative distances in nanometres. Readout errors are given by the symbol size; insets show two examples of a 2 µm bead at the pipette and mean intensities of ∼130 and ∼160, respectively.

3.4.10. Three-dimensional video tracking under white light illumination

To follow the XY-positions of up to two microspheres (one in the optical trap, the other at the pipette tip) with our CCD camera at 200 Hz, we apply the method of cross-correlation transformation as described in Ref. [Gosse and Croquette, 2002]. First of all, we needed to adjust the Z-position of the camera sensor such as to provide an optimum image of the beads for our tracking routine: a central bright spot and as few bright concentric rings as possible. Note that, since during pulling experiments – corresponding to the situation in Fig. 3.6b – the microspheres can come very close to each other, so that their intensity patterns may overlap, illumination from a standard white light source is the most convenient choice for our OT. Virtually monochromatic light like the one from LEDs would give rise to diffraction rings similar to those shown in Fig. 2.7, leading to undesired interference effects and associated tracking problems for beads in close proximity.

Figure 3.10a illustrates how a typical image of an optically trapped 2 µm bead, corresponding to a manually selected ROI from Fig. 3.6b, is exploited to obtain the bead centre position. Essentially, the pixels corresponding to a 10×10 px sub-ROI are

binned and normalised separately in X and Y, giving mean one-dimensional, Gaussian-like intensity profiles. In the case of 3 µm beads, we would make use of a slightly larger area instead (composed of e.g. 12×12 px). Note that we choose a quadratic rather than a rectangular array in order to minimise the chances of intensities from approaching beads to interfere. To obtain sub-pixel resolution, the cross-correlation of each profile with its inverse (i.e. with its mirror image with respect to the central sub-ROI axis) is calculated via a Fourier transform algorithm according to the convolution theorem [Gosse and Croquette, 2002]. The resulting function is subsequently fitted with a second-order polynomial ±2–3 px around the peak centre. The exact position of the maximum indicates the relative displacement of the bead with respect to the central sub-ROI axis, re-defined for every new frame and corresponding to the trap centre on average.

To obtain information about axial position changes of the microsphere held at the pipette, we employ an approach similar to the one proposed by Wagner and co-workers [Wagner et al., 2011], associating the mean pixel intensity inside a central window of the microsphere sub-ROI to its height relative to the optically trapped bead. Despite the limited number of pixels of our CCD camera, we are able to calibrate a dependence within a region of approximately ±1 µm about the trap centre position in Z, merely by using a window of $4 \times 4\,(6 \times 6)$ px in the case of 2 (3) µm beads (Fig. 3.10b). The plotted average pixel intensity at a certain height can be determined with a relative error of 1–3 % and is simply given by

$$\bar{A}(z) = \frac{1}{N^2} \sum_{i,j} A_{i,j}(z) \quad (0 \leq i, j \leq N-1)\,, \tag{3.16}$$

where $A_{i,j}$ is the intensity of the pixel with coordinates (i, j), and $N^2 = 16\,(36)$ the total number of summed pixels in the case of 2 (3) µm beads. Note that the total range of pixel intensities is 0–255 for our 8-bit CCD sensor. The resulting master curve could be fitted with a third-order polynomial to extract relative heights in nanometres. In practice, we exploit the observed behaviour foremost to establish a height clamp that minimises any (thermally induced) axial offset between beads during single-molecule measurements and do usually not need to convert pixels into nanometres.

Taken together, we can say that lateral and axial video microscopy enable us to employ active position feedbacks via movements of the piezoelectric XYZ-stage that minimise three-dimensional drift effects. It must be clear however that all these feedbacks are relatively slow because they are directly coupled to the camera frame rate, which is set to 200 Hz in most cases. But still, one great advantage of their use in the herein described setup is that, due to the improved coordination of piezo-controller-related functions by our software interface (see Fig. 3.7), they can be kept continuously activated – even during force–extension cycles –, which was not possible for instance in the instrument described in Ref. [Wagner et al., 2011].

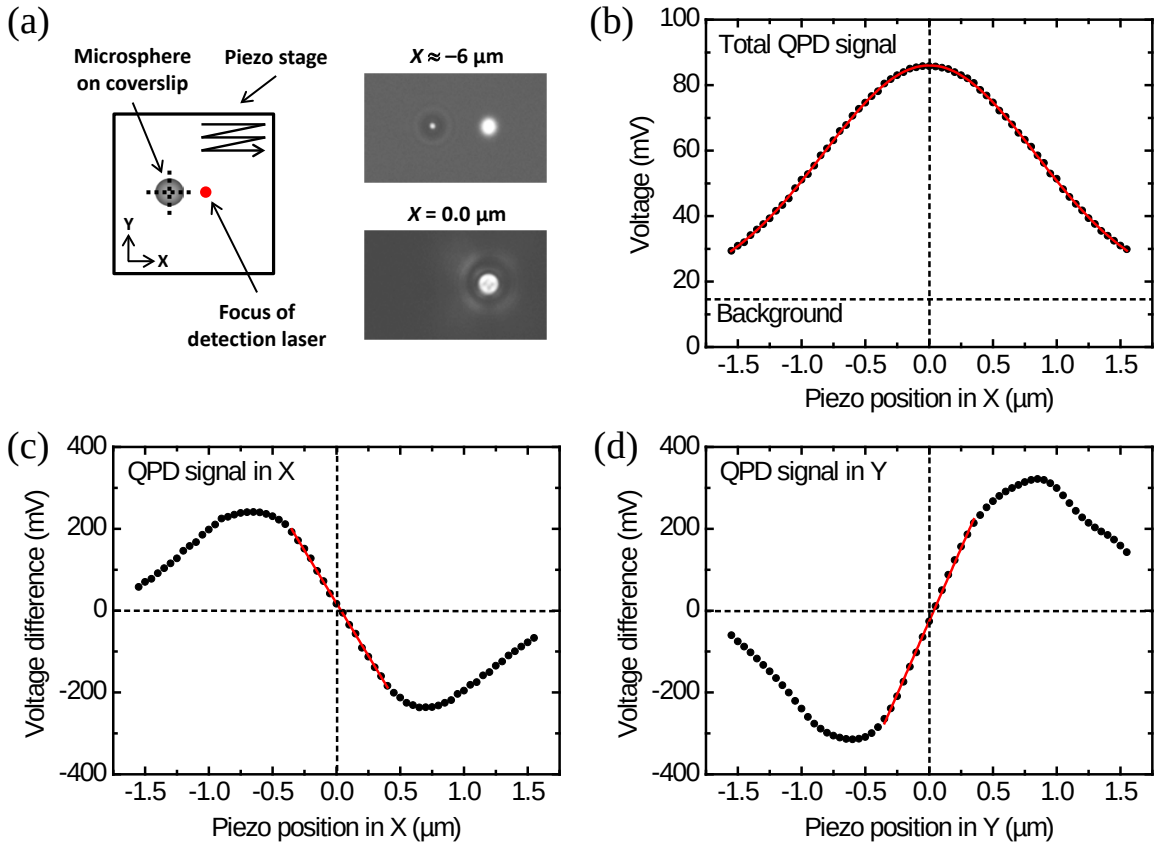

Figure 3.11. Inspection of quadrant photodiode (QPD) sensitivity and detection range. **(a)** Two-dimensional raster scan of a surface-bound 2 µm sphere through the detection laser focus. The two camera images indicate the bead far away from (*top*, white light on) and right on (*bottom*, white light off) the focal spot, yielding maximum reflection in the latter case. **(b)** Typical response of the QPD sum signal according to Eq. 2.31, as observed when scanning along one of the microsphere centrelines (dashed lines in (a)). The corresponding distribution can be fitted to a Gaussian (red curve) and decays down to the background reflection signal. **(c)/(d)** The differential voltages in X and Y, equally obtained along the centrelines, show characteristic S-shapes, with linear ranges and sensitivities (slopes indicated by red lines) whose absolute values are almost equivalent. Note that the voltages shown here are plain ones defined by Eqs. 2.30.

3.4.11. Validating quadrant photodiode detection range and sensitivity

Prior to using detection laser and QPD in conjunction for high-bandwidth position determination, we checked the response of the assembly to lateral position deviations of a microsphere in the sample plane. To this end, a polystyrene bead was unspecifically attached to the surface of the lower coverslip inside the fluid chamber and scanned stepwise in XY through the stationary focal spot created by the detection laser (with the trapping laser switched off). Figure 3.11a illustrates the measurement principle. The Z-position of the sample cell should be adjusted such as to provide a maximum total QPD voltage (Σ^{QPD} in Eq. 2.31) when the beam is centred on the bead. Note

that this procedure serves primarily to obtain an estimate of the sensitivity and the valid range of QPD detection, although an accurate comparison with the situation of a bead in the optical trap is difficult due to the immobilisation on the glass surface.

The results obtained during a raster scan across an area of $3 \times 3\,\mu\mathrm{m}$ for a $2\,\mu\mathrm{m}$ bead are shown in Fig. 3.11b–d. The Gaussian profile of the total QPD signal indicates that the laser was well focused on the bead surface. Plain differential signals in X and Y as defined by Eqs. 2.30 (averaged over 1000 readings at each position) represent derivatives of a Gaussian and show an approximate linear regime around the bead centre of $\pm 0.4\,\mu\mathrm{m}$ in both cases. This value complies with the rule of thumb of $\pm r_\mathrm{p}/2$ [Neuman and Block, 2004; Richardson et al., 2008] and is larger than the typical range observed by Huisstede and co-workers, who used a slightly different reflection-based detection scheme [Huisstede et al., 2005]. Small differences between the absolute sensitivities in X ($\sim 0.6\,\mathrm{V}/\mu\mathrm{m}$) and Y ($\sim 0.7\,\mathrm{V}/\mu\mathrm{m}$), obtained from linear fits of the relevant data points, can be explained by a not perfectly circular laser spot, which may be due to polarisation effects or astigmatism introduced by lenses and mirrors [Davidson and Abramowitz, 2002]. Note that, apart from different absolute ranges and sensitivity values, similar experiments performed with $3\,\mu\mathrm{m}$ beads gave rise to comparable results.

3.4.12. Trap stiffness calibration using two complementary methods

In principle, there exist two kinds of methods to calibrate the trap stiffness that describes the force response within a harmonic trapping potential according to Eq. 2.5. The first type comprehends so-called *passive* methods, which rely on the analysis of thermally induced position fluctuations of a microsphere confined near the trap centre, in accordance with the theoretical framework introduced in Sect. 2.1. The second type corresponds to *active* methods, which are able to probe the behaviour at larger deviations from the trap centre and can provide valuable information that is accessible even to systems with limited temporal bandwidth, such as those using CCD-based video microscopy. To probe the trapping potential within different displacement regimes, we used one method from each category to calibrate our OT.

Passive calibration: power spectral density (PSD) analysis

Calibration of the trap stiffness via analysis of Brownian fluctuation in Fourier space was already described in Subsect. 2.1.4. One advantage of this technique in combination with high-bandwidth laser-based position detection is that it can quickly deliver an approximate magnitude of the trap stiffness for a certain particle, and in addition is able to identify other noise sources that may be detrimental during an experiment.

Figure 3.12a shows the position fluctuations of a $2\,\mu\mathrm{m}$ bead trapped at 300, 600 and 900 mW of pre-objective trapping power P_OT, as monitored with our reflection-based detection scheme with the additional low-power laser. As expected, the standard

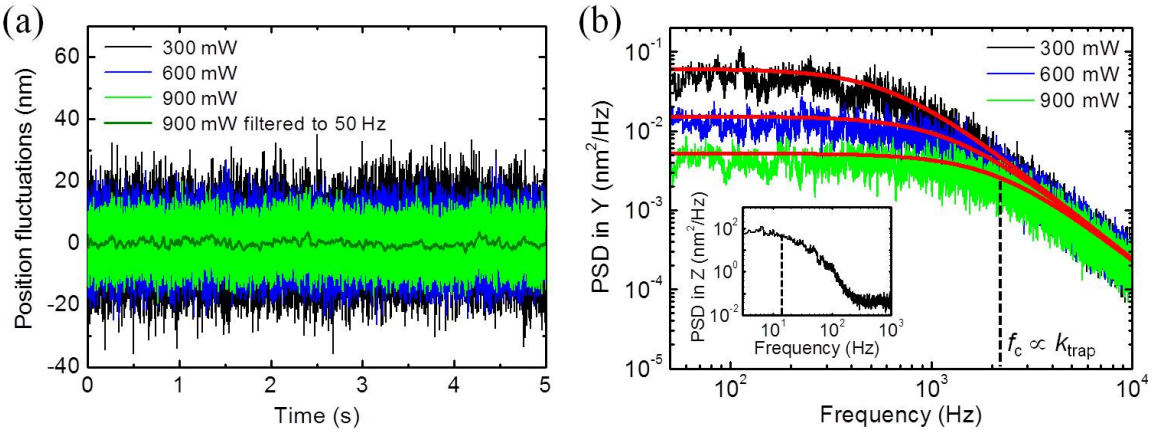

Figure 3.12. Trap stiffness calibration by position fluctuation analysis. **(a)** The random motion of a 2 µm bead confined in the optical trap at three different laser powers is measured at 50 kHz during 5 s. Note that low-frequency noise may set in after shorter time intervals and artificially inflate the observed signals. **(b)** Power spectral density (PSD) plots of the data depicted in (a). Only the frequency range relevant for curve fitting (0.05–10 kHz) is shown; additional noise sources as those presented in Fig. 2.3 would become visible at lower and higher values. The area under the Lorentzian fits (red curves) decreases with increasing laser power, with the corner frequency f_c (dashed vertical line) incrementing accordingly. The inset shows a typical spectrum of fluctuations in Z (at 300 mW), which drops to the electronic noise level at low frequencies already. It should be remarked that all distances in this figure were obtained (as usually done) from normalised voltages defined by Eqs. 2.33.

deviation decreases with increasing confinement of the particle, from 8.0 to 4.3 nm when going with P_{OT} from 300 to 900 mW, at an effective sampling bandwidth of 25 kHz. Filtering the latter signal down to 50 Hz, a value of 1.1 nm is achieved, which reflects more or less the resolution limit of our instrument.

Calculating the PSDs of the shown time series, characteristic Lorentzian dependences fulfilling Eq. 2.13 were recovered (Fig. 3.12b). The corner frequency f_c as defined in Eq. 2.12 – and consequently, the trap stiffness k_{trap} – was obtained in each case by numerical integration of the spectrum and subsequent fitting of an arctangent function according to Eqs. 2.28 and 2.29 between convenient frequency limits:

$$\int_{f_{\min}}^{f_{\max}} S_x(f)\,\mathrm{d}f = S_0 f_c \left[\arctan\left(\frac{f}{f_c}\right)\right]_{f_{\min}}^{f_{\max}}, \tag{3.17}$$

with f_c and $S_0 \equiv S_x(0) = k_{\mathrm{B}}T/(\pi^2\beta f_c^2)$ (see Eq. 2.14) as two independent fitting parameters. To avoid influences from low-frequency noise and aliasing, we chose limits $f_{\min} = 50$–200 Hz and $f_{\max} = 5$–10 kHz for the representative spectra shown in Fig. 3.12b, where f_c incremented from ~ 642 Hz at 300 mW to ~ 1324 Hz at 600 mW, up to ~ 2093 Hz at 900 mW. The mean k_{trap}-values turned out to be 69 ± 2, 143 ± 6 and 227 ± 7 pN/µm, respectively, with the error denoting the standard deviation from an

average of three measurements with the same microsphere at each laser power. Please note that probing several beads from the same batch would add another prominent contribution to the uncertainty due to particle size variations (see Subsect. 3.2.3). Note also that all data shown in this subsection correspond to the Y-direction as defined e.g. in Figs. 3.6b and 3.11a (results in X were similar), and that we take into account temperature changes that might affect the calculations.

Fluctuations in Z could also be detected (see inset of Fig. 3.12b) but – due to the tiny amount of detection laser power reaching the QPD and small axial sensitivities – showed much weaker spectral signals that got hidden behind background noise at frequencies above $\sim 200\,\mathrm{Hz}$. Still, one may identify tentative corner frequencies (e.g. around 15 Hz at 300 mW, vertical line in the inset) that are multiple times smaller than their lateral counterparts, corresponding to much lower axial stiffnesses. As a consequence, position amplitudes in Z converted to nanometres typically exceed the values in XY at least 10 times.

Active calibration: viscous drag measurements according to Stokes' law

One simple method that actively probes the optical trap stiffness is based on Stokes' definition of the hydrodynamic friction coefficient β for a spherical particle of radius r_p introduced in Eq. 2.10. A viscous drag force

$$F_\mathrm{drag} = \beta u \underset{(2.10)}{=} 6\pi\eta r_\mathrm{p} u \tag{3.18}$$

exerted on the bead (where η is the viscosity and u the linear velocity of the fluid), if balanced within the linear regime of the trap such that $F_\mathrm{drag} \equiv F_\mathrm{OT} = k_\mathrm{trap}\Delta x$, gives rise to a straightforward equation for the stiffness constant:

$$k_\mathrm{trap} = \frac{6\pi\eta r_\mathrm{p} u}{\Delta x}\,. \tag{3.19}$$

Here, Δx (> 0 for simplicity) denotes the drag-induced linear deviation of the bead from the trap centre, which – in order to be detected properly – has to be larger than the typical noise level from Brownian fluctuations. Figure 3.13a depicts an example (at $P_\mathrm{OT} = 100\,\mathrm{mW}$) of how this calibration method is used in practice: the nanopositioning stage was moved 40 µm back and forth at a speed of 150 µm/s, which can be taken as the fluid velocity felt by the trapped particle. The induced position deflections – measurable with both video- and laser-based means – were on the order of $\pm 140\,\mathrm{nm}$ in this case.

Plotting the resulting absolute positions in histograms as the one shown in Fig. 3.13b, two peaks corresponding to the bead in its displaced states can be fitted by Gaussian functions. By evaluating the difference between the peak centre values, k_trap according to the above equation follows immediately. In the particular example presented herein,

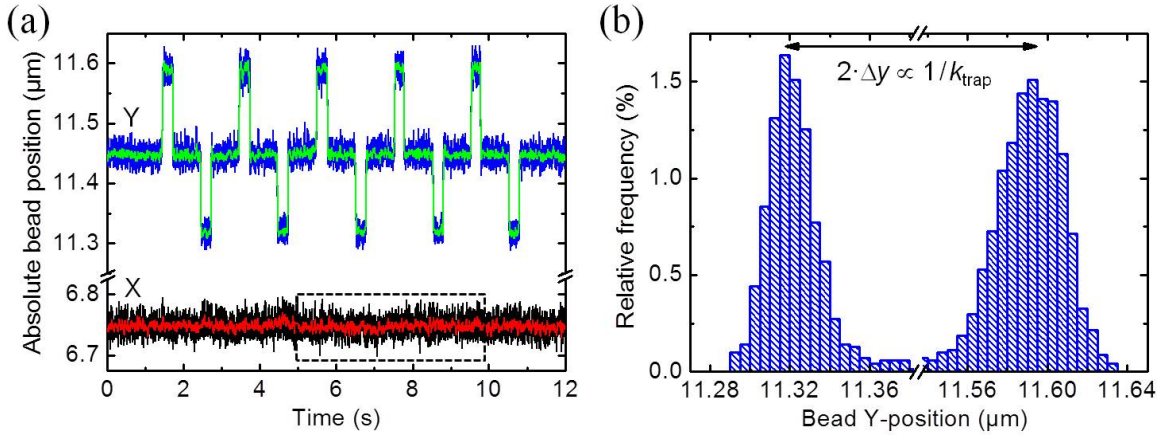

Figure 3.13. Trap stiffness calibration by viscous drag measurements. **(a)** Well-defined displacements of an optically trapped 2 µm bead, driven away from equilibrium by five moves of the piezoelectric positioning stage in $\pm Y$, detected in this case by the CCD camera at a frame rate of 600 Hz (using a reduced ROI). The X-position of the particle remains practically constant: within a time interval of 5 s (dashed rectangle), the raw signal (black) has a standard deviation of 13.3 nm, while filtering to 50 Hz (red signal) yields 5.6 nm. **(b)** Histogram of raw bead Y-positions from the data shown in (a). The large central peak corresponding to equilibrium near the trap centre is left out for clarity. As given by Eq. 3.19, the distance between the lateral peaks is inversely proportional to the trap stiffness.

the trap stiffness was found to be $23.3 \pm 1.0\,\mathrm{pN/\mu m}$, where the error stems from the sum of the uncertainties of the mean values of the normal distributions returned from the two fits.

3.4.13. Calibration results for two different particle sizes

Using the procedures described in the previous paragraphs, the OT instrument was calibrated for a wide range of laser powers and polystyrene beads of 2 and 3 µm in diameter. Anti-Dig-coated particles of 3 µm were preferred in most pulling experiments with DNA because they could be easily distinguished in solution from SA-coated 2 µm beads. For this reason, the graphs shown in this subsection correspond to the larger particle type only, although results for 2 µm beads (complying with the examples presented on the previous pages) are included in Table 3.1.

First of all, we needed to check the QPD sensitivity $\mathcal{S}$ at different trapping conditions. We did this (i) using the strategy described in Subsect. 2.3.2, by means of the ratio of calibrated and uncalibrated low-frequency limit (Eq. 2.32) of the respective power spectra, and (ii) performing drag experiments (see Fig. 3.13) at power-independent effective piezo stage velocities of 0.8–1.2 µm/(mW·s). In the latter case, for instance at 300 mW of pre-objective laser power, we chose stage velocities between 250 and 350 µm/s; $\mathcal{S}$ was then obtained by comparing drag-induced displacement amplitudes given in nanometres (from CCD data) and millivolts (from QPD data).

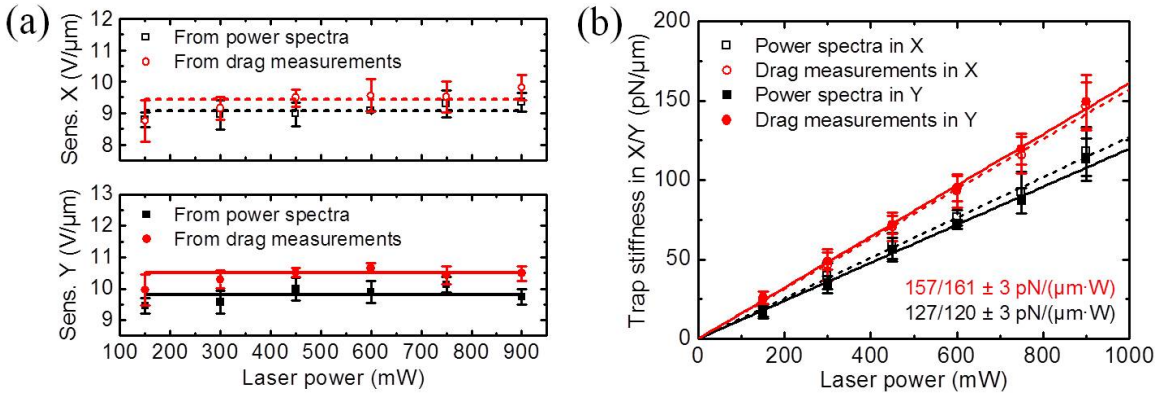

Figure 3.14. Results from quadrant photodiode (QPD) sensitivity and trap stiffness calibrations of 3 µm beads. **(a)** Sensitivities $\mathcal{S}$ in X and Y from both PSD analysis and drag measurements. Error bars indicate the standard deviation from at least five individual measurements with several microspheres. Horizontal lines correspond to the mean value of each data set as stated in the text, calculated over all laser powers. **(b)** Trap stiffness versus pre-objective laser power, as measured by PSD analysis and viscous drag measurements under the same conditions as in (a). Values in X and Y are similar within experimental error, but a significant difference between k_{trap} probed near and far from the trap centre is observed. Power-independent stiffnesses in X/Y defined by the linear fits are indicated. Again, error bars correspond to the standard deviation from various measurements.

The results from both methods are shown in Fig. 3.14a, separately for X and Y. We see that the absolute sensitivity values from PSD and drag measurements differ only slightly (by less than one standard deviation or 5 % in most cases). In addition, there appears to be a weak, yet insignificant dependence on laser power, probably due to changes in the axial equilibrium position of the particles within the trap as the power – and hence the scattering force (Eq. 2.2) – increases.

Apart from that, $\mathcal{S}$-values in Y were found to be about 10 % higher than their X-direction counterparts, confirming the results obtained from two-dimensional surface scans (see Fig. 3.11c/d). The averages over all laser powers for the data from PSD (drag) measurements (horizontal lines in Fig. 3.14a) were determined as 9.067 ± 0.188 (9.472 ± 0.204) V/µm in X and 9.795 ± 0.226 (10.507 ± 0.129) V/µm in Y (uncertainties indicate standard deviations). Please note that these numbers are much higher than those stated in Subsect. 3.4.11 because they refer to normalised voltages (see Eqs. 2.33) – which yield more reliable results and have been used throughout the whole chapter except for the mentioned subsection. That said, in spite of differing sensitivities a similar overall behaviour was observed for 2 µm beads (data not shown).

The experiments described in the previous paragraphs were also exploited to calculate the trap stiffness as a function of the applied laser power. The results shown in Fig. 3.14b confirm the expected linear dependence. In this case, no significant difference was observed between the values measured in X and Y, but a larger discrepancy became obvious when k_{trap}-calibrations from PSD and drag measurements were compared.

The offset in power-independent stiffness (i.e. between the slopes of the linear fits) resulted to be $\sim 20\,\%$. Such an elevated number indicates that – in contrast to the less affected QPD sensitivity – k_{trap} may not be constant over the range of studied deviations from the optical trap centre, i.e. the force response most probably contains some nonlinear contribution. It should be noted that no comparably high trap stiffness differences were observed in the case of 2 µm beads (data not shown).

3.4.14. Exploring nonlinearities in the force response

Relying on the results obtained for 3 µm beads in the previous subsection, we aimed at exploring the force field of our optical trap experimentally in more detail. Corresponding trials had previously been performed by Jahnel and co-workers using an instrument with dual-trap capability [Jahnel et al., 2011], leading to results that matched theoretical calculations [Nieminen et al., 2007]. In our case, we wanted to utilise the high-accuracy nanopositioning stage to carry out viscous drag measurements for a broader range of fluid velocities and thus probe the force response further away from the optical trap centre. While for the experiments corresponding to the results shown in Fig. 3.14, power-independent velocities of 0.8–1.2 µm/(mW·s) had been applied, the new trials embraced effective piezo speeds of 0.2–3.5 µm/(mW·s). The lowest velocities are determined by the minimum value necessary to observe a significant displacement signal as those shown in Fig. 3.13a, while the highest ones are limited by the maximum frame rate of the camera in the case of video detection, by the maximum speed at which the piezo stage movement can still be considered linear (~ 2 mm/s according to the manufacturer), and by the fact that the bead may be driven out of the trap at some point.

The results for the complete sets of measurements in Y at 300, 600 and 900 mW of pre-objective laser power are presented in Fig. 3.15a. For each induced fluid velocity, the observed distance between the relevant peaks of the overall position distribution (see Fig. 3.13b) was compared with the expected value, which per Eq. 3.19 is given by

$$2 \cdot \Delta y = \frac{12\pi\eta r_{\mathrm{p}} u}{k_{\mathrm{trap}}}\,, \tag{3.20}$$

where the trap stiffness was either set to the value from previous PSD or drag measurements according to Fig. 3.14b. We could identify a two-phase behaviour: at slower piezo movements, up to a PTP distance of 150–300 nm (depending on the laser power), observed deviations coincided with results from PSD analysis; larger velocities induced displacements that followed a regime of apparently stronger confinement, which by itself could be fitted to a linear equation for each power within the range of investigated distances but did *not* match the prediction from previous drag experiments. The encountered relationship is in agreement with the outcome of a study that used the Stokes method for smaller microspheres [Richardson et al., 2008] and with simulations

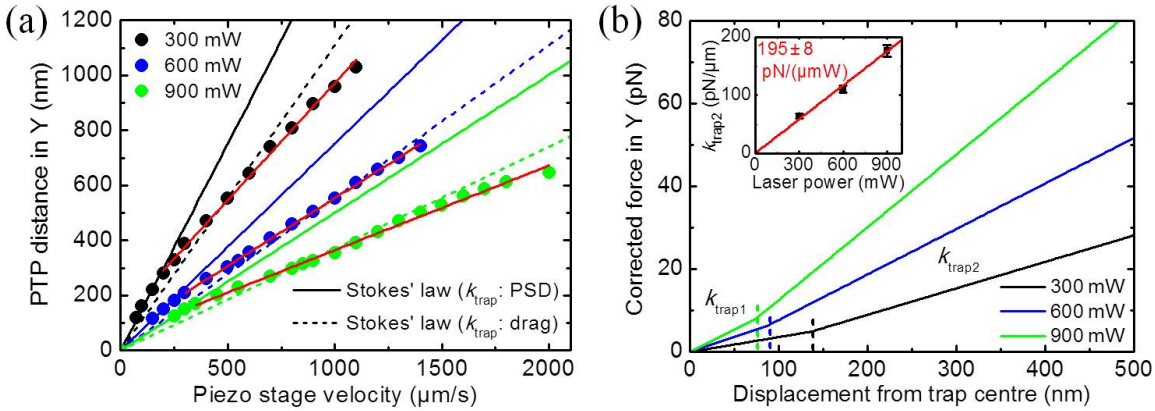

Figure 3.15. Probing the linearity of the optical trap for 3 µm beads. **(a)** Drag-induced displacements for a broad range of piezo stage velocities, obtained from data similar to those shown in Fig. 3.13, are determined at three different laser powers. Straight lines through the origin indicate the expected behaviour when considering the trap stiffness from PSD analysis (continuous lines) and drag measurements within a limited range of velocities (dashed lines). The red lines correspond to linear fits of the secondary stiffness regimes encountered. **(b)** Trap stiffness increase deduced from the results in (a). A transition from a lower value k_{trap1} to a higher value k_{trap2} at a certain distance (dashed vertical line for each power) from the trap centre – given by the intersection of the respective red and continuous lines in (a) – can serve as an approximation to describe the force response. As illustrated by the inset, k_{trap2} is also proportional to the applied laser power.

of the complete force field, based on the work by Jahnel et al. and carried out for particles only slightly larger than our 3 µm beads [Otto, 2011].

The results from drag measurements enabled us to describe the trapping potential as being governed by a stiffness that exhibits a change from a lower value k_{trap1} to a higher value k_{trap2} at a certain distance from the trap centre (Fig. 3.15b), with $k_{\mathrm{trap1}} = k_{\mathrm{trap,PSD}}$ from Fig. 3.14b and $k_{\mathrm{trap2}} \approx 195\,\mathrm{pN/(\mu m{\cdot}W)} \cdot P_{\mathrm{OT}}$. The approximate linear range of the first stiffness interval was determined as 140, 90 and 75 nm at 300, 600 and 900 mW, respectively, which is in accordance with previously observed ranges for another single-beam OT setup [Greenleaf et al., 2005].

Table 3.1 summarises some of the most important calibration results for both 2 and 3 µm beads along the Y-axis, which for all pulling experiments performed so far defines the more relevant direction: perpendicular to the fluid flow through the central channel and parallel to the pipette (see Fig. 3.6).

3.4.15. Proof-of-principle force–extension measurements

As a proof of concept for the force-measuring capabilities of our OT apparatus, we performed force–extension experiments with a known dsDNA molecule and a DNA hairpin construct, using 3 and 2 µm beads in the trap, respectively. Note that during

Parameter	2.10/2.16 µm beads	3.18 µm beads
Effective stiffness k'_{trap1} (pN/(µm·W))	251 ± 7	120 ± 3
Effective stiffness k'_{trap2} (pN/(µm·W))	—	195 ± 8
Effective QPD sensitivity (V/µm)	13.351 ± 0.608	10.151 ± 0.354
Maximum observed force (pN)	> 110	> 110

Table 3.1. Principal optical tweezers (OT) calibration parameters for 2 and 3 µm beads. All values correspond to the Y-direction as defined in Fig. 3.6b. In the case of the smaller particles, no second trap stiffness regime was encountered. The effective QPD sensitivity corresponds to the average of the mean values from PSD and drag measurements, calculated over all laser powers. Uncertainties are given by the standard error from the corresponding linear fit (effective stiffness) and the standard deviation (effective sensitivity). The maximum force derives from successful force–extension measurements with torsionally constrained dsDNA, which depicts an overstretching plateau at around 110 pN [Bustamante et al., 2003].

both types of assays, the height clamp feedback – exploiting real-time monitoring of relative particle Z-positions according to the method described in Subsect. 3.4.10 – was active at all times to avoid thermally induced axial offsets between the microspheres.

Pulling experiments with a 4 kbp DNA substrate

To carry out single-molecule measurements with the DNA (Fig. 3.16a) fabricated as stated in Subsect. 3.2.4, we first delivered SA-coated 2 µm spheres through the dispenser from channel 1 of the flow chamber (see Fig. 3.6a) and attached one of them to the micropipette by suction. An Anti-Dig-coated 3 µm bead – previously incubated with the DNA construct labelled with several Dig and Bio tags (D and B in Fig. 3.16a) – entered the central channel through the dispenser from channel 3 and was brought close to the pipette. Approaching the SA bead through piezo stage movements (see Fig. 3.6b) to the Anti-Dig bead in the OT, a connection between the two microspheres via the DNA tether could be established and the force probed by moving the pipette carefully in $-Y$.

Experiments were performed in a buffer containing Tris (10 mM, pH 8.0), EDTA (1 mM) and NaCl (150 mM), at 25 °C and a pre-objective laser power of 900 mW. Corrections of trap stiffness according to Fig. 3.15b yielded a dependence based on CCD data (green) that practically overlapped with a reference curve (black) obtained using a different (dual-beam) OT instrument* (Fig. 3.16b). Likewise, corrected results from QPD and light lever (LL; orange) match the black curve, although additional adjustments of the QPD sensitivity at forces above 20 pN were required in this case. This indicates that, in addition to non-linearities in the force response, the position detection system may also suffer from nonlinear effects (note that we could attribute

*The reference measurement was performed by Elías Herrero and corresponds to data shown in Ref. [Herrero-Galán et al., 2012].

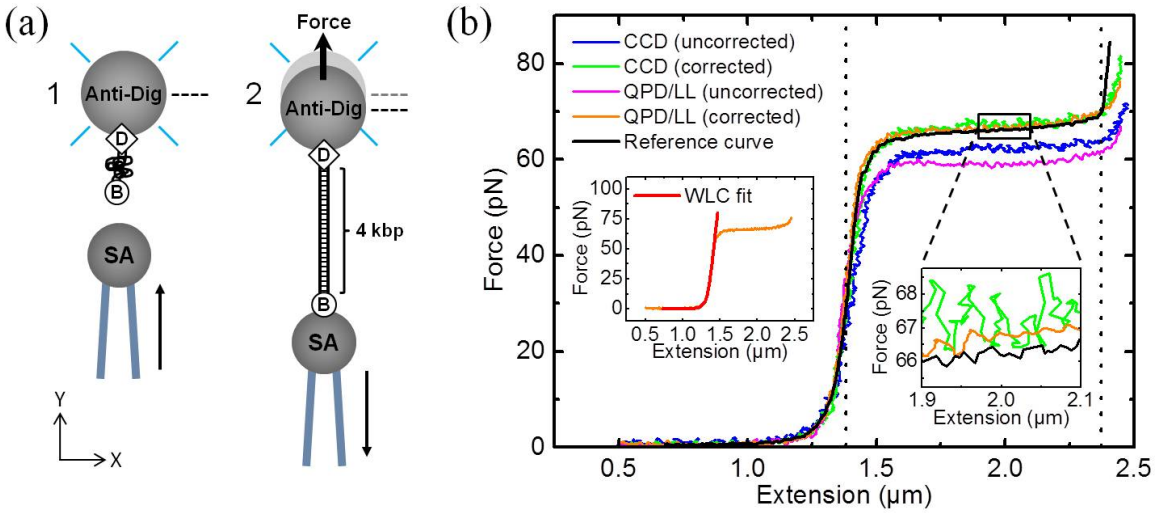

Figure 3.16. Force–extension relation of a 4 kbp dsDNA molecule. **(a)** The experimental configuration for pulling experiments, (1) before and (2) after an attachment between 2 µm SA- and 3 µm Anti-Dig-coated microspheres has been established via a DNA tether. Retracting the pipette while observing the force response, the signal from a single dsDNA molecule of the correct length can be identified as described in the left panel of Fig. 3.3. **(b)** Pipette-induced force response versus extension of the DNA tether at a pulling speed of 500 nm/s in a buffer with 150 mM NaCl. All data are represented at 50 Hz. Vertical dotted lines indicate extensions of L_0 ($\sim$1.36 µm) and $1.7L_0$ ($\sim$2.31 µm). Insets with details from the overstretching transition and a worm-like-chain (WLC) fit are explained in the text.

them solely to the QPD and not to the PsD of the LL assembly). These corrections were obtained by (i) plotting the displacements from the trap centre measured by video microscopy against the differential voltage signals from the quadrant detector for all relevant extensions and (ii) fitting a polynomial to the intervals that deviated considerably from a straight line (data not shown).

A detail around an extension of 2 µm (right inset in Fig. 3.16b) shows that only our data from laser-based detection methods are able to attain sub-pN resolution at 50 Hz, thus recovering the behaviour from the reference curve. As another quality check, we fitted an extensible WLC between 1 and 40 pN to these data (left inset in Fig. 3.15b), applying the following formula that corresponds to the so-called strong-stretching limit [Odijk, 1995]:

$$z(F) = L_0 \left[1 - \frac{1}{2} \left(\frac{k_\mathrm{B} T}{F L_\mathrm{p}} \right)^{1/2} + \frac{F}{K} \right] , \tag{3.21}$$

where K denotes the elastic stretch modulus of the polymer (for the sake of consistency, as in Eq. 2.24 we use z for the extension, even though the molecule is pulled along the Y-axis here). This procedure corresponds to the one employed in Ref. [Herrero-Galán et al., 2012] and yielded best fit parameters of $L_\mathrm{p} = 47 \pm 2$ nm and $K = 912 \pm 23$ pN

for our data – values that are similar to those obtained by Herrero-Galán et al. at equivalent experimental conditions. Please note that the curve presented in Fig. 3.16b corresponds to one of our best data sets and does not necessarily represent the average behaviour we observed while performing many different trials of this kind.

Pulling experiments with a DNA construct containing a 2.5 kbp hairpin

To set up assays with the hairpin substrate (Fig. 3.17a) mentioned in Subsect. 3.2.4, we followed the same procedure as for the 4 kbp dsDNA molecules, with the only difference being the use of smaller (2 µm) Anti-Dig-coated beads in this case.

These measurements were performed in a buffer containing Tris (20 mM, pH 7.5), EDTA (2 mM) and NaCl (50 mM), at 25 °C and a pre-objective laser power of 300 mW. Note that apart from offset corrections, no adjustments of trap stiffness or QPD sensitivity were necessary in this case to match the acquired data with a reference curve obtained with the aforementioned dual-beam OT instrument[†] (Fig. 3.17b). This proves the validity of the calibration parameters for the smaller 2 µm beads. The initial force increase corresponds mainly to the 2.6 kbp dsDNA portion of the substrate, after which the hairpin starts to open while the force stays more or less constant, at a mean value of ~ 14 pN and within a range of approximately ± 2 pN. These values are in agreement with a study that investigated the salt dependence of the forces involved in hairpin unzipping [Huguet et al., 2010].

A detail around an extension of 1 µm shows that at 50 Hz, photo detector data again exhibit a slightly better resolution than camera data, although the difference is less obvious in this case, probably due to the use of a smaller microsphere in the trap and because of the fact that the force signal shows stronger oscillations here anyway. In any case, we can be confident when saying that the sequence-dependent sawtooth pattern could be resolved by QPD/LL data with a resolution similar to the one obtained from the black reference curve. Subtle deviations may indicate somewhat different bead–DNA attachment geometries or merely be due to the inherent disorder of single-molecule experiments. Please note once again that our data set depicted in Fig. 3.17b reflects one of the best measurements we were able to carry out, others do not show such a neat force–extension behaviour.

3.5. Conclusion

This chapter has explained different aspects with respect to the construction and characterisation of a customised single-beam OT instrument. Similar to other works dedicated (in part) to the development of application-specific optical tweezers equipment (see e.g. Refs. [Gollnick, 2007; Hormeño Torres, 2010; Huguet i Casades, 2010;

[†]The reference measurement was performed by José A. Morín following the procedures described in Ref. [Morin Lantero, 2013].

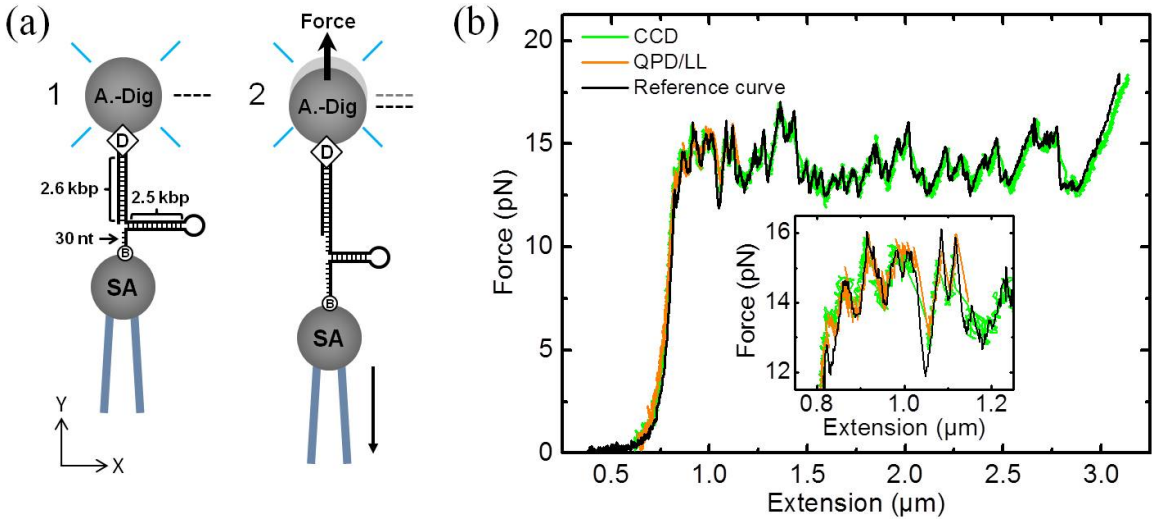

Figure 3.17. Force–extension relation of a 2.5 kbp DNA hairpin construct. **(a)** The experimental configuration for this experiment (1) before and (2) after applying a force with the miropipette on a single macromolecule tethered between 2 µm SA- and Anti-Dig-coated micrsophere. Note that the oligonucleotide end of the substrate contains a single Bio tag (B) in this case. Pulling on the molecule provokes unzipping of the hairpin structure after an initial force increase up to ∼13 pN, as described in the right panel of Fig. 3.3. **(b)** Pipette-induced force response from the DNA tether at a pulling speed of 100 nm/s in a buffer with 50 mM NaCl. All data sets are represented at 50 Hz. QPD/LL data were only grabbed up to an extension of ∼1.15 µm in this particular trial. The inset with a detail of the curves around an extension of 1 µm is commented on in the text.

Otto, 2011]), it has illustrated several important technical details that have to be considered when assembling a device meant to be used for single-molecule force spectroscopy experiments at piconewton and nanometre resolution.

A comprehensive software interface has been designed to orchestrate all hardware functions, enabling efficient measurements in real time. Some of its features are still under construction and have not been mentioned here in detail, such as the force feedback capabilities. Just like the position control loops used to minimise trapping-laser-induced thermal drift – counteracted by a combination of objective temperature control and active position corrections – the currently tested feedbacks in force are limited in their execution speed by the frame rate of the camera. As a consequence, efficient experiments with biomolecules at fixed loads might have to be carried out in a configuration that combines active and passive schemes, the latter of which rely on the range of displacements from the trap centre that correspond to a practically constant force already, as reported by Greenleaf and co-workers [Greenleaf et al., 2005].

The reflection-based position determination strategy with an additional low-power laser has been validated by complementary calibration experiments. Even though other configurations of backscattering detection may achieve superior stability and be more efficient in terms of the amount of exploited laser power (see e.g. Ref. [Carter et al.,

2007]), the herein presented approach has the benefit of being rather straightforward to implement and easy to use.

Non-linearities in the calibrated trapping potential have been identified, although a more thorough investigation of the complete force field may be beneficial to facilitate force–extension trials with spherical microparticles of different sizes (apart from being necessary for the passive force feedbacks mentioned above). Proof-of-principle experiments with different DNA substrate have demonstrated the reliability of force/distance measurements and encourage the realisation of future assays with DNA-binding proteins. To this end, some tests regarding the most convenient and feasible way to deliver small amounts of protein solution and/or ATP to the central reaction volume of the fluid chamber still need to be performed.

The necessity of only one microscope objective lends the herein presented OT layout a big advantage: free space above the sample stage, which may be used in the future for the combination with complementary techniques such as MT. On the other hand, a potential decoupling of the system from the (micropipette) surface – achieved e.g. by splitting the trapping laser beam in two orthogonally polarised parts and thus creating a pair of non-interfering optical traps – is also feasible due to the high output power of the IR laser. This way, an even more versatile instrument ready for use with multi-stream laminar flow cells might be constituted.

4. Optically confined microspheres as flow sensors

This chapter treats a recently discovered application of optical tweezers (OT) in combination with glass pipettes: the quantification of minute flow velocities via the rotations of slightly asymmetric colloids. In particular, the special case of electrically induced flows out of and into a capillary tip measuring around 150 nm is described. After a short presentation of nanopores in general, the phenomenon of electroosmosis in glass nano-capillaries and the way we have probed it with an OT instrument similar to the one presented in Chap. 3 will be discussed. The results comply with a theoretical model based on an analytical solution of the Navier–Stokes equations: the Landau–Squire formalism. It turns out that the sensitivity of our method comes close to the resolution limit of other types of flow measurement devices.

Parts of this chapter have been published in: Laohakunakorn et al. (2013), *Nano Letters* 13(11):5141–5146.

4.1. Introduction

4.1.1. Membrane transport in cells

Independent of additional reinforcements such as the cell walls found in plants or prokaryotes, the plasma membrane that separates the interior of each individual cell or cellular compartment from its environment is universal to all organisms. Acting as a selective filter for passive and active transport, it regulates many processes that are essential for viability under changing external conditions, such as the import/export of nutrients/waste or the maintenance of osmotic pressures [Alberts et al., 1989]. Depending on the size of the transported object, different types of channels and mechanisms – some of them highly specific – are required, which become available by means of proteins in a lipid bilayer, making up the dynamic structure of the membrane. For example, during gene expression in eukaryotes, synthesised and processed messenger RNA molecules need to exit the cell nucleus before their translation to polypeptides can occur, which corresponds to a fundamental transport process that is regulated by the nuclear pore complex [Alberts et al., 1989].

4.1.2. Nanopores as Coulter counters

Transmembrane channels and pores measure on the order of nanometres, i.e. roughly the size of the transported objects themselves, which makes them usable as accurate

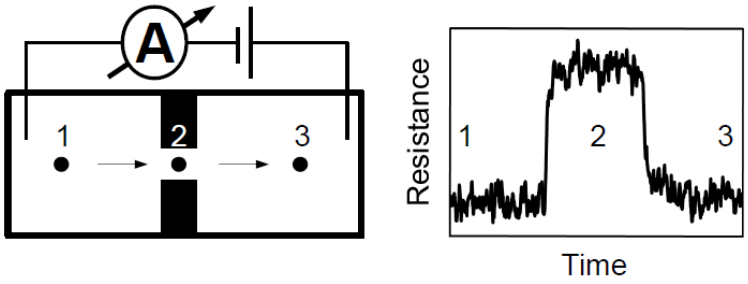

Figure 4.1. Resistive pulse detection scheme. **(Left)** Two reservoirs filled with electrolytic solution are connected by a small channel. The passage of particles can be detected by applying a voltage between electrodes submerged on either side of the orifice and using an ampere-meter to measure the ionic current going through. **(Right)** A graph showing the typical pulse-like resistance increase (equivalent to a conductance/current drop due to partial blockage of the constriction) corresponding to the movement of a particle that passes from the left reservoir (1) via the channel (2) to the right one (3). [Figure modified from [Steinbock, 2011].]

sensing devices [Bayley and Martin, 2000]. Detecting the passage of biomolecules through such *nanopores* can be achieved by applying the resistive pulse technique, which was first put into practice in the 1950s after the invention of the Coulter counter (named after its inventor, Wallace H. Coulter), an instrument developed for quantifying cells in solution that is still used in hospitals today [Coulter, 1953]. Figure 4.1 schematically illustrates the underlying detection principle.

Note that in order to detect the much smaller currents – on the order of picoamperes ($1\,\mathrm{pA} = 10^{-12}\,\mathrm{A}$) – involved when scaling the system down from micrometric pores for cells to nanometric ones for molecules, very sensitive measurement devices are needed, like those used since the late 1970s in patch clamp assays probing the signals through *single* ion channels [Neher and Sakmann, 1976]. Such high-resolution current amplifiers provide a sufficiently large signal-to-noise ratio to identify different shapes of the detected pulse, which contain information about the respective structures of individual molecules during translocation [Wanunu, 2012]. This fact opens a variety of possibilities for use, not only of biological nanopores [Bayley and Cremer, 2001], but also of artificial solid-state pores [Dekker, 2007] and hybrid systems [Bell et al., 2012; Hall et al., 2010; Hernández-Ainsa et al., 2013a], which have evolved in recent years to more and more sensitive and specific single-molecule sensors for studying transport phenomena involving nucleic acids and proteins [Wanunu, 2012]. In particular, configurations that rely on protein pores optimised for the passage of single-stranded DNA now provide the resolution to identify genome sequences [Schneider and Dekker, 2012], and the first nanopore-based sequencing device [Oxford Nanopore Technologies, 2012] has been extensively tested [Check Hayden, 2014]. Figure 4.2 depicts one member of each of the three pore types.

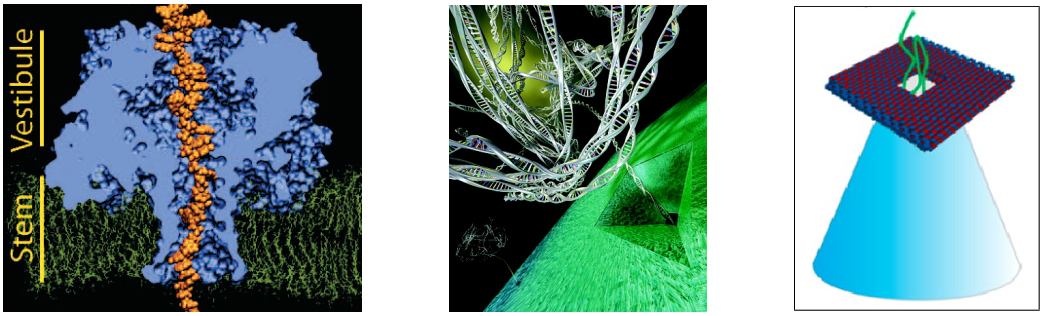

(a) Biological **(b)** Solid-state **(c)** Hybrid

Figure 4.2. Three different types of nanopores. **(a)** Cross-sectional view of the membrane-associated protein α-haemolysin (blue), depicting its characteristic "mushroom" shape with a vestibule exposed to the solution and a stem anchored in the lipid bilayer (green), as used in molecular dynamics simulations [Wells et al., 2007]. The central channel measures 1.5 nm at the smallest constriction and thus allows the passage of ssDNA (orange) only [Kasianowicz et al., 1996]. **(b)** Artistic view of dsDNA (white/grey chain) translocating through an artificial nanopore of about 10 nm in a silicon chip (green) [Storm et al., 2005]. **(c)** Schematic of a flat quadratic DNA origami structure (red/dark blue) with a central aperture of $\sim 14 \times 15$ nm, attached on top of a slightly larger glass capillary tip (light blue cone) to detect different folding states of DNA (green) [Hernández-Ainsa et al., 2013a].

4.1.3. Glass nanocapillaries combined with optical trapping

One of the major problems in translocation experiments is the very short time (on the order of microseconds) it takes biomolecules like DNA with a length of $\sim 1\,\mu$m to pass through the nanometric constriction, which corresponds to a finite number of ions contributing to the current signal [Wanunu, 2012]. There are different ways to improve resolution in (biological) nanopores by artificially slowing down the process via the implementation of additional protein motors [Schneider and Dekker, 2012]; alternatively, the pore can be integrated in a microscope capable of applying small loads with high sensitivity, e.g. in an OT apparatus. Using micron-sized probes attached to the molecule in question – as discussed in Chaps. 2 and 3 –, such a setup even allows stalling translocation and measuring the involved forces [Keyser et al., 2006].

Throughout the remaining chapter, I will exclusively consider bare solid-state nanopores made of glass, so-called *nanopipettes* or *-capillaries* [Steinbock et al., 2010a] – known for their use in electrophysiology and scanning ion-conductance microscopy [Siwy, 2006]. These can now achieve performances that are comparable to those of their relatives created inside thin membranes of silicon nitride [Steinbock et al., 2013], but have various advantages: they are (i) cheaper to fabricate, (ii) easier to handle and (iii) transparent when observed under white light [Steinbock, 2011]. The last point enables their implementation perpendicular to the optical axis (in the XY-plane), e.g. in fluorescence microscopes [Thacker et al., 2012], and thus allows for *lateral* force measurements with optical traps, which are easier to perform and entail better

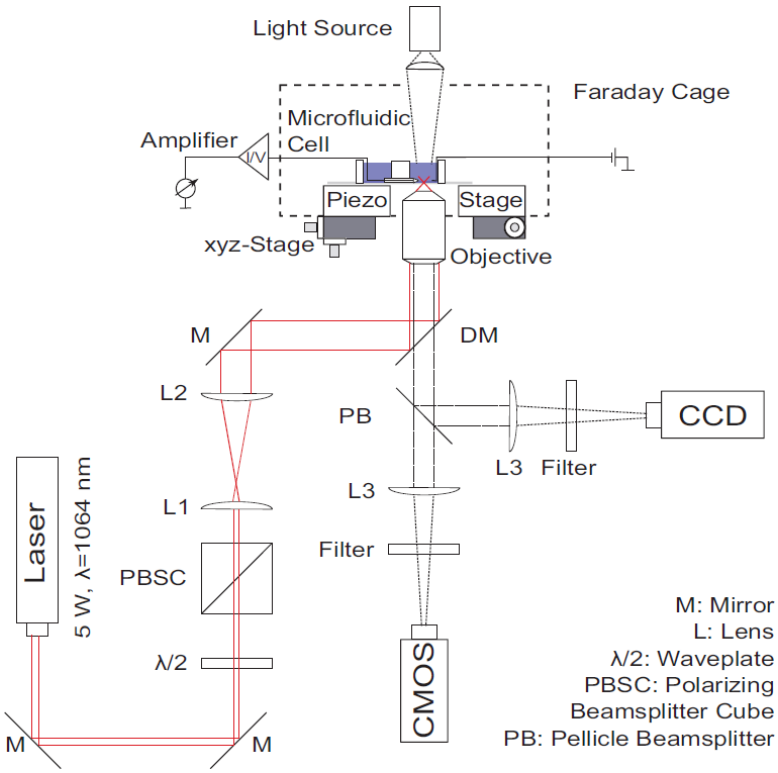

Figure 4.3. Optical tweezers (OT) scheme (*not to scale*) applied for ionic current measurements through nanocapillaries. The main differences with respect to the instrument shown in Fig. 3.5 are mentioned in the text; all other major components are equivalent. Essentially, nanopore measurements require a Faraday cage to minimise electromagnetic noise and a high-resolution amplifier to monitor picoampere currents. In addition, laser-based position determination is substituted by CMOS camera detection to reduce potential measurement errors due to laser instabilities. [Figure taken from [Otto, 2011].]

force resolutions than in Z due to the higher lateral stiffnesses (see Fig. 3.12b). The particular application described here exploits such a combination of nanopipettes and OT to efficiently quantify the tiny volume flows at the pore exit. The following paragraphs shortly introduce our experimental approach and provide the theoretical framework necessary to explain the measured data.

4.2. Experimental materials and methods

4.2.1. Optical tweezers setup

The laser tweezers instrument (Fig. 4.3) used for the experiments discussed in this chapter* corresponds to the one described in reference [Otto et al., 2011b] and resembles the one presented in Chap. 3 for the most part (if not stated otherwise, specific

*The system was assembled by Ulrich Keyser and Oliver Otto.

components can be considered identical). The major differences are: (1) a modified sample stage design, including a Faraday cage essential for reducing electromagnetic background noise, as well as a special flow cell optimised for the use of nanocapillaries probing one species of (DNA-coated) microspheres per trial; (2) a commercial patch-clamp amplifier (Axon Axopatch 200B, Molecular Devices, CA, USA) – including a pre-amplifier inside the Faraday cage – for accurate ionic current measurements at the pA level [Keyser et al., 2006]; and (3) a high-speed CMOS camera (MC1362, Mikrotron, Germany) substituting the QPD for fast video-based position detection in XY without the need of a detection laser [Otto et al., 2011a], as described in Subsect. 2.3.1. In addition, some minor distinctions are worth noting, such as the lack of a drift-reducing heater device and the smaller diameter (about 7 mm) of the trapping laser when entering the microscope objective, *under*-filling the back-aperture [Otto et al., 2010]. These characteristics prove to be sufficient because this particular setup was built for studies with a single colloid type at (i) weaker trap stiffnesses (with lower laser powers not striking the edges of the objective back aperture, thus inducing less thermal drift) and (ii) shorter distances from the coverslip surface (facilitating the trapping of particles even with less pronounced optical gradients) [Otto, 2011]. Figure 4.3 contains a scheme of the apparatus comparable to Fig. 3.5 on page 39; a representation of the sample cell layout is given in Fig. 4.4.

4.2.2. Ionic current measurements through nanocapillaries

The nanopores used for the experiments described here were fabricated by pulling quartz glass capillaries (inner/outer diameter = 0.3/0.5 mm; Hilgenberg, Germany) with a commercial pipette puller (P-2000, Sutter Instruments, CA, USA). Depending on the chosen pulling parameters, pores generated in this way can be as small as tens of nanometres [Steinbock et al., 2010a,b]; to achieve significant flow velocities resulting from the application of a voltage at the capillary back end, we fabricated relatively large pores with radii of 74 ± 13 nm as determined from scanning electron micrographs. The pulled capillaries were assembled into microfluidic chips (see Fig. 4.4) such as to connect two reservoirs filled with salt solution (10 mM KCl, 1 mM Tris–EDTA, pH 8). Ag/AgCl (silver/silver chloride) electrodes dipped into the solution and in contact with the patch-clamp amplifier allow for the application of voltages between -1 and $+1$ V as well as low-noise ionic current monitoring through the pore.

4.2.3. Trapping assays with dimpled microspheres

Asymmetric colloidal particles (with diameters of 1.5, 2, and 3 µm), made of 3-methacryl-oxypropyl-trimethoxysilane (TPM) with a mass density of 1.228 g/mL, were synthesised according to a protocol described by Sacanna and co-workers [Sacanna et al., 2010], which relies on encapsulation of a liquid particle core and subsequent

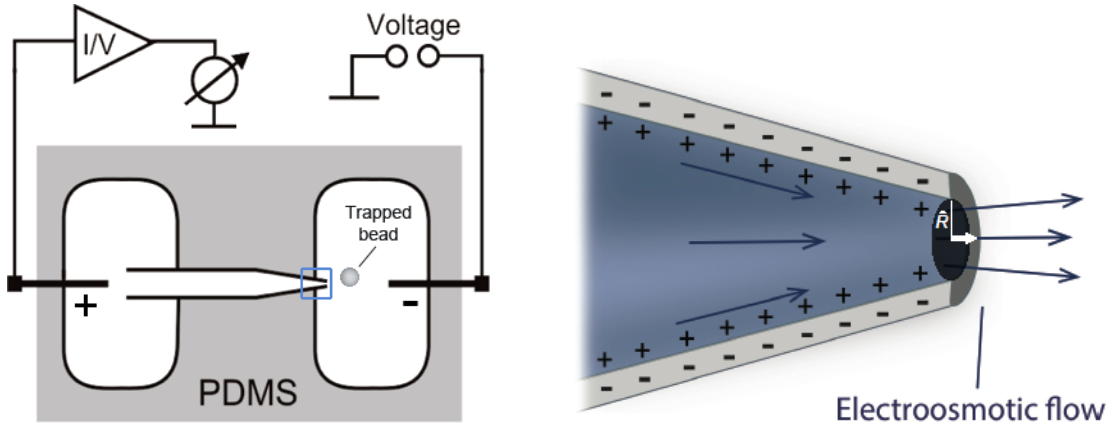

Figure 4.4. Glass nanopore assembly for probing electroosmotic flows. **(Left)** Schematic representation (*top view, not to scale*) of a sample cell made of polydimethylsiloxane (PDMS), with two reservoirs containing salt solution that are interconnected via a capillary (see Fig. 4.1). The electrode in the left reservoir is set to a positive potential, while the conical capillary tip (indicated by the blue rectangle) protrudes into the right reservoir, with an optically trapped microsphere located nearby. [Figure adapted from [Steinbock et al., 2010a].] **(Right)** Close-up view of a cross section corresponding to the glass nanopore tip marked on the left. Due to the applied voltage, the negative surface charge of the capillary leads to an electroosmotic outflow through the pore aperture (black circle with radius $\widetilde{R}$, shown in perspective), caused by the movement of a layer of positive counterions screening the surface. Dark blue arrows indicate qualitative linear flow velocities $\vec{u}$ (see Subsect. 4.3.2); the white arrow refers to the volumetric flow rate $\widetilde{Q}_0$ at the pore exit defined in Eq. 4.8.

buckling due to core polymerisation (see Fig. 4.5)[†]. These were added by hand in low concentrations to the right reservoir in the left panel of Fig. 4.4 and trapped with the OT at a pre-objective laser power of 300–500 mW, close to the pore exit around 30–50 µm above the coverslip surface. The trap stiffness was calibrated at a sampling frequency of 3 kHz using the power spectral density (PSD) method introduced in Subsect. 2.1.4, and relative movements of the nanopipette with respect to the trap centre were achieved by a piezolectric positioning system, just as described in Chap. 3.

4.3. Theoretical concepts

4.3.1. Electroosmosis in glass nanopores

The electrically induced flows treated in this part of the thesis can be easily understood by recalling the definition of *eletrophoresis*, a process that is utilised in any biochemistry laboratory to separate macromolecules by size and charge in gels [Patel, 1994]: the motion of a dispersed object relative to a static bulk solution, driven by an electric field [Lyklema, 2005]. *Electroosmosis* and the corresponding fluid flow can be considered

[†]All colloids were provided by Dirk Aarts and Roel Dullens.

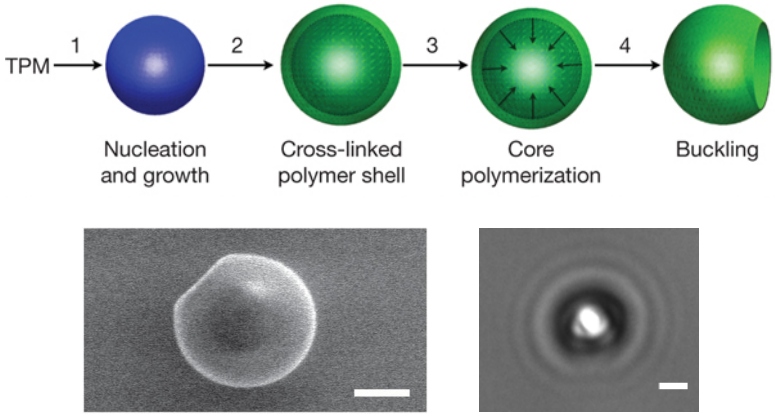

Figure 4.5. Asymmetric colloids used for flow measurements. **(Top)** Fabrication principle: monodisperse silicon oil droplets are (1) nucleated from a homogeneous solution of hydrolysed 3-methacryloxypropyl-trimethoxysilane (TPM) monomer, and (2) encapsulated into cross-linked polymer shells. The liquid core (3) contracts when polymerised and (4) drives a controlled shell buckling that forms spherical cavities. [Figure taken from [Sacanna et al., 2010].] **(Bottom)** Images of 3 µm beads clearly showing a dimple at one side, as observed on a surface with a scanning electron microscope (left) and when confined in the optical trap under standard illumination (right). The electron micgrograph was acquired by Nicholas Bell; the white scale bars correspond to 1 µm.

just the inverse effect of the same phenomenon: now the (charged) object is taken at rest, and the motion of the (electrolytic) bulk solution – dragged along by moving counterions – is considered (see the right panel of Fig. 4.4). Electroosmotic flows are known to have a strong influence on the translocation properties of biomolecules through nanopores [Ghosal, 2007; van Dorp et al., 2009]; outside the pore, their associated drag may completely outweigh the electrophoretic force (as illustrated by Eq. 4.23) and prevent the molecules from entering the constriction [Keyser et al., 2010]. It therefore comes as no surprise that characterisation [Bouzigues et al., 2008] and minimisation [Hernández-Ainsa et al., 2013b] of electroosmotic effects are ongoing fields of investigation for micro-/nanofluidic applications.

Just like their silicon nitride relatives, solid-state nanopores made of glass generally have a negative surface charge [Behrens and Grier, 2001] and are consequently screened by a layer of positive ions when placed in a (monovalent) electrolyte (see Fig. 4.4). Assuming a small electrostatic potential, the layer thickness can be approximated by the so-called Debye screening length

$$\kappa^{-1} = \sqrt{\frac{\epsilon\, k_\mathrm{B} T}{2\, c\, N_\mathrm{A}\, q^2}}\,, \tag{4.1}$$

where ϵ is the overall dielectric constant of the medium, c the molar ion concentration, N_A the Avogadro constant and q the elementary charge [Israelachvili, 2011]. The inverse Debye length κ stands for the characteristic decay constant of the potential. For

$c = 1\,(0.01)\,\mathrm{mol/L}$ in water, $\kappa^{-1} \approx 0.3\,(3)\,\mathrm{nm}$ at room temperature. This implies that, for nanocapillary tips measuring on the order of 100 nm, under high salt conditions most counterions gather very close to the capillary wall – only few diffuse in the vicinity of the pore axis –, which saturates the electroosmotic flow profile in the central region of the channel. Consequently, upon application of an electric field, the overall flux through the pore is stronger at *lower* ion concentration [Laohakunakorn, 2012]. For that reason, the experiments described in this chapter were all carried out at $c^{\mathrm{KCl}} = 0.01\,\mathrm{mol/L} = 10\,\mathrm{mM}$ only (see Subsect. 4.2.2).

4.3.2. Inferring flow rates at the pore from particle rotations/forces[‡]

An infinitesimal volume element in a fluid rotates at an angular velocity $\vec{\Omega} = \vec{\omega}/2$, where $\vec{\omega}$ is the vorticity vector, which describes the local tendency of spinning and is defined as the curl of the linear flow velocity $\vec{u}$, i.e. $\vec{\omega} := \vec{\nabla} \times \vec{u}$ [Batchelor, 2000].

Relation between microsphere angular velocity and flow vorticity

For a spherical particle of size r_p embedded in a steady flow field $\vec{u}$, the force $\vec{F}_\mathrm{p}$ and torque $\vec{T}_\mathrm{p}$ it experiences are given by Faxén's laws [Happel and Brenner, 1983]:

$$\vec{F}_\mathrm{p} = 6\pi\eta r_\mathrm{p}(\vec{u} - \vec{U}_\mathrm{p}) + \pi\eta r_\mathrm{p}^3 \nabla^2 \vec{u}\,, \tag{4.2}$$

$$\vec{T}_\mathrm{p} = 8\pi\eta r_\mathrm{p}^3 \left(\frac{\vec{\omega}}{2} - \vec{\Omega}_\mathrm{p}\right), \tag{4.3}$$

with η being the dynamic viscosity of the fluid and $\vec{U}_\mathrm{p}$ and $\vec{\Omega}_\mathrm{p}$ the translational and rotational velocity of the particle, respectively. If the particle is furthermore confined in an optical trap ($|\vec{U}_\mathrm{p}| = 0$) and fulfils the condition $r_\mathrm{p} \ll \widetilde{L}$, where $\widetilde{L}$ is a characteristic length over which the flow field varies, then the second summand ($\propto r_\mathrm{p}^3 \nabla^2 \vec{u}$) of the first law (Eq. 4.2) can be neglected, which reduces the equation to Stokes' law for the frictional force, as introduced already in Eqs. 2.10 and 3.18:

$$\vec{F}_\mathrm{p} \equiv \vec{F}_\mathrm{drag} = 6\pi\eta r_\mathrm{p} \vec{u}\,. \tag{4.4}$$

Since $\vec{T}_\mathrm{p} = I_\mathrm{p}(\mathrm{d}\vec{\Omega}_\mathrm{p}/\mathrm{d}t)$, with $I_\mathrm{p} = (2/5)mr_\mathrm{p}^2$ being the moment of inertia of a sphere with mass m – we assume that any particle asymmetry has only an insignificant effect on its dynamics –, the second law (Eq. 4.3) can be rewritten as

$$\tau_\Omega \frac{\mathrm{d}\vec{\Omega}_\mathrm{p}}{\mathrm{d}t} = \left(\frac{\vec{\omega}}{2} - \vec{\Omega}_\mathrm{p}\right), \tag{4.5}$$

[‡]Most of the derivations shown in this subsection were elaborated by Sandip Ghosal.

where

$$\tau_\Omega = \frac{2mr_\mathrm{p}^2}{40\pi\eta r_\mathrm{p}^3} = \frac{m}{\frac{4}{3}\pi r_\mathrm{p}^3}\cdot\frac{r_\mathrm{p}^2}{15\eta} = \frac{\rho_\mathrm{p} r_\mathrm{p}^2}{15\eta} \tag{4.6}$$

is the characteristic time of rotation onset/decay for a particle with mass density ρ_p when the external flow field is switched on/off. Inserting typical values ($\rho_\mathrm{p} = 1.2\cdot10^6\,\mathrm{g/m^3}$, $\eta = 1\,\mathrm{g/(m{\cdot}s)}$, $r_\mathrm{p} = 10^{-6}\,\mathrm{m}$) we obtain $\tau_\Omega \approx 10^{-7}\,\mathrm{s} = 0.1\,\mu\mathrm{s}$, which resembles τ_inert introduced right after Eq. 2.10 on page 13 and again indicates a process that is much faster than any detectable timescale during data acquisition. This shows that the trapped microsphere can be considered equivalent to a small fluid volume element (see above), as it starts/stops rotating practically instantaneously at its equilibrium rotation rate

$$\vec{\Omega}_\mathrm{p} \equiv \vec{\Omega} = \frac{\vec{\omega}}{2} \tag{4.7}$$

when the flow initiates/ceases, i.e. the torque $\vec{T}$ felt by the particle is negligibly small.

The Landau–Squire solution for a point jet

Our particular case of the electroosmotic flow through a nanocapillary tip with radius $\widetilde{R}$ into a large reservoir filled with motionless liquid can be modelled as a fluid jet with average linear flow speed $\bar{u}_0$ (in m/s) at the pore exit. Fluid volume flow $\widetilde{Q}_0$ (in $\mathrm{m^3/s}$) and momentum flow rate $\widetilde{P}_0$ (in $\mathrm{kg{\cdot}m/s^2}$ =: N) at the constriction are then given by

$$\widetilde{Q}_0 = \underbrace{\pi\widetilde{R}^2}_{\text{pore area}}\cdot\bar{u}_0\,, \tag{4.8}$$

$$\widetilde{P}_0 = \underbrace{\rho_0\widetilde{Q}_0}_{\text{mass flow}}\cdot\bar{u}_0 \underset{(4.8)}{=} \pi\widetilde{R}^2\rho_0\bar{u}_0^2 \underset{(4.8)}{=} \frac{\rho_0\widetilde{Q}_0^2}{\pi\widetilde{R}^2}\,, \tag{4.9}$$

with ρ_0 being the fluid density (check again the right panel of Fig. 4.4). If we consider the limit $\widetilde{R}\to 0$ but $\widetilde{P}_0$ fixed, which according to Eq. 4.9 implies $\widetilde{Q}_0 = \widetilde{R}(\pi\widetilde{P}_0/\rho_0)^{1/2} \to\ 0$, we can think of the jet as being caused by a *point source of momentum*, meaning that at the pore, the jet continuously adds momentum but *not* volume to its environment. As a consequence, even though $\widetilde{Q}(0)\equiv\widetilde{Q}_0 = 0$, due to the entrained fluid from the surrounding quiescent reservoir, $\widetilde{Q}(x)$ increases with distance $x > 0$ from the orifice. This idealised situation corresponds to an exact solution of the nonlinear Navier–Stokes equations of fluid mechanics, found in the early 1940s by Landau [Landau, 1944] and later, independently by Squire [Squire, 1951].

Since the Reynolds number of such a jet (corresponding to the flow through a pipe with diameter $2\widetilde{R}$) can be defined by [Happel and Brenner, 1983]

$$Re := \frac{2\widetilde{R}\rho_0\bar{u}_0}{\eta} \underset{(4.8)}{=} \frac{2\rho_0\widetilde{Q}_0}{\pi\widetilde{R}\,\eta}\,, \tag{4.10}$$

typical values according to the results shown in Sect. 4.4 ($\widetilde{Q}_0 \approx 10\,\mathrm{pL/s}$, $\widetilde{R} \approx 75\,\mathrm{nm}$, ρ_0 and η for water as before) yield $Re \approx 0.1$. In this limit of low Reynolds number, and assuming rotational symmetry with respect to the X-axis according to Fig. 4.6, the Landau–Squire formalism yields a stream function Ψ of the flow in a plane. By definition, such a two-dimensional function describes the volume flux *through* a curve (i.e. the flux perpendicularly crossing a curve) that connects any two given points in that plane [Batchelor, 2000]. Accordingly, two points with equal stream function values lie on the same *streamline*.

For the sake of convenience and in order to facilitate comparison with experimental data, we consider a stationary fluid flow field in XY (i.e. for $z = 0$). In consequence, the stream function $\Psi_\mathrm{B}(x, y)$ at any point B as indicated in Fig. 4.6 corresponds to the flux through a curve AB defined by

$$\begin{aligned}\Psi_\mathrm{B}(x,y) - \Psi_\mathrm{A}(x,y) &\underset{(\Psi_\mathrm{A}:=0)}{=} \Psi_\mathrm{B}(x,y) \\ &:= \int_\mathrm{A}^\mathrm{B} \vec{u}\cdot\mathrm{d}\vec{n} = \int_\mathrm{A}^\mathrm{B} \underbrace{(u_x\,\mathrm{d}y - u_y\,\mathrm{d}x)}_{\mathrm{d}\Psi}\,,\end{aligned} \tag{4.11}$$

where A is a reference point (with zero stream function for convenience), $\vec{u} = (u_x, u_y, 0)$ the linear flow velocity in the XY-plane, and $\mathrm{d}\vec{n} = (\mathrm{d}y, -\mathrm{d}x)$ the normal vector to the curve element $(\mathrm{d}x, \mathrm{d}y)$ [Batchelor, 2000]. The last integral implies that

$$u_x = \frac{\partial\Psi}{\partial y} \quad \text{and} \quad u_y = -\frac{\partial\Psi}{\partial x}\,. \tag{4.12}$$

In spherical polar coordinates centred at the pore (with $\phi = 0$, see Fig. 4.6), the stream function of a point jet is given by [Landau, 1944; Squire, 1951]

$$\Psi(r,\theta,0) = \frac{\widetilde{P}_0}{8\pi\eta} r\sin^2\theta\,. \tag{4.13}$$

In analogy to Eqs. 4.12, the components of the velocity field $\vec{u} = (u_r, u_\theta, 0)$ can then be obtained as [Batchelor, 2000]:

$$u_r = \frac{1}{r^2\sin\theta}\frac{\partial\Psi}{\partial\theta} = \frac{\widetilde{P}_0\cos\theta}{4\pi\eta r}\,, \tag{4.14}$$

$$u_\theta = -\frac{1}{r\sin\theta}\frac{\partial\Psi}{\partial r} = -\frac{\widetilde{P}_0\sin\theta}{8\pi\eta r}\,. \tag{4.15}$$

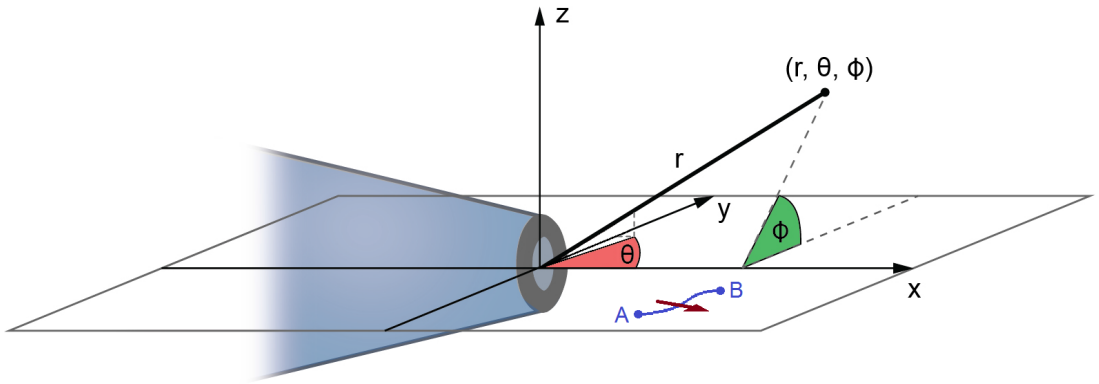

Figure 4.6. Coordinate system used for flow rate measurements. The propagation direction of the laser forming the optical trap is $+Z$. All measurements described in this chapter were carried out in the XY-plane, i.e. for $z = \phi = 0$ (note that the polar angle θ measured from the pore axis X is drawn here as the projection onto that plane). The volume flux (dark red arrow) across an arbitrary curve (blue line) connecting two points A and B is then given by the difference of their stream function values $\Psi_\mathrm{B} - \Psi_\mathrm{A}$ as defined by Eq. 4.11.

Volume flow through the nanopore as a function of rotation rate

From the previous equations, the vorticity vector reads [Batchelor, 2000]

$$\vec{\omega} = \nabla \times \vec{u} = \frac{1}{r}\left(\frac{\partial}{\partial r}(r u_\theta) - \frac{\partial u_r}{\partial \theta}\right)\hat{\phi} = \frac{\widetilde{P}_0 \sin\theta}{4\pi\eta r^2}\,\hat{\phi}\,, \tag{4.16}$$

$$\text{with} \qquad \hat{\phi} = -\sin\phi\cdot\hat{y} + \cos\phi\cdot\hat{z} \underset{(\phi=0)}{=} \hat{z} \tag{4.17}$$

indicating the unit vector in the direction of increasing ϕ. This implies that, depending on the sign of θ, rotations occur solely about the $\pm Z$-axis. As spherical and cartesian coordinates in the XY-plane as defined in Fig. 4.6 are related via the expressions

$$\begin{aligned} x &= r\cos\theta\,, \\ y &= r\sin\theta\,, \\ r &= \sqrt{x^2+y^2}\,, \end{aligned} \tag{4.18}$$

with x and y being longitudinal and transverse distance of the particle centre from the capillary tip, respectively, the angular velocity complies with $\vec{\Omega} = \Omega\,\hat{\phi}$, where

$$\Omega = \frac{\omega}{2} = \frac{\widetilde{P}_0 \sin\theta}{8\pi\eta r^2} = \frac{\widetilde{P}_0}{8\pi\eta}\frac{y}{(x^2+y^2)^{3/2}}\,. \tag{4.19}$$

Defining the similarity variable

$$y^* := \frac{y}{(x^2+y^2)^{3/2}}\,, \tag{4.20}$$

momentum and volume flow rate can hence be derived from linear regressions corresponding to functions $\Omega(y^*)$ fulfilling

$$\Omega = \frac{\widetilde{P}_0}{8\pi\eta}y^* \underset{(4.9)}{=} \frac{\rho_0\widetilde{Q}_0^2}{8\pi^2\eta\widetilde{R}^2}y^* \propto \widetilde{Q}_0^2\,y^*\,. \tag{4.21}$$

Volume flow through the nanopore as a function of frictional force

Apart from the rotational motion of the optically trapped colloid, the force it experiences because of the flow caused by the jet from the nanopore also serves for approximating the rate values. As per Eqs. 4.14 and 4.15, the absolute value of the linear velocity vector is

$$|\vec{u}| = u = \sqrt{u_r^2+u_\theta^2} = \frac{\widetilde{P}_0}{4\pi\eta r}\sqrt{\cos^2\theta+\frac{\sin^2\theta}{4}}\,. \tag{4.22}$$

Neglecting electrophoretic (EP) force contributions due to the surface charge of the colloid, to a first approximation the total jet-induced drag force amplitude F_{drag} according to Stokes' law (Eq. 4.4) completely balances the restoring force from the optical trap given by Eq. 2.6, such that

$$F_{\mathrm{drag}} - F_{\mathrm{EP}} \approx F_{\mathrm{drag}} \equiv F_{\mathrm{OT}} = 6\pi\eta r_{\mathrm{p}}u = \frac{3r_{\mathrm{p}}\widetilde{P}_0}{2r}\sqrt{\cos^2\theta+\frac{\sin^2\theta}{4}}\,. \tag{4.23}$$

The scaled inverse distance

$$\frac{1}{r^*} := \frac{1}{r}\sqrt{\cos^2\theta+\frac{\sin^2\theta}{4}} \underset{(4.18)}{=} \frac{1}{x^2+y^2}\sqrt{x^2+\frac{y^2}{4}} \tag{4.24}$$

again linearises the dependence and we end up with

$$F_{\mathrm{drag}} = \frac{3r_{\mathrm{p}}\widetilde{P}_0}{2r^*} \underset{(4.9)}{=} \frac{3r_{\mathrm{p}}\rho_0\widetilde{Q}_0^2}{2\pi\widetilde{R}^2r^*} \propto \frac{\widetilde{Q}_0^2}{r^*}\,. \tag{4.25}$$

In summary, flow-induced rotations (Eq. 4.21) and forces (Eq. 4.25) exhibited/felt by the trapped microsphere provide two independent ways of quantifying the volumetric flow rate at the nanopore exit.

4.4. Results and discussion

4.4.1. Tracking flow-induced rotations and forces of trapped microspheres

Rotation measurements and necessary controls

To probe the electroosmotic flow strength through a nanopipette, we positioned a practically spherical, but sufficiently asymmetric colloid close to the pore exit located at the origin, while held in the optical trap. Applying a positive voltage at the capillary back end resulted in a nanojet through the pore that caused the colloid to rotate when moved off-axis, i.e. for $y \neq 0$, acting as a microscopic anemometer (Fig. 4.7a). We followed the rotational motion with $\sim 2\,\mathrm{nm}$ accuracy at a frame rate of 1 kHz, by tracking a reduced region of interest ($128 \times 100\,\mathrm{px}$) of the CMOS camera and performing cross-correlation image analysis in real time, as reported by Otto and co-workers [Otto et al., 2010] and in equivalence to the methods employed for the setups described in Chaps. 3 and 5. At the same time, a standard CCD camera at slow shutter speed provided an optical image of the whole field of view (Fig. 4.7d).

Because of the slight non-uniformity of the trapped colloid introduced by the dimple (see Fig. 4.5), the "centre of mass" of the optical image was displaced from the rotational axis, so that particle revolutions could be detected as periodic modulations of the scattered light distribution centres in XY (Fig. 4.7b). These exhibited a phase shift of $\sim \pi/2$, tracing out almost circular paths (Fig. 4.7c). For sufficiently slow angular velocities, rotation rates were determined by counting revolutions (i.e. signal peaks/valleys in XY) manually within a certain time interval. Fast rates could be accurately quantified by analysing the power spectra of XY-position signals with customised software developed in LabVIEW, depicting a broad but well-defined peak corresponding to the angular frequency (data not shown).

Note that the asymmetry essential for rotation tracking does not significantly alter the mechanical properties of the particle, which can still be treated as a sphere of radius r_p. To rule out a possible dependence of rotations on trap stiffness, we performed test measurements at various laser powers, which did not alter the mean rotation rate at steady electroosmotic outflow (data not shown). In addition, despite a preferred orientation of the dimpled colloids in the optical trap – presumably due to a not perfectly circular laser spot –, the optical potential hardly affected the rotation onset, especially in case of the largest particles. This complies with results from a study that also used linearly polarised laser light for OT experiments: when probing spherical particles of various diameters, polarisation effects are minimised for those that are larger than the spot diameter (i.e. the laser wavelength in solution) [Rohrbach, 2005]. We can thus assume that in our case the optical trap does not exert a significant torque on the microsphere. Note also that the rotation approach has the advantage that particle revolutions are sensitive only to the hydrodynamic and not to the electric field – the charge of the colloid does not affect its torque at all (see Eq. 4.3).

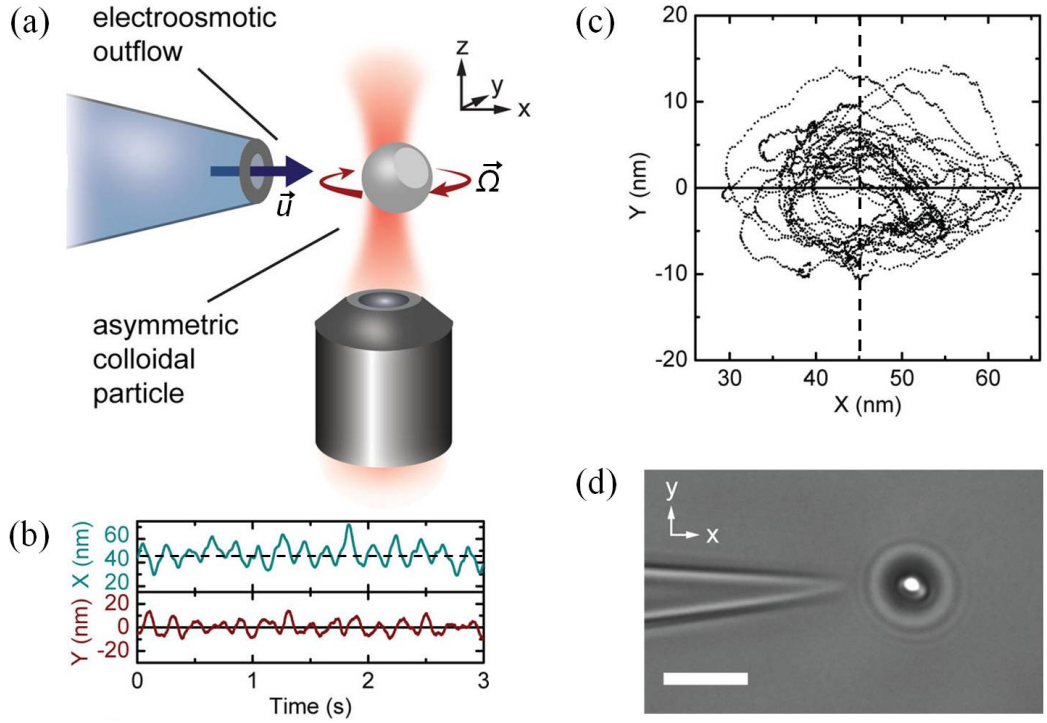

Figure 4.7. Flow sensor based on particle rotations in optical tweezers (OT). **(a)** Sketch of the experimental configuration (*not to scale*): a dimpled microsphere is confined in the optical trap close to the tip of a glass nanopore with inner radius of $\sim 75\,\mathrm{nm}$. Applying a voltage across the nanopipette as indicated in Fig. 4.4, the rotation rate $|\vec{\Omega}|$ of the colloid is measured, which is caused by linear fluid flow velocities $\vec{u}$ due to electroosmosis at the inner capillary walls. **(b)** Data of particle XY-positions relative to the trap centre are obtained by video tracking and filtered to 20 Hz. The offset of $\sim 45\,\mathrm{nm}$ in X (dashed line) is due to the flow-induced drag force exerted on the particle. **(c)** A two-dimensional plot of the signals from (b) reveals a roughly circular motion of the optical centre of the particle. **(d)** A camera snapshot depicting an experiment in progress. The scale bar denotes 5 µm. Note that the glass nanopore is too small to be resolved optically.

Force measurements as independent fluid velocity tests

Apart from the rotations, we also probed the flow-induced drag force felt by the particle in the trap (see Fig. 4.7a/b). We computed the total force from its components in X and Y according to Eq. 2.6: the mean values of the lateral deviations from the trap centre within a certain time interval multiplied by their respective, previously calibrated trap stiffness. To make sure that electrophoretic forces outside the pore were small for our experimental configuration (as assumed in Eq. 4.23), we performed control experiments with colloids of different surface charges, which presented no significant difference in their behaviour when measured at the smallest axial distance $x = 1.75\,\mu\mathrm{m}$ (data not shown). This is in agreement with results from numerical simulations showing that outside the pore the electric field decays rapidly (within a few pore diameters from the orifice) to negligible values [Laohakunakorn, 2012].

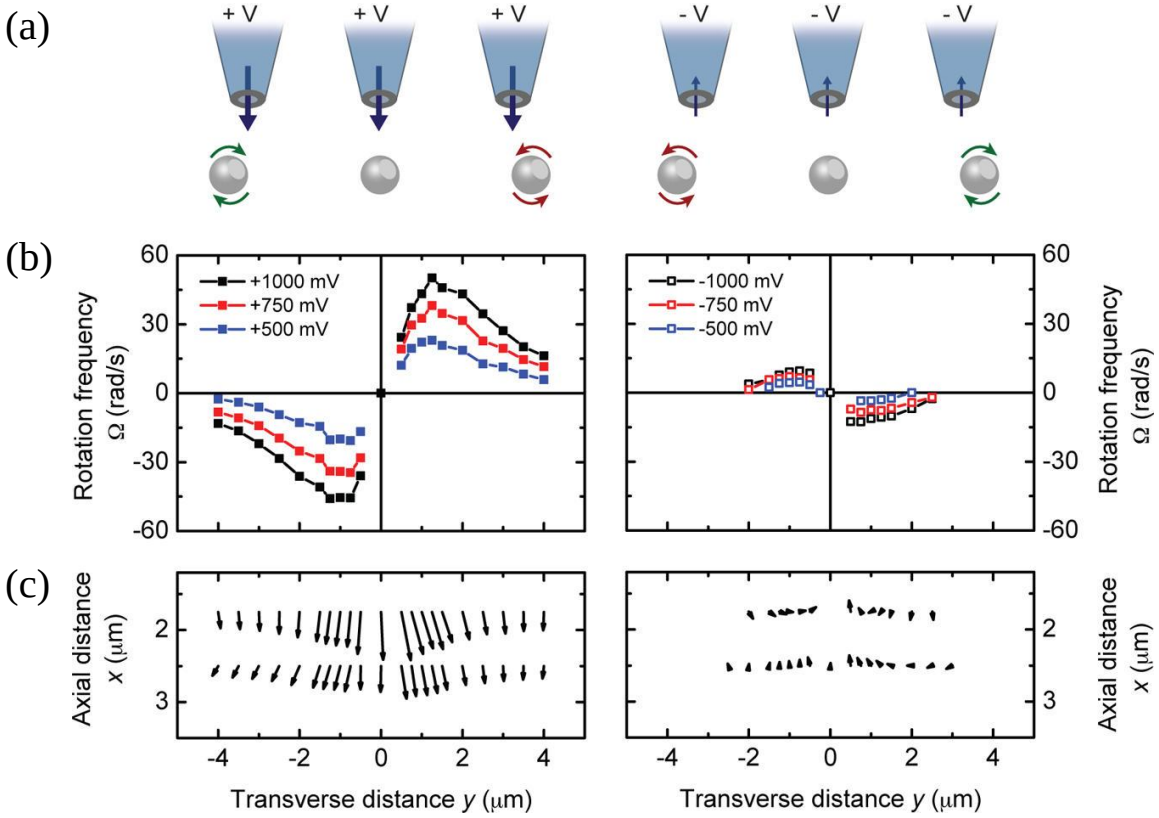

Figure 4.8. Concurrent rotation and force measurements to sense the flow field. **(a)** Layout of the experimental approach: starting at a certain axial distance x from the capillary tip, a trapped colloid is moved stepwise, transversely (in Y) to the pore axis. At each XY-position, angular velocity and force response are probed at positive (left panels) and negative (right panels) voltages. The measurement procedure is performed for up to three different x-values. **(b)** Scanning a 3 µm bead at $x = 1.75$ µm along the Y-axis, e.g. from positive to negative values, at $V = \pm 1000, \pm 750$, and ± 500 mV the rotation rate first increases, then decreases to zero on the jet axis, and finally reverses direction. We observe fast rates at positive, and slow ones in opposite direction at negative voltages. **(c)** The force vectors felt by the microsphere are shown for $x = 1.75$ and 2.50 µm at $V = \pm 1000$ mV, where the longest arrows indicate a total drag of ~ 14 pN. Also in this case, when compared with forces due to capillary outflow, negative voltages induce inverse vectors with much smaller amplitudes.

4.4.2. Mapping out the flow profile of the nanopore

In order to characterise the flow field created by the nanojet, we raster-scanned the colloid in the XY-plane in 250/500 nm steps (Fig. 4.8a), with $z \sim 0$ being adjusted such as to give maximum rotation/force signal always. At each coordinate, a set of at least six voltages within the maximum range of the current amplifier was applied and the responses probed during ~ 10 s (Fig. 4.8b/c). For positive voltages at $y \approx 0$, we measured a maximum force but no rotations. As we increased $|y|$, the force decreased gradually, while the rotation rate reached a peak at $|y| \sim x$, decaying slowly for larger

transverse offsets. Reversing the voltage yielded inverted rotation and force directions, but much smaller amplitudes, suggesting electroosmotic inflows to be much weaker than outflows in the case of conical glass nanopores.

Since the capillary tip is smaller than the diffraction limit of visible light, the exact position and shape of the glass nanopore cannot be observed under the microscope (see Fig. 4.7d). Optical trap, patch-clamp amplifier and three-dimensional piezoelectric stage in conjunction can however serve as a pore position detection assembly because laser-induced heating leads to a peak in ionic current when the orifice passes through the focal region of the beam [Keyser et al., 2005]. In our case, particle rotations and forces constitute more reliable indicators as they directly take into account the axial deviation of the particle from the optical trap centre (see the paragraphs about Mie scattering in Subsect. 2.1.2) and can easily identify (apparent) thermal drift in Z of the nanopipette, caused e.g. by laser-induced heating of the objective (see Chap. 3).

As a consequence, in order to probe consistent flow velocities during long-lasting experiments necessary to acquire complete data sets like the one presented here, sample cell reservoirs needed to be refilled with salt solution whenever necessary and the reference height defined by the Z-position of the piezo stage readjusted from time to time. This procedure also provides information about variations in the capillary tip orientation, which in most cases was found to be not perfectly symmetric near the pore exit with respect to the X-axis. Indeed, the data shown in Fig. 4.8b/c depict a slight asymmetry that becomes apparent when comparing rotation and force values measured at transverse distances $\pm y$.

4.4.3. Validation of the theoretical model[§]

For a quantitative comparison of rotation frequencies and forces acquired at different axial distances from the capillary tip, we re-plotted the type of data shown in the previous figure against similarity variables derived from the Landau–Squire solution for a point jet (see Subsect. 4.3.2). Figure 4.9a depicts the results of rotation rate measurements for one microsphere type at all probed positions (x, y) and voltages, represented as functions of the scaled quantity y^* defined in Eq. 4.20. The linear fits from the theoretical prediction according to Eq. 4.21 adjust very well to the various sets of data points, each slope corresponding to a different, voltage-dependent flow rate at the pore exit. Equivalently, force data were analysed as functions of the parameter $1/r^*$ – which is positive by definition – introduced in Eq. 4.24. Again, all measurements taken at the same voltage collapsed on a straight line given by the theory (Eq. 4.25); Figure 4.9b contains just one example. Note that the large error bars in force indicate the standard deviations from the mean values illustrated in Fig. 4.8c, due to particle rotations (i.e. apparent lateral position fluctuations) at off-axis positions.

[§]The data analysis described in this and the next subsection was carried out in large part by Nadanai Laohakunakorn.

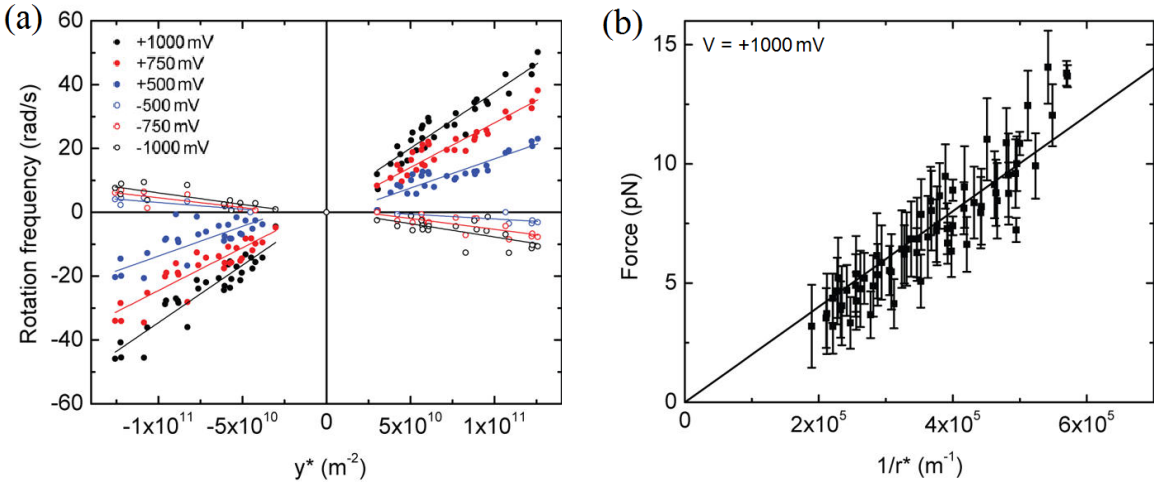

Figure 4.9. Testing the Landau–Squire scaling with our experimental data. **(a)** Rotation measurements with 3 µm particles for transverse positions $y \in [-4\,\mu\text{m}; 4\,\mu\text{m}]$ at three different axial distances $x = 1.75, 2$ and $2.5\,\mu\text{m}$. All data collapse on straight lines according to Eq. 4.21 when plotted against the similarity variable y^* defined in Eq. 4.20, where different voltages give rise to different slopes representing differing flow rates at the pore exit. **(b)** Using the scaled variable $1/r^* > 0$ (see Eq. 4.24) as abscissa, simultaneous force measurements with the same colloids also yield linear dependences, adjusting to Eq. 4.25 in this case (only one data set is shown here for clarity).

4.4.4. Volume flow and ion current values showing rectification effects

From the slopes in Fig. 4.9, provided the radius $\widetilde{R}$ of the capillary tip is known, the volumetric flow rate $\widetilde{Q}_0$ through the nanopore can be computed directly by relying on either rotation (Eq. 4.21) or force (Eq. 4.25) measurements. The data shown here correspond to a batch of glass nanopores with diameters around 150 nm (see Subsect. 4.2.2). While all preceding figures in this chapter have addressed measurements carried out with 3 µm beads, Fig. 4.10a depicts results of the flow rate at the pore exit for all particle sizes (1.5, 2 and 3 µm) studied. The values derived from both calculation methods turned out to be in agreement within experimental error, leading to volume flows around $10\,(-5)\,\text{pL/s}$ at positive (negative) voltages that appeared to be largely independent of the type of particle used. This result was not necessarily expected, also because our system only marginally fulfils the condition $r_\text{p} \ll \widetilde{L}$, stated at the beginning of Subsect. 4.3.2 and required for the assumption of Stokes' friction. In principle, due to the linearity of the Navier–Stokes equations in the limit of low Reynolds number [Batchelor, 2000], inverting the applied voltage should invert the flow field. In our case, the observed non-linearity in flow rate upon voltage reversal may intuitively be attributed to the tapered, symmetry-breaking nanopipette. The physical mechanism behind this *flow rectification* behaviour – quantified via the ratio $\widetilde{\alpha}_Q$ introduced in Table 4.1 for all three data sets – still needs further investigation though: it might be due to a local departure from the limit of small Reynolds num-

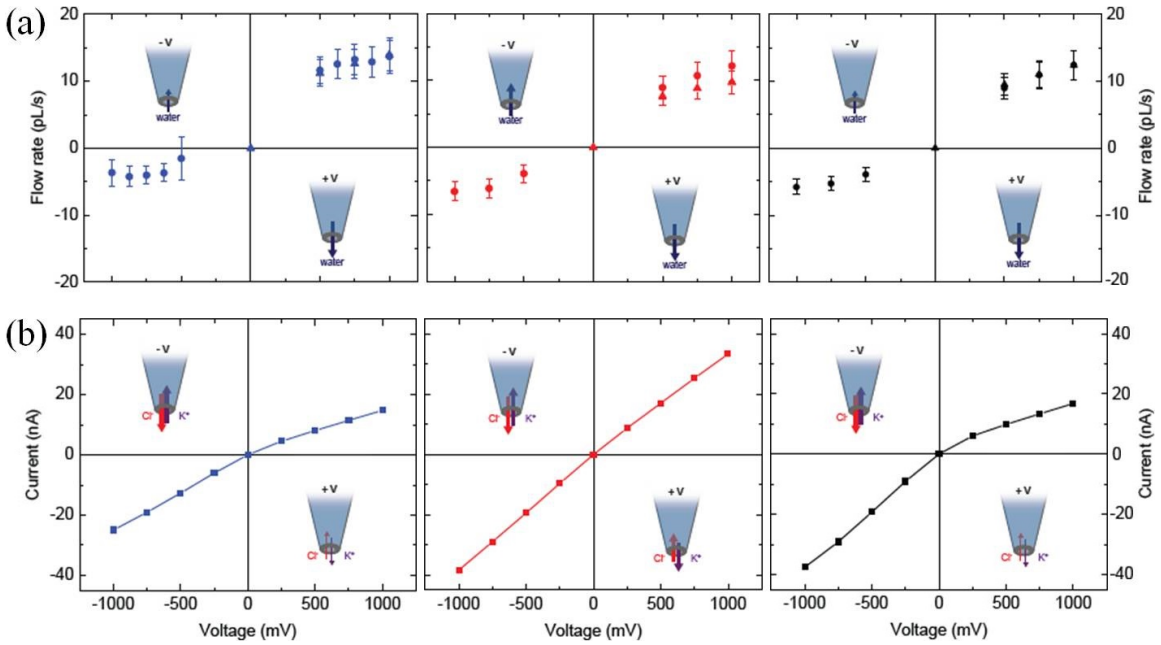

Figure 4.10. Flow and ionic current measurements through equivalent nanocapillaries using various microsphere types. **(a)** From rotation frequency (circles) and force (triangles) dependencies according to Fig. 4.9, the volume flow rates $\widetilde{Q}_0$ through pores with radii around 75 nm are derived for all applied voltages. From left to right, the results presented here correspond to asymmetric colloids of 1.5 (blue), 2 (red) and 3 µm (black) in diameter, all showing similar rates of up to ~ 15 pL/s, with error bars indicating the standard deviation. The smaller inflows at negative voltage values comply with the results shown in the previous figures and enable us to define a flow rectification parameter (Table 4.1). **(b)** Characteristic IV-curves acquired for the glass nanopores used to obtain the data described in (a). Note that in the particular example presented here, data corresponding to 2 and 3 µm particles were acquired with the same nanopore at different moments in time. Varying current–voltage dependences correspond to dissimilar rectification ratios as specified in Table 4.1.

ber very close to the pore entrance/exit, where fluid acceleration is considerable, or because of nonlinear electrokinetic effects due to the steeply increasing/decreasing electric filed.

When probing the local flow field lines with the described methods, we always measured the ionic current through the nanopore simultaneously. For a conically shaped glass nanocapillary, characteristic IV-curves at low salt concentrations typically describe functions that are not antisymmetric with respect to the origin, indicating a preferential direction of ion flow. This diode-like behaviour is known as "current rectification" and stems from interactions of ions in solution with excess surface charges at the pore [Siwy, 2006]. The curves corresponding to sample cells employed for rotation/force sensing showed variable current–voltage characteristics, as represented in Fig. 4.10b. Please note that in general, each set of measurements was accomplished using a new capillary tip, fabricated according to the same protocol always [Steinbock et al., 2010a]. Different

Data set colour (Fig. 4.10)	Particle diameter (μm)	Flow rectification (ratio $\widetilde{\alpha}_Q$)	Current rectification (ratio $\widetilde{\alpha}_I$)
blue	1.5	3.83	0.59
red	2	2.99	0.87
black	3	2.13	0.45

Table 4.1. Quantitative measures of rectifying flow and current behaviour. The parameters $\widetilde{\alpha}$ are defined by $\widetilde{\alpha}_Q := |\widetilde{Q}_0(+1\,\mathrm{V})/\widetilde{Q}_0(-1\,\mathrm{V})|$ and $\widetilde{\alpha}_I := |I(+1\,\mathrm{V})/I(-1\,\mathrm{V})|$. In agreement with the results shown in Fig. 4.10, the two effects behave in opposing manners: $\widetilde{\alpha}_Q > 1$ while $\widetilde{\alpha}_I < 1$.

rectification ratios $\widetilde{\alpha}_I$ (included in Table 4.1) indicate variabilities of parameters such as pore size/geometry, capillary charge and buffer ion concentration [Siwy, 2006] – which may change with time even for the same nanopipette (see Fig. 4.10b). Still, it seems that such parameter fluctuations affected the results presented in Fig. 4.10a only marginally.

4.4.5. Implications of the nanofluidic system

Comparison with other flow measurement techniques

The volume flow rate values of the nanocapillary jet probed here with OT-assisted methods are among the lowest that have been determined experimentally so far. Other small-scale flow speed quantification approaches rely for instance on the tracking of minute tracer particles to establish spatial velocity distributions [Santiago et al., 1998], on the size monitoring of droplets at both ends of a nanotube [Sinha et al., 2007], on the detection of the degree of photobleaching of a fluorescent dye forced through a laser focus [Wang, 2005], or on the definition of the passage time of local molecular density fluctuations by correlating the current signals from two adjacent electrodes along a nanometric channel [Mathwig et al., 2012]. One advantage of our technique is that it lacks the need of tracer particles or fluorescent dyes, which makes sporadic flow measurements during other types of assays feasible. Tracing would be difficult to implement anyway since the necessary particles might either respond to the electrophoretic force apart from the viscous drag (if charged) or tend to aggregate (if neutral).

Potential applications of the nanojet

Our novel method to assess tiny flow profiles across large areas of the sample cell is of great importance for a series of applications in nano-/biotechnology that rely on ultra-low-volume injection, such as drug delivery, nanoscale mixing or patterning [Ying, 2009]. Also, multiplexed nanopipette-based assays might contribute new high-throughput screening techniques in biology [Hong et al., 2009]. In addition, due to

the observed volumetric flow asymmetries manifested in Fig. 4.10a and Table 4.1, our electroosmotically induced jet might find use as a microfluidic "flow rectifier", a feature that is usually difficult to design because of the linear behaviour of systems functioning at low Reynolds numbers. Apart, the described rotation/force measurement procedure with colloids that exhibit a small dent provides a valuable measure of quality for nanocapillaries and their potential surface coatings (used e.g. to diminish undesired electroosmosis during single-molecule electrophoresis [Hernández-Ainsa et al., 2013b]), pushing the use of glass nanopores as efficient biomolecule detectors.

4.5. Conclusion

In this chapter, a new fluid anemometry technique based on OT and asymmetric microspheres has been presented. Rotations and forces induced on optically trapped particles directly correlate with the ambient flow velocity. The method has proven sensitive enough to probe the electroosmotic flow from a single glass nanopipette typically used for DNA translocation measurements.

Varying the relative position between laser trap and capillary tip, we have been able to construct a map of the flow field for different applied voltages. The results can be explained by an analytical model that considers the fluid flux out of the nanocapillary as caused by a point jet. The mean volume flow rates at the pore exit turn out to be on the order of 1–10 pL/s and therefore within a range that is difficult to access with other flow measurement approaches. The method described herein entails various applications in biology and nanotechnology and underlines the power of combining different single-molecule manipulation techniques such as OT and ionic current detection through nanopores.

5. Temperature-controlled magnetic tweezers for enzyme kinetics studies

In this chapter, a thermally stabilised magnetic tweezers (MT) instrument for single-molecule experiments between ambient and physiological conditions is presented. Its customised thermal control system requires little space and yields a precision of 0.1 °C at up to 40 °C inside the sample cell, which makes it attractive for other surface-coupled microscopy techniques. As a proof of concept, the setup is used to study the effect of temperature on the velocity by which the molecular motor AddAB – a bacterial protein complex involved in dsDNA break repair – unwinds and moves along the double helix. When compared with results from bulk measurements, MT data give rise to almost the same estimate of enzymatic activation energy according to Arrhenius kinetics. Exponentially increasing single-molecule translocation speeds turn out to reach the usually higher ensemble values at optimised ATP concentrations near the motor protein in the fluid chamber.

Parts of this chapter have been published online in: Gollnick et al. (2014), *Small*, DOI: 10.1002/smll.201402686.

5.1. Introduction

5.1.1. Managing thermal conditions while probing individual molecules

As motivated at the beginning of Chap. 2, single-molecule studies in solution explore phenomena that are governed by energies measured in multiples of $k_\mathrm{B}T$ ($\approx 4\,\mathrm{pN{\cdot}nm}$ at $T = 25\,^\circ\mathrm{C}$) and for that reason show a distinct sensitivity to temperature fluctuations within the surrounding medium [Neuman and Nagy, 2008; Ritort, 2006]. Probing reaction kinetics via individual proteins or nucleic acids thus requires both thermal accuracy and stability inside the sample cell – quantitative results will otherwise get biased [Maloney et al., 2011; Watanabe-Nakayama et al., 2008]. Many different approaches have tried to offer solutions for an efficient temperature management during experiments that address one molecule at a time: either microscopically via laser heating [Kato et al., 1999; Mao et al., 2005] or micro-/nano-fabrication [Arata et al., 2006; Mihajlović et al., 2004; Wang et al., 2011], or macroscopically by enclosing (parts of) the experimental setup [Bianco et al., 2001; Böhm et al., 2000] or warming and/or cooling components that are in close thermal contact with the sample [Mao et al., 2005; Williams et al., 2001b]. Figures 5.1 and 5.2 show examples of local and global temperature modulation strategies, respectively.

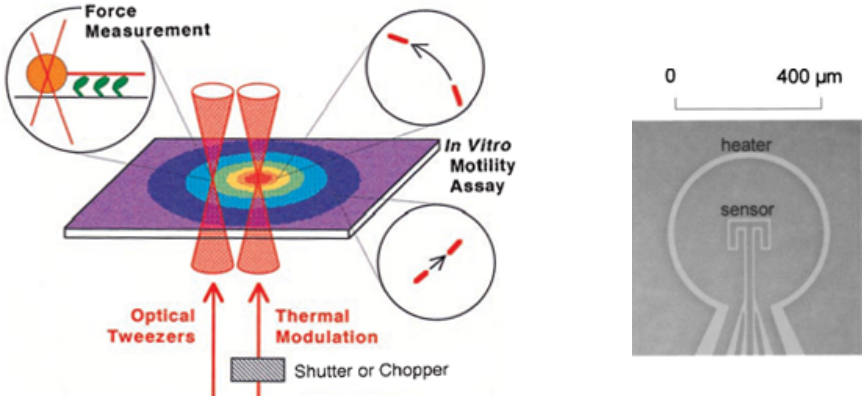

Figure 5.1. Two examples of *microscopic* temperature control methods. **(Left)** Laser heating of a surface covered with myosin proteins creates defined thermal gradients that affect the velocity by which actin filaments are transported. The use of an additional optical trap enables force response measurements at different temperatures. [Figure modified from [Kato et al., 1999].] **(Right)** (An array of) microfabricated heater/sensor pairs can serve as a means to control the temperature in a common flow cell locally. By dissipating only small amounts heat, large temperature changes with fast stabilisation times can be achieved. [Figure modified from [Arata et al., 2006].]

5.1.2. Macroscopic control methods for surface-bound assays

For experimental configurations that require thermal stability across a certain area of the cover glass surface and rely on high-numerical-aperture (high-NA) oil-immersion objectives, macroscopic control is effective and relatively easy to implement [Baker et al., 2011; Maloney et al., 2011]. Indeed, various sample stage and objective temperature controllers are commercially available (see Ref. [Bioptechs Inc., 2001] for instance). As explained in the following, in our case we have to cope with the additional task of keeping the size of the temperature management components as small as possible.

Requirements of magnetic tweezers microscopes

Recalling Sect. 2.2, permanent magnet–based MT constitute a single-molecule technique that is coupled to a glass surface and commonly relies on a customised inverted microscope. In the setup relevant for this thesis, magnet dimensions are similar to the fluid chamber width and very large in comparison with the size of the biological sample under study (see Sect. 5.2). Such a configuration exposes microspheres – which are tethered to the glass via DNA molecules (see Fig. 2.5) – to a homogeneous, upwards-directed force field within the typical field of view ($\sim 100 \times 100\,\mu m$) corresponding to the camera image.

To apply high forces, the magnet pair needs to approach the sample cell from above down to very short distances (see Fig. 2.6). As a result, maximising the force requires spacer and upper cover of the fluid chamber to be as thin as possible. At the same time,

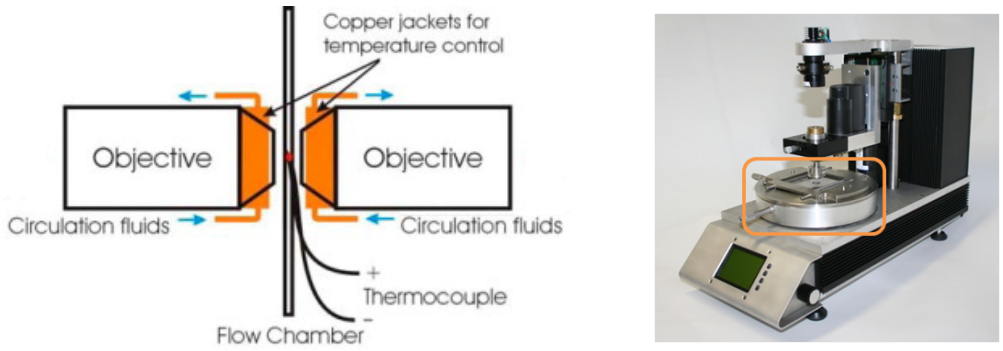

Figure 5.2. Two examples of *macroscopic* temperature control methods. **(Left)** Two metal collars ("jackets") attached to the frontal parts of microscope objectives serve as heaters/coolers by means of circulating liquid kept at a certain temperature. A thermocouple probes the thermal conditions of the buffer in a sample cell used for experiments with dual-beam optical tweezers (OT). [Figure modified from [Mao et al., 2005].] **(Right)** A Peltier-controlled metal housing (indicated by the orange rectangle) encloses the sample stage of a commercial magnetic tweezers (MT) instrument, thus minimising thermal drift of the focal plane. [Figure modified from [PicoTwist, 2006].]

for accurate tracking of axial microsphere positions, the objective is usually mounted on a piezoelectric positioning device (see the comment at the end of Subsect. 2.2.3) that restricts the available space nearby. Consequently, measuring in a MT microscope at different thermal conditions and high forces requires temperature management components that fit into the limited room on both sides of the sample stage and around the objective.

In addition and independent of any space constraints, for proper buffer temperature calibrations the flow cell assembly must also allow for the possibility to probe the thermal conditions near the location of the experiment itself.

Challenges of thermal control in magnetic tweezers

Even when only heating above room temperature is needed, meeting the requirements stated in the previous paragraphs with macroscopic temperature control methods is not easy and often involves custom-built solutions. For instance, Hong and co-workers used a resistive microscope slide to heat the fluid chamber of a MT setup from above [Lee et al., 2010; Park et al., 2008], which however limited the maximum applicable force. Likewise, Seidel and colleagues warmed the sample cell of their MT by placing thin heating elements on top of it, apart from adjusting the ambient temperature in the laboratory [Seidel et al., 2008]. On the other hand, a commercial MT apparatus with thermally stabilised sample stage [PicoTwist, 2006] has been employed for monitoring enzyme activity at different temperatures [Manosas et al., 2013, 2009] but – to the best of our knowledge – lacks an accurate measurement of the temperature in the interior of the cell.

Our approach of temperature management evades the commonly encountered drawbacks by minimising any interference with essential MT components, hence preserving the maximum range of measurable forces. In addition, we provide a simple way of calibrating the temperature inside the sample cell.

5.1.3. AddAB: a model DNA motor protein

To perform proof-of-principle measurements with our thermostated MT, we employed the protein complex AddAB from *Bacillus subtilis*, which had been studied at the single-molecule level in our laboratory before [Carrasco et al., 2013; Yeeles et al., 2011b]. As illustrated in Fig. 5.3a/b, AddAB is a modular enzymatic assembly that contains a single functional helicase [Yeeles et al., 2011a] and two nucleases [Yeeles and Dillingham, 2007]. It catalyses the conversion of dsDNA ends into ssDNA overhangs (Fig. 5.3c) and is therefore functionally equivalent to the related, more widely studied protein complex RecBCD from *Escherichia coli* [Yeeles and Dillingham, 2010].

In vivo, DNA-end resection activity exhibited by AddAB/RecBCD represents an essential step of homologous recombination, a mechanism that is crucial for the repair of dsDNA breaks [Yeeles and Dillingham, 2010]. Damage of the double helix originates from both internal and external sources, occurs continuously in practically all cells of our body, and can lead to genome instability and associated medical conditions if not accounted for properly [van Gent et al., 2001]. At the molecular level, to initiate homologous repair of such DNA lesions, AddAB unwinds and degrades dsDNA upon translocation, being triggered by the recognition of a specific regulatory sequence called crossover hotspot instigator (Chi), which in the case of the protein complex from *B. subtilis* is 5 bp long (see Fig. 5.3a) [Chédin et al., 2000].

Distinguished features of AddAB include a high processivity and fast translocation rates – which depend on the available amount of adenosine triphosphate (ATP) [Carrasco et al., 2013]. In this chapter, we make use of a biotinylated version of wild-type AddAB to study the dependence of helicase motor activity on temperature modulations at single-molecule resolution.

5.2. Experimental materials and methods

5.2.1. Magnetic tweezers setup

The instrument employed in combination with the thermal control system is based on the simple design shown in Fig. 2.4 – first described by Strick and this team [Strick et al., 1996] and similar to the one used in Ref. [Seidel et al., 2008]. Along the lines of Subsect. 2.2.3, to be able to address complementary force ranges, we employ two setup configurations (MT_1/MT_2)* with different magnet alignments but

*Both systems were assembled by Fernando Moreno.

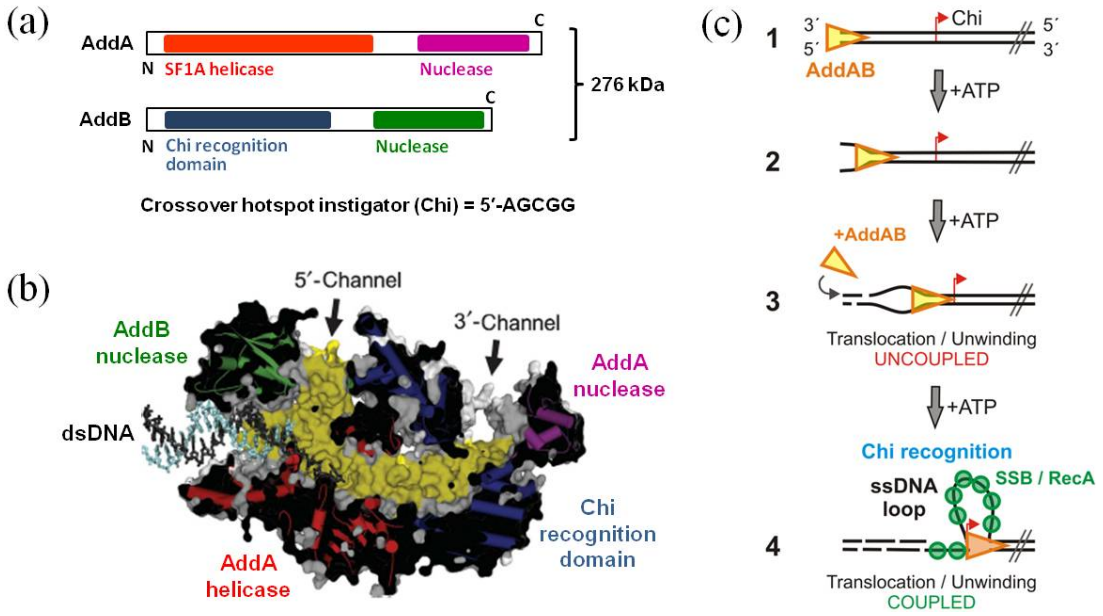

Figure 5.3. Structure and function of the molecular motor AddAB. **(a)** Schematic diagram of the heterodimeric protein sequence content from the amino (N) to the carboxy (C) termini, comprising a total mass of 276 kilodaltons (kDa). The AddA subunit consists of one Superfamily (SF) 1A (3' → 5') DNA helicase and one nuclease domain, whereas AddB contains a domain that senses characteristic Chi sequences along the substrate, apart from another nuclease. [Figure adapted from [Yeeles and Dillingham, 2010].] **(b)** Cross-sectional view of the three-dimensional structure corresponding to the modular protein complex. Completely enclosing the double helix, the helicase motor moves along dsDNA triggering a physical separation of the two single strands, which are cleaved stochastically by their respective nucleases at separate exit channels. Chi recognition can occur only along the 3'-strand. [Figure modified from [Saikrishnan et al., 2012].] **(c)** DNA end resection by AddAB. The protein (1) binds tightly to blunt duplex ends (such as those arising from dsDNA breaks) and (2) starts to move in an ATP-dependent manner. As the motor advances, due to low and unsynchronised nuclease activities, the two single strands may (3) reanneal behind and additional proteins may bind, which uncouples translocation from DNA unwinding. If a Chi sequence is (4) successfully detected, tight binding of the recognition domain shown in (b) to the 5 bp sequence triggers the formation of a 3'-terminated ssDNA loop and couples translocation to unwinding. The resulting overhang is a substrate for proteins such as SSB or RecA, the latter being important for the subsequent steps of dsDNA break repair by homologous recombination. [Figure modified from [Yeeles et al., 2011b].]

the same inverted microscope layout; any further distinctions do not affect temperature calibration inside the fluid chamber. For either MT version, essential parts include (i) a pair of gold-coated, cubic NdFeB magnets (Supermagnete, Germany), (ii) a high-NA oil-immersion objective (Olympus, Japan), and (iii) a CCD (JAI Pulnix, CA, USA) or CMOS (Mikrotron, Germany) camera for video-based position detection under bright-field LED illumination. Table 5.1 contains the exact references and some more details of the main components.

Feature	MT_1	MT_2
Permanent magnets	W-05-G	W-05-N50-G
Magnet orientation	horizontal	vertical
Gap between magnets	$\geq 2\,\mathrm{mm}$	$\approx 0.2\,\mathrm{mm}$
Microscope objective (NA)	PLAPON 60XO (1.42)	UPLSAPO 100XO (1.40)
Video camera (type)	TM-6710CL (CCD)	MC1362 (CMOS)
Maximum frame rate	120 Hz	500 Hz

Table 5.1. Principal differences between both magnetic tweezers (MT) configurations. Switching between them does not compromise temperature measurements inside common flow cells. Permanent cubic magnets have an edge length of 5 mm; reference W-05-N50-G corresponds to an extra high magnetisation. The maximum frame rate indicated refers to the image frequency at full sensor readout.

In analogy to our optical tweezers (OT) cells, MT fluid chambers constitute a sandwich of two #1 coverslips (BB024060A1, Menzel-Gläser, Germany), but with either two (*standard* layout: inner height $\sim 200\,\mu\mathrm{m}$, for temperature calibrations and experiments at 3 pN in MT_1/MT_2) or just one (*thin* layout: inner height $\sim 100\,\mu\mathrm{m}$, for experiments at 3–14 pN in MT_2) layer of plastic paraffin film (Parafilm M, Bemis, WI, USA) in between, creating a single central channel through which the buffer volume flow is controlled via a syringe pump (NE-1000, New Era Pump Systems, NY, USA). Just as for the OT, Parafilm gaskets as well as coverslips with buffer inlets and additional apertures for temperature sensors (see Fig. 5.5b) were prepared with a laser engraver (VLS2.30, Universal Laser Systems, AZ, USA).

In both MT configurations, pulling forces in Z were calibrated[†] with 5–10 % precision at ambient conditions following the procedure explained in Subsect. 2.2.4. Note that, according to the equipartition theorem (Eq. 2.19) and as proven experimentally [Zhang et al., 2012], the obtained values are invariant to temperature changes. To accommodate two heating elements and one permanent temperature sensor to the sample cell holder as shown in Fig. 5.4, an appropriate stainless-steel baseplate was designed and fabricated. Apart from this, the apparatus (in MT_1-configuration) relevant for the measurements shown in this chapter is equivalent to the one used for previous single-molecule studies of AddAB [Carrasco et al., 2013].

5.2.2. Proteins and DNA substrates[‡]

For MT proof-of-principle measurements we used wild-type AddAB proteins that were biotinylated close to the carboxy terminus of the AddA subunit (see Fig. 5.3a/b) and purified as described by Fili and co-workers [Fili et al., 2010]. DNA molecules for MT experiments were fabricated by polymerase chain reaction (PCR) as stated

[†]Calibration measurements for different magnet alignments were performed by César L. Pastrana.
[‡]All proteins and DNA plasmids were provided by Neville Gilhooly and Mark Dillingham.

in Ref. [Carrasco et al., 2013]. Note that, in contrast to the substrates used in OT stretching experiments (see Subsect. 3.2.4), no handles were ligated to the DNA ends because MT experiments at forces below 15 pN can live without enhanced attachment strengths from multiple antibody–antigen interactions; they can be performed just fine with molecules containing *single* biotin and digoxigenin tags only. The results shown in this chapter were obtained with a 7.8 kbp substrate deficient of regulatory *B. subtilis* Chi sites within the first 5 kbp[§] (see Fig. 5.8).

Bulk experiments with the stopped-flow technique (see below) were carried out with wild-type AddAB – purified as described in Ref. [Yeeles et al., 2009] – and DNA substrates based on a plasmid named pSP73-JY0-TFO, which shares the same parent plasmid with DNA molecules used in MT experiments (pSP73-JY0; check the supplementary data of Ref. [Fili et al., 2010] for details of construction). Stopped-flow substrates also lack Chi sequences within the relevant DNA region but contain in addition (at a certain restriction enzyme sequence) an engineered binding site for a third DNA strand – a triplex-forming oligonucleotide (TFO). The final substrate molecules for ensemble measurements were obtained as described in Ref. [Gilhooly and Dillingham, 2014], from linearisation of the purified plasmid by restriction enzyme cleavage and subsequent annealing to a 22-nucleotides(nt)-measuring TFO (5'-TTCTTTTCTTTCTTCTTTCTTT) that was fluorescently labelled with tetramethylrhodamine (TAMRA) at its 5'-end.

5.2.3. Stopped-flow ensemble measurements[¶]

AddAB kinetics were measured in bulk via TFO displacement assays, performed in a stopped-flow fluorimeter (SF-61DX2, TgK Scientific, UK) using slight modifications of previously published methods [Gilhooly and Dillingham, 2014; McClelland et al., 2005]. The TAMRA-labelled triplex – located with its far end at 924 or 2065 bp from the proximal DNA end (compare with Fig. 5.9a) – was excited at a wavelength of 547 nm and the emitted fluorescence signal monitored above 570 nm. Wild-type AddAB (5 nM) was pre-bound to substrate DNA (0.2 nM) in a buffer containing Tris acetate (25 mM, pH 7.5), magnesium acetate (2 mM), dithiothreitol (DTT; 1 mM) and BSA (100 µg/mL). Rapid mixing against a solution of the same buffer containing ATP (1 mM) at time $t_0 = 0$ initiated (synchronous) translocation of a large population of AddAB molecules (note that all concentrations given in this paragraph correspond to the final values after mixing).

The fluorescence increase resulting from (protein-induced) TFO dissociation was recorded at a bandwidth of ~ 1 kHz and the average data from at least three traces fitted to a single exponential function that was offset on the X-axis to define a lag time $t_1 \sim 1$ s before TFO displacement. This value is taken as the sum of the time

[§]This DNA substrate was prepared by Carolina Carrasco.

[¶]Bulk experiments described in this subsection were carried out by Mark Dillingham.

constants for all processes that result in the arrival of the enzyme at the triplex (see Ref. [McClelland et al., 2005] for further details about the method). As translocation initiation events are very brief for AddAB [Gilhooly and Dillingham, 2014; Yeeles et al., 2011b], the distance travelled by the helicase motor from the near DNA end (924 or 2065 bp) divided by the lag time – which decreases with temperature – yields an approximate translocation rate for any given thermal condition. The temperature values stated in Fig. 5.9 correspond to the measurements returned from a circulating water bath that controls the fluorimeter and yields an estimated accuracy of $\pm 0.1\,^{\circ}\mathrm{C}$ (see supplementary data of Ref. [Seidel et al., 2008] for details).

5.3. Theoretical concepts

5.3.1. Corrected temperatures from platinum resistance thermometers

The relationship between resistance R and temperature T (measured in °C) of resistive sensors made of platinum can be expressed by the linear equation

$$R(T) = R(0)(1 + \alpha_{\mathrm{Pt}} T) =: R_{\mathrm{l}}(T)\,, \tag{5.1}$$

where $\alpha_{\mathrm{Pt}} = 3.85 \cdot 10^{-3}/\,^{\circ}\mathrm{C}$ is the standard temperature coefficient of Pt100 devices (with $R(0) \equiv 100\,\Omega$) according to the European industry norm EN 60751, obtained empirically by comparing resistances at $T = 0$ and 100 °C and valid within this limited temperature range [Ehinger et al., 2013].

To correct for non-linearities in the behaviour of the temperature sensor (for $T > 0$) and obtain better results in high-precision measurements, the following quadratic expression, based on an equivalent formulation first introduced by H. L. Callendar more than hundred years ago [Callendar, 1887], can be used:

$$R(T) = R(0)(1 + A_{\mathrm{Pt}} T + B_{\mathrm{Pt}} T^2) =: R_{\mathrm{nl}}(T)\,. \tag{5.2}$$

Here, $A_{\mathrm{Pt}} = 3.9083 \cdot 10^{-3}/\,^{\circ}\mathrm{C}$ and $B_{\mathrm{Pt}} = -5.775 \cdot 10^{-7}/\,^{\circ}\mathrm{C}^2$ are the reference constants according to EN 60751, which again can be derived from separately determined parameters through calibrations at $T = 0$, 100 and e.g. 200 °C, and are valid up to much higher temperatures [Ehinger et al., 2013].

If, as in our case, the temperature is obtained experimentally from a linear expression that relates it directly to the voltage output of a temperature converter (Eq. 5.11), i.e. $T_{\mathrm{meas}} \propto V_{\mathrm{conv}} \propto R_{\mathrm{l}}(T_{\mathrm{meas}})$, a corrected measure T_{corr} in terms of T_{meas} can be obtained by claiming that $R_{\mathrm{l}}(T_{\mathrm{meas}}) \equiv R_{\mathrm{nl}}(T_{\mathrm{corr}})$. From the two previous equations, it then follows that

$$T_{\mathrm{corr}}(T_{\mathrm{meas}}) = \frac{\sqrt{A_{\mathrm{Pt}}^2 + 4B_{\mathrm{Pt}}\alpha_{\mathrm{Pt}} T_{\mathrm{meas}}} - A_{\mathrm{Pt}}}{2B_{\mathrm{Pt}}}\,. \tag{5.3}$$

Both the last formula and Eq. 5.2 are sometimes referred to as the Callendar–van Dusen equation, although – strictly speaking – this name should only be used for a refined version (elaborated by M. S. van Dusen) of the original formulation equivalent to Eq. 5.2 – which is also valid at negative temperatures [McGee, 1988].

5.3.2. Arrhenius kinetics of enzymatic activity

At the end of the 19$^{\text{th}}$ century, based on observations made while studying the acid-induced inversion of sugar, Swedish scientist Svante Arrhenius formulated an empirical equation to describe the temperature dependence of reaction rates k^* [Arrhenius, 1889]:

$$k^*(T) = A^* \cdot \mathrm{e}^{-E_\mathrm{a}/k_\mathrm{B}T} \,. \tag{5.4}$$

Here, A^* is a pre-exponential factor that depends on the nature of the reaction and E_a denotes the so-called activation energy (per molecule), which defines an energetic barrier that needs to be overcome for the reaction to occur. Note that this simple exponential relationship can in principle be used to model any temperature-dependent molecular process that relies on a single rate-limiting step. Note also that, when considering experimental data taken at temperatures within a limited range around ambient conditions, any weak temperature dependences of pre-factor and activation energy can be neglected [Nelson, 2003].

Applying this reasoning to the description of the temperature dependence of motor protein movement along a substrate molecule, the Arrhenius equation can be written as follows:

$$v(T) = v_\infty \cdot \mathrm{e}^{-E_\mathrm{a}/k_\mathrm{B}T} \,, \tag{5.5}$$

where $v(T)$ denotes the protein speed at a certain thermal energy and v_∞ is the hypothetical value for $T \to \infty$. The meaning of this pre-factor becomes clearer if we rearrange the equation such that

$$\frac{v(T)}{v_\infty} = \mathrm{e}^{-E_\mathrm{a}/k_\mathrm{B}T} \propto \mathcal{P}(E_\mathrm{a}) \tag{5.6}$$

and make use of Boltzmann statistics, which says that for a thermally equilibrated system within a heat bath at temperature T, the probability $\mathcal{P}(E_\mathrm{a})$ to encounter a molecule in a state with energy E_a is just proportional to the Boltzmann factor $\exp(-E_\mathrm{a}/k_\mathrm{B}T)$ [Nelson, 2003]. Consequently, the limiting case of $v(T) \to v_\infty$ (in equivalence to $E_\mathrm{a} \to 0$) would comprehend a maximum number of molecules at that energy.

The activation energy barrier can be evaluated from the slope of a linear fit when plotting experimental data as $\ln v(T)$ versus $1/T$ and rewriting Eq. 5.5 as

$$\ln v(T) = -\frac{E_\mathrm{a}}{k_\mathrm{B}} \cdot \frac{1}{T} + \ln v_\infty \,. \tag{5.7}$$

5.3.3. Laminar flow profiles in microfluidic channels

The uniform laminar flow through a practically infinite channel of length l and rectangular cross section ($d \times w$, where d and w are channel height and width, respectively) can be approximated by the same type of flow through a circular tube with hydraulic radius $r_\mathrm{h} := (d \times w)/(d + w)$ [Çengel and Cimbala, 2006]. For our single-channel flow cells with $l \approx 25\,\mathrm{mm}$, $w \approx 7\,\mathrm{mm}$ (see Fig. 5.4) and $d \approx 200\,(100)\,\mu\mathrm{m}$ in standard (thin) layout (see Fig. 5.11b), this corresponds to hydrodynamic radii $r_\mathrm{h} \approx 190\,(100)\,\mu\mathrm{m}$. Note that, if we make use of the formalism introduced in Eq. 4.10 and consider the typical flow rates of $\sim 1\,\mu\mathrm{L/s}$ specified in the next subsections, we can compute a Reynolds number $Re \sim 10$–100, which indeed still corresponds to the laminar regime for the flow through a pipe.

If the coordinate system is defined as in Fig. 5.11b (with $z = 0$ at the lower glass surface), the linear flow velocity profile $u(z)$ along the long axis (X) of the channel obeys the following parabolic equation (far from the entrance):

$$u(z) = u_\mathrm{max} \left(1 - \frac{(r_\mathrm{h} - z)^2}{r_\mathrm{h}^2} \right) , \tag{5.8}$$

where $u_\mathrm{max} = u(r_\mathrm{h})$ denotes the maximum linear velocity encountered at the channel centre. Setting $r' := r_\mathrm{h} - z$ as the radial distance measured from the centreline, the total volume flow rate $\widetilde{Q} := \pi r_\mathrm{h}^2\, \overline{u}$ (where $\overline{u}$ is the average linear flow velocity in the channel) can be recovered by integrating Eq. 5.8 over all cross-sectional surface elements $\mathrm{d}A = 2\pi r' \mathrm{d}r'$ of the tube:

$$\widetilde{Q} = \int_0^{r_\mathrm{h}} u(r')\, 2\pi r' \mathrm{d}r' \underset{(5.8)}{=} \int_0^{r_\mathrm{h}} u_\mathrm{max} \left(1 - \frac{r'^2}{r_\mathrm{h}^2} \right) 2\pi r' \mathrm{d}r' \tag{5.9}$$

$$= 2\pi u_\mathrm{max} \left[\frac{r'^2}{2} - \frac{r'^4}{4 r_\mathrm{h}^2} \right]_0^{r_\mathrm{h}} = \pi r_\mathrm{h}^2\, \frac{u_\mathrm{max}}{2} \,. \tag{5.10}$$

This implies that $u_\mathrm{max} \equiv 2\,\overline{u}$ [Çengel and Cimbala, 2006].

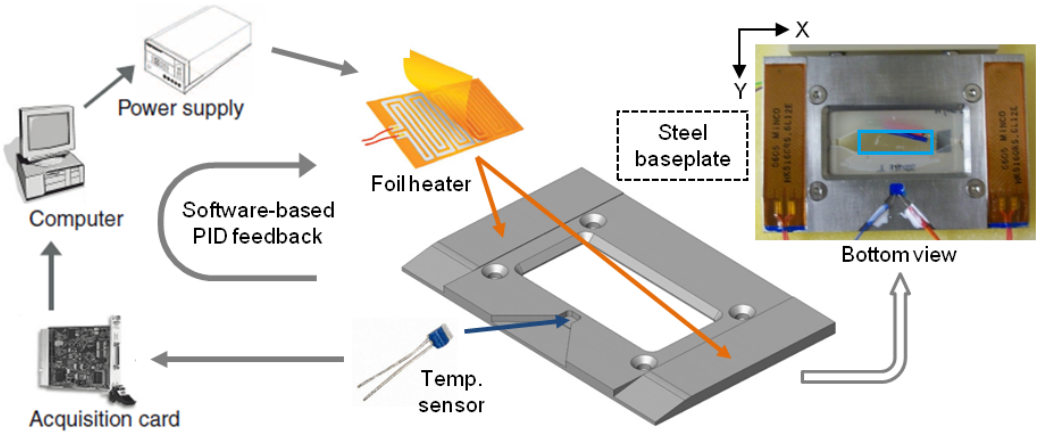

Figure 5.4. Heating circuit of the sample cell holder baseplate. In addition to a heater/sensor pair attached to the microscope objective as introduced in Chap. 3, a second heating assembly is needed to maintain a constant temperature above ambient conditions across the whole MT fluid chamber. The voltage applied to two resistive foil heaters (orange/gold), which are attached close to the edges of the bottom surface of the metal baseplate is modulated according to the signal from a centrally located platinum resistance thermometer (dark blue). The light blue rectangle within the photograph of the sample cell assembled to the baseplate indicates the central channel region ($\sim 25 \times 7\,\mathrm{mm}$) considered for laminar flow velocity calculations (see Subsect. 5.3.3).

5.4. Results and discussion

5.4.1. A bespoke thermostat assembly for MT-type instruments[‖]

We implemented a macroscopic thermal control unit in a widely used MT setup based on an inverted microscope. To study the behaviour of individual protein–DNA constructs between room temperature and 40 °C without compromising the functionality of the MT, we combined thin heating foil elements and resistive temperature sensors both at the objective (similar to how it is done in our OT apparatus, see Subsect. 3.4.9) and underneath the baseplate of the sample cell holder. As described in Chap. 3, this strategy relies on an approach originally proposed by Mahamdeh and Schäffer to reduce laser-induced drift in OT [Mahamdeh and Schäffer, 2009].

Essential components of the stabilised heating circuits

Similar to how it was done in our OT instrument and as shown in Figs. 5.4 and 5.5a, polyimide foil heaters (Minco, France) were attached to the barrel of the MT oil-immersion objective (Heater 1: resistance $R_1 = 33.9\,\Omega$) and the bottom of the tailor-made stainless steel baseplate (Heaters 2a/b: resistance $R_2 = R_{2a} + R_{2b} =$

[‖]Part of the results shown in this and the following two subsections was accomplished with the help from Francesca Zuttion.

$2 \cdot 5.6\,\Omega = 11.2\,\Omega$) with silicone stretch tape (Minco) and pressure-sensitive adhesive (Minco), respectively. The heating foils were connected to the voltage outputs of two programmable power supply units (Thurlby Thandar Instruments, UK) with a resolution of 1 mV, controlled by a computer via USB. Resistive platinum (Pt100) temperature detectors (Correge, France) with a precision of $\pm\,0.04\,\Omega$ ($\widehat{=}\,\pm 0.01\,°\mathrm{C}$) were fixed to objective and baseplate via thermally conductive double-sided adhesive tape (Thorlabs, NJ, USA) and thermally conductive epoxy (Minco), respectively.

To compensate for measurement errors due to lead resistances, each Pt100 sensor was connected to the readout electronics in a three-wire configuration, i.e. one of the two sensor legs was soldered to two wires (with all three of them having the same length). This way, the resistance contribution from the wires could be subtracted from the total value, yielding the resistance corresponding to the active sensor region only (for more details, see Refs. [McGee, 1988; Zuttion, 2013]). We used commercial temperature converters (Brodersen, Denmark), which provided a voltage signal of the following type for each thermometer:

$$V_{\mathrm{conv}} = \frac{T_{\mathrm{meas}} + 50\,°\mathrm{C}}{15\,°\mathrm{C/V}}\,, \tag{5.11}$$

with $0 \leq V_{\mathrm{conv}} \leq 10\,\mathrm{V}$ corresponding to a maximum temperature range of $-50 \leq T_{\mathrm{meas}} \leq 100\,°\mathrm{C}$. For accurate temperature readings, we first had to adjust offset and gain for the system to return the desired voltages at two reference temperatures, for which we chose the melting and boiling points of (deionised) water. It is important to check if all components – in particular any thin wires/cables – can bear such a large temperature range. The voltage signals were subsequently fed into an external data acquisition (DAQ) module (National Instruments, TX, USA) that was connected to the computer by USB. Table A.2 in the appendix contains the exact references of – and more details about – the most relevant components used for the heating circuits.

Signal processing and PID feedback

Temperature data were acquired and processed, and heating foil voltages updated at a frequency of 2 Hz by means of customised software developed in LabVIEW (National Instruments). The control algorithm contains two standard PID controllers – equivalent to the ones used in our OT (see Subsect. 3.3.2) – working in parallel, one for each heating circuit. We applied Eq. 5.3 to the acquired temperatures to correct for non-linearities in the $R(T)$-response of the Pt100 thermometers. Sensitivities s (in $\mathrm{V}^2/°\mathrm{C}$) for calculating the initial voltage setpoints delivered to the power supplies were determined offline by independently raising the voltage of each heater circuit stepwise and annotating the mean equilibrated temperature at least 40 minutes after each step (Fig. 5.6a). To check for repeatability, we lowered the voltage in the same way afterwards, which gave rise to equivalent temperature values. The conversion factors s' (in $\mathrm{V}/°\mathrm{C}$), actually used to quantify the voltage corrections during continuous PID

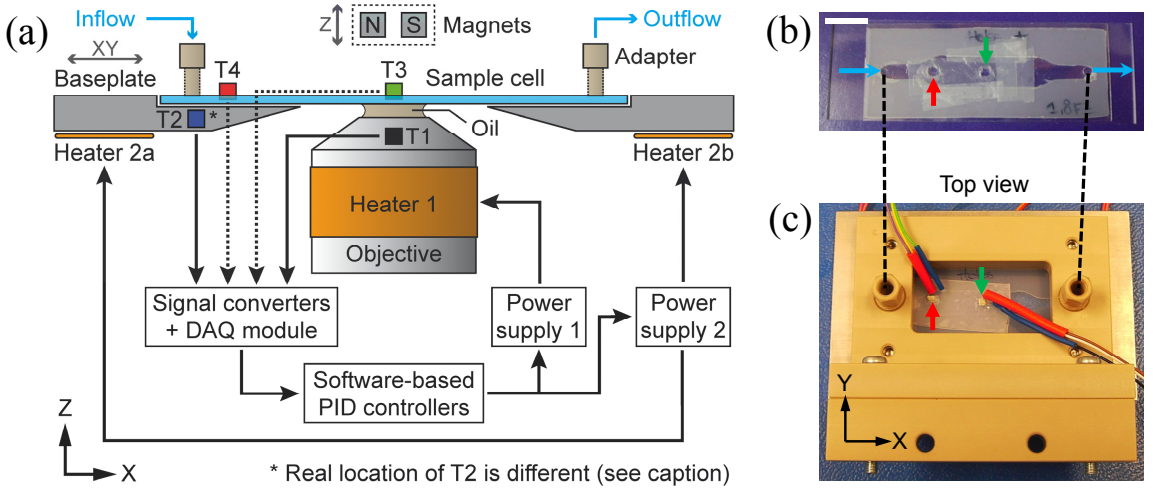

Figure 5.5. Thermal control system for magnetic tweezers (MT) experiments. **(a)** Schematic of the thermostated inverted microscope (*side view*). The setup contains one resistive heating foil (Heater 1) around the objective barrel and another two (Heaters 2a/b, connected in series) underneath the baseplate (represented in cross-sectional view) as indicated in Fig. 5.4. Up to four Pt100 sensors (T1–T4) probe different temperatures that are subsequently converted into voltages and digitised by a DAQ unit. T1 (black) and T2 (blue) are permanently fixed and provide the signals for two separate PID feedbacks, which control the voltage applied to the heating foils of each circuit via programmable power supply units. The real location of T2 is as shown in Fig. 5.4. T3 (green) and T4 (red) are attached only for calibrating the buffer temperature inside a modified flow cell, as described in (b)/(c). **(b)** Picture of a single-channel sample chamber (*top view*) assembled from two layers of Parafilm spacers sandwiched between two cover glasses, with additional apertures to calibrate the buffer temperature near centre (green arrow) and inlet (red arrow). Parafilm pieces for sealing are visible on top. The flow direction is as in (a) and indicated by the blue arrows. The white scale bar represents 1 cm. **(c)** The complete sample cell assembly ready for temperature calibration. The fluid chamber from (b) now sits between the baseplate and a top part made of polyether ether ketone (PEEK). Arrows indicate sensor T3 (green) and T4 (red), both contacting the buffer and sealed from the outside with Parafilm and vacuum grease.

feedback, were optimised empirically online. The proportional (K_P), integral (K_I) and derivative (K_D) gains were tuned according to the Ziegler–Nichols step response (open-loop) and frequency response (closed-loop) methods (see Refs. [Åström and Hägglund, 1995; Zuttion, 2013] for details). Our best feedback parameters yielded system performances as shown in Fig. 5.6b. In general, K_P and K_I had to be chosen small with respect to K_D in order to partially compensate for the significant delays due to conduction of thermal energy from the heat sources to the sensing thermometers, located at a considerable distance.

5.4.2. Performance of heating/heat-sensing elements

Linear measurement range and heating efficiency

The thin-foil heater circuits showed ohmic behaviour up to $\sim 40\,^{\circ}\mathrm{C}$ (grey-shaded area in Fig. 5.6a): the observed temperatures increased linearly with the heating power according to Joule's first law:

$$P_{\mathrm{heat}} = I^2 R \underset{(\mathrm{Ohm})}{=} \frac{V^2}{R}\,, \tag{5.12}$$

where V is the voltage drop across, I the current going through, and R the resistance of the heating element(s); "Ohm" indicates the validity of Ohm's law, i.e. $I = V/R$. Above $40\,^{\circ}\mathrm{C}$, baseplate temperatures presented an apparent departure from Joule heating and adjusted to a polynomial function of heating power rather than to the ideal straight line (see Fig. 5.6a). This nonlinear response – which becomes significant for temperatures $\geq 45\,^{\circ}\mathrm{C}$ not addressed during MT experiments – originates most likely from increased heat dissipation to the surroundings: even though the baseplate is physically disconnected from other (metallic) microscope components, its bottom surface with the attached heating elements (see Fig. 5.4) floats only $\sim 1\,\mathrm{mm}$ above a large aluminium breadboard. An additional layer of thermally insulating material would be difficult to implement due to space restrictions. In any case, when used simultaneously, the setpoints of both temperature control circuits never exceeded $43\,^{\circ}\mathrm{C}$. Note that this makes other potentially detrimental effects such as self-heating of the Pt100 sensors or nonlinear IV-characteristics of the foil heaters negligible.

As far as an effectiveness of objective and baseplate heating is concerned, the initial calibration of sensitivities s (see Fig. 5.6a) resulted in a roughly four-times higher value for the Heater 1 circuit in comparison with Heaters 2a/b (which are connected in series), with a resistance ratio of $R_1/R_2 = 33.9\,\Omega/11.2\,\Omega \approx 3$. Neglecting other losses, this leads to effective heating powers per unit temperature of $P_{\mathrm{eff.heat1}} = s_1/R_1 \approx 130\,\mathrm{mW/^{\circ}C}$ and $P_{\mathrm{eff.heat2}} = s_2/R_2 \approx 90\,\mathrm{mW/^{\circ}C}$, respectively, showing that in our configuration baseplate heating is slightly more efficient than objective heating in terms of the dissipated thermal energy per time and temperature interval.

Step response and upper temperature limit

As practically all macroscopic techniques, our temperature control method requires relatively long stabilisation times, in particular when lowering a previously raised setpoint. Note that the objective – aside from the baseplate (see above) – is not thermally isolated from the rest of the microscope. Without any active cooling mechanism, the use of plastic spacers for instance may reduce temperature fluctuations [Maloney et al., 2011] but normally leads to additional, undesired delays during relaxation [Mahamdeh and Schäffer, 2009]. Apart from that, due to inevitable signal oscillations after a

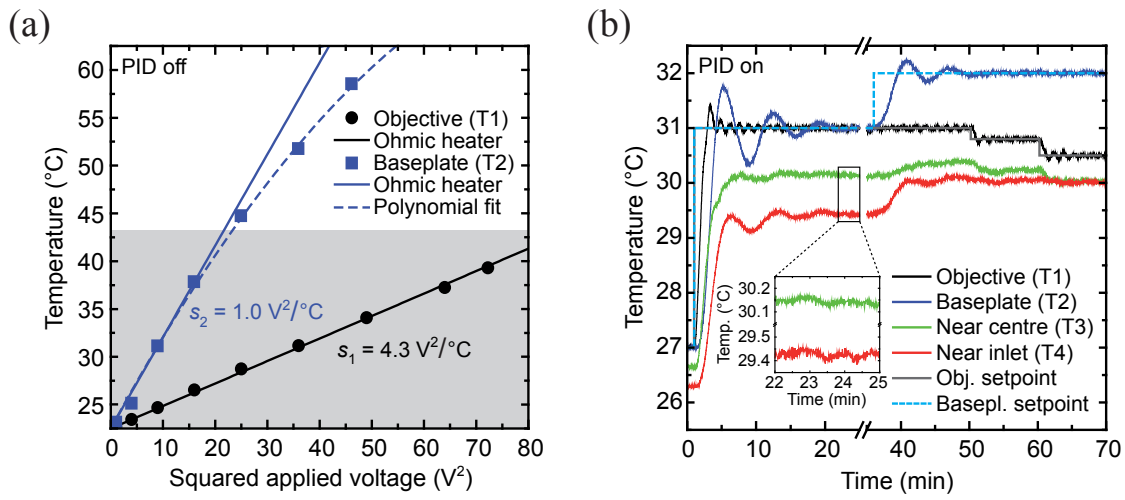

Figure 5.6. Evaluation of heater sensitivities and PID control performance. **(a)** Dependences of stationary objective (black: Heater 1 ↔ T1) and baseplate (blue: Heaters 2a/b ↔ T2) temperatures as functions of the applied heating power $P_{\text{heat}} \propto V^2$ (without feedback). Sensitivities s can be considered valid within a feasible measurement range up to ∼43 °C (inside the grey-shaded area), which corresponds to $\Delta T \approx 20$ °C above room temperature. **(b)** After a typical setpoint change (27 → 31 °C), the step response with PID feedback is monitored using all four Pt100 sensors (*before axis break*). Past ∼20 min, the temperature inside the sample cell stabilises to ±0.1 °C of precision or better (*inset*) and can be kept at this level for hours. Convenient adjustments of objective (grey) and baseplate (cyan) setpoints yield similar temperatures near centre (green) and inlet (red) of the sample cell (*after axis break*).

significant setpoint change (see Fig. 5.6b), our system is most useful for measurements at constant temperatures. To account for these issues, one might place the whole apparatus in a refrigerated environment, which is hardly possible in our case, or use a better heat conductor for the baseplate. We chose stainless steel as the preferred compound because its superior chemical resistance and mechanical stability outweighs the only modest thermal conductivity when compared to e.g. aluminium.

The upper temperature limit (∼40 °C) inside the fluid chamber derives from the maximum value that we considered for safe operation of our oil-immersion objective (43 °C) after having consulted the manufacturer and taking into account initial temperature overshoots. It has been shown that higher values are possible [Galburt et al., 2014], but since (long-term) detrimental effects on the equipment can no longer be excluded [Bioptechs Inc., 2001], we do not advocate setpoints above 43 °C. The lower boundary is given by the temperature in the laboratory (kept constant at 24.5±1.5 °C), resulting in a measurement interval that is sufficient for studying the activity of proteins from most mesophilic organisms. In experiments that necessitate a broader temperature range, values below ambient conditions, fast temperature changes or defined gradients, other strategies of thermal control may be preferred (see Subsect. 5.1.1).

However, one key advantage of MT assays addressing large areas of the fluid chamber

surface is that they are able to follow many activities in parallel [de Vlaminck et al., 2011; Ribeck and Saleh, 2008], which favours macroscopic temperature management. This also implies that, even if we could actively lower the temperature of our setup and accelerate its step response, the time needed to reach stability in single-molecule trials would still be determined by thermal equilibration within the relevant chamber regions – achieved when no more significant drift is observed on the camera image.

Thermal stability

After optimisation of the PID gains (see Subsect. 5.4.1), the system achieved at least 0.1 °C of precision – a value that could be maintained during the whole day if necessary – within less than half an hour upon a considerable temperature setpoint change (see inset of Fig. 5.6b). Despite a slower response and larger initial overshoots, baseplate temperatures always stabilised to the noise level of objective temperatures within the same amount of time (Fig. 5.6b, before axis break). Thermometers T3 and T4 (in contact with the buffer solution) depicted values that were in general lower than those of T1 and T2 and normally unlike, but which could be balanced by adjusting the setpoints conveniently. Besides, the heating circuits showed little cross-talk, i.e. objective (baseplate) heating mainly influenced sensor T3 (T4) – provided the setpoints were close to each other (Fig. 5.6b, after axis break).

5.4.3. Buffer temperature calibrations

Experimental procedure

Using a modified fluid chamber with extra apertures in the top cover glass, we could integrate two additional thermometers for probing the buffer temperature directly and in this way calibrate a homogeneous temperature profile throughout the flow cell. For all such measurements, the sample stage was centred in XY as represented in Fig. 5.5a. We located auxiliary Parafilm pieces with rectangular apertures of the size of the Pt100 temperature sensors onto a fluid chamber with extra openings of slightly larger dimensions near channel centre and inlet (see Fig. 5.5b/c). With the help of some vacuum grease we could thus establish a leak-free seal for thermometers T3 and T4 to probe the temperature inside the chamber without touching the lower coverslip. The ambient temperature during all measurements lay in the range of 23–26 °C. To determine the heat transfer efficiencies between objective (baseplate) and sample cell centre (edges), equal pairs of at least four increasing setpoints between 27 and 39 °C were applied to the two heating circuits and sensors T3 and T4 monitored with the buffer at rest (Fig. 5.7a). To rule out any hysteresis effects, we decreased the setpoints afterwards, which resulted in similar temperature readings (data not shown). Subsequently, the corrected setpoints yielding equivalent thermal conditions near centre and inlet were checked for accuracy within a range of 25–41 °C by collecting data from several fluid chambers under different buffer flow conditions (Fig. 5.7b).

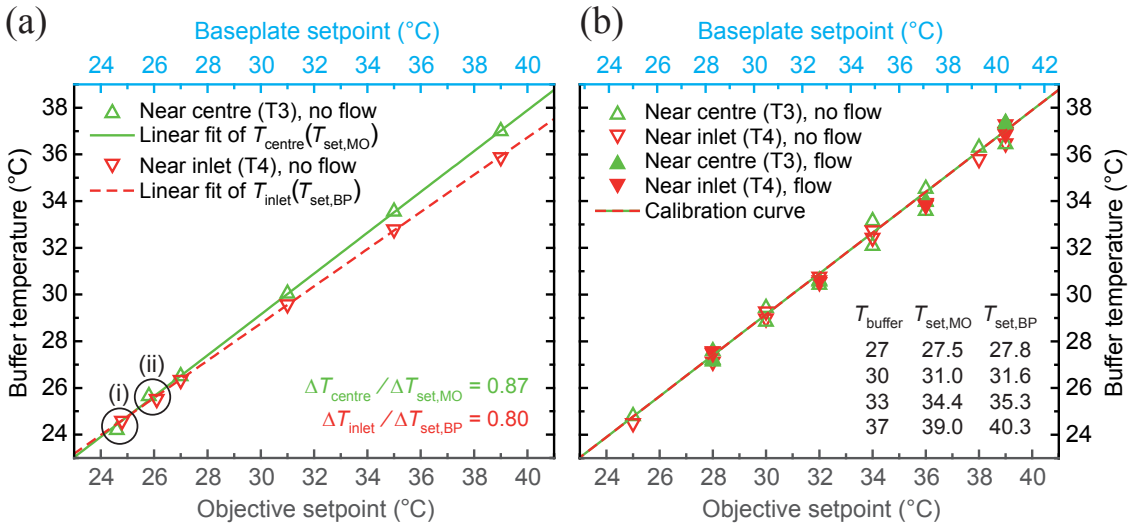

Figure 5.7. Calibration of the buffer temperature for single-molecule studies. **(a)** Heat transduction from the outside to the inside of the sample cell is sensed near centre (T_{centre}, green) and inlet (T_{inlet}, red) by setting objective ($T_{\mathrm{set,MO}}$, grey) and baseplate ($T_{\mathrm{set,BP}}$, cyan) to equivalent temperatures. Highlighted data points correspond to ambient conditions (no heating/feedback) before (i) and after (ii) addressing setpoints $T_{\mathrm{set,MO}} \equiv T_{\mathrm{set,BP}} \in [27\,^{\circ}\mathrm{C}, 39\,^{\circ}\mathrm{C}]$. Linear fits correspond to independent heat transfer efficiencies of around 87 and 80 % for objective and baseplate, respectively. **(b)** Based on the straight lines in (a), the condition $T_{\mathrm{centre}} \equiv T_{\mathrm{inlet}}$ defines an optimum relation between $T_{\mathrm{set,MO}}$ and $T_{\mathrm{set,BP}}$: adjusting the baseplate setpoints while keeping the objective values fixed, all temperatures measured inside the flow cell – even with a constant flow velocity of $\sim$1 µL/s – now fall onto a linear calibration curve (green/red, valid for $T_{\mathrm{ambient}} \geq 23\,^{\circ}\mathrm{C}$). A small table with characteristic buffer temperatures and typically required setpoints is shown as an inset.

Heat transfer relationships

For an experimental configuration as in Fig. 5.5a and equal setpoints T_{set}, the two heat transfer processes – (i) from the objective (MO) via the immersion oil drop towards the sample cell centre and (ii) from the baseplate (BP) towards the sample cell edges (near buffer in-/outlet) – satisfied slightly differing linear relations

$$T_{\mathrm{sense}}(T_{\mathrm{set}}) = \eta_{\mathrm{trans}} \cdot T_{\mathrm{set}} + T_0\,, \tag{5.13}$$

where T_{sense} corresponds to the temperature measured inside the flow cell (with $T_{\mathrm{ambient}} \leq T_{\mathrm{sense}} \leq T_{\mathrm{set}}$), η_{trans} defines a thermal transfer efficiency and T_0 denotes a hypothetical temperature for $T_{\mathrm{set}} = 0\,^{\circ}\mathrm{C}$. Assuming negligible mutual influence of the two heating circuits – in accordance with the results shown in Fig. 5.6b – we obtained two representative, phenomenological equations that fitted the data of our system:

$$T_{\text{centre}} = 0.875 \cdot T_{\text{set,MO}} + 2.91\,^{\circ}\text{C}\,, \tag{5.14}$$

$$T_{\text{inlet}} = 0.796 \cdot T_{\text{set,BP}} + 4.87\,^{\circ}\text{C}\,. \tag{5.15}$$

These straight lines intersect at a temperature of about 25 °C, close to the mean room temperature during the calibrations (see Fig. 5.7a). To minimise any gradient across the long direction (X) of the fluid chamber, we imposed the condition $T_{\text{centre}} \equiv T_{\text{inlet}} \equiv T_{\text{buffer}}$. From the linear fits above, simple arithmetic then leads to the following desired relation between objective and baseplate setpoint:

$$T_{\text{set,BP}} \equiv 1.098 \cdot T_{\text{set,MO}} - 2.46\,^{\circ}\text{C}\,, \tag{5.16}$$

Adjusting $T_{\text{set,BP}}$ relative to $T_{\text{set,MO}}$ accordingly, measurements corresponding to equivalent setpoint combinations – but performed on various days or with different sample cells – resulted in similar temperatures inside the fluid chamber with a typical repeatability of ±0.5 °C (see Fig. 5.7b).

Validity of the calibrated parameters

Ideally, the temperature inside the sample cell should be tracked at all times. In our case, attaching the thermometers as shown in Fig. 5.5c while performing MT experiments would however affect the optical image essential for accurate position detection. Conversely, the introduction of an appropriate sensor into the fluid chamber from the side would require further changes to the holder parts, potentially change chamber thickness, and ultimately make sample preparation more complicated – thus reducing the throughput of experiments. Fortunately, due to the small channel height of our sample cells (100–200 µm, see Fig.5.8a), we can assume that single-molecule measurements conducted a few micrometres above the lower coverslip surface are subject to the thermal settings calibrated beforehand.

Still, the results presented in Fig. 5.7 are only accurate for a specific configuration of the inverted microscope: the setpoints to achieve a certain temperature inside the fluid chamber depend on the thermal profiles of objective and sample cell holder, apart from the exact XY-positions of thermometers T3 and T4 relative to the immersion oil drop. After a substantial change of any of these parameters the temperature calibration procedure should therefore be repeated. On this account, the confidence intervals of ±0.5 °C extracted from Fig. 5.7b do include uncertainties due to (i) changes in the XY-position of the sample stage relative to the objective during consecutive experiments with different fluid chambers and (ii) variations in the experimental conditions when comparing data acquired on various days. In summary, we can safely say that our system works properly without direct monitoring of the buffer temperature during single-molecule experiments.

Please note as well that our values of thermal precision ($\sim 0.1\,^{\circ}\mathrm{C}$) and accuracy ($\sim 0.5\,^{\circ}\mathrm{C}$) are comparable to those obtained in other recently described single-molecule microscopes with macroscopic temperature control [Stephenson et al., 2014; Zhang et al., 2012], whose specific realisations are however completely different and not easily compatible with our type of MT apparatus.

5.4.4. Probing thermally sensitive single-molecule activity

To test-drive our newly implemented thermostat assembly, we made use of a well-established MT assay with the ATP-dependent helicase–nuclease AddAB from *B. subtilis* (see Subsects. 5.1.3 and 5.2.2) [Carrasco et al., 2013]. In order to gain deeper knowledge about the kinetic parameters that define the coupled unwinding and translocation activities of this enzymatic model system, we compared results from MT experiments at several temperatures** with data obtained from stopped-flow bulk measurements under equivalent conditions and using related DNA substrates (see Subsects. 5.2.2 and 5.2.3).

Magnetic tweezers assay for translocation experiments

At a stabilised buffer temperature inside the flow cell, we first bound biotinylated AddAB enzymes (Bio-AddAB) to 7.8 kbp DNA substrates (see Subsect. 5.2.2) and streptavidin (SA)-coated superparamagnetic microspheres of 1 µm in diameter (MyOne Dynabeads, Invitrogen, CA, USA). Subsequently, these bead–protein–DNA constructs were introduced in a flow cell functionalised with anti-digoxigenin (Anti-Dig), so that upon application of the magnetic field, the protein remained tethered between microsphere and coverslip surface via *single* B(io)–SA and D(ig)–Anti-Dig interactions, respectively (see Fig. 5.8a).

An identical bead, firmly attached to the glass surface via unspecific DNA-mediated interactions, acted as a reference for inferring Z-positions of AddAB from microsphere height differences (as introduced in Subsect. 2.3.1) at a constant camera frame rate of 60 Hz in both MT configurations (spatial resolution $\sim$5–10 nm at 3 pN of force). For all single-molecule measurements, the reaction buffer was equivalent to the one used in bulk experiments (see Subsect. 5.2.3) and included Tris acetate (25 mM, pH 7.5), magnesium acetate (2 mM), and DTT (1 mM); ATP (1 or 4 mM) was added to start AddAB activity. The assays shown herein were carried out in a constant flow of (preheated) buffer at 65 µL/min $\approx$ 1 µL/s (a compromise ensuring reliable video tracking at sufficiently short reaction onset times) and with a pulling force F_{MT} between 3 and 14 pN.

**All MT measurements with AddAB proteins were carried out by Carolina Carrasco.

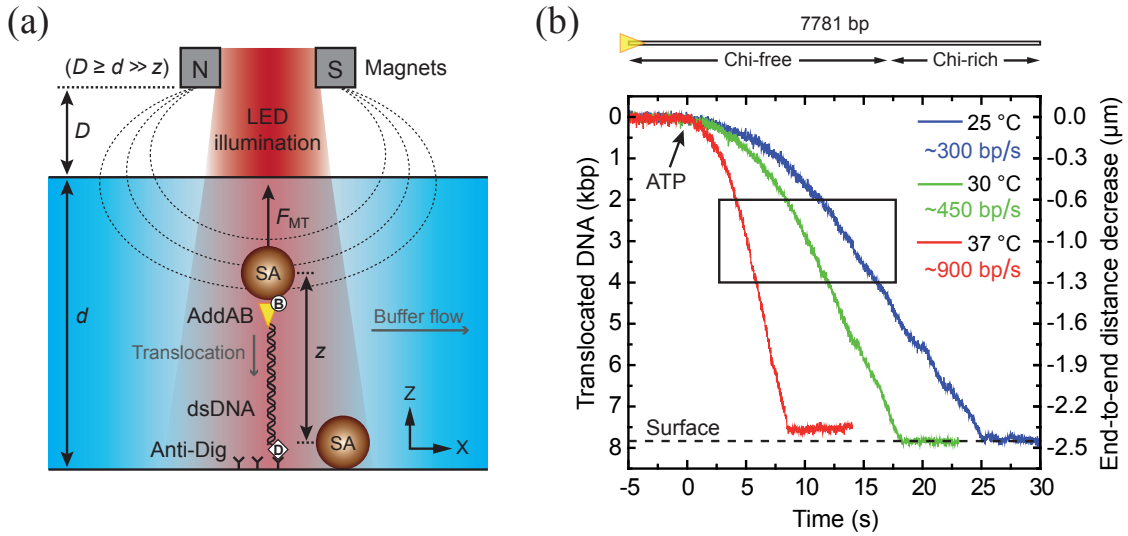

Figure 5.8. Proof-of-principle measurements with the AddAB helicase–nuclease. **(a)** Schematic view (*not to scale*) of the experimental configuration in the magnetic tweezers microscope. As introduced in Sect. 2.2, a pair of permanent magnets at a distance D above the flow cell (thickness d) exerts a constant pulling force F_{MT} on superparamagnetic microspheres in solution. Bio-AddAB can link a SA-coated bead to the coverslip via a dsDNA molecule as described in the text. Partial stretching of the tether defines an end-to-end distance z, measured as the height with respect to a bead on the surface. Flushing buffer with ATP starts translocation. **(b)** Three examples of time traces (taken at $F_{\mathrm{MT}} = 3\,\mathrm{pN}$ and 1 mM ATP) showing the movement of individual AddAB molecules along a 7.8 kbp DNA substrate devoid of Chi sites within the first 5 kbp, as measured with our thermally controlled MT. Time $t_0 \approx 0$ denotes the apparent arrival of ATP at the enzyme. As AddAB is not necessarily attached to the "south pole" of the sphere (which is not free to rotate), not all traces correspond to the maximum z-range. The black rectangle indicates the substrate region (2–4 kbp) considered for the analysis of instantaneous velocities (see Fig. 5.10).

Corrections of data acquired at different thermal conditions

From single-molecule translocation measurements, time-dependent position traces as shown in Fig. 5.8b were obtained. Conversion of the raw distance data given in micrometres to kilo-base-pairs of DNA was performed through division by the factor $\mathcal{K}$ (in nm/bp), defined in Eq. 2.25 according to the inextensible worm-like chain model. This implies that the temperature dependences of fractional extension z/L_0 and persistence length L_{p} of the molecule have to be taken into account. These can be most easily addressed when considering the following formula [Marko and Siggia, 1995], which – to a first approximation – can be considered the inverse function of Eq. 2.24 and is valid up to $\sim 10\,\mathrm{pN}$ [Hormeño et al., 2012]:

$$z(F) = L_0 \left[1 - \frac{1}{2} \left(\frac{k_{\mathrm{B}} T}{F L_{\mathrm{p}}} \right)^{1/2} \right] . \tag{5.17}$$

T (°C)	L_p (nm)	z/L_0	$\mathcal{K}$ (nm/bp)	$\mathcal{K}/\mathcal{K}(25\,^\circ\mathrm{C})$
24–25	48	0.9229	0.3138	1.0000
27–28	47	0.9212	0.3132	0.9981
30	46	0.9185	0.3123	0.9952
33	45	0.9156	0.3113	0.9919
37	44	0.9109	0.3097	0.9871

Table 5.2. Temperature dependence of rise-per-bp factor $\mathcal{K}$ at 3 pN of force. The chosen temperature values correspond to MT measurements with AddAB. The dependence of the persistence length was approximated by a linear interpolation between experimentally obtained $L_\mathrm{p}(25\,^\circ\mathrm{C})$ and estimated $L_\mathrm{p}(37\,^\circ\mathrm{C})$.

We can see that z/L_0 depends on the temperature directly and through L_p: $z(T) \propto \sqrt{T/L_\mathrm{p}(T)}$ (note that $F \equiv F_\mathrm{MT} = \text{const.}$ and T is the absolute value given in kelvins). For the dependence of the persistence length, we considered the data presented in Ref. [Geggier et al., 2011] and assumed a linear decrease of L_p (by $\sim 10\,\%$ relative to the value measured at ambient conditions) when increasing the temperature from $T_\mathrm{i} = 25\,^\circ\mathrm{C} \approx 298\,\mathrm{K}$ to $T_\mathrm{f} = 37\,^\circ\mathrm{C} \approx 310\,\mathrm{K}$. Table 5.2 contains representative dependences of L_p, z/L_0 and $\mathcal{K}$ we used for processing MT data obtained when applying a force $F_\mathrm{MT} = 3\,\mathrm{pN}$. It is worth noting that values of $\mathcal{K}(T)$ change by less than 2 % across the whole temperature range.

5.4.5. Temperature dependence of DNA translocation by AddAB

We applied the MT microscope with thermal control unit to investigate AddAB helicase activity at various temperatures (Fig. 5.8a). Traces recorded between 24 and 37 °C (at 3 pN of load applied on the protein) presented common features such as an onset phase due to ATP influx and occasional slowdowns at characteristic positions, corresponding to Chi sequences located beyond the initial 5 kbp (Fig. 5.8b).

Comparison of mean translocation rates and activation energies

Average single-molecule velocities of AddAB were determined from derivatives of corrected position traces, previously smoothed from 60 to 3 Hz of bandwidth – without taking into account the early ATP gradient interval (the first 5–10 s in Fig. 5.8b) and random pauses (if any) of the enzyme along its track.

Raising the temperature from ambient to physiological conditions increased the mean speed v_MT about threefold (see Figs. 5.8b and 5.9a). An exponential fit defined by the Arrhenius equation (Eq. 5.5, with E_a representing the activation energy barrier of coupled unwinding and translocation) yielded a temperature coefficient $Q_{10} := v_\mathrm{MT}(T+10\,^\circ\mathrm{C})/v_\mathrm{MT}(T) \approx 2$. This parameter remained valid for the equivalent fits of translocation rates v_bulk obtained from two different stopped-flow fluorimetry data sets (see Fig. 5.9a and Subsect. 5.2.3).

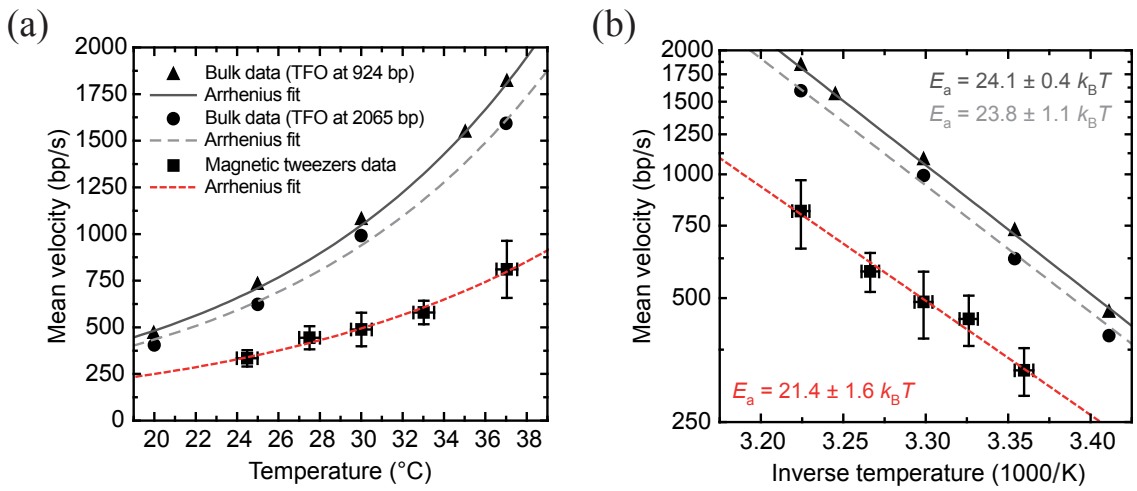

Figure 5.9. Average translocation velocities of AddAB at different temperatures. **(a)** Single-molecule MT experiments at 3 pN are compared with two data sets from stopped-flow bulk measurements relying on different DNA substrates – with fluorescently labelled triplex-forming oligonucleotides (TFOs) located at distinct positions from the near DNA end. All data were acquired with 1 mM of ATP in the reaction buffer and could be fitted by the Arrhenius relation (Eq. 5.5). Error bars of single-molecule results in Y and X represent the standard deviation of the velocity and the accuracy in temperature (±0.5 °C), respectively, the latter being estimated from the typical spread in Fig. 5.7b. For the ensemble measurements, uncertainties in temperature and velocity correspond to the symbol size. **(b)** Arrhenius plots according to Eq. 5.7 of the results presented in (a): the exponential fits now show as straight lines with systematic offset but similar slopes, representing comparable activation energies $E_a \approx 21$–$24\,k_BT$. Uncertainties of E_a correspond to the standard errors returned from the fits; all remaining errors are as in (a).

Re-plotting of the dependencies in a semi-logarithmic representation given by Eq. 5.7 shed light on (i) a systematic difference corresponding to $v_{bulk}(T) \approx 2 \cdot v_{MT}(T)$ when comparing the average single-molecule and bulk velocities obtained under equal volumetric ATP conditions, and – at the same time – (ii) activation energy constants of 21 ± 2 and $24 \pm 1\,k_BT$ (equivalent to values around 52 and 59 kJ/mol, or 12 and 14 kcal/mol), respectively, which were similar within experimental error (Fig. 5.9b).

Note that none of the shown fits are error-weighted because the scattering of the mean rate values contributes more than the standard error of the mean at each temperature [Seidel et al., 2008]. Indeed, applying e.g. a statistical error weight to the single-molecule data does not change the corresponding fit significantly. On the other hand, a Gaussian uncertainty propagation for $E_a(v(T), T)$ according to Eq. 5.7 adds at most another $\pm 0.2\,k_BT$ to the total error (data not shown). Consequently, the overall uncertainties of E_a consist for the most part of the standard errors returned from the fitting routines. These comprise (i) random error sources apart from temperature fluctuations that may play a role in stopped-flow measurements [Seidel et al., 2008]

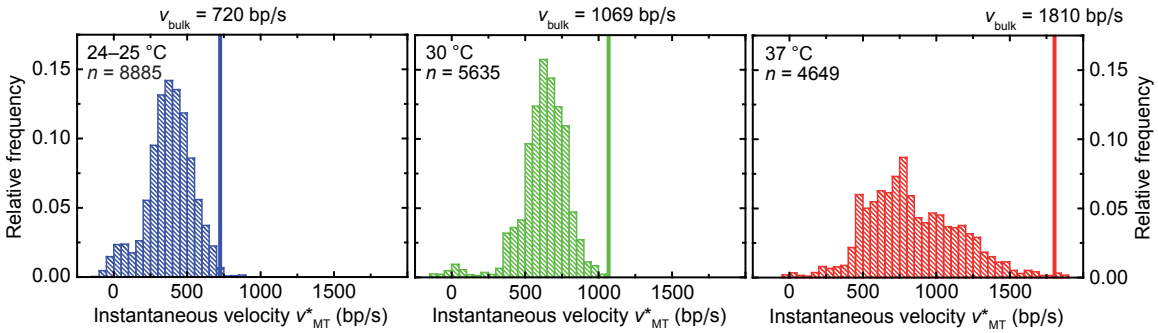

Figure 5.10. Instantaneous translocation velocities of AddAB according to magnetic tweezers (MT) data at 3 pN of force. Considering the region between 2 and 4 kbp from the proximal end of the 7.8 kbp DNA substrate used in single-molecule assays (black rectangle in Fig. 5.8b), instantaneous rates v^*_{MT} derived from translocation traces (n = total number of respective rate values) at 24–25 (blue), 30 (green) and 37 °C (red) are accumulated in histograms. Static and dynamic disorder among the proteins determine the broadened shape of the resulting distributions [Carrasco et al., 2013]. Random pauses corresponding to rate values close to zero mainly occur at lower temperatures. Mean velocities v_{bulk} from stopped-flow experiments (TFO at 924 bp) are represented by straight vertical lines and located close to the highest instantaneous rates.

and (ii) intrinsic heterogeneities among the set of individually studied molecules that primarily determine the stochastic uncertainty in MT experiments [Carrasco et al., 2013]. Slight variations in the protocols used for different bulk assays (see Subsect. 5.2.3) can most likely explain the small offset between the two stopped-flow data sets.

Analysis of instantaneous translocation speeds

We performed a detailed analysis of instantaneous single-molecule velocities of AddAB v^*_{MT} along a 2-kbp-long section of all translocation traces. To obtain the histograms – corresponding to measurements at 3 pN and three different temperatures – shown in Fig. 5.10, the interval ∼ 2001–4000 bp from the proximal end of the 7.8 kbp DNA substrate was chosen because it provided maximum statistics within a region after the initial ATP concentration rise and prior to any individual Chi sites (see Fig. 5.8b).

The shape of the accomplished distributions was in accordance with previously obtained results of DNA translocation by AddAB [Carrasco et al., 2013]. Furthermore, the analysis revealed an overlap of average ensemble rates $v_{\mathrm{bulk}}(T)$ plotted in Fig. 5.9 (measured by stopped-flow in combination with triplex displacement assays, see Subsect. 5.2.3), with the high-velocity tails of the v^*_{MT}-histograms. This shows that at all thermal conditions studied, the enzyme is at least transiently able to move at the speed assessed in bulk.

5.4.6. Control experiments to elucidate the origin of rate differences

In principle, one might attribute the rather systematic discrepancy between absolute helicase speeds measured at equivalent temperatures in single-molecule and bulk experiments to two features of the MT assay that do not apply to the stopped-flow technique: (i) a thousandfold larger microsphere directly attached to the biotinylated AddAB complex and (ii) a constant upwards-directed force applied by the magnets (see Fig. 5.8a).

Bead-induced effects are negligible

With respect to the microsphere argument, as previously determined by MT in our laboratory, the use of an alternative version of biotinylated AddAB – with a longer linker between protein motor and biotin tag peptide sequence – gave rise to identical results in control experiments [Carrasco et al., 2013]. This excludes a steric hindrance effect of the magnetic bead on the motor for the data presented in this thesis. In addition, if the protein moves at a maximum speed of $\sim 1\,\mathrm{kbp/s} \approx 0.3\mu\mathrm{m/s}$, it only feels an insignificant drag force of $\sim 0.003\,\mathrm{pN}$ induced by the sphere. Likewise, the lateral drag caused by the laminar flow of buffer close to the coverslip surface is too small to have any impact.

Incrementing the force hardly influences AddAB activity

To check for a potential force dependence of the rate of translocation, we switched our MT system from configuration MT_1 to MT_2 to be able to address loads on the protein above 3 pN (see Subsect. 5.2.1). This implied a change of the fluid chamber layout from *standard* to *thin*, i.e. a reduction of the channel height d by 50 % (see Figs. 5.8a and 5.11b).

As shown in Fig. 5.11a, with thin flow cells at room temperature or 30 °C, under otherwise invariant experimental conditions, increasing the magnetic pulling force – pointing opposite to the direction of movement of AddAB – up to 14 pN did not reduce the pause-free unwinding rate significantly. This observation is remarkable, yet in accordance with a previous single-molecule study showing forward motion of the closely related RecBCD complex (see Subsect. 5.1.3) at non-saturating ATP concentrations against loads of up to 8 pN applied on the protein [Perkins et al., 2004].

Theoretically, nucleic acid motors that exploit the energy derived from nucleoside triphosphate hydrolysis are able to generate forces up to the DNA overstretching transition (and beyond), depending on their step size. If for instance one cycle of ATP hydrolysis yields a free energy difference on the order of $25\,k_\mathrm{B}T \approx 100\,\mathrm{pN{\cdot}nm}$ (for typical concentrations encountered in living cells), a DNA motor protein with a step size of 3 bp could induce a force of up to 100 pN [Seidel and Dekker, 2007]. Note that the Φ29 viral packaging motor – exerting up to 57 pN – represents the strongest

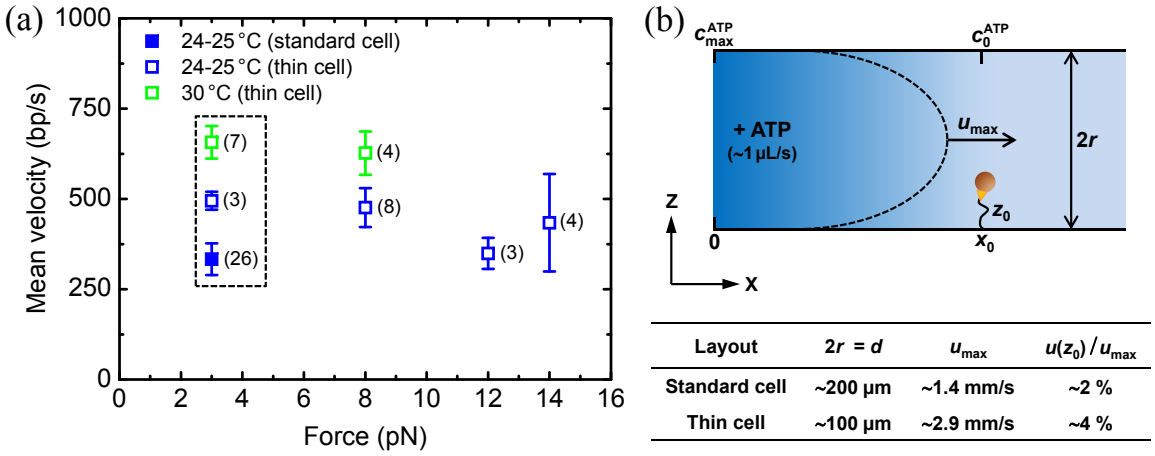

Layout	$2r = d$	u_{max}	$u(z_0)/u_{max}$
Standard cell	~200 µm	~1.4 mm/s	~2 %
Thin cell	~100 µm	~2.9 mm/s	~4 %

Figure 5.11. Force and flow cell height dependence of AddAB activity. **(a)** Average translocation velocity versus load applied on the protein. Data taken at $F_{\mathrm{MT}} \geq 3\,\mathrm{pN}$ (open squares) require an enhanced MT configuration with thinner (100 µm) sample cells. At both temperature settings, no drastic rate change occurs within the studied force range. For comparison, the – fairly smaller – mean velocity obtained with standard (200 µm) cells at 3 pN (filled square, shown in Fig. 5.9) is depicted, too. The digit next to each data point indicates the number of DNA molecules used for calculating the average. Error bars represent the standard deviation, the typical relative error in F_{MT} (no error bars shown) being 5–10 %. The dashed rectangle encloses values at 3 pN shown in Fig. 5.12. **(b)** All measurements corresponding to the results in (a) were carried out with 1 mM of ATP in the reaction buffer, injected at $\sim 1\,\mu\mathrm{L/s}$. The highest linear flow velocity $u_{\max}$ is encountered along the channel centreline (for $z = r = d/2$) and doubles when the thickness d is shrunk by one half. The table shows rate values corresponding to a single, practically infinite channel in XY ($l \approx 25\,\mathrm{mm}$, $w \approx 7\,\mathrm{mm}$) with a flow profile as introduced in Subsect. 5.3.3. Close to the coverslip surface, for a protein–DNA construct with initial extension $z_0 \sim 2\,\mu\mathrm{m}$ (see Fig. 5.8) at position x_0, flow rates below 5 % of the maximum correspond to long ATP saturation ($c_0^{\mathrm{ATP}} \rightarrow c_{\max}^{\mathrm{ATP}}$) times and can thus explain an increase in AddAB velocity upon channel height reduction.

protein machine working on nucleic acids that has been observed experimentally so far [Smith et al., 2001]. It is therefore not surprising that molecular assemblies like AddAB/RecBCD that show very stable unwinding can exhibit sufficiently high strengths to remove obstacles along their way [Mackintosh and Raney, 2006], e.g. streptavidin blocks used in certain biochemical assays [Yeeles et al., 2011a].

Improved chemical energy conditions in slimmer flow cells

Apart from the aforementioned, the results in Fig. 5.11a also indicate an increase of the mean translocation speed merely after substitution of standard fluid chambers by thinner ones – with all remaining parameters left untouched. This observation could only be explained by higher effective ATP concentrations close to the motor protein and was indeed independent of other technical modifications: various magnet

alignments used to create forces of 3 pN generated equivalent translocation traces for the same sample cell layout (data not shown).

Instead, an increase of the linear flow velocity through the channel – according to an altered parabolic profile defined by Eq. 5.8 – makes the difference: at a constant volume flow rate $\widetilde{Q} \approx 1\,\mu\text{L/s}$ through our fluid chambers (see Subsect. 5.3.3), reducing the channel height from 200 to 100 µm implies an increase of the *average* linear speed $\overline{u} = u_{\max}/2$ from ~ 0.7 to $\sim 1.5\,\text{mm/s}$. At the same time, in compliance with the numbers indicated in Fig. 5.11b, the velocity close to the initial height $z_0 \sim 2\,\mu\text{m}$ of the molecular motor in translocation experiments is much smaller – but exhibits a fourfold increase, from ~ 30 to $\sim 120\,\mu\text{m/s}$.

If we neglect diffusive effects and assume for simplicity that, after adding ATP, a constant (linear) concentration gradient over a characteristic length of $\sim 1\,\text{mm}$ is formed along the X-axis (see Fig. 5.11b), the flow estimates in the previous paragraph imply that, for $z \leq z_0$, the transition $(c^{\text{ATP}}(x_0, z) = c_0^{\text{ATP}}) \rightarrow c_{\max}^{\text{ATP}}$ takes at least 33 (8) s of flushing buffer at $\sim 1\,\mu\text{L/s}$ through standard (thin) sample cells, respectively. From the representative traces depicted in Fig. 5.8b, it appears that only in the latter case saturating ATP conditions could be reached within the finite duration ($\sim$ 10–25 s) of AddAB activity.

As a direct consequence, the incongruity of absolute speeds measured by MT and in bulk stems from the nature of the different ways to start the translocation reaction: while stopped-flow devices provide a defined reaction volume with homogeneous chemical energy distribution (1 mM ATP everywhere) after practically instantaneous, turbulent mixing of two reservoirs, (surface-coupled) single-molecule techniques that rely on a *single* stream of buffer depend on the much slower, laminar phenomena described above. When injecting reaction buffer with ATP in MT sample cells, due to the gradual concentration rise close to the walls, during the course of a translocation run there may be insufficient time to reach the desired (volumetric) level of chemical energy (1 mM) at the protein. Accordingly, this means that most single-molecule data presented in this chapter were in fact acquired at sub-saturating ATP concentrations.

5.4.7. Recovery of bulk velocities with a large excess of ATP

To ultimately confirm the previous arguments explaining reduced AddAB velocities in MT assays by non-saturating ATP conditions, we performed measurements with thin sample cells and a fourfold higher concentration of biological fuel in the reaction buffer. When adding all mean translocation rates obtained at 3 pN in thin cells to the previous results already shown in Fig. 5.9, it becomes clear that velocities acquired at 4 mM of ATP and increased laminar flows are indeed able to catch up with the rate values assessed at room temperature in stopped-flow experiments (Fig. 5.12a).

Along the same lines, comparing histograms of instantaneous single-molecule rates at ambient conditions and 3 pN, corresponding to combinations of (i) standard cells +

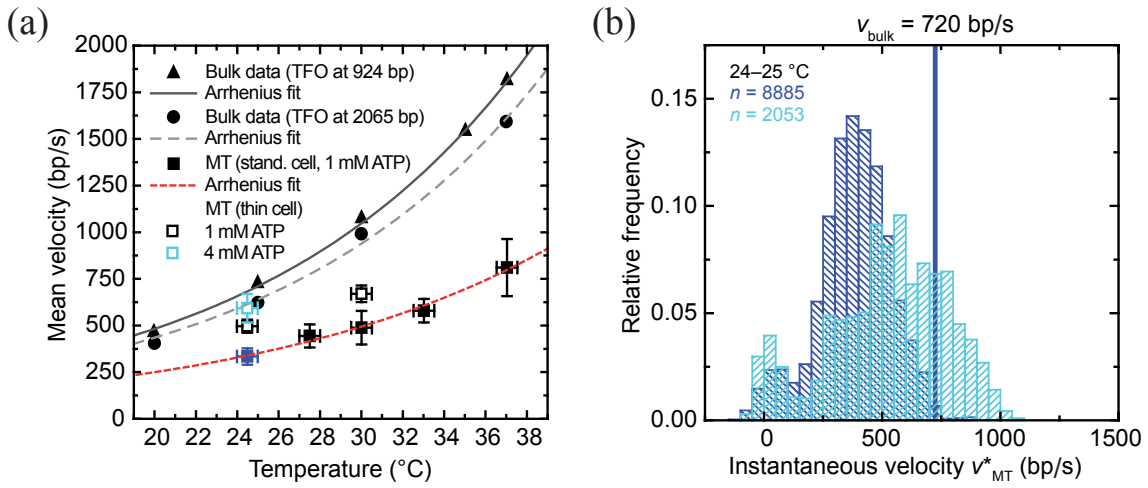

Figure 5.12. Equivalence of single-molecule and bulk velocities under optimised chemical energy conditions. **(a)** Starting from Fig. 5.9a, mean translocation rate values obtained with thin MT sample cells at 3 pN – and 1 mM (see Fig. 5.11a) or 4 mM ATP in the initial reaction buffer mixture – approach the results from bulk measurements. The cyan data point corresponding to ambient temperature and high ATP practically recovers the typical range of stopped-flow velocities. **(b)** Superimposing the histogram of instantaneous rates measured at these conditions onto the previous one (left panel of Fig. 5.10) obtained with standard cells (blue data point in (a)), a clear broadening/shift of the distribution to higher speeds is observed.

1 mM ATP (already shown in Fig. 5.10) and (ii) thin cells + 4 mM ATP, respectively, reveals that – even though AddAB eventually reaches the average bulk velocities at sub-saturating conditions – the molecular motor can only maintain (and transiently surpass) them in the case of faster laminar flows and optimised amounts of chemical energy (Fig. 5.12b).

Evidently, these circumstances set a new standard in terms of ATP concentrations to be used in our MT from now on: to be able to reach saturating conditions, we should increase at least by four the amount of biological fuel flushed into the sample cell. Please note that, although we might also just increase the volume flow determined by the syringe pump to achieve similar results at lower concentrations of ATP, inconveniences due to more frequent video tracking errors and detachments of DNA tethers from the surface limit us to some extent to a volumetric velocity of $\sim 1\,\mu L/s$.

5.5. Conclusion

This chapter has demonstrated the versatility of a customised thermal control unit implemented in vertical MT. By measuring the single-molecule kinetics of a DNA motor protein at various temperature, force and ATP settings with two different MT

configurations, we have shown quite plainly that applying heat from underneath is a good choice for permanent-magnet-based layouts. The temperature management device allows for accurate calibration of the thermal conditions inside the sample cell and can in principle be tailored to any other inverted microscope configuration, which suggests an important benefit for state-of-the-art techniques such as hybrid DNA origami nanopores [Hernández-Ainsa et al., 2013a], photo-activated localisation microscopy (PALM) [Betzig et al., 2006] or optical torque wrenches [La Porta and Wang, 2004].

Proof-of-principle experiments with the bacterial helicase–nuclease complex AddAB comply with bulk assays and yield an apparent activation energy of translocation that falls in the range between 19 and 25 $k_{\mathrm{B}}T$ and therefore matches published data for related enzymes, e.g. for the RecBCD complex with an associated activation energy of 17–32 $k_{\mathrm{B}}T$.

In addition, we have been able to identify one of the reasons that makes a direct comparison of results from surface-coupled single-molecule experiments and bulk assays – at supposedly identical conditions – complicated: variable reagent concentrations close to the glass surface due to the slow nature of laminar flows far from the channel centre. This does not only refer to energy conversion processes, but might also affect protein–substrate binding reactions, e.g. when studying DNA-condensing agents. For all that, the results presented here show that our thermally stabilised optical microscope is well-suited for precise studies of thermally induced activity changes of (biological) objects in the micro-/nanometre size range. We expect the rather simple and compact design to find use as a powerful tool for exploring fundamental processes at the interface between biophysics and nanotechnology.

6. Final conclusions

In this thesis, the development and application of instruments for single-molecule force spectroscopy of DNA and proteins has been described. The following paragraphs sum up the most important conclusions from the three main projects (corresponding to Chaps. 3, 4 and 5) that have been pursued:

Tailor-made optical tweezers (OT)

- A bespoke OT setup, consisting of both commercial and custom-built components, has been assembled from scratch. Its layout is based on an inverted microscope without condenser and therefore constitutes a versatile solution for sensitive measurements at biologically relevant length, force and time scales.
- In a micropipette-coupled configuration, external heating of the microscope objective and continuous position corrections via movements of the piezoelectric sample stage can alleviate thermal drift effects induced by the trapping laser.
- Through the combination of photodiode and video camera detection schemes, complementary trap stiffness calibration methods can be used to probe the linearity of the OT force field and double-check other parameters such as detector sensitivity.
- Results from test measurements with known DNA substrates show that, by taking advantage of high-bandwidth data from (i) the reflected intensity of an independent detection laser and (ii) the signal of a light-lever device, the system is able to reproduce previous results and achieve resolutions in force and extension of a different, well-established optical trapping microscope.

Microspheres as flow sensors

- An OT apparatus similar to the one described before has been used together with a low-noise current amplifier to quantify the fluid flows passing through nanometric pipettes – so-called glass nanopores.
- For a certain voltage applied between both pipette ends, the flow field outside the tip – induced by electroosmosis at the inner glass walls – can be explored via both the rotations and the force response of slightly asymmetric microspheres confined in the optical trap.
- To infer the volumetric flow rate at the pore exit from rotation and force measurements at different relative positions of trap and pore in a plane, the

Landau–Squire solution of the Navier–Stokes equations can be used, which describes the nanofluidic jet as a point source of momentum and explains the experimental results remarkably well.

- The obtained values fall in the range of tens of picolitres per second and thus come close to the lower detection limit of other flow measurement techniques. Also, a flow rectification effect upon voltage reversal has been observed and could be exploited in potential applications of such a nanojet.

Thermally stabilised magnetic tweezers (MT)

- A customised thermostat assembly for single-molecule experiments between 25 and 40 °C at ±0.5 °C of accuracy has been implemented and characterised in a vertical MT setup.
- The modular arrangement serves for measurements at constant temperatures and requires very little extra space, which suggests its use in other types of surface-coupled techniques that rely on inverted microscopes.
- To test the temperature-controlled MT with a biological system, the thermally dependent helicase activity of the molecular motor AddAB has been studied and compared with results from bulk experiments. A common Arrhenius-like increase of the translocation velocity along double-stranded DNA has been identified.
- Absolute velocity differences, encountered between single-molecule and ensemble measurements at equivalent temperatures, can be attributed to reduced effective ATP concentrations near the motor protein in MT assays. AddAB velocities from both data sets can be balanced by raising volume rate and amount of ATP flushed into MT flow cells.

6a. Conclusiones finales

En esta tesis se han descrito el desarrollo y la aplicación de instrumentos de espectroscopia de fuerza a nivel de molécula individual para caracterizar sustratos de ADN y proteínas. Los siguientes párrafos resumen las conclusiones más importantes de los tres proyectos principales (correspondientes a los Capítulos 3, 4 y 5) que se han llevado a cabo:

Pinzas ópticas (OT) construidas a medida

- Se ha montado desde cero un aparato de OT personalizado que incluye componentes tanto comerciales como fabricados apropiadamente. El diseño está basado en un microscopio invertido que carece de condensador, por lo que constituye una solución versátil para mediciones sensibles a escalas de longitud, fuerza y tiempo biológicamente relevantes.
- En una configuración acoplada a una micropipeta, los efectos de deriva térmica causados por el láser de atrapamiento se pueden reducir calentando el objetivo del microscopio externamente y aplicando correcciones contínuas en posición mediante movimientos de la mesa de muestras piezoeléctrica.
- Combinando los modos de detección de posición por fotodiodo y cámara de video, se pueden explotar métodos complementarios de calibración de la rigidez de la trampa para sondear la linealidad del campo de fuerza de las OT y comprobar otros parámetros como la sensibilidad del detector.
- Los resultados de los experimentos de prueba de concepto con moléculas de ADN conocidas demuestran que, aprovechando los datos de ancho de banda alto provenientes de (i) la reflexión de un láser de detección independiente y (ii) un sistema basado en la refracción de la luz (o *light-lever*), el equipo es capaz de reproducir resultados previos y alcanzar resoluciones en extensión y fuerza de un microscopio de atrapamiento óptico diferente y bien establecido.

Microesferas usadas como sensores de flujo

- Un instrumento de OT similar al descrito previamente se ha utilizado junto con un amplificador de corriente de bajo ruido para cuantificar los flujos de fluido que atraviesan pipetas nanométricas, también llamadas nanoporos de vidrio.
- Aplicando un cierto voltaje entre los dos extremos de la pipeta, el campo de flujo en el exterior de la punta – inducido por electroosmosis en la superficie

interna del vidrio – se puede explorar tanto a través de las rotaciones como de la respuesta en fuerza de microesferas ligeramente asimétricas, confinadas en la trampa óptica.

- Para inferir el flujo volumétrico en la salida del poro de medidas de rotación y fuerza a diferentes posiciones relativas de trampa y poro en un mismo plano, se puede usar la solución de Landau–Squire de las ecuaciones de Navier–Stokes, que describe el chorro nanométrico como una fuente puntual de momento lineal y explica los resultados experimentales notablemente bien.
- Los valores obtenidos de flujo se encuentran en el rango de decenas de picolitros por segundo y se acercan por lo tanto al límite inferior de detección de otras técnicas de medición de flujo. También se ha observado un efecto de rectificación de flujo al invertir el voltaje que podría ser utilizado en potenciales aplicaciones de semejantes fluidos nanométricos.

Pinzas magnéticas (MT) con control de temperatura

- Se ha implementado y caracterizado un termostato a medida en un sistema de MT vertical, con el fin de realizar experimentos a nivel de molécula individual entre 25 y 40 °C con ±0.5 °C de exactitud.
- La construcción modular sirve para experimentos a temperature constante y requiere muy poco espacio adicional, lo que sugiere su uso en otros equipos que estén acoplados a una superficie y basados en un microscopio invertido.
- Para probar las MT controladas térmicamente con un sistema biológico, se ha estudiado la actividad helicasa del motor molecular AddAB en función de la temperatura, y se han contrastado los resultados con otros obtenidos mediante técnicas en volumen. Se ha identificado un incremento común tipo Arrhenius de la velocidad de traslación a lo largo del ADN de cadena doble.
- Las diferencias de velocidad absoluta encontradas al comparar medidas a nivel de molécula individual y en volumen a temperaturas equivalentes, se pueden atribuir a concentraciones de ATP reducidas cerca de la proteína motora en los ensayos con las MT. Las velocidades de AddAB de ambos conjuntos de datos se pueden asemejar elevando el flujo volumétrico y la cantidad de ATP inyectado en la celda líquida de las MT.

Abbreviations and nomenclature

α	half-angle of a converging light cone
α_{Pt}	standard temperature coefficient of a Pt100 sensor
α_{p}^{*}	particle polarisability
$\bar{u}_0$	average linear flow speed at the pore exit
β	hydrodynamic drag coefficient
$\delta(t)$	Dirac delta function
ϵ	dielectric constant
η	dynamic viscosity
η_{trans}	thermal transfer efficiency
κ^{-1}	Debye screening length
λ	wavelength of light in solution
λ_0	wavelength of light in air
$\mathcal{F}\{...\}$	Fourier transform of {...}
$\mathcal{I}(\vec{r})$	laser intensity distribution
$\mathcal{I}_0$	total intensity of incident laser beam
$\mathcal{K}$	rise per base pair (conversion factor in nm/bp)
$\mathcal{S}$	detector sensitivity (in V/µm)
$\mathcal{T}_{\mathrm{I}}$, $\mathcal{T}_{\mathrm{D}}$	integral and derivative time of a PID feedback
$\mathcal{X}_{\mathrm{P}}$, $\mathcal{X}_{\mathrm{I}}$, $\mathcal{X}_{\mathrm{D}}$	proport., integr. and derivat. contribution to a PID feedback
μ_{e}	induced electric dipole moment
μ_{m}	induced magnetic dipole moment
$\overline{u}$	average linear flow speed in a microfluidic channel
ϕ	azimuthal angle
ρ	volumetric mass density
τ_{c}	characteristic relaxation time constant
τ_{inert}	time constant of inertial effects
τ_{Ω}	time constant of the rotation onset
θ	polar/inclination angle
$\varphi(t)$	stochastic Gaussian process
Ψ	stream function
Σ^{QPD}	total QPD (sum) signal
Θ	beam divergence angle

$\vec{\omega}$ ..... vorticity vector
$\vec{\Omega}$ ..... angular velocity vector
$\vec{B}$ ..... magnetic field vector
$\vec{E}$ ..... electric field vector
$\vec{r}$ ..... (radial) distance vector
$\widetilde{Q}_0$ ..... volume flow rate at the pore exit
$\widetilde{R}$ ..... pore radius
$\widetilde{\alpha}_I$ ..... current rectification ratio
$\widetilde{\alpha}_Q$ ..... flow rectification ratio
$\widetilde{L}$ ..... characteristic length of flow field variations
$\widetilde{P}_0$ ..... momentum flow rate at the pore exit
$\widetilde{Q}$ ..... volume flow rate in a microfluidic channel
A_{Pt}, B_{Pt} ..... temperature reference constants of a Pt100 sensor
c ..... molar concentration
c_0^{ATP} ..... initial ATP concentration
$c_{\mathrm{max}}^{\mathrm{ATP}}$ ..... maximum (saturating) ATP concentration
c_0^* ..... speed of light in vacuum
D ..... axial distance between magnets and sample cell
D_{beam} ..... diameter of a collimated laser beam
d_{p} ..... particle diameter
E ..... energy
e ..... error between setpoint and measured process variable
E_{a} ..... activation energy barrier
F ..... (applied) force
f ..... frequency
F_{B} ..... random (Brownian) force
F_{drag} ..... viscous drag force
F_{grad} ..... gradient force
f_{L} ..... focal length of a lens
F_{MT} ..... applied force in magnetic tweezers
F_{OT} ..... applied force in optical tweezers
F_{R} ..... restoring force
F_{scat} ..... scattering force
f_{c} ..... corner/cut-off frequency
I ..... measured current
K ..... elastic stretch modulus
k^* ..... reaction rate
K_{P}, K_{I}, K_{D} ..... proportional, integral and derivative gain of a PID controller

k_{trap} ..... trap stiffness
$k_{\mathrm{trap}}^{\mathrm{MT}}$ ..... magnetic force constant ("trap stiffness")
$k_{\mathrm{trap}}^{\mathrm{OT}}$ ..... optical trap stiffness
k_{B} ..... Boltzmann constant
l, w, d ..... length, width and thickness of a rectangular channel
L_0 ..... contour length of a molecule
l_{coh} ..... coherence length
L_{p} ..... persistence length of a molecule
m ..... mass of a particle
N_{A} ..... Avogadro constant
n_{m} ..... refractive index of the medium
n_{p} ..... refractive index of a particle
p ..... linear momentum in solution
$P_{\mathrm{eff.heat}}$ ..... effective heating power per unit temperature
P_{heat} ..... Joule heating power
P_{OT} ..... pre-objective laser power used for optical trapping
P_{out} ..... laser output power
P_{scat} ..... scattered laser power in solution (close to the optical trap)
P_0 ..... total incident laser power in solution (close to the optical trap)
q ..... elementary charge
Q_{scat} ..... ratio of scattered and total incident laser power
R ..... resistance
r' ..... radial distance measured from the channel centreline
r^* ..... scaled distance from the pore exit
r_{h} ..... hydraulic radius
R_{l} ..... linear resistance from a Pt100 sensor
R_{nl} ..... nonlinear resistance from a Pt100 sensor
r_{p} ..... particle radius
Re ..... Reynolds number
s ..... quadratic conversion factor (sensitivity)
s' ..... linear conversion factor (sensitivity)
S_0^{u} ..... low-frequency limit of the uncalibrated PSD
S_0 ..... low-frequency limit of the calibrated PSD
$S_{\{...\}}(f)$ ..... power spectral density of {...}
T ..... (absolute) temperature
t ..... time
t_0 ..... reaction initiation time
t_1 ..... lag time before triplex displacement

T_{centre} ..... temperature inside the flow cell (near the centre)
T_{inlet} ..... temperature inside the flow cell (near the inlet)
T_{corr} ..... corrected temperature
T_{meas} ..... measured temperature
$T_{\text{set,BP}}$ ..... baseplate temperature setpoint
$T_{\text{set,MO}}$ ..... objective temperature setpoint
u ..... linear fluid flow speed
u_{max} ..... maximum linear flow speed in a microfluidic channel
U_{MT} ..... potential energy of a magnetically trapped superparamagnetic particle
U_{OT} ..... potential energy of an optically trapped Rayleigh particle
V ..... (applied) voltage
$v(T)$ ..... temperature-dependent rate of a motor protein
v_∞ ..... hypothetical rate of a motor protein at infinite temperature
v_{bulk} ..... mean bulk velocity (measured with the stopped-flow technique)
V_{conv} ..... voltage output of a temperature converter
v_{MT} ..... mean single-molecule velocity (measured with MT)
v^*_{MT} ..... instantaneous single-molecule velocity (measured with MT)
w ..... radius of a Gaussian laser beam
w_0 ..... radius of the focal spot of a Gaussian laser beam
x^{QPD}, y^{QPD} ..... differential QPD signals
x_0 ..... equilibrium position in X
X_{corr} ..... corrected process variable
X_{meas} ..... measured process variable
$x^{\text{QPD}}_{\text{norm}}$, $y^{\text{QPD}}_{\text{norm}}$ ..... normalised differential QPD signals
X_{set} ..... setpoint of the process variable
y^* ..... scaled XY-position with respect to the pore exit
Y_{out} ..... manipulated output variable
z, L ..... molecular extension
z_0 ..... initial extension in translocation assays
z_{R} ..... Rayleigh range (half the focal depth of a Gaussian laser beam)
AddAB ..... ATP-dependent *B. subtilis* helicase–deoxyribonuclease complex
ADN ..... ácido desoxirribonucleico
AFM ..... atomic force microscopy
AL ..... aspheric lens
Anti-Dig ..... anti-digoxigenin
AT ..... adenine–thymine base pair
ATP ..... adenosine triphosphate

BE ..... beam expander
Bio ..... biotin
BNC ..... bayonet Neill–Concelman
BP ..... baseplate
bp ..... base pair(s)
BSA ..... bovine serum albumin protein
CAD ..... computer-aided design
CCD ..... charge-coupled device
Chi ..... crossover hotspot instigator
CMOS ..... complementary metal-oxide-semiconductor
CPU ..... central processing unit
DAQ ..... data acquisition
Dig ..... digoxigenin
DM ..... dichroic mirror
DMP ..... dimethyl pimelimidate
DNA ..... deoxyribonucleic acid
dsDNA ..... double-stranded DNA
DTT ..... dithiothreitol
e.g. ..... for example (from Latin *exempli gratia*)
EDTA ..... ethylenediaminetetraacetic acid
et al. ..... and others (from Latin *et alii*)
et seqq. ..... and those which follow (from Latin *et sequentia*)
GC ..... guanine–cytosine base pair
GPIB ..... general purpose interface bus
i.e. ..... that is to say (from Latin *id est*)
IR ..... infrared
L ..... standard lens
LabVIEW ..... laboratory virtual instrument engineering workbench
LED ..... light-emitting diode
LL ..... light lever
M ..... standard mirror
MO ..... microscope objective
MSD ..... mean squared displacement
MT ..... magnetic tweezers
NA ..... numerical aperture
NA_{beam} ..... numerical aperture of a converging laser beam
Nd:YAG ..... neodymium-doped yttrium–aluminium garnet
NdFeB ..... neodymium–iron–boron alloy

nt ..... nucleotide(s)
OT ..... optical tweezers
PBS ..... phosphate-buffered saline
PBSC ..... polarising beam splitter cube
PCR ..... polymerase chain reaction
PDMS ..... polydimethylsiloxane
PEEK ..... polyether ether ketone
PhD ..... doctor of philosophy
PID ..... proportional–integral–derivative
PS ..... pellicle beam splitter
PSD ..... power spectral density
PsD ..... position-sensitive detector
Pt100 ..... platinum resistance temperature detector (with $R(0\,^\circ\mathrm{C}) \equiv 100\,\Omega$)
PTP ..... peak-to-peak
px ..... pixel(s)
QPD ..... quadrant photodiode
RecA ..... ATPase triggering strand exchange in recombinat. DNA repair
RecBCD ..... ATP-dependent *E. coli* helicase–deoxyribonuclease complex
RMS ..... root mean square
RNA ..... ribonucleic acid
ROI ..... region of interest
SA ..... streptavidin
SLD ..... superluminescent diode
SSB ..... single-stranded binding protein
ssDNA ..... single-stranded DNA
T ..... temperature sensor
TAMRA ..... tetramethylrhodamine
TEM ..... transverse electromagnetic
TEM_{00} ..... fundamental TEM mode of a Gaussian laser beam
TFO ..... triplex-forming oligonucleotide
TPM 3-methacryloxypropyl-trimethoxysilane
Tris ..... tris(hydroxymethyl)aminomethane
USB ..... universal serial bus
Var ..... variance
WLC ..... worm-like chain

List of Figures

List of Tables

List of Publications

Chapter 3

- **Gollnick, B.** and Moreno-Herrero, F.

  Optical tweezers with backscattering detection and continuous drift control under white-light illumination

  In preparation for *Review of Scientific Instruments*

Chapter 4

- Laohakunakorn, N.*, **Gollnick, B.***, Moreno-Herrero, F., Aarts, D. G. A. L., Dullens, R. P. A., Ghosal, S., and Keyser, U. F.

  A Landau–Squire nanojet

  Nano Letters, 13(11):5141–5146 (2013)

Chapter 5

- **Gollnick, B.**, Carrasco, C., Zuttion, F., Gilhooly, N. S., Dillingham, M. S., and Moreno-Herrero, F.

  Probing DNA helicase kinetics with temperature-controlled magnetic tweezers

  Small, DOI: 10.1002/smll.201402686 (2014)

*These authors contributed equally to this work.

A. Appendix

A.1. Essential parts of the optical tweezers setup

See table on the following page.

Item	Manufacturer	Quantity	Reference	Comments
Trapping laser	IPG Photonics	1	YLM-5-LP-SC	$P_0 \leq 5\,\mathrm{W}$, $\lambda_0 = 1070\,\mathrm{nm}$, SM, TEM_{00}, $D_0 = 5\,\mathrm{mm}$
Detection laser	Schäfter+Kirchhoff	1	51nanoFCM	$P_0 \leq 30\,\mathrm{mW}$, $\lambda_0 = 658\,\mathrm{nm}$, SM, TEM_{00}, $D_0 = 1\,\mathrm{mm}$
Microscope objective	Olympus	1	UPLSAPO 60XW	Water immersion, NA = 1.2, WD = 130 µm
Piezoelectric stage	Physik Instrumente	1	P-517.3CD	$100 \times 100 \times 20\,\mu\mathrm{m}$ range, 1 nm resolution
Stage controller	Physik Instrumente	1	E-710.3CD	GPIB interface (add. USB adapter needed)
Fibre-coupled laser diode	Thorlabs	1	LPS-635-FC	$P_0 \leq 2.5\,\mathrm{mW}$, $\lambda_0 = 635\,\mathrm{nm}$, SM
Aspheric lens	Thorlabs	1	C140TME-B	$f_\mathrm{L} = 1.45\,\mathrm{mm}$, NA = 0.55, AR: 600–1050 nm
Position-sensitive detector	Thorlabs	1	PDP90A	WL: 320–1100 nm, $< 0.7\,\mu\mathrm{m}$ resol. at 100 µW
Air pressure controller	Fluigent	1	MFCS(-3C-25)	3 × (0–25 mbar) out, 0.1 mbar resolution, 500 mbar input
Tube lens	Newport	1	PAC064AR.14	achr. doublet, $f_\mathrm{L} = 200\,\mathrm{mm}$, AR: 430–700 nm
CCD camera	JAI Pulnix	1	TM-6740CL	640×480 px, 200 Hz max. at full readout
Quadrant photodiode	New Focus	1	2901-M	WL: 190–1050 nm, $3 \times 3\,\mathrm{mm}$ chip, $\leq 100\,\mathrm{kHz}$
BNC connector block	National Instruments	1	NI BNC-2120	8×AI, 2×AO, 8×DI/O, amongst others
Data acquisition card	National Instruments	1	NI PCIe-6351	≤ 16 AI, 1 MHz multi-channel, 16 bit, ±10 V

Table A.1. References to the most relevant commercial components of the optical tweezers (OT) instrument. AI/O: analog in/out; DI/O: digital in/out; AR: anti-reflection coating; SM: single-mode; WD: working distance; WL: wavelength range.

A.2. Essential parts of the temperature control system

See table on the following page.

Item	Manufacturer	Quantity	Reference	Comments
Polyimide heater (Heaters 1)	Minco	1	HK5210R33.9L12A	Without adhesive backing
Polyimide heater (Heaters 2a/b)	Minco	2	HK5160R5.6L12E	Backed with pressure-sensitive adhesive
Pt100 temperature sensor (T1–T4)	Correge	4	PTFC101T	Probe size ($W \times L$): $2.0 \times 2.3\,\mathrm{mm}$
Pt100 temperature signal converter	Brodersen	4	PXT-10.924	One for each sensor
Data acquisition (DAQ) module	National Instruments	1	NI 9215 BNC	Provides up to four readouts in parallel
Chassis for DAQ module	National Instruments	1	cDAQ-9171	Connects to PC by USB
Programmable power supply unit	Thurlby Thandar Instruments (TTi)	2	PL303-P	One per heating circuit; controlled via USB
Silicone stretch tape	Minco	1	#20 stretch tape	Fixes Heater 1 to microscope objective
Thermally conductive double-sided tape	Thorlabs	1	TCDT1	Fixes sensor T1 to microscope objective
Thermally conductive epoxy glue	Minco	1	#15 epoxy	Fixes sensor T2 to baseplate of sample cell holder

Table A.2. References to the main commercial components of the magnetic tweezers (MT) temperature control assembly.

Bibliography

Abbondanzieri, E. A., Greenleaf, W. J., Shaevitz, J. W., Landick, R., and Block, S. M. (2005). Direct observation of base-pair stepping by RNA polymerase. *Nature*, 438(7067):460–465.

Alberts, B., Bray, D., Hopkin, K., Johnson, A., Lewis, J., Raff, M., Roberts, K., and Walter, P. (2013). *Essential cell biology*. Garland Science, 4th edition.

Alberts, B., Bray, D., Lewis, J., Raff, M., Roberts, K., and Watson, J. D. (1989). *Molecular biology of the cell*. Garland Science, 2nd edition.

Arata, H. F., Noji, H., and Fujita, H. (2006). Motion control of single F1-ATPase rotary biomolecular motor using microfabricated local heating devices. *Applied Physics Letters*, 88(8):83902.

Arrhenius, S. (1889). Über die Reaktionsgeschwindigkeit bei der Inversion von Rohrzucker durch Säuren. *Zeitschrift für Physikalische Chemie*, 4:226–248.

Ashkin, A. (1970). Acceleration and trapping of particles by radiation pressure. *Physical Review Letters*, 24(4):156–159.

Ashkin, A. (1992). Forces of a single-beam gradient laser trap on a dielectric sphere in the ray optics regime. *Biophysical Journal*, 61(2):569–582.

Ashkin, A. and Dziedzic, J. (1987). Optical trapping and manipulation of viruses and bacteria. *Science*, 235(4795):1517–1520.

Ashkin, A., Dziedzic, J. M., Bjorkholm, J. E., and Chu, S. (1986). Observation of a single-beam gradient force optical trap for dielectric particles. *Optics Letters*, 11(5):288–290.

Ashkin, A., Dziedzic, J. M., and Yamane, T. (1987). Optical trapping and manipulation of single cells using infrared laser beams. *Nature*, 330(24):769–771.

Åström, K. J. and Hägglund, T. (1995). Controller design. In *PID controllers: theory, design, and tuning*, chapter 4. ISA, 2nd edition.

Baker, M. A. B., Inoue, Y., Takeda, K., Ishijima, A., and Berry, R. M. (2011). Two methods of temperature control for single-molecule measurements. *European Biophysics Journal*, 40(5):651–660.

Batchelor, G. K. (2000). *An introduction to fluid dynamics*. Cambridge University Press, 1st edition.

Baumann, C. G., Smith, S. B., Bloomfield, V. A., and Bustamante, C. (1997). Ionic effects on the elasticity of single DNA molecules. *Proceedings of the National Academy of Sciences of the United States of America*, 94(12):6185–6190.

Bausch, A. R., Ziemann, F., Boulbitch, A. A., Jacobson, K., and Sackmann, E. (1998). Local measurements of viscoelastic parameters of adherent cell surfaces by magnetic bead microrheometry. *Biophysical Journal*, 75(4):2038–2049.

Bayley, H. and Cremer, P. S. (2001). Stochastic sensors inspired by biology. *Nature*, 413(6852):226–230.

Bayley, H. and Martin, C. R. (2000). Resistive-pulse sensing from microbes to molecules. *Chemical Reviews*, 100(7):2575–2594.

Behrens, S. H. and Grier, D. G. (2001). The charge of glass and silica surfaces. *The Journal of Chemical Physics*, 115(14):6716–6721.

Bell, N. A. W., Engst, C. R., Ablay, M., Divitini, G., Ducati, C., Liedl, T., and Keyser, U. F. (2012). DNA origami nanopores. *Nano Letters*, 12(1):512–517.

Berg-Sørensen, K. and Flyvbjerg, H. (2004). Power spectrum analysis for optical tweezers. *Review of Scientific Instruments*, 75(3):594.

Betzig, E., Patterson, G. H., Sougrat, R., Lindwasser, O. W., Olenych, S., Bonifacino, J. S., Davidson, M. W., Lippincott-Schwartz, J., and Hess, H. F. (2006). Imaging intracellular fluorescent proteins at nanometer resolution. *Science*, 313(5793):1642–1645.

Bianco, P. R., Brewer, L. R., Corzett, M., Balhorn, R., Yeh, Y., Kowalczykowski, S. C., and Baskin, R. J. (2001). Processive translocation and DNA unwinding by individual RecBCD enzyme molecules. *Nature*, 409(6818):374–378.

Bioptechs Inc. (2001). Live cell microscopy environmental control systems. Available from: `http://www.bioptechs.com`.

Block, S. M., Goldstein, L. S., and Schnapp, B. J. (1990). Bead movement by single kinesin molecules studied with optical tweezers. *Nature*, 348(6299):348–352.

Bockelmann, U., Thomen, P., Essevaz-Roulet, B., Viasnoff, V., and Heslot, F. (2002). Unzipping DNA with optical tweezers: high sequence sensitivity and force flips. *Biophysical Journal*, 82(3):1537–1553.

Böhm, K. J., Stracke, R., Baum, M., Zieren, M., and Unger, E. (2000). Effect of temperature on kinesin-driven microtubule gliding and kinesin ATPase activity. *FEBS Letters*, 466(1):59–62.

Bouzigues, C. I., Tabeling, P., and Bocquet, L. (2008). Nanofluidics in the Debye layer at hydrophilic and hydrophobic surfaces. *Physical Review Letters*, 101(11):114503.

Brutzer, H. (2012). *Mechanics and dynamics of twisted DNA*. PhD thesis, Technische Universität Dresden.

Brutzer, H., Schwarz, F. W., and Seidel, R. (2012). Scanning evanescent fields using a pointlike light source and a nanomechanical DNA gear. *Nano Letters*, 12(1):473–479.

Bustamante, C., Bryant, Z., and Smith, S. B. (2003). Ten years of tension: single-molecule DNA mechanics. *Nature*, 421(6921):423–427.

Bustamante, C., Macosko, J. C., and Wuite, G. J. L. (2000). Grabbing the cat by the tail: manipulating molecules one by one. *Nature Reviews Molecular Cell Biology*, 1(2):130–136.

Bustamante, C., Marko, J. F., Siggia, E. D., and Smith, S. B. (1994). Entropic elasticity of lambda-phage DNA. *Science*, 265:1599–1600.

Callendar, H. L. (1887). On the practical measurement of temperature: experiments made at the Cavendish Laboratory, Cambridge. *Philosophical Transactions of the Royal Society of London. A*, 178:161–230.

Carrasco, C., Gilhooly, N. S., Dillingham, M. S., and Moreno-Herrero, F. (2013). On the mechanism of recombination hotspot scanning during double-stranded DNA break resection. *Proceedings of the National Academy of Sciences of the United States of America*, 110(28):E2562–E2571.

Carrasco Pulido, C. and Moreno-Herrero, F. (2011). Magnetic tweezers. In *Encyclopedia of Life Sciences*, pages 1–9. Wiley.

Carter, A. R., King, G. M., and Perkins, T. T. (2007). Back-scattered detection provides atomic-scale localization precision, stability, and registration in 3D. *Optics Express*, 15(20):13434–13445.

Çengel, Y. A. and Cimbala, J. M. (2006). *Fluid mechanics: fundamentals and applications*. McGraw-Hill, 1st edition.

Chatfield, C. (2013). *The analysis of time series: an introduction*. CRC Press, 6th edition.

Check Hayden, E. (2014). Data from pocket-sized genome sequencer unveiled. *Nature*, (doi:10.1038/nature.2014.14724). Available from: `http://www.nature.com/news/data-from-pocket-sized-genome-sequencer-unveiled-1.14724`.

Chédin, F., Ehrlich, S. D., and Kowalczykowski, S. C. (2000). The Bacillus subtilis AddAB helicase/nuclease is regulated by its cognate Chi sequence in vitro. *Journal of Molecular Biology*, 298(1):7–20.

Cheezum, M. K., Walker, W. F., and Guilford, W. H. (2001). Quantitative comparison of algorithms for tracking single fluorescent particles. *Biophysical Journal*, 81(4):2378–2388.

Coulter, W. H. (1953). Means for counting particles suspended in a fluid. US patent number 2,656,508. Available from: `http://www.google.com/patents/US2656508`.

Crick, F. H. C. and Hughes, A. F. W. (1950). The physical properties of cytoplasm: a study by means of the magnetic particle method, part I. Experimental. *Experimental Cell Research*, 1:37–80.

Davidson, M. W. and Abramowitz, M. (2002). Optical microscopy. In *Encyclopedia of Imaging Science and Technology*, pages 1–40. Wiley.

de Vlaminck, I. and Dekker, C. (2012). Recent advances in magnetic tweezers. *Annual Review of Biophysics*, 41:453–472.

de Vlaminck, I., Henighan, T., van Loenhout, M. T. J., Pfeiffer, I., Huijts, J., Kerssemakers, J. W. J., Katan, A. J., van Langen-Suurling, A., van der Drift, E., Wyman, C., and Dekker, C. (2011). Highly parallel magnetic tweezers by targeted DNA tethering. *Nano Letters*, 11(12):5489–5493.

Debye, P. (1909). Der Lichtdruck auf Kugeln von beliebigem Material. *Annalen der Physik*, 335(11):57–136.

Dekker, C. (2007). Solid-state nanopores. *Nature Nanotechnology*, 2(4):209–215.

Deniz, A. A., Mukhopadhyay, S., and Lemke, E. A. (2008). Single-molecule biophysics: at the interface of biology, physics and chemistry. *Journal of the Royal Society Interface*, 5(18):15–45.

Dholakia, K., Reece, P., and Gu, M. (2008). Optical micromanipulation. *Chemical Society Reviews*, 37(1):42–55.

Doi, M. (1988). *The theory of polymer dynamics*. Clarendon Press, 1st edition.

Dulin, D., Barland, S., Hachair, X., and Pedaci, F. (2014). Efficient illumination for microsecond tracking microscopy. *PLoS ONE*, 9(9):e107335.

Ehinger, K., Flach, D., Gellrich, L., Horlebein, E., Huck, R., Ilgner, H., Kayser, T., Müller, H., Schädlich, H., Schüssler, A., and Staab, U. (2013). *Industrial temperature measurement – Basics and practice*. ABB Automation Products GmbH. Available from: `http://www05.abb.com/global/scot/scot211.nsf/veritydisplay/c037f06cf0fe45d1c1257bf600344ae9/`.

Farré, A., Marsà, F., and Montes-Usategui, M. (2012). Optimized back-focal-plane interferometry directly measures forces of optically trapped particles. *Optics Express*, 20(11):1443–1454.

Fazal, F. M. and Block, S. M. (2011). Optical tweezers study life under tension. *Nature Photonics*, 5(6):318–321.

Fili, N., Mashanov, G. I., Toseland, C. P., Batters, C., Wallace, M. I., Yeeles, J. T. P., Dillingham, M. S., Webb, M. R., and Molloy, J. E. (2010). Visualizing helicases unwinding DNA at the single molecule level. *Nucleic Acids Research*, 38(13):4448–4457.

Galburt, E. A., Tomko, E. J., Stump, W. T., and Ruiz Manzano, A. (2014). Force-dependent melting of supercoiled DNA at thermophilic temperatures. *Biophysical Chemistry*, 187-188:23–28.

Geggier, S., Kotlyar, A., and Vologodskii, A. (2011). Temperature dependence of DNA persistence length. *Nucleic Acids Research*, 39(4):1419–1426.

Ghosal, S. (2007). Electrokinetic-flow-induced viscous drag on a tethered DNA inside a nanopore. *Physical Review E*, 76(6):061916.

Gibson, G. M., Leach, J., and Keen, S. (2008). Measuring the accuracy of particle position and force in optical tweezers using high-speed video microscopy. *Optics Express*, 16(19):405–412.

Gilhooly, N. S. and Dillingham, M. S. (2014). Recombination hotspots attenuate the coupled ATPase and translocase activities of an AddAB-type helicase-nuclease. *Nucleic Acids Research*, 42(9):5633–5643.

Gittes, F. and Schmidt, C. F. (1998a). Interference model for back-focal-plane displacement detection in optical tweezers. *Optics Letters*, 23(1):7–9.

Gittes, F. and Schmidt, C. F. (1998b). Signals and noise in micromechanical measurements. *Methods in Cell Biology*, 55:129–156.

Gollnick, B. (2007). *Optical tweezers combined with ionic current detection*. Master's thesis, Universität Leipzig.

Gosse, C. and Croquette, V. (2002). Magnetic tweezers: micromanipulation and force measurement at the molecular level. *Biophysical Journal*, 82(6):3314–3329.

Grange, W., Husale, S., Güntherodt, H.-J., and Hegner, M. (2002). Optical tweezers system measuring the change in light momentum flux. *Review of Scientific Instruments*, 73(6):2308–2316.

Greenleaf, W. J., Woodside, M. T., Abbondanzieri, E. A., and Block, S. M. (2005). Passive all-optical force clamp for high-resolution laser trapping. *Physical Review Letters*, 95(20):208102.

Greulich, K. O. (2004). Single molecule techniques for biomedicine and pharmacology. *Current Pharmaceutical Biotechnology*, 5(3):243–259.

Grimm, R., Weidemüller, M., and Ovchinnikov, Y. B. (2000). Optical dipole traps for neutral atoms. *Advances In Atomic, Molecular, and Optical Physics*, 42:95–170.

Haber, C. and Wirtz, D. (2000). Magnetic tweezers for DNA micromanipulation. *Review of Scientific Instruments*, 71(12):4561–4570.

Hall, A. R., Scott, A., Rotem, D., Mehta, K. K., Bayley, H., and Dekker, C. (2010). Hybrid pore formation by directed insertion of α-haemolysin into solid-state nanopores. *Nature Nanotechnology*, 5(12):874–877.

Happel, J. and Brenner, H. (1983). *Low Reynolds number hydrodynamics: with special applications to particulate media*. Springer, 1st edition.

Hecht, E. (2002). *Optics*. Addison Wesley, 4th edition.

Heidarzadeh, T. (2008). *A history of physical theories of comets, from Aristotle to Whipple*. Springer, 1st edition.

Hernández-Ainsa, S., Bell, N. A. W., Thacker, V. V., Göpfrich, K., Misiunas, K., Fuentes-Perez, M. E., Moreno-Herrero, F., and Keyser, U. F. (2013a). DNA origami nanopores for controlling DNA translocation. *ACS Nano*, 7(7):6024–6030.

Hernández-Ainsa, S., Muus, C., Bell, N. A. W., Steinbock, L. J., Thacker, V. V., and Keyser, U. F. (2013b). Lipid-coated nanocapillaries for DNA sensing. *Analyst*, 138(1):104–106.

Herrero-Galán, E., Fuentes-Perez, M. E., Carrasco, C., Valpuesta, J. M., Carrascosa, J. L., Moreno-Herrero, F., and Arias-Gonzalez, J. R. (2012). Mechanical identities of RNA and DNA double helices unveiled at the single-molecule level. *Journal of the American Chemical Society*, 135(1):122–131.

Hong, J., Edel, J. B., and DeMello, A. J. (2009). Micro- and nanofluidic systems for high-throughput biological screening. *Drug Discovery Today*, 14(3):134–146.

Hormeño, S. and Arias-Gonzalez, J. R. (2006). Exploring mechanochemical processes in the cell with optical tweezers. *Biology of the Cell*, 98(12):679–695.

Hormeño, S., Ibarra, B., Valpuesta, J. M., Carrascosa, J. L., and Arias-Gonzalez, J. R. (2012). Mechanical stability of low-humidity single DNA molecules. *Biopolymers*, 97(4):199–208.

Hormeño Torres, S. (2010). *Biofísica de centrosomas y ADN mediante manipulación óptica*. PhD thesis, Universidad Autónoma de Madrid.

Huguet, J. M., Bizarro, C. V., Smith, S. B., Ritort, F., Forns, N., and Bustamante, C. (2010). Single-molecule derivation of salt dependent base-pair free energies in DNA. *Proceedings of the National Academy of Sciences of the United States of America*, 107(35):15431–15436.

Huguet i Casades, J. M. (2010). *Statistical and thermodynamic properties of DNA unzipping experiments with optical tweezers*. PhD thesis, Universitat de Barcelona.

Huisstede, J. H. G., Subramaniam, V., and Bennink, M. L. (2007). Combining optical tweezers and scanning probe microscopy to study DNA-protein interactions. *Microscopy Research and Technique*, 70(1):26–33.

Huisstede, J. H. G., van der Werf, K. O., Bennink, M. L., and Subramaniam, V. (2005). Force detection in optical tweezers using backscattered light. *Optics Express*, 13(4):1113–1123.

Israelachvili, J. N. (2011). *Intermolecular and surface forces*. Academic Press, 3rd edition.

Jackson, J. D. (1975). *Classical electrodynamics*. Wiley, 2nd edition.

Jahnel, M., Behrndt, M., Jannasch, A., Schäffer, E., and Grill, S. W. (2011). Measuring the complete force field of an optical trap. *Optics Letters*, 36(7):1260–1262.

JPK Instruments (2014). NanoTracker 2 – optical tweezers platform. Available from: `http://www.jpk.com/nanotracker-2-overview.388.en.html`.

Kasianowicz, J. J., Brandin, E., Branton, D., and Deamer, D. W. (1996). Characterization of individual polynucleotide molecules using a membrane channel. *Proceedings of the National Academy of Sciences of the United States of America*, 93(24):13770–13773.

Kato, H., Nishizaka, T., Iga, T., Kinosita Jr., K., and Ishiwata, S. (1999). Imaging of thermal activation of actomyosin motors. *Proceedings of the National Academy of Sciences of the United States of America*, 96(17):9602–9606.

Keyser, U. F., Krapf, D., Koeleman, B. N., Smeets, R. M. M., Dekker, N. H., and Dekker, C. (2005). Nanopore tomography of a laser focus. *Nano Letters*, 5(11):2253–2256.

Keyser, U. F., van der Does, J., Dekker, C., and Dekker, N. H. (2006). Optical tweezers for force measurements on DNA in nanopores. *Review of Scientific Instruments*, 77(10):105105.

Keyser, U. F., van Dorp, S., and Lemay, S. G. (2010). Tether forces in DNA electrophoresis. *Chemical Society Reviews*, 39(3):939–947.

Kim, K. and Saleh, O. A. (2009). A high-resolution magnetic tweezer for single-molecule measurements. *Nucleic Acids Research*, 37(20):e136.

La Porta, A. and Wang, M. D. (2004). Optical torque wrench: angular trapping, rotation, and torque detection of quartz microparticles. *Physical Review Letters*, 92(19):190801.

Landau, L. D. (1944). A new exact solution of the Navier–Stokes equations. *Doklady Akademii Nauk SSSR*, 43(7):299–301.

Laohakunakorn, N. (2012). *Combined optical tweezers and nanocapillaries for single-molecule analysis*. Thesis for the Certificate of Postgraduate Studies, University of Cambridge.

Lee, M., Kim, S. H., and Hong, S.-C. (2010). Minute negative superhelicity is sufficient to induce the B–Z transition in the presence of low tension. *Proceedings of the National Academy of Sciences of the United States of America*, 107(11):4985–4990.

Lee, W. M., Reece, P. J., Marchington, R. F., Metzger, N. K., and Dholakia, K. (2007). Construction and calibration of an optical trap on a fluorescence optical microscope. *Nature Protocols*, 2(12):3226–3238.

Lionnet, T., Allemand, J.-F., Revyakin, A., Strick, T. R., Saleh, O. A., Bensimon, D., and Croquette, V. (2012). Single-molecule studies using magnetic traps. *Cold Spring Harbor Protocols*, 2012(1):34–49.

Lipfert, J., Hao, X., and Dekker, N. H. (2009). Quantitative modeling and optimization of magnetic tweezers. *Biophysical Journal*, 96(12):5040–5049.

Lipfert, J., Kerssemakers, J. W. J., Jager, T., and Dekker, N. H. (2010). Magnetic torque tweezers: measuring torsional stiffness in DNA and RecA–DNA filaments. *Nature Methods*, 7(12):977–980.

Lyklema, J. (2005). *Fundamentals of interface and colloid science – volume V: soft colloids*. Academic Press, 1st edition.

Mackintosh, S. G. and Raney, K. D. (2006). DNA unwinding and protein displacement by Superfamily 1 and Superfamily 2 helicases. *Nucleic Acids Research*, 34(15):4154–4159.

Mahamdeh, M., Pérez Campos, C., and Schäffer, E. (2011). Under-filling trapping objectives optimizes the use of the available laser power in optical tweezers. *Optics Express*, 19(12):11759–11658.

Mahamdeh, M. and Schäffer, E. (2009). Optical tweezers with millikelvin precision of temperature-controlled objectives and base-pair resolution. *Optics Express*, 17(19):17190–17199.

Maiman, T. H. (1960). Stimulated optical radiation in ruby. *Nature*, 187:493–494.

Maloney, A., Herskowitz, L. J., and Koch, S. J. (2011). Effects of surface passivation on gliding motility assays. *PLoS ONE*, 6(6):e19522.

Manosas, M., Perumal, S. K., Bianco, P. R., Ritort, F., Benkovic, S. J., and Croquette, V. (2013). RecG and UvsW catalyse robust DNA rewinding critical for stalled DNA replication fork rescue. *Nature Communications*, 4(2368):1–11.

Manosas, M., Spiering, M. M., Zhuang, Z., Benkovic, S. J., and Croquette, V. (2009). Coupling DNA unwinding activity with primer synthesis in the bacteriophage T4 primosome. *Nature Chemical Biology*, 5(12):904–912.

Mao, H., Arias-Gonzalez, J. R., Smith, S. B., Tinoco Jr., I., and Bustamante, C. (2005). Temperature control methods in a laser tweezers system. *Biophysical Journal*, 89(2):1308–1316.

Marko, J. F. and Siggia, E. D. (1995). Stretching DNA. *Macromolecules*, 28(26):8759–8770.

Mathwig, K., Mampallil, D., Kang, S., and Lemay, S. G. (2012). Electrical cross-correlation spectroscopy: measuring picoliter-per-minute flows in nanochannels. *Physical Review Letters*, 109(11):118302.

Maxwell, J. C. (1861). XXV. On physical lines of force: part I. – The theory of molecular vortices applied to magnetic phenomena. *The London, Edinburgh, and Dublin Philosophical Magazine and Journal of Science*, 21(139):161–175.

McClelland, S. E., Dryden, D. T. F., and Szczelkun, M. D. (2005). Continuous assays for DNA translocation using fluorescent triplex dissociation: application to type I restriction endonucleases. *Journal of Molecular Biology*, 348(4):895–915.

McGee, T. D. (1988). Electrical resistance temperature measurement using metallic sensors. In *Principles and methods of temperature measurement*, chapter 8. Wiley, 2nd edition.

Mihajlović, G., Brunet, N. M., Trbović, J., Xiong, P., von Molnár, S., and Chase, P. B. (2004). All-electrical switching and control mechanism for actomyosin-powered nanoactuators. *Applied Physics Letters*, 85(6):1060–1062.

Moffitt, J. R., Chemla, Y. R., Smith, S. B., and Bustamante, C. (2008). Recent advances in optical tweezers. *Annual Review of Biochemistry*, 77:205–228.

Morin, J. A., Cao, F. J., Lázaro, J. M., Arias-Gonzalez, J. R., Valpuesta, J. M., Carrascosa, J. L., Salas, M., and Ibarra, B. (2012). Active DNA unwinding dynamics during processive DNA replication. *Proceedings of the National Academy of Sciences of the United States of America*, 109(21):8115–8120.

Morin Lantero, J. A. (2013). *Estudio a nivel de moléculas individuales de la actividad de replicación del ADN de la polimerasa del bacteriófago Phi29*. PhD thesis, Universidad Autónoma de Madrid.

Murphy, M. C., Rasnik, I., Cheng, W., Lohman, T. M., and Ha, T. (2004). Probing single-stranded DNA conformational flexibility using fluorescence spectroscopy. *Biophysical Journal*, 86(4):2530–2537.

Neher, E. and Sakmann, B. (1976). Single-channel currents recorded from membrane of denervated frog muscle fibres. *Nature*, 260(5554):799–802.

Nelson, P. (2003). *Biological physics: energy, information, life*. W. H. Freeman, 1st edition.

Neuman, K. C. and Block, S. M. (2004). Optical trapping. *Review of Scientific Instruments*, 75(9):2787–2809.

Neuman, K. C., Chadd, E. H., Liou, G. F., Bergman, K., and Block, S. M. (1999). Characterization of photodamage to Escherichia coli in optical traps. *Biophysical Journal*, 77(5):2856–2863.

Neuman, K. C., Lionnet, T., and Allemand, J. F. (2007). Single-molecule micromanipulation techniques. *Annual Review of Material Research*, 37:33–67.

Neuman, K. C. and Nagy, A. (2008). Single-molecule force spectroscopy: optical tweezers, magnetic tweezers and atomic force microscopy. *Nature Methods*, 5(6):491–505.

Nieminen, T. A., Loke, V. L. Y., Stilgoe, A. B., Knöner, G., Brańczyk, A. M., Heckenberg, N. R., and Rubinsztein-Dunlop, H. (2007). Optical tweezers computational toolbox. *Journal of Optics A: Pure and Applied Optics*, 9(8):S196–S203.

Odijk, T. (1995). Stiff chains and filaments under tension. *Macromolecules*, 28(20):7016–7018.

Otto, O. (2011). *Single macromolecules under tension and in confinement*. PhD thesis, University of Cambridge.

Otto, O., Czerwinski, F., Gornall, J. L., Stober, G., Oddershede, L. B., Seidel, R., and Keyser, U. F. (2010). Real-time particle tracking at 10,000 fps using optical fiber illumination. *Optics Express*, 18(22):22722–22733.

Otto, O., Gornall, J. L., Stober, G., Czerwinski, F., Seidel, R., and Keyser, U. F. (2011a). High-speed video-based tracking of optically trapped colloids. *Journal of Optics*, 13(4):044011.

Otto, O., Gutsche, C., Kremer, F., and Keyser, U. F. (2008). Optical tweezers with 2.5 kHz bandwidth video detection for single-colloid electrophoresis. *Review of Scientific Instruments*, 79(2):23710.

Otto, O., Steinbock, L. J., Wong, D. W., Gornall, J. L., and Keyser, U. F. (2011b). Note: Direct force and ionic-current measurements on DNA in a nanocapillary. *Review of Scientific Instruments*, 82(8):86102.

Oxford Nanopore Technologies (2012). The MinION device: a miniaturised sensing system. Available from: `http://www.nanoporetech.com/technology/the-minion-device-a-miniaturised-sensing-system`.

Park, J.-S., Lee, K. J., Hong, S.-C., and Hyon, J.-Y. (2008). Temperature dependence of DNA elasticity and cisplatin activity studied with a temperature-controlled magnetic tweezers system. *Journal of the Korean Physical Society*, 52(6):1927–1931.

Patel, D. (1994). *Gel electrophoresis: essential data*. Wiley, 1st edition.

Perkins, T. T., Li, H.-W., Dalal, R. V., Gelles, J., and Block, S. M. (2004). Forward and reverse motion of single RecBCD molecules on DNA. *Biophysical Journal*, 86(3):1640–1648.

Peterman, E. J. G., Gittes, F., and Schmidt, C. F. (2003). Laser-induced heating in optical traps. *Biophysical Journal*, 84(2):1308–1316.

PicoTwist (2006). Magnetic trap apparatus. Available from: `http://www.picotwist.com`.

Purcell, E. M. (1977). Life at low Reynolds number. *American Journal of Physics*, 45(1):3–11.

Reihani, S. N. S., Mir, S. A., Richardson, A. C., and Oddershede, L. B. (2011). Significant improvement of optical traps by tuning standard water immersion objectives. *Journal of Optics*, 13(10):105301.

Ribeck, N. and Saleh, O. A. (2008). Multiplexed single-molecule measurements with magnetic tweezers. *Review of Scientific Instruments*, 79(9):94301.

Richardson, A. C., Reihani, S. N. S., and Oddershede, L. B. (2008). Non-harmonic potential of a single beam optical trap. *Optics Express*, 16(20):15709–15717.

Rickgauer, J. P., Fuller, D. N., and Smith, D. E. (2006). DNA as a metrology standard for length and force measurements with optical tweezers. *Biophysical Journal*, 91(11):4253–4257.

Ritort, F. (2006). Single-molecule experiments in biological physics: methods and applications. *Journal of Physics: Condensed Matter*, 18(32):R531–R583.

Rohrbach, A. (2005). Stiffness of optical traps: quantitative agreement between experiment and electromagnetic theory. *Physical Review Letters*, 95(16):168102.

Rondelez, Y., Tresset, G., Nakashima, T., Kato-Yamada, Y., Fujita, H., Takeuchi, S., and Noji, H. (2005). Highly coupled ATP synthesis by F1-ATPase single molecules. *Nature*, 433(7027):773–777.

Rotman, B. (1961). Measurement of activity of single molecules of beta-D-galactosidase. *Proceedings of the National Academy of Sciences of the United States of America*, 47:1981–1991.

Sacanna, S., Irvine, W. T. M., Chaikin, P. M., and Pine, D. J. (2010). Lock and key colloids. *Nature*, 464(7288):575–578.

Saikrishnan, K., Yeeles, J. T. P., Gilhooly, N. S., Krajewski, W. W., Dillingham, M. S., and Wigley, D. B. (2012). Insights into Chi recognition from the structure of an AddAB-type helicase-nuclease complex. *The EMBO Journal*, 31(6):1568–1578.

Santiago, J. G., Wereley, S. T., Meinhart, C. D., Beebe, D. J., and Adrian, R. J. (1998). A particle image velocimetry system for microfluidics. *Experiments in Fluids*, 25(4):316–319.

Schneider, G. F. and Dekker, C. (2012). DNA sequencing with nanopores. *Nature Biotechnology*, 30(4):326–328.

Seidel, R., Bloom, J. G. P., Dekker, C., and Szczelkun, M. D. (2008). Motor step size and ATP coupling efficiency of the dsDNA translocase EcoR124I. *The EMBO Journal*, 27(9):1388–1398.

Seidel, R. and Dekker, C. (2007). Single-molecule studies of nucleic acid motors. *Current Opinion in Structural Biology*, 17(1):80–86.

Shivashankar, G. V., Stolovitzky, G., and Libchaber, A. (1998). Backscattering from a tethered bead as a probe of DNA flexibility. *Applied Physics Letters*, 73(3):291–293.

Simmons, R. M., Finer, J. T., Chu, S., and Spudich, J. A. (1996). Quantitative measurements of force and displacement using an optical trap. *Biophysical Journal*, 70(4):1813–1822.

Simpson, N. B., McGloin, D., Dholakia, K., Allen, L., and Padgett, M. J. (1998). Optical tweezers with increased axial trapping efficiency. *Journal of Modern Optics*, 45(9):1943–1949.

Sinha, S., Rossi, M. P., Mattia, D., Gogotsi, Y., and Bau, H. H. (2007). Induction and measurement of minute flow rates through nanopipes. *Physics of Fluids*, 19(1):013603.

Siwy, Z. S. (2006). Ion-current rectification in nanopores and nanotubes with broken symmetry. *Advanced Functional Materials*, 16(6):735–746.

Smith, D. E., Tans, S. J., Smith, S. B., Grimes, S., Anderson, D. L., and Bustamante, C. (2001). The bacteriophage phi29 portal motor can package DNA against a large internal force. *Nature*, 413(6857):748–752.

Smith, S. B. (2008). TweezersLAB – pipette puller assembly. Available from: `http://tweezerslab.unipr.it/cgi-bin/mt/assemblies.pl/Show?_id=7c1b`.

Smith, S. B., Cui, Y., and Bustamante, C. (1996). Overstretching B-DNA: the elastic response of individual double-stranded and single-stranded DNA molecules. *Science*, 271(5250):795–799.

Smith, S. B., Cui, Y., and Bustamante, C. (2003). Optical-trap force transducer that operates by direct measurement of light momentum. *Methods in Enzymology*, 361:134–162.

Smith, S. B., Finzi, L., and Bustamante, C. (1992). Direct mechanical measurements of the elasticity of single DNA molecules by using magnetic beads. *Science*, 258(5085):1122–1126.

Squire, H. B. (1951). The round laminar jet. *The Quarterly Journal of Mechanics and Applied Mathematics*, 4(3):321–329.

Steinbock, L. J. (2011). *Micro- and nanocapillaries for resistive pulse analysis of microparticles and single molecules*. PhD thesis, University of Cambridge.

Steinbock, L. J., Bulushev, R. D., Krishnan, S., Raillon, C., and Radenovic, A. (2013). DNA translocation through low-noise glass nanopores. *ACS Nano*, 7(12):11255–11262.

Steinbock, L. J., Otto, O., Chimerel, C., Gornall, J., and Keyser, U. F. (2010a). Detecting DNA folding with nanocapillaries. *Nano Letters*, 10(7):2493–2497.

Steinbock, L. J., Otto, O., Skarstam, D. R., Jahn, S., Chimerel, C., Gornall, J. L., and Keyser, U. F. (2010b). Probing DNA with micro- and nanocapillaries and optical tweezers. *Journal of Physics: Condensed Matter*, 22(45):454113.

Stephenson, W., Keller, S., Santiago, R., Albrecht, J. E., Asare-Okai, P. N., Tenenbaum, S. A., Zuker, M., and Li, P. T. X. (2014). Combining temperature and force to study folding of an RNA hairpin. *Physical Chemistry Chemical Physics*, 16(3):906–917.

Storm, A. J., Storm, C., Chen, J., Zandbergen, H. W., Joanny, J.-F., and Dekker, C. (2005). Fast DNA translocation through a solid-state nanopore. *Nano Letters*, 5(7):1193–1197.

Strick, T. R., Allemand, J. F., Bensimon, D., Bensimon, A., and Croquette, V. (1996). The elasticity of a single supercoiled DNA molecule. *Science*, 271(5257):1835–1837.

Strick, T. R., Allemand, J. F., Bensimon, D., and Croquette, V. (1998). Behavior of supercoiled DNA. *Biophysical Journal*, 74(4):2016–2028.

Strick, T. R., Croquette, V., and Bensimon, D. (2000). Single-molecule analysis of DNA uncoiling by a type II topoisomerase. *Nature*, 404(6780):901–904.

Svoboda, K. and Block, S. M. (1994). Biological applications of optical forces. *Annual Review of Biophysics and Biomolecular Structure*, 23(1):247–285.

Svoboda, K., Schmidt, C. F., Schnapp, B. J., and Block, S. M. (1993). Direct observation of kinesin stepping by optical trapping interferometry. *Nature*, 365(6448):721–727.

Thacker, V. V., Ghosal, S., Hernández-Ainsa, S., Bell, N. A. W., and Keyser, U. F. (2012). Studying DNA translocation in nanocapillaries using single molecule fluorescence. *Applied Physics Letters*, 101(22):223704.

van Dorp, S., Keyser, U. F., Dekker, N. H., Dekker, C., and Lemay, S. G. (2009). Origin of the electrophoretic force on DNA in solid-state nanopores. *Nature Physics*, 5(5):347–351.

van Gent, D. C., Hoeijmakers, J. H. J., and Kanaar, R. (2001). Chromosomal stability and the DNA double-stranded break connection. *Nature Review Genetics*, 2(3):196–206.

van Loenhout, M. T. J., de Vlaminck, I., Flebus, B., den Blanken, J. F., Zweifel, L. P., Hooning, K. M., Kerssemakers, J. W. J., and Dekker, C. (2013). Scanning a DNA molecule for bound proteins using hybrid magnetic and optical tweezers. *PLoS ONE*, 8(6):e65329.

van Mameren, J., Wuite, G. J. L., and Heller, I. (2011). Introduction to optical tweezers: background, system design, and commercial solutions. In *Single Molecule Analysis – Methods and Protocols*, chapter 1. Humana Press.

Verdeny, I., Farré, A., Mas, J., López-Quesada, C., Martín-Badosa, E., and Montes-Usategui, M. (2011). Optical trapping: a review of essential concepts. *Óptica Pura y Aplicada*, 44(3):527–551.

Vermeulen, K. C., Wuite, G. J. L., Stienen, G. J. M., and Schmidt, C. F. (2006). Optical trap stiffness in the presence and absence of spherical aberrations. *Applied Optics*, 45(8):1812–1819.

Vilfan, I. D., Lipfert, J., Koster, D. A., Lemay, S. G., and Dekker, N. H. (2009). Magnetic tweezers for single-molecule experiments. In *Handbook of Single-Molecule Biophysics*, chapter 13. Springer.

Wagner, C., Stangner, T., Gutsche, C., Ueberschär, O., and Kremer, F. (2011). Optical tweezers setup with optical height detection and active height regulation under white light illumination. *Journal of Optics*, 13(11):115302.

Wang, B., Ho, J., Fei, J., Gonzalez Jr., R. L., and Lin, Q. (2011). A microfluidic approach for investigating the temperature dependence of biomolecular activity with single-molecule resolution. *Lab on a Chip*, 11(2):274–281.

Wang, G. R. (2005). Laser induced fluorescence photobleaching anemometer for microfluidic devices. *Lab on a Chip*, 5(4):450–456.

Wanunu, M. (2012). Nanopores: a journey towards DNA sequencing. *Physics of Life Reviews*, 9(2):125–158.

Watanabe-Nakayama, T., Toyabe, S., Kudo, S., Sugiyama, S., Yoshida, M., and Muneyuki, E. (2008). Effect of external torque on the ATP-driven rotation of F1-ATPase. *Biochemical and Biophysical Research Communications*, 366(4):951–957.

Watson, J. D. and Crick, F. H. C. (1953). Molecular structure of nucleic acids: a structure for deoxyribose nucleic acid. *Nature*, 171(4356):737–738.

Wells, D. B., Abramkina, V., and Aksimentiev, A. (2007). Exploring transmembrane transport through α-hemolysin with grid-steered molecular dynamics. *The Journal of Chemical Physics*, 127(12):125101.

Wenner, J. R., Williams, M. C., Rouzina, I., and Bloomfield, V. A. (2002). Salt dependence of the elasticity and overstretching transition of single DNA molecules. *Biophysical Journal*, 82(6):3160–3169.

Williams, M. C., Wenner, J. R., Rouzina, I., and Bloomfield, V. A. (2001a). Effect of pH on the overstretching transition of double-stranded DNA: evidence of force-induced DNA melting. *Biophysical Journal*, 80(2):874–881.

Williams, M. C., Wenner, J. R., Rouzina, I., and Bloomfield, V. A. (2001b). Entropy and heat capacity of DNA melting from temperature dependence of single molecule stretching. *Biophysical Journal*, 80(4):1932–1939.

Yeeles, J. T. P., Cammack, R., and Dillingham, M. S. (2009). An iron-sulfur cluster is essential for the binding of broken DNA by AddAB-type helicase–nucleases. *Journal of Biological Chemistry*, 284(12):7746–7755.

Yeeles, J. T. P. and Dillingham, M. S. (2007). A dual-nuclease mechanism for DNA break processing by AddAB-type helicase–nucleases. *Journal of Molecular Biology*, 371(1):66–78.

Yeeles, J. T. P. and Dillingham, M. S. (2010). The processing of double-stranded DNA breaks for recombinational repair by helicase–nuclease complexes. *DNA repair*, 9(3):276–285.

Yeeles, J. T. P., Gwynn, E. J., Webb, M. R., and Dillingham, M. S. (2011a). The AddAB helicase–nuclease catalyses rapid and processive DNA unwinding using a single Superfamily 1A motor domain. *Nucleic Acids Research*, 39(6):2271–2285.

Yeeles, J. T. P., van Aelst, K., Dillingham, M. S., and Moreno-Herrero, F. (2011b). Recombination hotspots and single-stranded DNA binding proteins couple DNA translocation to DNA unwinding by the AddAB helicase–nuclease. *Molecular Cell*, 42(6):806–816.

Ying, L. (2009). Applications of nanopipettes in bionanotechnology. *Biochemical Society Transactions*, 37(4):702–706.

Zhang, X., Chen, H., Fu, H., Doyle, P. S., and Yan, J. (2012). Two distinct overstretched DNA structures revealed by single-molecule thermodynamics measurements. *Proceedings of the National Academy of Sciences of the United States of America*, 109(21):8103–8108.

Ziemann, F., Rädler, J., and Sackmann, E. (1994). Local measurements of viscoelastic moduli of entangled actin networks using an oscillating magnetic bead microrheometer. *Biophysical Journal*, 66(6):2210–2216.

Zuttion, F. (2013). *Construction of a temperature-controlled fluid cell assembly to study molecular motors with magnetic tweezers*. Master's thesis, Università degli Studi di Trieste.